In-situ Präparation von komplexen supraleitenden und ferroelektrischen Heterostrukturen mittels gepulster Laser Deposition

Dissertation
zur Erlangung des Grades

Doktor der Naturwissenschaften (Dr. rer. nat.)

am Fachbereich Physik
der Johannes Gutenberg Universität
in Mainz

von
Dipl. Phys. Markus Maier
geb. in Traunstein

Mainz, 2001

D77

Jahr der Prüfung : 2001

In-situ Preparation of Complex Superconducting and Ferroelectric Heterostructures by Pulsed Laser Deposition

by

Markus Maier

universität mainz

Mainz, Germany

2001

Contents

1. Introduction 1

2. Technical Aspects of Pulsed Laser Deposition 7

2.1 Principles of Pulsed Laser Deposition 8

2.2 Conception and Construction of a PLD-System 10

2.2.1 The Deposition Chamber 11

2.2.2 The Laser System 14

3. Theoretical Approaches in Pulsed Laser Deposition 17

3.1 Laser-Target Interaction - Ablation 19

3.1.1 Primary Mechanisms 20

3.1.2 Secondary Mechanisms 24

3.2 Plasma Formation and Propagation 26

3.3 Plasma-Substrate Interaction - Film Nucleation 29

3.3.1 Fundamental Growth Modes of Thin Films 29

3.3.2 Interrelation of Pulsed Material Deposition and Processing Parameters 32

4. Controlling Thin Film Growth by Heterostructures 39

4.1 Epitaxy and Lattice Mismatch Accommodation 39

4.2 Material Properties 46

4.3 The Role of Buffer Layers in General 52

4.4 Buffers for Functional Oxides on Silicon 53

4.4.1 Deposition of YSZ as the first Buffer Layer on Silicon 54

4.4.2 Dielectric Properties of YSZ 57

4.5 $BaZrO_3$ as a Buffer Layer for HTSC Applications 61
4.5.1 Dielectric Properties of $BaZrO_3$ 61
4.5.2 $BaZrO_3$ as a Buffer Layer for $YBa_2Cu_3O_{7-\delta}$ 63
4.5.3 $BaZrO_3$ as a Buffer Layer for HTSC on Silicon 66

5. Lattice Engineering for Artificial Josephson Junctions 71

5.1 Preliminary Remarks on the Josephson Effect 71

5.2 Types of Josephson Junctions 75
5.2.1 Josephson Contacts with Artificial Barriers 76
5.2.2 Grain Boundary Contacts 77

5.3 Growth and Control of In-plane Orientation 81
5.3.1 Superconducting Properties of the $YBa_2Cu_3O_{7-\delta}$ Layer 85
5.3.2 Structuring Steps for Bi-epitaxial Junctions 87

6. Buffer Layers for Ferroelectric $SrBi_2Ta_2O_9$ on Silicon 97

6.1 Fundamentals of Ferroelectricity 99

6.2 Growth of $SrBi_2Ta_2O_9$ Thin Films on Silicon 103
6.2.1 Properties of $SrBi_2Ta_2O_9$ 104
6.2.2 Structural Characterisation 105

6.3 Dielectric and Ferroelectric Properties of $SrBi_2Ta_2O_9$ 111
6.3.1 Preliminary Remarks on Diode Structures 111
6.3.2 Results on Diode Structures 113
6.3.3 Results on Capacitor Structures 117

6.4 Ferroelectric Domains in $SrBi_2Ta_2O_9$ 121

6.5 $SrZrO_3$ as an Alternative Buffer Layer for $SrBi_2Ta_2O_9$ 129
6.5.1 Structural Characterisation 130
6.5.2 Dielectric Properties 142

7. Conclusion 149

8. Appendix 153

Bibliography 157

List of Figures

Figure 2.1: Schematic illustration of the PLD chamber and principle of the PLD process ... 8
Figure 2.2: Picture of the PLD system. ... 11
Figure 2.3: Schematic illustration of the sixfold rotatable target holder ... 12
Figure 2.4: Schematic drawing and picture of the heater ... 13
Figure 2.5: Schematic drawing of the laser beam guidance ... 15
Figure 3.1: Plasma formation, propagation and condensation ... 18
Figure 3.2: Cone formation on a $YBa_2Cu_3O_{7-\delta}$ target ... 22
Figure 3.3: Exfoliational sputtering ... 23
Figure 3.4: Hydrodynamic sputtering ... 24
Figure 3.5: $R(t)$-plots of the plasma expansion front ... 28
Figure 3.6: Schematic diagram of atomic processes in thin film nucleation ... 30
Figure 3.7: Vollmer-Weber nucleation and growth ... 30
Figure 3.8: Frank-van der Merwe nucleation and growth ... 31
Figure 3.9: Stanski-Kratinov nucleation and growth ... 31
Figure 4.1: Schematic illustration of a cube-to-cube orientation ... 40
Figure 4.2: Schematic illustration of a 45° in-plane orientation ... 41
Figure 4.3: Schematic illustration of a 45° out-of-plane rotation ... 41
Figure 4.4: Simple cubic lattice of a perovskite ... 46
Figure 4.5: The crystal structure of $SrZrO_3$ ... 49
Figure 4.6: The crystal structure of $YBa_2Cu_3O_{7-\delta}$ ... 51
Figure 4.7: Low-angle XRD patterns of YSZ on silicon ... 56

Figure 4.8: XRD patterns of YSZ on silicon deposited by one- and two-step deposition technique 57
Figure 4.9: *C(V)*-characteristics of YSZ films deposited on silicon 59
Figure 4.10: Dielectric constant of a $BaZrO_3$ film on Nb-doped $SrTiO_3$ and cole-cole plot 62
Figure 4.11: XRD patterns of a $YBa_2Cu_3O_{7-\delta}$ film deposited on a $BaZrO_3$ buffer layer on $SrTiO_3$ 64
Figure 4.12: Resistivity measurements of $YBa_2Cu_3O_{7-\delta}$ films deposited on bare $SrTiO_3$ and BZO-buffered $SrTiO_3$ substrates. 65
Figure 4.13: XRD pattern of a Si/YSZ/$BaZrO_3$/$YBa_2Cu_3O_{7-\delta}$ heterostructure with (011)-oriented $BaZrO_3$ 67
Figure 4.14: In-plane orientation of $YBa_2Cu_3O_{7-\delta}$ deposited on silicon with a YSZ/$BaZrO_3$ buffer layer combination. 68
Figure 4.15: Resistivity measurement and AFM measurement of a $YBa_2Cu_3O_{7-\delta}$ film deposited on YSZ/$BaZrO_3$-buffered silicon 69
Figure 5.1: *I(V)*-characteristics of overdamped and underdamped Josephson junctions 74
Figure 5.2: Schematic illustration of a step-edge Josephson contact 76
Figure 5.3: Schematic illustration of a ramp-junction Josephson contact 77
Figure 5.4: Schematic illustration of a bi-crystal Josephson contact 77
Figure 5.5: Schematic illustration of a step-edge Josephson contact 78
Figure 5.6: Schematic illustration of a bi-epitaxial Josephson contact 79
Figure 5.7: Schematic illustration of two possible layer sequences with continuos lattice match by $BaZrO_3$ and YSZ. 82
Figure 5.8: XRD patterns of a $YBa_2Cu_3O_{7-\delta}$ film on a CeO_2/$BaZrO_3$ and a CeO_2/YSZ/$BaZrO_3$ buffer layer set on $SrTiO_3$ 83
Figure 5.9: XRD pattern of a $YBa_2Cu_3O_{7-\delta}$ film deposited on a $BaZrO_3$/YSZ/CeO_2 buffer layer sequence on $SrTiO_3$ 84
Figure 5.10: In-plane relation of the layer sequence 85
Figure 5.11: Resistivity and critical current of a $YBa_2Cu_3O_{7-\delta}$ layer deposited in-situ on a trilayer layer set on $SrTiO_3$ 86
Figure 5.12: Possible deposition and structuring sequences for the manufacture of a bi-epitaxial junction 89
Figure 5.13: Low-angle XRD pattern of a $BaZrO_3$/YSZ bi-layer on $SrTiO_3$ 90

Figure 5.14: Surface of a $YBa_2Cu_3O_{7-\delta}$ film deposited on a structured seedlayer ... 91
Figure 5.15: Susceptibility measurement of a $YBa_2Cu_3O_{7-\delta}$ film deposited on an etched heterostructure ... 92
Figure 5.16: Scanning electron microscopy (SEM) measurement of a $YBa_2Cu_3O_{7-\delta}$ film deposited on a $SrTiO_3$ substrate ... 93
Figure 5.17: $R(T)$-curves and $U(I)$-characteristic of a bi-epitaxial Josephson junction ... 94
Figure 5.18: AFM image of a grain boundary junction and optical microscopy image of the structure ... 96
Figure 6.1: Circuit and cross section of a FRAM device ... 98
Figure 6.2: Cross section of a MFS-FET device ... 98
Figure 6.3: Frequency dependence of the dielectric constant ε and the dielectric loss tan(δ) according to the Debye-model ... 101
Figure 6.4: The structure of $SrBi_2Ta_2O_9$ ... 104
Figure 6.5: XRD pattern of a $SrBi_2Ta_2O_9$ film deposited directly on silicon ... 106
Figure 6.6: XRD patterns of pc-SBT on a YSZ buffer layer and *c*-axis oriented $SrBi_2Ta_2O_9$ on a YSZ/CeO_2 buffer layer set ... 107
Figure 6.7 In-plane orientations of $SrBi_2Ta_2O_9$ under utilisation of a YSZ buffer layer and a YSZ/CeO_2 buffer layer set ... 108
Figure 6.8: AFM measurements of polycrystalline and *c*-axis oriented $SrBi_2Ta_2O_9$ ... 109
Figure 6.9: SEM micrographs of $SrBi_2Ta_2O_9$ films deposited at different oxygen pressures ... 110
Figure 6.10: Simulation of a *C(V)*-characteristic for an ideal MIS diode ... 111
Figure 6.11: *C(V)*-characteristic of a $SrBi_2Ta_2O_9$ film deposited on silicon ... 114
Figure 6.12: Frequency dependence of dielectric constant and loss of a polycrystalline $SrBi_2Ta_2O_9$ film on silicon ... 115
Figure 6.13: *C(V)*-characteristics of pc-SBT and *c*-axis oriented $SrBi_2Ta_2O_9$ films on silicon ... 117
Figure 6.14: *C(V)*-characteristic and *P*(*E*)-curve of a Pt/SBT/Au capacitor ... 118
Figure 6.15: Frequency dependence of the dielectric constant and Rayleigh parameters ... 119

Figure 6.16: Polarisation change between two ferroelectric domains 121
Figure 6.17: Typical *P*(*E*)-hysteresis of a ferroelectric 122
Figure 6.18: Topography and piezoelectric response of $SrBi_2Ta_2O_9$ imaged by AFM 124
Figure 6.19: Ferroelectric domain and domain wall width within a $SrBi_2Ta_2O_9$ grain 125
Figure 6.20: Switching of domains in $SrBi_2Ta_2O_9$ 126
Figure 6.21: Surface oscillation amplitude of a $SrBi_2Ta_2O_9$ film versus distance in nc-AFM mode 128
Figure 6.22: XRD pattern of a $SrZrO_3$ film deposited on YSZ-buffered silicon 132
Figure 6.23: XRD patterns of $SrBi_2Ta_2O_9$ films deposited on YSZ/$SrZrO_3$-buffered silicon at different pressures and temperatures 133
Figure 6.24: AFM measurements of $SrBi_2Ta_2O_9$ films deposited on YSZ/$SrZrO_3$-buffered silicon at different oxygen pressures 135
Figure 6.25: In-plane alignment of $SrBi_2Ta_2O_9$ grains on YSZ/$SrZrO_3$-buffered silicon 136
Figure 6.26: Four circle XRD measurement of a Si/YSZ/$SrZrO_3$ hetero-structure 137
Figure 6.27: Growth model for *a*-axis oriented $SrZrO_3$ on top of YSZ 138
Figure 6.28: Plane scans of a $SrBi_2Ta_2O_9$ film deposited on YSZ/$SrZrO_3$-buffered silicon 139
Figure 6.29: Growth model of (100)- and (116)-oriented $SrBi_2Ta_2O_9$ on top of a single $SrZrO_3$ domain 140
Figure 6.30: *C(V)*-characteristics of a YSZ layer and a YSZ/$SrZrO_3$ bi-layer on silicon 142
Figure 6.31: Frequency dependence of capacitance and dielectric constant of YSZ/SZO and the YSZ/SZO/$SrBi_2Ta_2O_9$ 144
Figure 6.32: *C(V)*-characteristic of a $SrBi_2Ta_2O_9$ layer with mixed (100)/(116)-orientation 145
Figure 6.33: Grain morphology and ferroelectric domains in differently oriented $SrBi_2Ta_2O_9$ films 146

List of Tables

Table 3.1: Measurement techniques for target properties and plasma diagnostics. 19

Table 4.1: Lattice mismatch and observed in-plane relations..... 42

Table 4.2: Material properties 47

Table 5.1: Layer sequences for bi-epitaxial Josephson junctions..... 80

Table 6.1: Properties of $SrBi_2Ta_2O_9$ 105

Table 8.1: History of pulsed laser deposition..... 153

Table 8.2: Deposition parameters 155

Table 8.3: Target preparation parameters 156

1. Introduction

Interest in pulsed laser deposition (PLD) as a versatile technique to deposit thin films of complex materials is growing rapidly. The success PLD has had in the deposition of a wide variety of materials has spurred activities world wide. The reasons for this increase of research activity is, that virtually any material from pure elements to multi-component materials can be deposited. The major breakthrough of PLD was triggered by the successful growth of high-T_c superconducting films in 1987 [Bed 87], which literally lifted the PLD method off the ground [Dij 87, Wu 90]. The ease, with which oxide ceramic materials can be grown as high quality thin films nowadays makes PLD an important research tool in physics, materials science and the development of next generation electronics.

The basis for the application of ceramic oxides in electronic circuits was built in the 1950´s, 60´s and 70´s, when high purity materials became available. It has been the driving force for many scientists to explore the multifaceted physical properties of this group of materials. An exceptional example of complex oxidic ceramics is the high-T_c superconductor $YBa_2Cu_3O_{7-\delta}$, which is presently being used for the fabrication of sophisticated multi-layered circuits. Passive devices in high frequency technology or active devices, such as superconducting quantum interference devices (SQUID) for ultra precise detection of magnetic field are assumed to have a technological relevance in the future. Ferroelectric ceramics such as $BaTiO_3$, $Pb(Zr_{1-x}Ti_x)O_3$ and $SrBi_2Ta_2O_9$ are currently employed into state-of-the-art devices for non-volatile memory with improved cycling and fatigue properties. Moreover, the combination of both classes of materials into superconductor-ferroelectric hybrid devices is a challenging subject, currently reported in a variety of publications [Gri 97,

Cer 96, Sch 98]. Another actual application of ceramic oxides is the observed colossal magneto resistance effect, which makes the class of manganates ($La_{1-x}Ca_xMnO_{3-\delta}$, Sr_2FeMO_6 and others) promising materials for magnetic memory devices (MRAM) and magnetic field sensors for read heads of hard disks.

In general, this small selection of a wide variety of ceramic oxide materials and their applications, can be classified into the group of “functional layers”. In contrast, the more simple but nevertheless essential ceramic oxides such as CeO_2, YSZ, and others, in some sense can be classified into the group of “buffer layers”, however, without ignoring their physical properties. The application of these materials in order to allow and to control the growth of functional layers on technical substrates, is the main requirement for all the previously mentioned technological applications of ceramic oxides.

Scope of the Thesis

This work will start describing practical and theoretical aspects of PLD. Consequently, the aspects of epitaxy in complex heterostructures consisting of simple ceramics playing the role as buffers layers and complex ceramics playing the role of functional layers will be discussed. Finally, the last chapters will focus on the use of buffer layers for the growth of functional $YBa_2Cu_3O_{7-\delta}$ and $SrBi_2Ta_2O_9$ thin films, being two important examples for technologically relevant oxidic heterostructures.

The wide field of applications mentioned previously, encouraged us to establish this thin film deposition technique in our group. Thus, *chapter 2* presents the technological aspects of PLD that have been considered. The technological and historical development of PLD is comprehensively reported, and the most essential design criteria and practical construction of a deposition system for the growth of oxidic materials is discussed. The requirements for high quality multilayer devices are met by the development of (i) a multifunctional high temperature substrate heater that guarantees a homogenous substrate temperature and fast sample exchange, (ii) a sophisticated laser beam scanning optics that ensures homogeneous laser energy density and optimal ablation of the target material, and (iii) a sixfold target holder that allows in-situ material selection.

Apart from the technical advantages of PLD and the physical phenomena of various materials that can be deposited by this technique, the PLD process itself is an extremely complex as well as a theoretically challenging physical phenomenon. Theoretical descriptions are multidisciplinary and combine both equilibrium and non-equilibrium processes, thermodynamics and hydrodynamics, and a variety of models, suitable only for parts, but never able to describe the whole PLD process. Hence, *chapter 3* is dedicated to give a review of the presently discussed theoretical approaches in PLD, focussing on the relevant processes and structured according to the sequence of the PLD process itself. However, the last part of chapter 3 might be the one, which attracts the attention of those, who use PLD as a tool for thin film deposition. Herein, the accent is on the influence of processing parameters on film nucleation.

In general, a high crystalline quality and in most cases a specific crystallographic orientation of functional oxidic layers is an important requirement for the investigation of their fundamental properties. Thus, in *chapter 4*, the emphasis is on the use and applicability of a selection of buffer materials in order to allow and even to control the growth of functional layers by heterostructures. Here, PLD proves to be a high flexible tool in order to fabricate most epitaxial heterostructures, consisting of different materials which serve certain purposes. After some general concepts of epitaxy and lattice mismatch accommodation are reported, the focus is on lattice mismatch and resulting epitaxial relations of the materials used in this work. Consecutively, some important material properties are described, and the general requirements to a buffer layer are discussed. Because of its particular chemical and physical properties, YSZ is so far the only buffer layer, which allows the deposition of crystalline oxides on silicon. Therefore, a detailed investigation of deposition methods and thin film properties is reported. Moreover, the ability to control the growth of functional layers on technical substrates by the introduction of additional buffer layers is emphasised by the example of the high-T_c superconductor $YBa_2Cu_3O_{7-\delta}$ on (001)-oriented silicon substrates. Within those examples, the dielectric properties of the buffer layers are investigated.

Being the initial motivation for the design of this PLD system, the aspects of lattice engineering for bi-epitaxial grain boundary Josephson junctions in

high-T_c superconductors (HTSC) are discussed in *chapter 5*. After a general introduction into the physics of Josephson junctions [Jos 62] and a short review of the technical approaches realised hitherto, the accent is on the idea of continuous lattice match [Wu 92] in order to realise bi-epitaxial Josephson junctions. The ability to manufacture such artificial junctions opens a wide field of both technical applications as well as fundamental physics. On the one hand, the optimisation of contact properties and the integration into sophisticated circuits leads to technologically relevant active and passive devices, such as SQUIDs and ultra high frequency oscillators. Due to the complexity of processing steps, these applications in some sense represent a threshold between science and technology. On the other hand, a challenging physical phenomenon is found in the investigation of vortex dynamics (guided vortex motion) in one dimensional pinning potentials of JJ arrays, based on bi-epitaxial grain boundary junctions. However, the basis for both subjects is an adequate deposition and structuring technology for a single junction. Thus, chapter 5 is dedicated to the introduction of $BaZrO_3$ into a new layer sequence for bi-epitaxial grain boundary junctions, using the technique of continuous lattice match. The epitaxy relations of this layer sequence are clarified by means of X-ray diffraction measurements and the exceptional transport properties of an in-situ deposited $YBa_2Cu_3O_{7-\delta}$ layer are presented. Moreover, some preliminary investigations are reported, which focus on the embedding of an etching step into the preparation process of the layer sequence in order to generate a single grain boundary junction. Herein, the interaction of an ion beam with a surface and its impact on the resulting surface morphology of the superconductor is a main issue. Finally, first results on the transport properties of such junctions are reported and the influence of the grain boundary morphology is discussed by means of AFM measurements.

Until the mid-90´s, investigations of ferroelectric ceramics tending to their application in memory device technology, were mainly concentrated on materials such as $Pb(Zr_{1-x}Ti_x)O_3$, $Bi_4Ti_3O_{12}$ and $BaMgF_4$ [Sco 88, Nak 94, Sin 91]. Several reasons, for instance the deterioration of ferroelectric properties with decreasing film thickness, fatigue or interdiffusion with the electrode material, hitherto circumvented the extensive industrial application of those materials. With $SrBi_2Ta_2O_9$, a material that shows no fatigue behaviour up to

10^{12} polarisation switching processes was rediscovered [Mit 69, Des 95]. This fact gained interest of numerous memory manufacturers into this non-volatile and radiation resistant memory material. Thus, as the fundamental memory devices, the Metal-Ferroelectric-Semiconductor-Field-Effect-Transistor (MFS-FET) and the Ferroelectric-Random-Access-Memory (FRAM) as well as some basic principles of ferroelectricity are the starting point of *chapter 6.* Hereafter, the possibility to use buffer layers for ferroelectric $SrBi_2Ta_2O_9$ on silicon in order to control epitaxial *c*-axis growth of $SrBi_2Ta_2O_9$ films by the use of the materials introduced in chapter 4, is clearly shown. The third part of this chapter reports on the investigation of dielectric and ferroelectric properties of $SrBi_2Ta_2O_9$ in MFS-diode- and capacitor-structures, corresponding to an approach to the fundamental units of a memory device and describing the macroscopic properties of the ferroelectric. Moreover, resulting from increasing miniaturisation of device structures, ferroelectric domains are assumed to have a crucial impact on those properties. Thus, the consecutive subchapter concentrates is on microscopic investigations of the ferroelectric domain structure by means of Atomic-Force-Microscopy (AFM) measurements in the “piezo-response” mode. Moreover, “non-contact” AFM measurements have been performed in order to estimate the local magnitude of remanent polarisation and the dielectric constant. Finally, in chapter 6.5 an attempt has been made, to introduce $SrZrO_3$ as an innovative buffer layer to force the growth of $SrBi_2Ta_2O_9$ with its *a*-axis aligned along the substrate normal, in order to take full advantage of the ferroelectric properties of this material.

2. Technical Aspects of Pulsed Laser Deposition

The fabrication of sequential heterostructures consisting of multi-component individual layers requires a versatile technology that allows the in-situ deposition of high quality thin films. Among the many existing deposition techniques, pulsed laser deposition (PLD) is one of the few that allows epitaxial growth of multi-component thin films from single targets. Compared to other techniques like sputtering and molecular beam epitaxy (MBE), PLD incorporates many benefits while overcoming most of their drawbacks. In particular, a relatively simple vacuum system and the wide range of materials that can be deposited are worth mentioning.

In 1965, shortly after the first high-power ruby laser became available (1963), Smith and Turner [Smi 65] demonstrated the possibility of thin film deposition by the use of laser vaporisation. However, the first major breakthrough came in the mid-1970´s when the electronic Q-switch was developed to deliver short pulses with very high peak power density. But a second major breakthrough was triggered by the successful growth of high-T_c superconducting films in 1987 [Bed 86], that literally lifted the PLD method off the ground [Dij 87, Wu 90]. A historical overview can be found in the appendix.

One of the main issues of this work was to establish this technique in our group. Therefore, the following chapter will deal with the principle of PLD, followed by a description of the system, which was built in Mainz.

2.1 Principles of Pulsed Laser Deposition

Conceptually and experimentally, PLD is probably one of the simplest thin film growth techniques. Figure 2.1 shows a schematic diagram of an experimental set-up. Inside a vacuum chamber, a heated substrate holder is positioned opposite to a target holder within a distance of a few centimetres. A high power laser is used as an external energy source. A short laser pulse (τ<20ns) is focused onto the target using a set of optical components placed outside of the vacuum chamber. If the laser beam energy density exceeds the ablation[1]-threshold[2], congruent evaporation of all components of the material will occur.

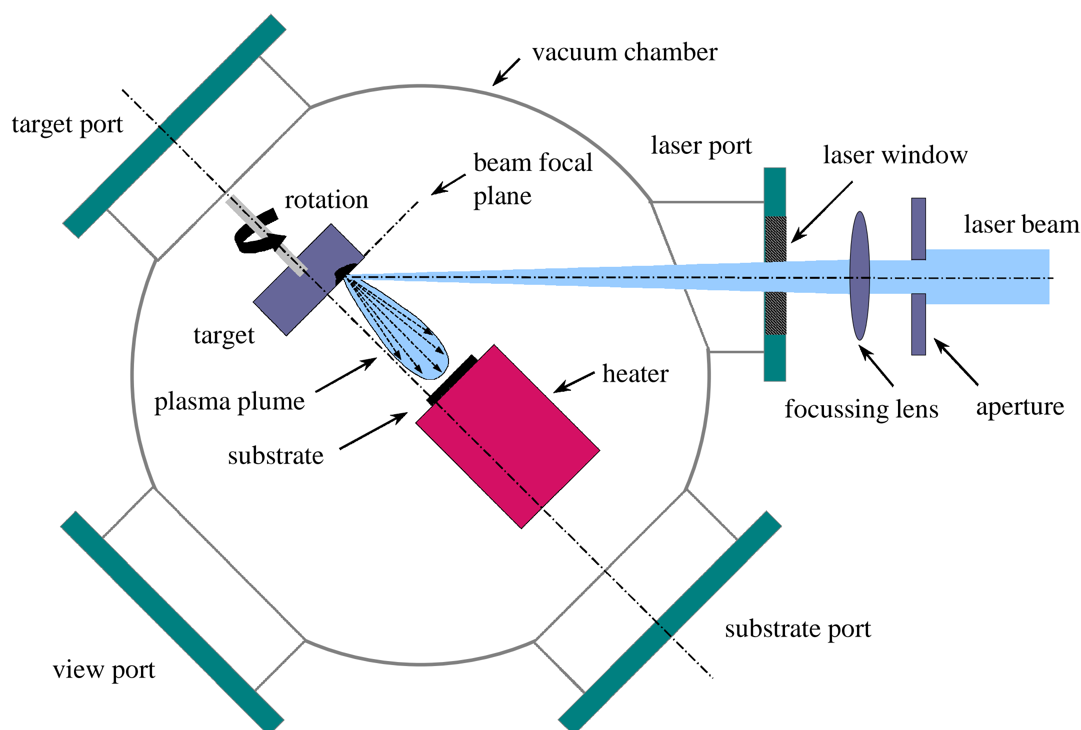

Figure 2.1: Schematic illustration of the PLD chamber and principle of the PLD process.

[1] Latin: take off. Moreover, *ablation* is used in the aviation industry and stands for the erosion of material.

[2] For most perovskites, this threshold is above 1 J/cm². The exact physical definition of the ablation threshold is rather difficult and will be discussed in chapter 3.

Consequently, a plasma with a stoichiometry corresponding to that of the target is formed and expands in a forward-directed manner away from the target surface. Finally, the components of the plasma plume[3] condensate on a single crystalline substrate. In the case of properly chosen deposition parameters (substrate temperature, deposition pressure, etc.) and a lattice matched substrate a grows epitaxially on the substrate. In this sense the concept "deposition" describes the relevant process of film growth, while the term "ablation" relates to the erosion of the target material.

One of the main advantages of this technique is the decoupling of the vacuum system and the evaporation power source (i.e. the laser)[4]. This fact is crucial for the high flexibility of this technique, offering an easy adaptation to different operation modes without the constraints imposed by the use of internally powered evaporation sources. Film growth can be carried out in a reactive or in an inert environment containing any kind of gas. It can also be operated in conjunction with plasma excitation or other types of evaporation sources in a hybrid approach (e.g. Ion Beam Assisted Deposition, IBAD). In contrast to other techniques (e.g. DC-sputtering) the electrical properties of the target material do not play decisive role in the plasma formation. Consequently, this deposition method is applicable for conductors as well as insulators. To attain a significant ablation rate and therefore a significant deposition rate, sufficient optical absorption of the laser radiation[5] by the target material is crucial. This condition is met for all the perovskite-like materials prepared in this work. Although these advantages led to a wide spread of the PLD technique (mainly in research), two crucial disadvantages should be mentioned: First, as a result of the forward-directed expansion of the plasma plume (mainly along the target normal), the area of homogeneous film deposition lies in the range of about 10x10 mm^2, which hitherto circumvented the enforcement of the PLD method in industry. The formation of droplets[6] is the

---

[3] A term that is commonly used because of the plume like shape of the plasma.

[4] Which additionally gives the possibility to operate several PLD systems with a single laser in order to minimise the cost per system.

[5] In this work, a wavelength of $\lambda = 248$ nm (KrF) is used exclusively.

[6] µm-sized particles on top of the film surface (see chapter 3).

second problem, especially for applications, where extremely smooth surfaces are required (e.g. high frequency devices and heterostructures).

2.2 Conception and Construction of a PLD-System

The previously mentioned flexibility of the PLD method and a high degree of process automation are the requirements to investigate the growth properties of a large number of different compounds and related heterostructures. Therefore a new PLD system (Figure 2.2) has been built in order to fulfil these requirements. The main considered issues are:

Deposition Chamber:

- A high vacuum system that allows reliable oxygen pressure control from chamber base pressure (10^{-7} mbar) up to 100 mbar.
- A multi-target holder including target rotation and straight forward target change and exchange.
- A substrate heater, which includes a water-cooled shield and enables homogenous deposition temperatures up to 1000°C. Fast substrate exchange and exact positioning relative to the plasma plume (rotatable and tiltable) is ensured.

Laser-System:

- A KrF-Excimer Laser with a suitable gas supply and adequate security features for laser radiation and laser gas (fluoride).
- An optical system to focus the laser beam onto the target and to scan the beam over the target surface.
- An on-line energy measurement[7] set-up to monitor the laser beam energy density on the target surface.

[7] Since the energy sensor is suited outside the deposition chamber, the attenuation factors of the optical components (especially the laser window) have to be taken into account.

2.2.1 The Deposition Chamber

Figure 2.2: Picture of the PLD system. In the centre, the vacuum chamber is visible. On the right side, the encapsulated optics and the laser are situated.

The high vacuum chamber allows thin film deposition in a reactive gas environment in a pressure range from 10^{-7} mbar to several mbar in oxygen flow. The oxygen pressure is one of the crucial deposition parameters for complex oxides and must be reliably controlled. This is realised by a two stage pumping system consisting of rotary pump and a turbo molecular pump. The deposition pressure is adjusted manually by two dosing valves. The first controls the oxygen inlet, while the latter stabilises the pumping power. The pressure measurement is performed by a set of pressure gauges adequate for a pressure range from 10^{-7} mbar to 100 mbar.

The disk-shaped targets[8] are mounted on a sixfold rotatable target holder, which is designed as a carrousel that simultaneously enables the rotation of the targets and the selection of a single target by rotation of the complete holder by a rotational feed-through. The two independent rotations are

[8] With a diameter of 25 mm and a thickness from 1 to 4 mm.

realised by a planetary gear. An internal vacuum motor drives the target rotation ($f_r \approx 1/s$). A shield (not shown) is mounted to avoid target cross contamination. The simple design allows the targets to be easily accessible and exchanged within a few minutes. This is especially useful for doping experiments of new compounds, where quite a number of targets with different compositions are needed. A further advantage of the design is, that target surface must be sanded flat ex-situ at regular intervals in order to guarantee reproducible film quality and ablation rate.

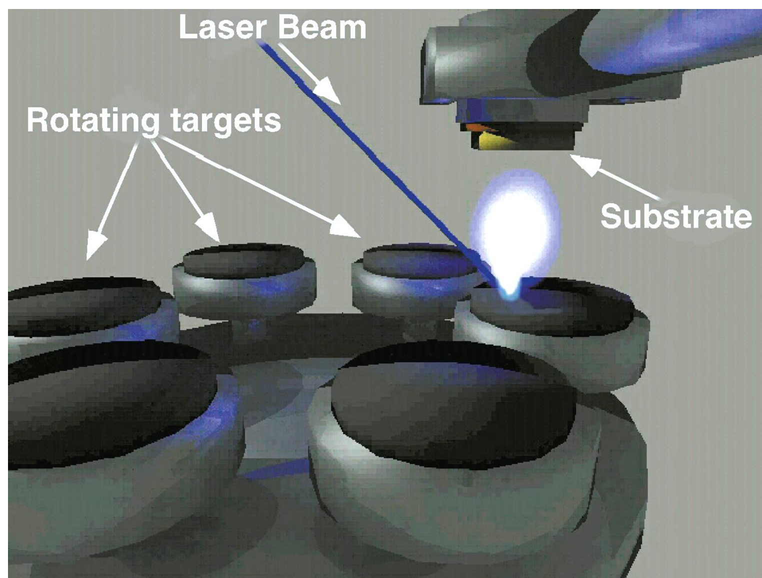

Figure 2.3: Schematic illustration of the sixfold rotatable target holder. By the use of a planetary gear, simultaneous rotation of the targets and target selection by rotation of the whole holder is possible.

In order to preserve stoichiometric ablation and uniform erosion of the target, the laser beam is scanned over the whole target surface. This is realised by the combination of target rotation and simultaneous horizontal scanning of the laser beam along the radial direction of the target. Thus, laser irradiation of the same target region is avoided, which would lead to strong surface damage by local heating, followed by irregularities in the plasma plume composition and therefore incorrect stoichiometry of the film. This aspect will be discussed in chapter 3.1, wherein the focus is on laser-target interaction.

As with most thin film deposition methods, the manner in which the substrate is heated plays an important role. For many of the complex oxides

deposited by PLD, substrate temperatures above of 800°C must be regulated with stability better than ±0.5 °C in oxygen atmosphere. The target-substrate distance is a crucial deposition parameter that has to be optimised for each compound. The lateral position of the substrate relative to the plasma plume must also be adjustable in a reliable way. This is accomplished by step motors in the x-, y- and z-directions. Rotation axes along the y- and z-directions (refer to Figure 2.5) enable off-axis PLD and the movement of the heater outside the plasma during pre-ablation[9].

Temperatures up to 1000°C can be reached by a contact-type heater design. As illustrated in Figure 2.4a, a corrosion-free Inconell® cylinder (orange) is heated by a winded coaxial heating conductor (red) and thermally screened by a water cooled copper shield (not shown). The substrate itself is glued or clamped onto a small cone (blue) which is screwed into a corresponding depression of the heated cylinder. In Figure 2.4b, a picture of the cylindrical heater with mounted cone and glued substrate is shown. Moreover, the mounting tool with four pins and the corresponding holes in the cone are visible.

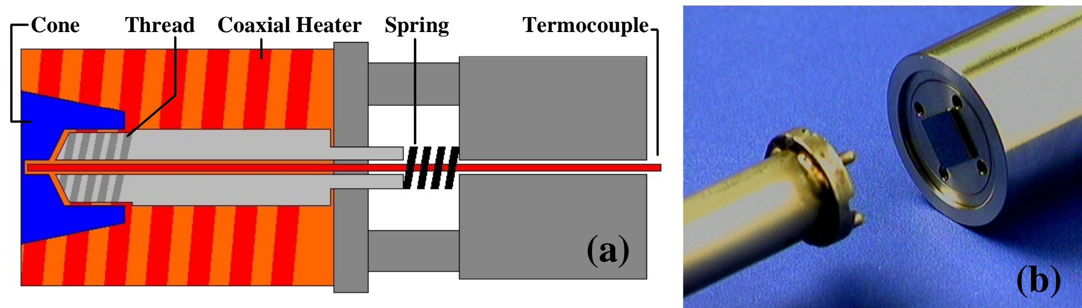

Figure 2.4: **(a)** Schematic drawing of the heater. **(b)** The heater and a substrate glued onto the cone is shown. The tool, that is used to screw the cone into the corresponding depression without touching the substrate is visible at the left side.

The cone shape ensures a homogenous thermal contact to the cylinder. This newly developed design allows fast substrate mounting without removing the whole heater construction out of the chamber. The substrate temperature is measured with a thermocouple, which is fed through the cylinder and pressed by a spring from the backside into a hole of the cone with a

[9] Usually a certain number (≈2000) of laser shots is used to clean the target surface in order to avoid formation of droplets due to loose particles after target-sanding.

distance of 0.5 mm from the cone surface. The temperature is regulated within ±0.5 °C from 500 - 1000 °C with an Eurotherm 2416 temperature controller. Optimal temperature homogeneity over the whole substrate surface is obtained by gluing it directly onto the cone with silver paint. In contrast, clamping of the substrate onto the cone results in reduced temperature homogeneity, but ensures fast and secure removal of fragile substrates. Moreover, organic contamination on the substrate surface, originating from the use of glue, is avoided.

2.2.2 The Laser System

In general, the useful range of laser wavelengths for PLD is between 200 nm and 400 nm. The most common materials exhibit strong absorption in this spectral region. As one moves towards shorter wavelengths, the absorption coefficients tend to increase while the penetration depth into the target and the ablation threshold decreases. Below 200 nm, strong absorption by Schumann-Runge bands of molecular oxygen makes beam guidance in air impossible and requires special optics. Solid-state Nd^{3+}:YAG and pulsed excimer gas lasers are the most popular radiation sources in the UV range. In order to achieve high laser energies at appropriate wavelength however, the best choice is the KrF-excimer laser[10], which directly emits UV radiation at 248 nm. Also commonly used Excimer laser wavelengths are 196nm (ArF) and 308 nm (XeF_2). These systems achieve pulse repetition rates up to several hundred hertz with energies above of 1 J/pulse and a pulse duration τ of 10 ns to 20 ns.

One of the most complex and sensitive parts of a PLD system is the optics. A uniform laser spot as well as a non-divergent beam are the requirements for homogenous energy densities on the target and therefore high quality thin film deposition. Due to the design and the orientation of the laser tube electrodes in the used KrF-excimer laser, the beam energy distribution exhibits a nearly gaussian-like profile along the horizontal axis, whereas along the vertical axis the distribution is best described as nearly “top hat”. A first aperture

[10] Detailed information on the principles of excimer lasers and the used model (Lambda Physik Compex 301) can be found in [Lam 00].

(25 x 12.5 mm²) is used to cut out the homogenous part of the original beam (Figure 2.5). Using two mirrors[11], the beam is guided to a beamsplitter that decouples about 7% of the intensity into an energy sensor with an adjustable attenuation factor in order to display online the real energy focussed onto the target. The energy density, i.e. the attenuation factor of the beamsplitter, can be calculated if the effective spot size and the losses of the optical elements are taken into account. A third mirror directs the beam into a spherical lens (f_c = 50 mm) through a second exchangeable aperture (4x4 mm to 10x10 mm), which reduces the spherical aberration. The beam enters the PLD chamber through a laser window[12] after passing a fourth movable[13] mirror (Figure 2.5, scanning mirror). Additionally a potential shield is mounted directly after the chamber window to reduce the formation of a graphite layer due to laser induced ionised hydro-carbonates which diffuse to the window that is polarised by laser irradiation. For security reasons, the whole optical system is encapsulated in a perspex box.

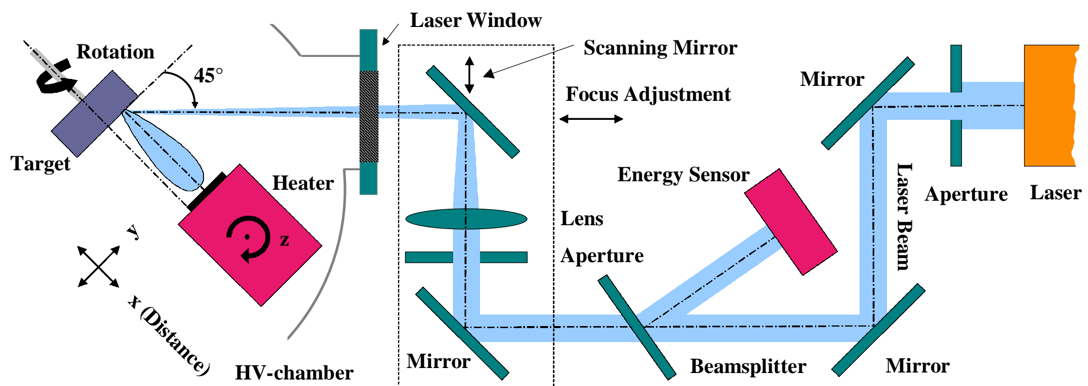

Figure 2.5: Schematic drawing of the laser beam guidance.

By moving the last mirror, the laser beam may also be scanned horizontally over the target surface to provide, in conjunction with the target rotation, an uniform erosion of the material [Arn 99]. Beside this positive effect, the main reason for this operation mode is to improve the thickness homogeneity

[11] MgF_2 with a high reflection coating optimised for 248nm.

[12] Fused silica (Suprasil®); the outer side is anti-reflection coated (optimised for 248nm) to improve transmission ($T \approx 96\%$). For cleaning purposes, the inner side is uncoated.

[13] Step motor driven and computer controlled.

and the compositional uniformity of the film. Additionally, the formation of particulates (droplets) on the substrate and film surface is reduced, since intense irradiation of the same target area leads to surface roughening and structure formation by material erosion, followed by decrease of ablation rate, increase of particulates and instabilities of the plume alignment. By rotation and translation of the focus these problems can be suppressed or even completely avoided [Bäu 96, Dou 95].

In order to guarantee constant energy densities, the laser beam is scanned by linear movement of the last mirror (Figure 2.5, scanning mirror). Consequently, the change in the optical path length due to the movement of this mirror is compensated by the reverse 45° arrangement of the target. Moving the laser beam focus just by motor controlled obliquity of a mirror in the beam line would lead to a change in the position of the lens focus relative to the target. This would result in an undesired modification of the energy density on the target during scanning, and therefore inhomogeneous film properties. Furthermore, simultaneous movement of the optical elements within the dotted rectangle in Figure 2.5 allows to adjust the lens focus relative to the target in order to change the energy density at a given laser energy.

Furthermore, for technical applications this scanning mode can be used to compensate the small deposition area of the plasma plume. The scanning of the laser beam leads to a plume which moves horizontally relative to the substrate heater, spatially fixed in the lateral plane. Combined with a vertical step motor controlled movement of the heater, this in principle allows a homogeneous large area deposition in a line-by-line manner. However, this deposition technique is limited only by geometric factors such as the size of the currently used heater and the target radius.

3. Theoretical Approaches in Pulsed Laser Deposition

In contrast to the simplicity of the experimental hardware, the laser-target interaction is an extremely complex physical phenomenon. Theoretical descriptions are multidisciplinary and combine both equilibrium and non-equilibrium processes. The mechanism that leads to light absorption depends on laser characteristics, as well as optical, topological (surface morphology) and thermodynamical properties of the target. When laser radiation is absorbed by a solid surface, electromagnetic energy is converted first into electronic excitation and then into thermal, chemical and even mechanical energy to cause evaporation, ablation, excitation, plasma formation and exfoliation. Material removed from the target form a "plume" consisting of a mixture of energetic species including atoms, molecules, electrons, ions, clusters, micron-sized solid particles and molten globules.

A short high energetic laser pulse leads to rapid local heating of the target material. As a result, within nano-seconds the material reaches a temperature that, under equilibrium conditions at a given pressure, would correspond to a much lower density. Due to the large density gradient between target and ambient pressure, the material then rapidly expands from the target surface. This expansion can be treated similarly to that of a nozzle jet with hydrodynamic flow characteristics. This process creates many advantages as well as disadvantages. The advantages are flexibility, fast response, high energetic species and congruent removal of the target components. The disadvantages are the presence of micron-sized particulates and the forward-directed, narrow angular distribution of the plasma, that makes large-area deposition a very difficult task.

Based on the nature of interaction of the laser beam with the target and the evaporated material, the PLD process can be classified into three separate regimes: (i) interaction of the laser beam with the bulk target, (ii) plasma formation, heating, and initial one dimensional isothermal expansion, and (iii) anisotropic (3 dimensional) adiabatic expansion and finally nucleation onto the substrate (illustrated in Figure 3.1). The first two regimes start with the laser pulse and continue during the pulse duration, while the last regime starts after the laser pulse terminates. The issues discussed in the subsequent theoretical chapters will be structured according to this process.

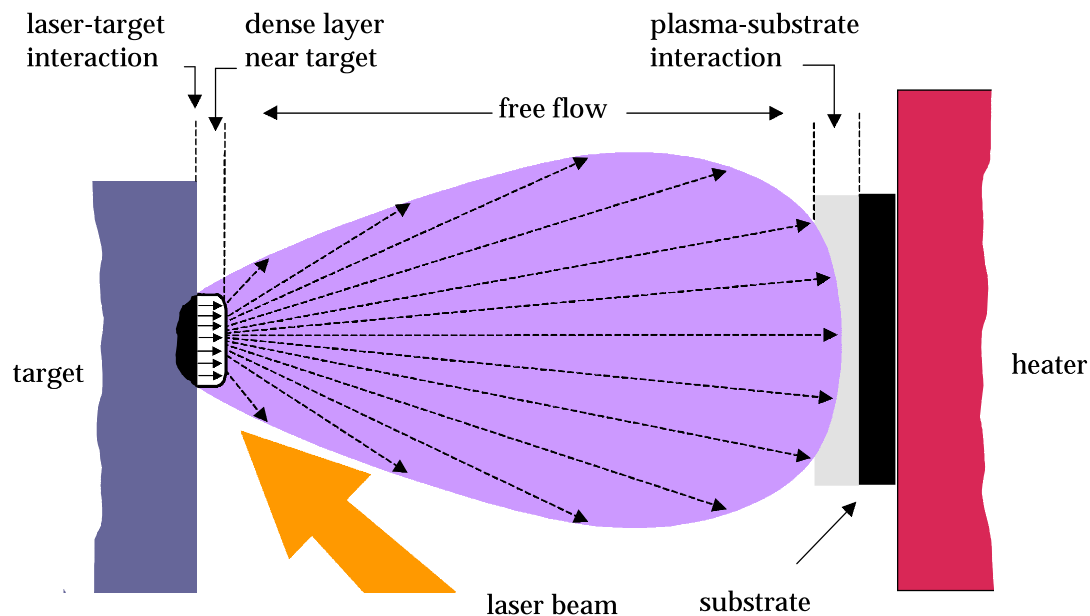

Figure 3.1: Plasma formation, propagation and condensation.

(i)	Laser-target interaction	"Ablation"
(ii)	Plasma formation and initial expansion	"Plume"
(iii)	Expansion and plasma-substrate interaction	"Nucleation"

In order to confirm the theoretical interpretation and models of these processes, a wide range of diagnostic methods is useful to efficiently correlate the formation, propagation and properties of plasma plumes with thin film properties such as stoichiometry, morphology, uniformity and crystallinity. Some of the important measurement techniques used to investigate the laser-target interaction and the plasma plume are listed in Table 3.1.

Method	Species/Properties of the plasma
time of flight mass spectroscopy (TOF)	Velocity distribution of the species; indirect: target surface temperature
Scanning electron microscopy (SEM)	Sputtering mechanism of the target
High speed photography	Emissive species (temporal and spatial evolution, not species specific)
Ion probe	Velocity and spatial distribution of positive ions (not element specific, not sensitive on emission or degree of ionisation)
Optical emission spectroscopy	Species specific on emissive species (velocities of ions, neutrals, molecules); Plasma temperature (if LTE is assumed)
Intensified CCD (ICCD)	Hydrodynamics of the plume propagation and reactive scattering; plume emission
Laser induced fluorescence spectroscopy (LIF)	Ground state atoms and molecules, determining local vibrational and rotational temperatures

Table 3.1: Measurement techniques for target properties and plasma diagnostics.

3.1 Laser-Target Interaction - Ablation

The bombardment of a target by ions, electrons or photons, and in the case of PLD, by a pulsed photon beam, leads to particle emission through sputtering, also commonly termed ablation or desorption. In pulsed laser sputtering, it is necessary to distinguish between the underlying primary and secondary mechanisms. The former include the well known thermal, collisional, electronic and macroscopic (exfoliational) processes. The only

substantially new process arising with PLD is termed hydrodynamic sputtering, which is equivalent to droplet emission. The secondary mechanisms include various types of pulsed flow processes that can be described within the laws of gas dynamics.

3.1.1 Primary Mechanisms

Thermal Sputtering

Considered in the sense of vaporisation from a transiently heated target, thermal sputtering by PLD requires effective temperatures well above the melting or boiling point of the target material. The thermal history (heating rate, melting, evaporation) caused by the nanosecond laser-solid interaction depends on the laser parameters (pulse energy density J, pulse duration τ, shape and wavelength) and on the time- and temperature-dependent optical (reflectivity, absorption coefficient) and thermo-physical (heat capacity, density, thermal conductivity, binding energy, etc.) properties of the target material[14]. The fluid-solid interface of the melt will propagate into the target and the direction will be inverted after the pulse (10-20ns). The material in the molten zone will be evaporated and accelerated into a 1-dimensional movement perpendicular to the target surface due to the predominant temperature- and pressure gradient. Herein, the evaporation threshold can be understood by the increase of the vapor pressure with temperatures predicted by the Clausius-Clapeyron equation.

The laser irradiation is absorbed by the target material in a depth of $d \approx \alpha^{-1}$, which is approximately determined by the temperature- and wavelength dependent absorption coefficient α. Being a condition for stoichiometric material ablation (important especially for multi-component ceramic materials), the heat has to be generated in a thin surface layer and the heat diffusion into the bulk has to be slow. Consequently, the ablated layer thickness per pulse Δx_t has to be larger than the heat diffusion depth $\Lambda = (2D\tau)^{½}$ [15]. In general, for

---

[14] Dependencies, which are a priori not known for most of the target materials.

[15] At large absorption, the heat is conducted into the target according to the heat diffusion equation with the thermal diffusion coefficient is $D = k/\rho C_v$.

metals and small band-gap semiconductors the thermal diffusion depth Λ is larger than the absorption depth of the laser beam in the target material ($d < \Lambda$), so that the thermal conductivity of the material is an important factor. However, if the relation $d > \Lambda$ holds, the thermal conductivity does not play a major role in the evaporation process. Therefore, the evaporated depth will depend mainly on the absorption depth, which in turn is influenced by the laser wavelength [Sin 90]. In particular, most of the perovskite materials strongly absorb UV-radiation at a wave length of 248 nm (as used in this work). Hence, the absorption length is big compared to the thermal diffusion depth, which allows relatively low laser energy densities for stoichiometric correct thin film deposition.

Based on the usual expression for the vaporising flux from a condensed phase (equals the condensing flux) it is possible to estimate the thickness of the ablated layer form the target per pulse due to thermal sputtering:

$$\Delta x_i \approx (p\hat{T}^{1/2}\tau / M^{1/2}\Delta H_v)\times 1.53\times 10^6 nm \qquad (3.1)$$

where p is the ambient pressure, $\hat{T}$ the maximum surface temperature[16], M is the molecular weight of the vaporising species, ΔH_v the heat of vaporisation [eV] and τ the laser pulse duration [Kel 94]. It is important to mention, that because of the slowness of the vaporisation process, kinetics has to be taken into account. Expressions based exclusively on energetic considerations lead to wrong results [Bat 73], i.e. to elevated deposition rates and temperatures[17].

Collisional Sputtering

Compared to electrons or ions the photon momentum transfer due to direct beam-surface interaction is negligible. The total maximum energy transfer of an incident photon (10 eV) on aluminium can be estimated to roughly $8.0\text{x}10^{-9}$ eV, in comparison to approximately 4.5 eV for an incident He^+ ion on Al [Kel 94]. However, indirect collisional effects with photons do exist due to laser-plasma interaction. This leads to acceleration of plasma-ions up to 1 keV and nearby surfaces are ion-bombarded [Akh 82, Gap 77]. An experimental

---

[16] Ideally determined experimentally.

[17] TOF (time of flight) measurements indicate the real surface temperature.

indication of this effect is cone formation of the bombarded target surface as can be seen by SEM measurements of a $YBa_2Cu_3O_{7-\delta}$ target in Figure 3.2.

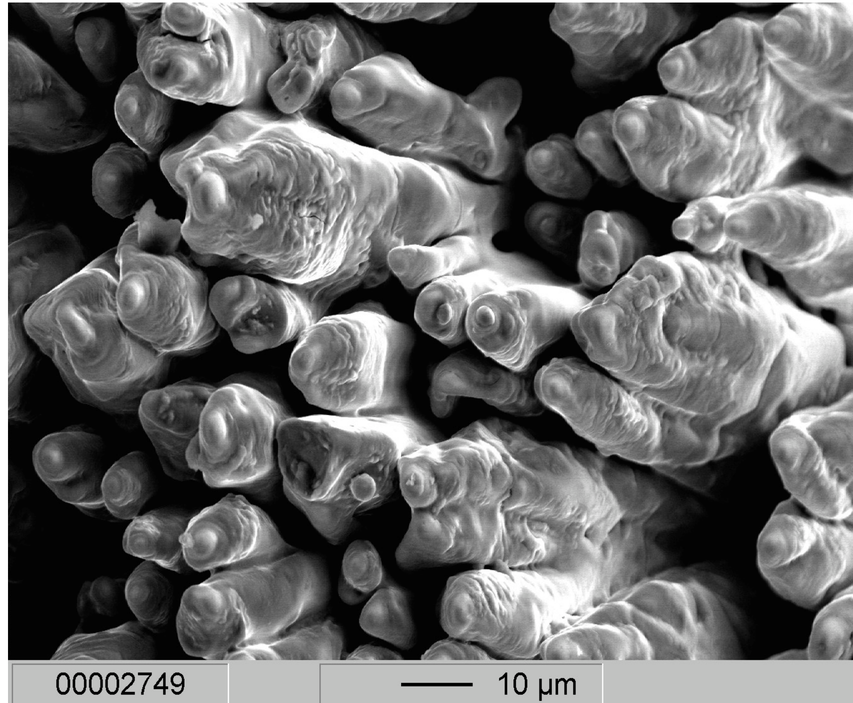

Figure 3.2: Cone formation due to collisional sputtering revealed by a scanning electron microscope (SEM) picture of a $YBa_2Cu_3O_{7-\delta}$ target used in this work. Typical PLD parameters: $p_{O2} \approx 0.3$ mbar, $J \approx 2.5\,\mathrm{J/cm^2}$, $\tau = 15$ ns, $\lambda = 248$ nm.

Electronic Sputtering

This term actually applies to a family of processes whose common feature is the involve of some form of excitation or ionisation, such as ionic explosions [Fle 65], "hole-pair " mechanism [Ito 82, Hag 93], defect formation [Nak 91] or surface plasmon excitation [Hel 89, Hoh 91]. It is normally confined to dielectrics and wide band gap semiconductors, except when due to surface plasmons. To consider a specific example, dense electron excitations can be expected for sufficiently large laser pulse energies resulting in extremely high electrical fields. This is followed by an energy increase in the range of a few eV for each atom, and thus by an increase of the vapor pressure by orders of magnitude or even unbinding of the lattice due to strong Coulomb interaction.

A possible description is that a rapid non-adiabatic transition takes individual ions directly into antibonding states, i.e. into a densely packed repulsive gas system, that expels particles energetically [Jös 82, Kis 87]. Furthermore, the time constants τ of the processes are substantially smaller than those of electron-phonon interaction. Thus, no heat is transferred to the lattice, resulting in the absence of melting processes. The details of what constitutes an electronic process are not straightforward, but some features can be used as an indication: existence of a threshold energy density for emission; kinetic energies of the order of a few eV; low internal energies; high degree of directionality; non-thermodynamic yield of molecules and ions. In general however, electronic processes due to high photon densities in the laser pulse are assumed to be responsible for the possibility to ablate materials, which are transparent for UV irradiation, such as MgO.

Exfoliational Sputtering

Owing to repeated thermal shocks, material flakes are detached from the target surface, which results in an obvious and characteristic topography, as illustrated in Figure 3.3. This process can be expected to occur at relatively high energy densities ($>2.5\,J/cm^2$) and whenever the system has a high linear thermal expansion, a high Young´s modulus, a high melting point (e.g. W, Al_2O_3), and when the laser-induced temperature approaches but does not exceed the melting point T_m. Consequently, thermal shocks occur repeatedly and lead to high stress. Since these thermal shocks are not relieved by melting, they lead to cracking [Kel 85].

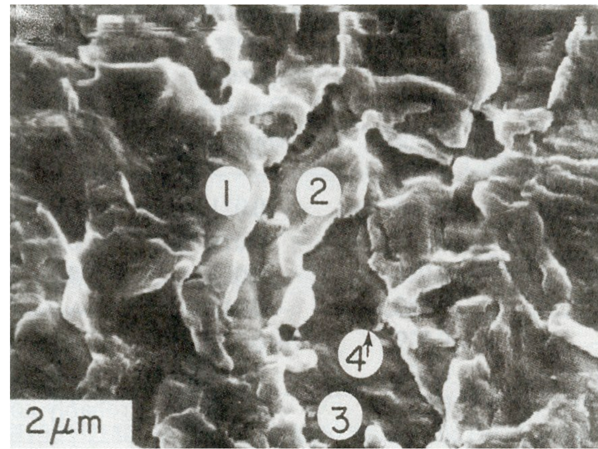

Figure 3.3: Exfoliational sputtering of polycrystalline wolfram in vacuum ($\tau = 12$ ns, $\lambda = 193$ nm, $J = 2.5\,J/cm^2$, 2000 P) [Kel 85].

Hydrodynamic Sputtering

This process of formation and repulsion of material droplets occurs exclusively for PLD and is known as a crucial problem of this technique. Various solutions have been suggested to minimise this effect, which results in µm-sized particles on top of the thin film surface (e.g. mechanical rotation filters). Among the different descriptions, such as target recoiling due to emitted particles [Bat 73], differential etching [Nov 88], the one based on a thermal expansion argument will be discussed. At laser pulse energies sufficiently large for melting, asperities[18] of the target surface are accelerated away from the target (Figure 3.4). This is due to the combination of volume change on melting, followed by instantaneous thermal expansion of the liquid and the re-cooling that begins at the bottom of the melted substrate.

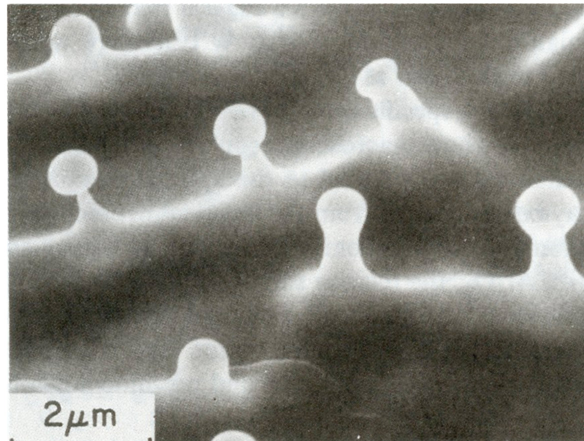

Figure 3.4: Hydrodynamic sputtering of gold in air (τ =12 ns, λ = 193 nm, J = 2.5 J/cm², 4320 P) [Kel 85].

3.1.2 Secondary Mechanisms

A high density of pulsed photons can lead to a sufficiently high density of the emitted particles, so that they interact. The sequential flow processes will cause the system to lose memory of the primary mechanisms, and the processes are therefore better described in terms of what can be called a secondary mechanism[19]. At least four of those are currently understood: *outflow* and *effusion* either with reflection or recondensation of the backscattered particles, respectively. In a simple model these mechanisms refer to a gas initially confined to small dimensions that is suddenly allowed to expand into vacuum. This initial expansion is not affected by an ambient background gas pressure. *Outflow* can be understood as a gas in a finite reservoir that expands

---

[18] The asperity could arise from a variety of effects, including turbulence and differential etching.
[19] Happens also with ions at extremely high yield [Urb 93, Kel 90, Wie 92].

into vacuum when a confining wall is suddenly removed. On the other hand *effusion* (which occurs with ordinary vaporisation) refers to a gas in a semi-finite reservoir that effuses into vacuum when a wall becomes porous until the wall is resealed again. From a mathematical point of view the movement of the particles in these mechanisms can be described within the laws of gas dynamics.

When the quantity of particles per unit time emitted from the target surface exceeds a value of the order of 0.5 monolayers per nanosecond [Noo 87, Noo 88] the ensuing collisions are sufficient to lead to quasi equilibrium [Ytr 77, Cer 81, Kel 88a, b] in the so-called Knudsen-layer (KL). This results in a small flow velocity u_k and a forward peaking flux with a $\cos^4\theta$ angular distribution. The gas-kinetic (thermal) velocity v_i follows a Maxwell[20]-distribution shifted by u_k:

$$
\begin{aligned}
& f(v_x, v_y, v_z, t) \propto \exp\langle -m\left((v_x - u_k)^2 + v_y^{\,2} + v_z^{\,2}\right)/2k_B T_K\rangle \\
& u_k = (\gamma\, k_B T_K / m)^{1/2}\,, \qquad (-\infty < v_x, v_y, v_z < \infty)
\end{aligned}
\tag{3.2}
$$

The gas particles go into flight at the target surface with a velocity $v_x > 0$ [21] and flow velocity $u = 0$, while at the KL boundary the velocities are $-\infty < v_x < \infty$ and $u = u_k$. After passing the KL boundary the particles go into free flight (Figure 3.1) with constant velocities (under vacuum conditions)[22]. In real systems, the role of gas dynamics ends at a critical gas density, collisions cease abruptly and free flight sets in. This transition has been modelled with the “sudden freeze” approximation [McC 79, Sae 81, Sae 91]. TOF measurements in conjunction with the ratio T_k / T_s out of the KL theory and $M = u/a$ [23] might be used to derive the target surface temperature T_s [Der 87, Jod 93].

For still larger quantities of particles, an unsteady adiabatic expansion (UAE, i.e. time-dependent) occurs, followed by a more marked forward peaking in the flux. Consequently, under vacuum conditions the forward peaking (i.e. the shape of the plume) can be separated in to three regimes,

---

[20] Which does not necessarily denote a primary thermal mechanism.

[21] Where the x-direction corresponds to the direction along the target normal.

[22] At ambient gas pressures a deceleration of the particles takes place (see chapter 3.2).

[23] Where a is the sound of speed $a=(\gamma k_B T/m)^{1/2}$.

depending on the amount of material removed from the target: (i) $\cos\theta$ at low particle densities (same as for thermal evaporation), (ii) $\cos^4\theta$ when a KL is formed, and (iii) up to $\cos^{50}\theta$ when a UAE occurs [Sae 91].

It is the purpose of these pulsed flow models to describe the initial expansion mechanisms of the plasma and to give predictions on the particle densities, velocity distributions and thus on the energy distribution of the species in the plasma. However, under typical PLD conditions the ambient gas pressure plays an important role and will change the properties drastically.

3.2 Plasma Formation and Propagation

Ionisation and Heating - Energetic Properties of the Plasma Species

The dense layer of vapor near the target surface, discussed in the previous chapter, interacts with the laser beam, leading to the formation of a high temperature (HT) and high pressure (HP) gaseous plasma [Rea 71] that expands as a result of the predominant pressure/density gradient. Due to the high plasma expansion velocity, the particle density of the plasma decreases rapidly in time, which makes the plasma transparent beyond the edge of the dense vapor layer and the interaction with the laser beam ceases[24]. The fractional ionisation of the dense layer, i.e. the flux of ions and electrons, is predicted by the Langmuir-Saha and Richardson equations[25], respectively [Che 74]. In these equations, the exponential dependence of the degree of ionisation on the plasma temperature leads to a sudden rise of the ionisation at a certain value, followed by plasma formation. Different mechanisms as (i) impact ionisation, (ii) photo-ionisation, (iii) thermal ionisation of photon activated species, and (iv) electronic excitation may affect the concentration of the excited species.

The further heating of the plasma due to absorption is generated mainly by the inverse-Bremstrahlung process [Hug 75], where electron-ion collisions lead to the absorption of a photon by a free electron. The absorption

---

[24] [Rea 71] refers to IR radiation, resulting in much larger absorption. For 248nm, most of the absorption occurs in vicinity of the target and is less important at larger distances.

coefficient α_P is affected by the evaporation rate, average charge of the species, plasma temperature and laser wavelength [Sin 90]. Resulting plasma temperatures are in the range of 10^4 K ($\approx$ 1eV), depending on the laser power density and frequency, although the surface evaporation temperature is much lower [Ven 88]. However, apparent contradictions to the results predicted by these mechanisms, show the need for hydrodynamic modelling of the plasma [Sin 90].

Influence of the Background Gas

In *vacuum* the relatively weak plasma luminescence is only due to inter-beam collisions. The highly forward directed spatial distribution of the plume maintains its shape during propagation. However, the deposition of oxides needs in most cases sufficient oxygen pressure. Hence, the interaction of the plasma with the *ambient gas* will influence the dynamics, chemistry, ionisation and thermalisation of the plasma [Kum 93], changing important film growth parameters such as spatial distribution of the plume, deposition rate and kinetic energy distribution of the plasma species, which is still somewhat controversial [Geo 92, Kim 89]. Furthermore, reactive scattering can result in the formation of molecules or clusters which can aid in the incorporation of the oxygen into the film [Lyn 89, Gir 89]. In general, raising the background pressure results in the following effects: (i) an increase of fluorescence from all species compared to vacuum, due to collisions at the expansion front and subsequent inter-plume collisions; (ii) a sharpening of the plume boundary, which is an indicative of a shock front; (ii) a slowing of the plume relative to the propagation in vacuum, resulting in (iv) spatial confinement of the plume.

Propagation, Velocity and Stopping of the Plume

Under typical background gas conditions, during the first microsecond the dense plasma expands in much the same manner as in vacuum, virtually unhindered by the gas. Thereafter, collisions at the expanding front slow down the species of the plume and the gas atoms are swept up by the plasma plume like a “snowplow”. Increased species density at the front of the plume and species-gas reactions lead to increased fluorescence in this region. However,

---

[25] For a gas in local thermal equilibrium (LTE).

the slower moving bulk of the plume appears unaffected at this point. As the plume continues to expand, the pressure in the plume continues to decrease, the expansion front is slowed more noticeably, and the shielded slower components propagate to coalescence with the material on the contact front.

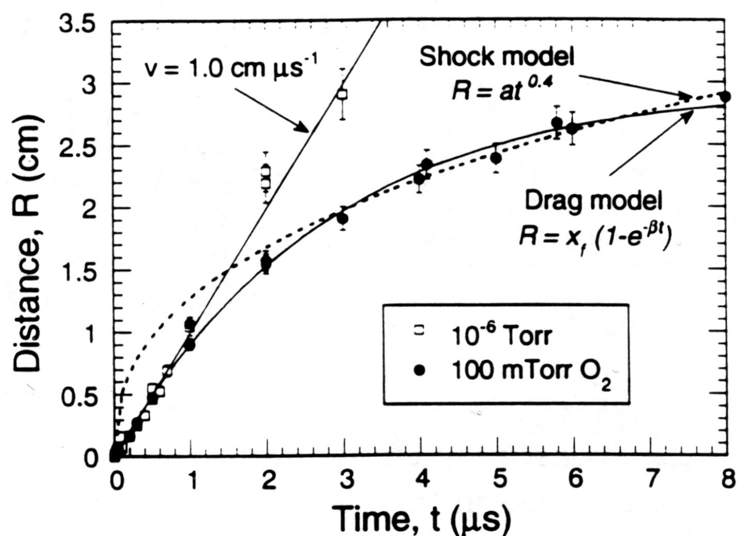

Figure 3.5: *R(t)* plots of the plasma expansion front boundary from gated ICCD images [Chr 92].

The velocity of the shock front [Kel 91], propagating ahead of the plume, may be measured by different diagnostic methods (see Table 3.1.) in order to establish the hydrodynamic models of the plasma plume expansion. Figure 3.5 gives a *R(t)* plot of the leading edge of the plasma emission. In vacuum, this leading edge maintains a constant velocity in the order of 1.0 cm/µs ("free flow"), depending on the laser energy. At ambient gas pressures, the progressive slow down can be fitted using two models, the "shock model" and the "drag model", which will be briefly discussed below.

Based on the blast wave model [Zel 66] the propagation of a shock wave through a background gas, caused by the sudden release of energy (explosion), can be described by the following relation:

$$R = at^n \qquad (n \geq 0.4) \tag{3.3}$$

This model strictly applies only when the mass of the ejected species is small compared with the mass of the background gas which is swept up, a situation that does not typically apply for PLD conditions. A plot of this

model, given in Figure 3.5, shows strong deviation from the measured data, especially at early times. At higher background pressures the model fits the data increasingly well [Dye 88].

A classic drag-force model shows better agreement at low pressures and early times. The ejected pulse of ablation products is regarded as an ensemble that experiences a viscous force proportional to its velocity through the background gas. The equation of motion $a = -\beta v$ gives:

$$R = x_f (1 - e^{-\beta t}) \tag{3.4}$$

Here, β is the slowing coefficient (which depends on the ambient gas density) and $x_f = v_0/\beta$ is the stopping distance of the plume [Geo 92].

For experimental purposes, it is of major interest to predict a real value of a stopping distance of the plume, or even better a distance where the ablation conditions are optimal. For practical applications, however, neither of the two discussed models reflect the exact physical conditions practically existing for PLD. Thus, experimental observations of PLD plumes are best described by a composite of these two models. Furthermore, both models contain fitting parameters that are not readily measurable. Some more applicable models considering interaction between the ablated particles in the expanding plume with the substrate [Nak 94] and the background gas [Str 98] are currently discussed in terms of the optimal deposition distance for thin film deposition.

3.3 Plasma-Substrate Interaction - Film Nucleation

It is the purpose of this chapter to review some fundamental mechanisms, to discuss the aspects of pulsed deposition of material and to analyse the influence of deposition parameters on film nucleation.

3.3.1 Fundamental Growth Modes of Thin Films

The nucleation of a thin film involves several processes, as illustrated in Figure 3.6: (i) Arrival and re-evaporation of species on (from) the bare substrate; (ii) Arrival and re-evaporation of species on (from) pre-existing clusters

or film atoms; (iii) Cluster nucleation and (iv) Diffusion and dislocation to (of) the cluster.

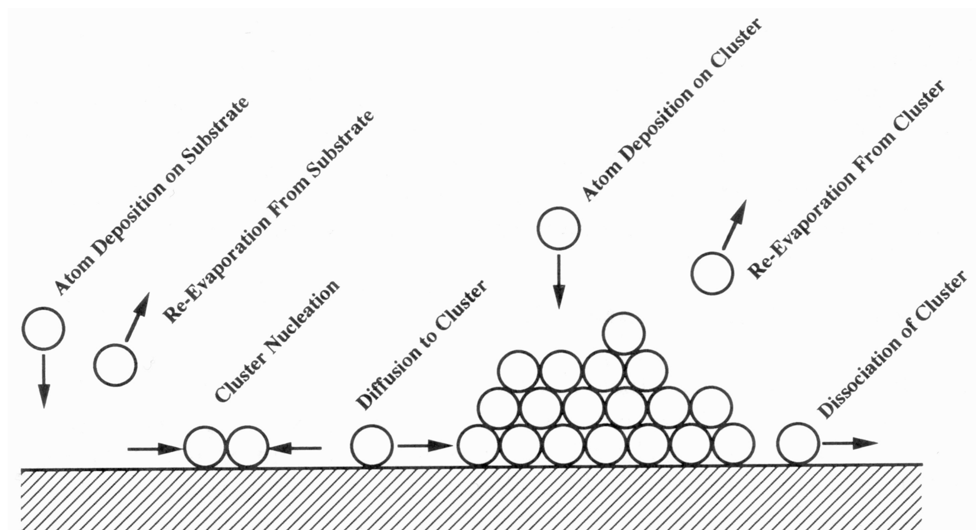

Figure 3.6: Schematic diagram of atomic processes in thin film nucleation [Hor 94].

The balance between growth and dissolution for a given cluster will be governed by the total free energy of the cluster relative to an assembly of individual atoms. Using Green´s notation, the free energy is formed by the sum of the interface energies $a_1\Gamma_{C,-V} + a_2\Gamma_{S-C} - a_2\Gamma_{S-V}$ (between cluster, substrate and vapor, respectively), and the change in volume free energy up on condensation of the cluster $\Delta G_V = -kT/\Omega \ln(\zeta)$ [26]. If the derivative of ΔG_V is negative (positive) the cluster is (not) stable and will grow (shrink) on average. Depending on the net interface energy, negative volume free energy ΔG_V (i.e. cluster growth) will lead to

- *Vollmer-Weber nucleation and growth.* Provided that surface free energy terms will be positive, three dimensional cluster growth occurs (Figure 3.7). The total free energy for cluster formation will increase with atom addition up to a maximum which is reached for

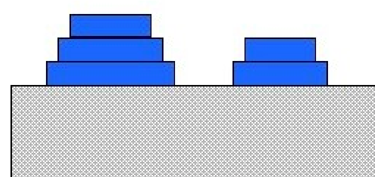

Figure 3.7: Vollmer - Weber nucleation and growth.

[26] A simplified equation, that only takes the free condensation of a cluster into account but will not affect the general conclusions. Ω is the volume and ζ is the super saturation P/P_e (pressure of arriving atoms P and equilibrium vapor pressure P_e of film atoms). Alternatively, ζ can be defined by (R/R_e), with R corresponding to the deposition rate.

a critical cluster size r^*, followed by a decrease for clusters larger than r^*. The critical cluster size can be used to calculate a free energy barrier for nucleation ΔG^*.

- *Frank-van der Merwe nucleation and growth.* If the net surface energy term is negative, it will be energetically more favourable for the film to form islands of monolayers (Figure 3.8). The growth to complete island coalescence (full monolayer) before significant clusters are developed on the next film layer corresponds to a situation with no barrier to nucleation. Concerning film growth on similar substrates, this condition is satisfied. For deposition on dissimilar substrates, this growth mode will be promoted by (i) strong film-surface bonding, (ii) low film surface energy and (iii) high substrate surface energy.

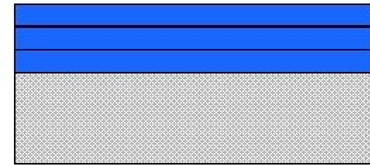

Figure 3.8: Frank-van der Merwe nucleation and growth.

- *Stranski-Kratinov nucleation and growth.* Film atoms initially form monolayers on the bare substrate and consecutively nucleate three dimensional clusters on these layers (Figure 3.9). This growth mode is driven by an increase of stress due to film-substrate lattice mismatch with increasing layer thickness, changing the surface energy of the initial layers typically after 3-5 monolayers. In cases for which three dimensional nucleation occurs at layer thickness of one or two monolayers, strong chemical bonding could also be involved.

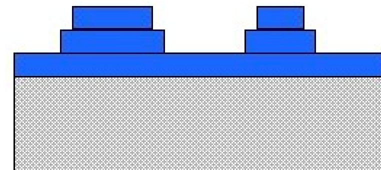

Figure 3.9: Stanski-Kratinov nucleation and growth.

The significance of the preceding mathematics is, that either a *decrease* of the net surface/interface free energy or an *increase* of the negative volume free energy ΔG_V will produce (i) a *decrease* in the critical cluster size beyond a cluster will be stable, (ii) a *decrease* in the total free-energy barrier for cluster nucleation, and (iii) an *increase* in the cluster nucleation rate. In practice, for a given film-substrate combination one has only little control over the surface/interface energy terms. Being accessible and thermodynamically most important deposition parameters however, the *increase* of the deposition rate (i.e. increase of supersaturation ζ) or the *decrease* of the deposition temperature (i.e. decrease of the velocity of diffusion and crystallisation processes)

will *increase* the magnitude of the negative volume free energy ΔG_V, resulting in the previously discussed impact on (i)-(iii). However, it will become clear in the subsequent chapters that the mutual interrelation of a variety of PLD parameters as well as material and substrate properties avoids a simple picture for the occurrence of growth modes. Therefore, only isolated aspects of deposition parameters and related growth processes can be discussed.

3.3.2 Interrelation of Pulsed Material Deposition and Processing Parameters

A crucial difference between PLD and conventional deposition methods such as sputtering or molecular beam epitaxy (MBE) is the sudden (within approximately 1 μs) arrival of energetic species from a saturated or supersaturated (10^5 J/mole) plasma with a high degree of ionisation (≈ 50%) onto the substrate [Met 89], separated by periods of no vapor flux (≈10-1000 ms)[27]. A second feature that separates PLD from conventional methods are impinging ions with energies in keV range, and neutral atoms with energies of several eV. Furthermore at background pressures of several tenths of mbar, a high flux of background gas particles virtually bombards the substrate surface during deposition. However, it is difficult to separate the relative importance of material-inherent mechanisms (i.e. phase stability, growth anisotropy, defect formation) from those related to the growth mechanisms characteristic for the PLD technique. In addition, interpretation is often complicated by the fact, that variation of a single parameter may change several aspects of the ablation and deposition process simultaneously.

Laser Pulse Frequency

Within a periodic deposition cycle, the first laser pulse will generate the nucleation of a high density of clusters with a size, which is smaller than what would be stable for a lower instantaneous deposition rate. Once the laser pulse decays, these in-stable (sub-critical) clusters will tend to dissociate into mobile species that nucleate new clusters on a different scale during the time of no vapor arrival. The next pulse will initiate the same sequence, with some

[27] Depending on the pulse repetition rate, usually 1-10 Hz, possible up to 100 Hz.

of the mobile atoms being added to the clusters formed after the first pulse. The effect of this cyclical nucleation and dissociation process can be evaluated in three frequency regimes. If the period of PLD duty cycle is much shorter or much longer than the time constants for all the relevant processes (diffusion, agglomeration and dissociation phenomena[28]), the pulsing is not expected to have any effect on the final microstructure. However, if the pulse period approximately matches one ore more of the atomic process time constants, the film formation path will be altered, similar to many resonance phenomena [Spr 72, Hor 92].

By using RHEED at typical PLD deposition pressures (up to 0.15 mbar), Rogalla et. al. [Rij 97, Bla98-99] show, that pulsed deposition results in the recovery of RHEED intensity after one laser pulse is terminated. The exponential behaviour of the intensity indicates typical relaxation time constants of $\tau = 0.1$ to 0.5 s. A clear tendency to increased relaxation times ($\tau = 0.8$ s) is observed at higher oxygen pressures and lower deposition temperatures, corresponding to decreased surface mobility. Thus, typical pulse repetition rates from $f = 1$ to 10 Hz indeed influence growth modes at thin film deposition by PLD. However, since such diagnostic methods naturally require UHV conditions, only little information about fundamental principles is available for PLD at deposition conditions which are necessary for oxides.

Laser Wavelength

The laser wavelength λ comes into play mainly in the effectiveness of the absorption of the laser power in the target. For most metals, the absorption coefficient α decreases with decreasing λ. Hence, the laser penetration depth is larger in the UV range than in the infrared (IR) range. For other materials, the variation of absorption coefficient with wavelength is more complex since various absorption mechanisms, such as lattice vibration, free carrier absorption, impurity centres, or bandgap transitions, can take place. Especially with $YBa_2Cu_3O_{7-\delta}$ thin films it has been demonstrated, that the density and size of particulates is much lower at UV wavelengths, resulting in smoother films with fewer and smaller particulates [Kor 89, Mis 91]. A further fragmentation

[28] Depending on temperature, the time constants are in the range of ms.

of the particulates in the hotter plume due to absorption of the UV-laser irradiation is assumed to be the responsible mechanism [Kor 91].

However, the primary effect of the laser wavelength is most likely due to the absorption coefficient of the target material. In particular for $YBa_2Cu_3O_{7-\delta}$, the absorption coefficient α *increases* with decreasing wavelength by nearly two orders of magnitude between UV light and near IR [Kau 90], which is somewhat reverse to the behaviour of metals. Scanning electron microscope investigations of the laser irradiated targets reveal characteristic melting-solidification processes and resulting grain structures which provide a coarse measure for the maximum depth of light absorption and heat propagation. As the wavelength increases, the depth and width of the grooves, generated on the target surface, increases. The corresponding SEM micrographs of deposited $YBa_2Cu_3O_{7-\delta}$ films show a remarkable correlation between the ejected particulate size and the depth and width of the grooves [Kau 90].

Laser Energy Density and Spot Size

The energy density influences mainly the laser-target interaction, discussed in chapter 3.1. As a consequence, a sufficient energy density is required in order to guarantee a congruent ablation of the constitutes of a multi-component target material. Above this ablation threshold, the laser fluence affects the instantaneous deposition rate (i.e. the particle size and density) and the degree of supersaturation of the vapor. With respect to thin film growth processes, a high laser fluence ($> 1\,J/cm^2$) results in a high degree of supersaturation and as a consequence, a small critical nucleus (practically only a few atoms). Under these conditions, two dimensional island nucleation of monatomic height is proposed [Met 89]. At even higher fluences, additionally a layer-by-layer growth mode on top of these islands is observed, which is not totally unexpected since the deposited material is growing on an identical surface.

Furthermore, the laser fluence can be varied by varying the laser power or spot size. Assuming a constant total laser beam intensity, tightening the focus results in an increase of particulate number density [Che 92] and an increase of the average particulate size [Mis 91]. In general, there exists a material dependent laser fluence threshold, below which particulates are barely

observable ($\approx 1\,J/cm^2$ for $YBa_2Cu_3O_{7-\delta}$, [Bla 92]). Moreover, being a striking and consistently observed finding, the resulting film thickness profiles become more peaked as the spot dimensions *increase*[29]. With PLD, there is a clear non-equivalence between a single large spot and a small spot scanned over the target surface, the latter providing a much broader angular distribution, resulting in a more homogeneous film thickness [Mue 90]. This fact is considered in the built system (see chapter 2.2). In addition, film-based studies on the angular distribution of the plasma plume frequently suggest that the degree of forward peaking is intensively increasing with laser fluence [Ven 88, Fog 90]

Target-to-Substrate Distance and Ambient Background Gas Pressure

The material flux changes drastically with distance L from the target. At a characteristic distance L_0 the flux loses its unidirectional velocity, scatters with the gas particles, and thermalises. It has been experimentally proven that this situation provides the optimum deposition distance [Kim 92]. The specific effect of the distance L and the ambient gas pressure p_0 are interrelated. Due to increased collisions between the plume constituents and the background gas, the plume dimension decreases as the background pressure increases. As a role of thumb, at given gas pressures, the optimal distance is to be found some few mm beyond the visible shape of the plasma plume. An upper limit of the distance and pressure in order to achieve a significant deposition rate, is given by the mean free path of the particles $\Lambda \approx (\sqrt{2}\, n\sigma)^{-1}$, where n is the number density of gas particles ($\sim p$) and σ is the cross section. Alternative theoretical approaches are currently discussed in order to optimise the processing parameters for a given material by modelling the scaling of L as a function of the relevant parameters (temperature, pressure, energy density) [Dye 90, Smi 92, Str 98].

Apart from the plume hydrodynamics, a background gas influences the chemical composition of the species i.e. that of the deposited thin film. For example, oxygen is used to compensate the tendency to oxygen loss or deficiency of ceramics occurring in vacuum PLD. On the other side and in

---

[29] Providing the laser spot dimensions are much smaller than the target-substrate distance.

contrast to vacuum, with increasing background pressure, the vapour species ejected from the target undergo enough collisions that nucleation and growth can occur to form particulates before their arrival at the target. As a result, the increasing residence time in the vapour controls the size of the particulates. Additionally, it allows the enrichment of the specific elements of the gas (e.g. O_2, N_2 or H_2) into the particulates. Apart from the chemical reactions, the molecular mass of the gas will strongly influence the scattering processes and the resulting particle trajectories and angular distribution of the plume [Geo 91, Chr 90, Mue 91].

Deposition Temperature

Among the various processing conditions, the substrate temperature is one of the most important parameters governing the crystallisation process [And 94, Mis 94]. Being a feature that separates PLD from conventional methods, a high kinetic energy of the species (up to 1 keV)[30] leads to a higher resulting surface mobility and thus allows a lower deposition temperature compared to other methods. In the film deposition case, the amount of atoms arriving at the substrate is not affected by the deposition temperature. A decrease of temperature can, however, reduce the mobility of the species across the substrate (i.e. the surface diffusion coefficient). Thus, the formation of an equilibrium compound or crystal structure is slowed down so that a metastable microstructure is produced, affecting the final surface microstructure and the film crystallinity. A common example of this phenomenon is the change of crystalline to amorphous phases at low temperatures or the preferential growth with another crystallographic orientation, such as *a*-axis growth of $YBa_2Cu_3O_{7-\delta}$.

Substrate Surface Microstructure

In contrast to the preceding descriptions, assuming homogeneous nucleation on random locations, substrate defects (e.g. atomic steps, point defects, dislocation intersections) provide low energy sites at which nucleation preferentially occurs. At sufficiently high supersaturation, the homogeneous nucleation rate can overwhelm this heterogeneous rate. In practice, an important

[30] Which in turn is reduced by collisions at relative high background pressures.

fact to note is that differences in substrate preparation can dominate any differences in kinetics. Polishing, annealing as well as chemical treatment of the substrate can drastically change film nucleation process and the resulting film morphology. Concerning epitaxial growth of complex oxide ceramics however, it will become clear in the subsequent chapters, that the formation of a desired crystal structure of such compounds strongly depends on the lattice match between growth base (i.e. the substrate) and the consecutively deposited material.

Target Properties

Assuming a correct stoichiometry, both target surface roughness and bulk density can have some effect on deposition and particulate generation rate. Coinciding with observations made in this work, it is commonly believed, that a polished target surface produces somewhat fewer particulates and smoother film surfaces [Mis 91]. The major effect on film quality however, is due to the target density. First, the particulate density is as well minimised by working with dense targets. Above a target density in the range of 80%, Ijsselstein et al. [Ijs 92] reported only little observable effect on particulate generation. Secondly, the thermal conductivity will be changed significantly and affects the ablation process. For dispersed pores in a solid it is known, that thermal conductivity decreases nearly linearly with increasing porosity [Che 92]. Moreover, at high temperatures radiation across pores contributes to heat transfer, in addition to true conductivity. As a result, melting zones at the target and subsequent particulate and droplet formation will deteriorate the final film surface morphology. Furthermore, the change in target surface morphology due to the ablation process (see chapter 3.1) can lead to enhanced forward peaking due to a focussing effect of a crater and an in-stable alignment of the plume axis, a fact that is considered in the design of the PLD system (see chapter 2.2.3).

4. Controlling Thin Film Growth by Heterostructures

4.1 Epitaxy and Lattice Mismatch Accommodation

As discussed in the previous chapter, a variety of processing parameters will influence the deposition of thin films. Assuming complete control on stoichiometry by adequate deposition conditions, two main aspects remain: First, the interplay between deposited material and material employed as underlying template. And secondly, a small window of deposition parameters, wherein the crystalline properties of the film are optimised.

Thus, this chapter will focus on the growth of epitaxial thin films on single crystalline substrates or underlying films. Apart from this ideal case, films can grow amorphous, polycrystalline, or textured[31]. Even when two materials have the same structure (here mostly ceramic oxides), their periodicity of atoms – being the template for epitaxy - is generally not identical, i.e. their lattice parameters are different. If the film grows coherently[32], the difference in lattice parameters gives rise to a residual strain in the film. The in-plane strain in directions parallel to the film surface is either compressive or tensile, depending on whether the lattice constant a_{top} is either greater or smaller than a_{bottom}, respectively. In general, coherent films are rarely observed unless the lattice mismatch is very small or the film is extremely thin. Instead, it is well

---

[31] Oriented along one axis.

[32] I.e. the periodicity of the film exactly reproduces the periodicity of the substrate.

known, that a network of dislocations[33] forms at or near the interface in order to relax most of the strain and to allow the film to have its unconstrained lattice parameters at very short distances away from the interface [Mat 75]. Below a critical film thickness, no dislocations are observed, above this limit however, the expansion of dislocation loops is driven by the residual strain energy in the film, proportional to the film thickness [Bal 95][34].

Lattice Mismatch and In-plane Relations in General

For cubic materials, the lattice mismatch between a top layer with a lattice constant a_{top} and an underlying bottom layer (or the substrate) with a lattice constant a_{bottom} is calculated by:

$$\Delta a = 2(a_{top} - a_{bottom})/(a_{top} + a_{bottom}) \tag{4.1}$$

Within the small parameter window, wherein crystalline properties of a heterostructure can be optimised, the lattice mismatch is assumed to be the crucial parameter, allowing highly oriented film growth, but enforcing a specific growth direction. In this sense, important deposition parameters such as deposition temperature, pressure and laser energy density are playing a secondary role. However, there are situations, where the deposition temperature can favour a certain growth orientation. For example, with $YBa_2Cu_3O_{7-\delta}$ on $SrTiO_3$ substrates, a decrease of the deposition temperature is known to favour *a*-axis growth, whereas at elevated deposition temperatures ($T_{dep} \geq 750$ °C) *c*-axis growth is obtained.

Considering a simple (001)-oriented substrate or bottom layer material (c-axis aligned parallel to the surface normal), some common terminology is illustrated by the following figures. In the case of approximately equal in-plane lattice parameters, a "cube-to-cube" growth may occur, which means parallel aligned main axis of top and bottom layer as

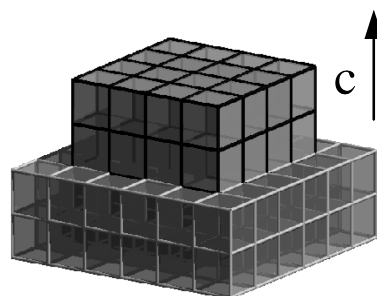

Figure 4.1: Schematic illustration of a cube-to-cube orientation.

[33] Terminus for extra or missing lattice planes, depending on the sign of the interface strain.

[34] Transmission electron microscopy (TEM) and high resolution electron microscopy (HRTEM), are adequate methods in order to investigate interfaces.

illustrated in Figure 4.1. Moreover, in literature, the term “cube-to-cube” is also used for tetragonal structures with in-plane aligned *a*-and *b*-axes[35].

If the difference of the in-plane lattice parameters approximately matches a factor $\sqrt{2}$, a 45° in-plane rotation of the top layer in conjunction with *c*-axis orientation can be favoured. Many deviations from these two epitaxial relations are known. For instance, a lattice match factor of $\sqrt{3/2}$ results in a 45° out-of-plane rotation $(001)^{bot.} \| (110)^{top}$, associated with a ±9° in-plane rotation. This growth behaviour is illustrated in Figure 4.3 and reported for the growth of $BaZrO_3$ on YSZ in chapter 4.5.3. The film growth of such extraordinary epitaxy relations requires a sufficient small resulting lattice mismatch of the according lattice directions and will always compete with a polycrystalline growth. In that case, a mixture of differently oriented grains and polycrystalline fractions is often obtained.

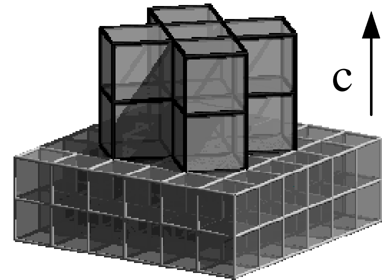

Figure 4.2: Schematic illustration of 45° in-plane orientation.

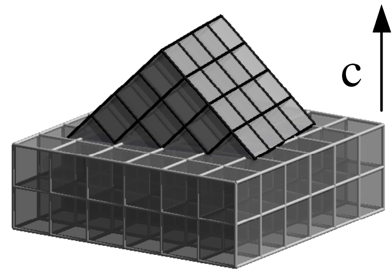

Figure 4.3: Schematic illustration of a 45° out-of-plane rotation.

Lattice Mismatch and In-plane Relations of Materials used in this Work

Using the simple equation 4.1, mutual mismatches of the materials investigated in this work are calculated in Table 4.1. The shadowed fields with bold faced numbers correspond to material combinations investigated in this work. This overview will be used in the following chapters, where the measurements proving the orientations are presented within the particular application of the materials. Apart from column SZO ^{h}, line SZO ^{d}, and separately indicated fields, the mismatches are calculated for cube-to-cube and (/) 45° relative in-plane rotation, assuming *c*-axis orientation of both top and bottom layers.

[35] This applies also for orthorhombic structures with approximately equal lattice constants $a \approx b$.

<table>
<tr><th>top ⇒
bottom</th><th>a
[nm]</th><th>STO
[001] | [011]</th><th>BZO
[001] | [011]</th><th>MgO
[001] | [011]</th><th>YSZ
[001] | [011]</th><th>CeO_2
[001] | [011]</th><th>SZO
[001] | [011]</th><th>SZO [h]
[010] | [001]</th><th>SBT
[001] | [011]</th><th>YBCO
[001] | [011]</th></tr>
<tr><td>Si</td><td>0.543</td><td>-32.7 | 1.69
- [7, f]</td><td>-25.7 | 8.8
-</td><td>-25.3 | 9.2
- [8, f]</td><td>-5.4 | 29.6
0°</td><td>-0.37 | -34.7
0° [9, f]</td><td>5.2 | -29.2
e</td><td>0.62 | 5.2
e</td><td>1.82 | -32.5
e</td><td>-34.8 | -0.51
e</td></tr>
<tr><td>$SrTiO_3$</td><td>0.390</td><td>0 | -
0°</td><td>7.2 | 41.2
0°</td><td>-7.52 | 41.6
0°</td><td>27.4 | -7.2
45°</td><td>32.3 | -2.04
45°</td><td>37.7 | 3.51
45°</td><td>33.3 | 37.7
-</td><td>34.5 | 0.14
45°</td><td>-2.2 | 32.2
0°</td></tr>
<tr><td>$LaAlO_3$ [1]</td><td>0.379</td><td>2.99 | 37.2
0°</td><td>10.1 | 44.03
0°</td><td>10.5 | 44.4
0°</td><td>33.3 | -4.1
45°</td><td>35.2 | 0.95
45°</td><td>40.6 | 6.5
-</td><td>36.2 | 40.6
-</td><td>37.3 | 3.1
-</td><td>0.79 | -33.6
0°</td></tr>
<tr><td>$BaZrO_3$</td><td>0.419</td><td>-7.11 | -41.8
0°</td><td>0 | -
0°</td><td>-0.4 | 33.9
0°</td><td>20.4 | -14.2
0°</td><td>25.4 | -9.15
0° [3]</td><td>30.8 | -3.6
-</td><td>26.3 | 30.8
-</td><td>27.5 | 6.98
-</td><td>-9.3 | 25.2
0° [a, (2)]</td></tr>
<tr><td>MgO</td><td>0.421</td><td>-7.52 | 37.2
0°</td><td>0.4 | −33.9
0°</td><td>0 | -
0°</td><td>20 | −14.75
0°</td><td>-25 | -9.55
0° [3]</td><td>30.4 | -4.0
-</td><td>-25.9 | 30.4
-</td><td>-27.1 | -7.4
-</td><td>-9.7 | -43.7
0° [2]</td></tr>
<tr><td>YSZ</td><td>0.514</td><td>-27.4 | 7.2
- [5]</td><td>-20.4 | 14.2
(011) [b, 6]</td><td>-20 | 14.75
(011) [6]</td><td>0/-
0°</td><td>5.04 | -29.4
0°</td><td>10.6 | -24
-</td><td>6.01 | 10.6 [i]
(100)</td><td>7.21 | -27.3
e</td><td>-29.6 | 4.88
45° [4]</td></tr>
<tr><td>CeO_2</td><td>0.541</td><td>-32.2 | 2.04
45°</td><td>-25.4 | 9.15
(011) [c, 6]</td><td>-25 | 9.55
(011) [6]</td><td>-5.04 | 29.4
0°</td><td>0 | -
0°</td><td>5.55 | -28.9
-</td><td>0.97 | 5.55
-</td><td>2.18 | -32.2
0°</td><td>-34.5 | 0.16
45°</td></tr>
<tr><td>SZO [d]</td><td>0.572</td><td>-
-</td><td>-
-</td><td>-
-</td><td>-
-</td><td>-
-</td><td>-
-</td><td>-</td><td>-5.1 | 1.76
g</td><td>-</td></tr>
</table>

Table 4.1: Lattice mismatch and observed in-plane relations between materials used in this work and some additional results from literature (not separately indicated values are taken from [Wu 92]). The shadowed fields with bold faced values correspond to results obtained in this work. If nothing else is specified, *c*-axis orientation of both layers and a [001] in-plane orientation of the bottom layer is supposed. Negative signs are used, when the lattice constant of the top layer is smaller than that of the bottom layer, corresponding to a tensile force.

Notes on this work: (a) Results of this work show a clear cube-to-cube growth of $YBa_2Cu_3O_{7-\delta}$ on $BaZrO_3$. This likewise applies to the inverted layer sequence (chapter 4.5.2); **(b)** Thick (d > 20 nm) $BaZrO_3$ films on YSZ exhibit a 45° out-of-plane growth, associated with a ±9° in-plane rotation. Thin films (d ≈ 3 nm) are cube-to-cube oriented (chapter 4.5.3); **(c)** In contrast to [Boi 97], a 45° in-plane rotation associated with 45° (011) out-of-plane orientation is observed (chapter 5.3) **(d)** For the $SrZrO_3$ bottom layer, *a*-axis orientation is assumed (chapter 6.6); **(e)** no epitaxial growth observed (chapter 6.3.2); **(f)** only observed after chemical treatment of the silicon substrate; **(g)** The lattice mismatch of *a*-axis $SrBi_2Ta_2O_9$ on *a*-axis $SrZrO_3$ is calculated with SBT[010] along SZO[010] and SBT[001] along SZO[003], respectively. The epitaxial relation is a still an open question, some evidence for *a*-axis growth has been found (chapter 6.6); **(h)** The lattice mismatch for *a*-axis $SrZrO_3$ on the *c*-axis oriented cubic template is calculated with SZO[002] along template[300] and SZO[010] along template[010], respectively**;** **(i)** Due to the large mismatch, indeed *a*-axis growth is observed, but the in-plane relations are not trivial (chapter 6.6).

Notes from [Wu 92]: (1) A single crystal substrate is used; **(2)** Partially, 45° in-plane rotated grains are present; **(3)** An additional 45° in-plane rotated component is observed; **(4)** Already at low deposition temperatures; **(5)** no pure (001)-orientation; **(6)** 45° out-of-plane growth is observed. **Notes from other authors: (7)** A mixed (001)- and (011)-orientation is observed by [San 92]; **(8)** no pure (001)-orientation [For 91]; **(9)** [Tsh 90].

First, due to a natural amorphous SiO_2 layer, epitaxial growth on *silicon* is only observed, if this layer is removed prior to deposition by chemical treatment (e.g. CeO_2, [Ued 90]) or the material deposited on top is able to reduce the SiO_2 layer. To the authors knowledge, only YSZ shows this ability (details in chapter 4.4). Without chemical treatment, the complex functional layers $YBa_2Cu_3O_{7-\delta}$ and $SrBi_2Ta_2O_9$, as well as the buffer layers CeO_2 and $SrZrO_3$ show only polycrystalline growth, although the lattice mismatch is small compared to that of YSZ.

Being a striking result from the table, nearly similar growth behaviour of MgO and *$BaZrO_3$* is observed on a variety of materials, although their physical properties and deposition parameters significantly differ. This means, that in most applications, MgO can be substituted by $BaZrO_3$. On the other hand, the epitaxy relations of MgO and $BaZrO_3$ with CeO_2 and YSZ, respectively, are an example for the fact, that the inversion of a layer sequence not necessarily leads to the same in-plane relations. In particular, the deposition of $BaZrO_3$ on top of CeO_2 or YSZ, is resulting in an (011)-orientation of the top layer, observed in the Si/YSZ/BZO/YBCO heterostructures in chapter 4.5.3 and in the STO/(YSZ)/CeO2/YBCO heterostructures of chapter 5.3. In contrast, a YSZ layer on top of $BaZrO_3$ exhibits a clear cube-to-cube orientation. This is remarkable, since the lattice mismatch for a 45° in-plane rotation is significantly smaller. Moreover, the influence of film thickness is illustrated by this layer sequence. Herein, a thin $BaZrO_3$ layer adopts the lattice constant of YSZ within certain limit, whereas a thicker layer tends to compensate internal lattice stress by forming grains with a (011)-orientation, as discussed in chapter 4.5.3.

Moreover, the use of buffer layers for the growth of ferroelectric $SrBi_2Ta_2O_9$ on silicon proves the possibility to enable epitaxial growth of a complex ceramic on silicon and even to control its crystallographic orientation[36]. Here, *c*-axis orientation of the $SrBi_2Ta_2O_9$ layer achieved within the layer sequence Si/YSZ/CeO_2/SBT, whereas *a*-axis orientated growth is favoured in a Si/YSZ/SZO/SBT heterostructure.

[36] Detailed discussion in chapter 6.

The Influence of Lattice Mismatch and PLD Conditions on Growth Modes

Due to a variety of processing parameters and material inherent properties, it is difficult to correlate growth behaviour and lattice mismatch in PLD. In general, a small lattice mismatch between top and bottom layer will result in a tendency to two dimensional layer by layer growth (especially observed in metals) [Nix 89], whereas at large mismatches, a tendency to island growth is assumed to occur [Pas 91]. Moreover, at certain conditions, the combination of both, known as Stranski-Kratinov growth mode (chapter 3.3.1) is proposed. However, thin film growth in a high background gas pressure, leads to restrictions of using standard diagnostics and monitoring methods.

Blank et. al [Rij 97, Bla 98,99] recently presented a technique of using in-situ reflective high energy electron diffraction (RHEED[37]) in conjunction with PLD at typical deposition pressures (up to 0.15 mbar). By this method, (i) two dimensional layer-by-layer growth, (ii) three dimensional island growth, (iii) a mixture of both, and (iv) step flow growth can be determined by the investigation of the RHEED pattern and the spot intensity. Thus, the growth mechanisms (i) to (iv) are indicated by (i) spot intensity oscillations with maxima corresponding to the completion of a monolayer, (ii) an overall decrease of the RHEED signal, (iii) damping of the signal oscillations, and (iv) a constant RHEED diffraction pattern and spot intensity, since the surface morphology remains unchanged. The analysis of homoepitaxial growth behaviour of $SrTiO_3$ (i.e. no mismatch) and the growth behaviour of $YBa_2Cu_3O_{7-\delta}$ on $SrTiO_3$ (2.2% mismatch) shows, that in the first case, true 2D layer-by–layer growth is observed, whereas at increased lattice mismatch in the second case, a Stranski-Kratinov growth mode is observed. Apart from lattice mismatch however, increased surface mobility by increased temperature and decreased ambient pressure, strongly influences the tendency to a specific growth mode.

Although RHEED can give information on initial steps of film nucleation and growth, it corresponds to a sequence of two dimensional snap shots of

---

[37] Generally, electron diffraction or spectroscopy methods require ultra high vacuum (UHV) conditions. In this system, a two stage differential pumping stage is employed. RHEED measurements are performed with an electron beam at grazing incidence angle, making it surface sensitive and yielding diffraction patterns on a phosphor screen, which can, in first approximation, be understood by the construction of a Ewald sphere.

the process. In contrast, information on thin film orientation, crystallinity and stress is obtained from X-ray measurements. However, a rough evidence on the growth mode can also be extracted from this method, but only the integral quality of the deposited films can be investigated ex-situ and thus, no predications about the early stages of film growth can be obtained. In particular, an improvement of the crystallographic orientation is indicated by decreasing FWHM of reflections in ω-scans (rocking curve), whereas the FWHM of a film reflection in $\theta/2\theta$-scans gives information about the coherence and size of crystallites. A rough estimation of the average grain size D_f of the grains within the film is possible to calculate from the FWHM of the (00*l*)-reflections by applying Scherrer´s and Warren´s formulas [Cul 78]. Moreover, a shift of a (00*l*)-reflection in relation to theoretical values allows the calculation of real *c*-axis lattice constants from (00*l*)-reflections using Bragg´s equation[38] if volume conservation of the unit cell and accordingly changed in-plane lattice constants are assumed. Such a peak shift may either result from stress within the film due to lattice accommodation to the bottom layer or residual stresses, for example owing to a thermal expansion mismatch, phase transformations, defects, interdiffusion (see e.g. $BaCeO_3$ at a $YBa_2Cu_3O_{7-\delta}/CeO_2$ reported in chapter 5.3) or a partial combination of those.

In general, from the investigations summarised in Table 4.1, a clear epitaxy relation is only observed, if the lattice mismatch for a certain orientation does not exceed a critical value of approximately 7-9%. If the mismatch lies within this limit, the most likely growth orientation can be predicted. The only exception within these results is found in the layer sequence $YSZ/BaZrO_3$, wherein the Zr sub-lattices of both materials are assumed to play an important role. Moreover, no clear relation between lattice mismatch and crystalline quality is observed. Such investigations are only possible by the comparison of chemically approximately identical layer combinations, that show only a small difference in corresponding lattice mismatches and no change in epitaxial relations to the template [Lan 98]. Thus, in the investigated layer combinations, different mismatches which change the epitaxial relations and

[38] $2d\sin\theta = n\lambda$ with $\lambda = 0.1541838$ nm (SI international standard).

interface chemistry (interdiffusion) avoid a simple picture of the relation between lattice mismatch and crystalline quality.

4.2 Material Properties

Before the results on the different heterostructures are discussed in detail, some preliminary remarks about the material properties are mentioned.

Perovskites

The class of perovskites[39] is characterised by the structural formula ABO_3, illustrated in Figure 4.4. Per unit cell, two differently co-ordinated cation sites (A, B) and three equivalent bivalent anion sites (diamagnetic oxygen) are available. The smaller B-cation is co-ordinated in an oxygen octahedron in the centre of the cube. The simple cubic unit cell is formed by larger cations, placed at the A-sites in the corners. Chemically, the system is characterised by a variety of possible cations, which can either occupy the corners or the centre of the cube.

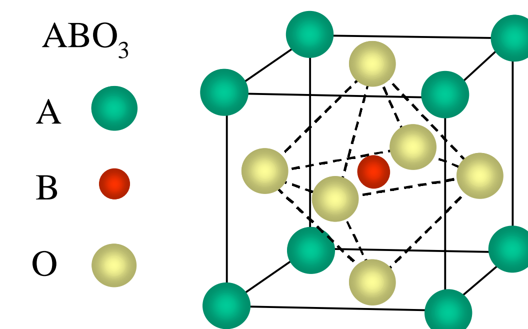

Figure 4.4: Simple cubic lattice of a perovskite.

On the other hand, the unit cell can be represented as cubic face centred packed structure with large B-cations at the cube corners, oxygen-anions in the centroid, and the small A-cation as additional ion in the centre of the cube. From the ion radii, a prediction about the packing density can be derived. As a result, the mobility of the A-cation in an ideally packed structure tends to zero. Within such a sphere model, the perovskite structure is only stable, if the ratio of the empirical ion-radii is within certain limits. In terms of Goldschmidt´s tolerance factor t[40] [Gol 58, Jin 94], this means a value of $0.89 < t < 1.02$ [Rie 94], whereas the value $t = 1$ corresponds to the ideal

[39] The name of this material class is derived from the mineral perovskite ($CaTiO_3$), discovered firstly in a Russian city of the same name.

[40] $t = R_1 / R_2\sqrt{2} = (r_A + r_O)/(r_B + r_O)\sqrt{2}$.

perovskite structure. Modifications in the tolerance factor, induced by different bivalent and trivalent metal-ion combinations results in a lattice distortion and deformation of the oxygen octahedron. This influences the electronic and magnetic properties of the system [Hwa 95, Fon 96]. In particular with doping series, effects like ion radii misfits or oxygen deficiency can lead to co-operative torsion, alternating obliquity, or strain of the octahedrons, resulting in a variety of derivatives of the ideal cubic structure. This broad spectrum of crystal symmetries (cubic, tetragonal, rhombohedral, orthorhombic, monoclinic) are related and mutual transformable and thus aggravate the analysis of the crystal structure by standard X-ray measurements. In Table 4.2, the crystal data, the thermal expansion coefficients, and the dielectric constants of materials used in this work are given.

material	$SrTiO_3$	Si	$BaZrO_3$	YSZ	CeO_2	SZO	SBT	YBCO
symmetry	cubic	cubic	cubic	cubic	cubic	orthor.	orthor.	orthor.
spacegroup	Pm3m	Fd3m	Pm3m	Fm3m	Fm3m	Pbnm	Fmm2	Pmmm
a [nm]	0.3905	0.5431	0.4193 [a]	0.512(6)	0.5411	0.581	0.5531	0.382
b [nm]	-	-	-	-	-	0.579	0.5534	0.388
c [nm]	-	-	-	-	-	0.8204	2.498	1.168
α [10^{-6} K^{-1}]	9.4	3.8	5.6 [b]	11.4	10.6	0.298		13-16
ε	≈ 300 [e]	≈ 11.9 [d]	32-40 [b]	≈ 4	≈ 22	≈ 25 [f]	≈ 180 [e]	

Table 4.2: Properties of the materials used in this work: Crystal structure, lattice constant a, thermal expansion coefficient α, and dielectric constant ε at T = 300 K. Notes: Values are taken from [Mau 98] or separately indicated by (a) [JCP 96], (b) [Lan 81], (c) [Wec 92], (d) [Büt 91], (e) [Sch 99], (f) [deL 95].

$BaZrO_3$

$BaZrO_3$ exhibits a cubic perovskite structure (Pm3m) with a lattice constant of 0.4193 nm [JCP 96], and a thermal expansion coefficient of $\alpha_{300K} = 5.6 \times 10^{-6}\ K^{-1}$ [Lan 81]. As illustrated in Figure 4.4, the Ba^{2+}-ion corresponds to the larger A-cation and the Zr^{4+}-ion corresponds to the smaller B-cation, respectively [Sch 96]. Being a possible reason for its inertness [Ger 97], $BaZrO_3$ shows an extraordinary high melting point of more than 2500°C. Resulting from the extraordinary high temperatures and incorporated experimental difficulties, the exact value is difficult to measure. From a melting point diagram, a melting point of 2640 °C is obtained for the BaO-ZrO_2 system with 44.6% percentage by weight of ZrO_2 ($BaZrO_3$)[War 30]. Moreover,

$BaZrO_3$ is an ion conductor with a specific conductivity that follows the Arrhenius-law with an activation energy of $E_A = 2.5$ eV and a specific resistance of $\rho = 3.3 \times 10^{-9}\ \Omega$cm at 300 K [Taw 87]. Due to its structural relation to the ferroelectric ceramics $BaTiO_3$ and $PbTiO_3$ and a high dielectric constant of $\varepsilon \approx 32$ [Lan 81], $BaZrO_3$ is frequently associated to ferroelectrics, although no ferroelectric phase transition was ever observed [Lev 76]. $BaZrO_3$ is mainly employed as inert crucible material for $YBa_2Cu_3O_{7-\delta}$ single-crystal preparation. Furthermore, $BaZrO_3$ thin films are often applied as capacitor material or as passivation layer for semiconductors [Gie 97]. However, there is only very little information available on the dielectric properties of $BaZrO_3$ thin films. Therefore, dielectric measurements have been performed and will be a subject of chapter 4.5.1.

Yttrium stabilised Zirconium

By addition of 9-40 mol % Y_2O_3, the monoclinic zirconium dioxide is stabilised in the cubic phase corresponding to a fluorite structure analogous to CeO_2. The thermal expansion coefficient of Yttrium stabilised Zirconium (YSZ) amounts $\alpha_{300K} = 11.4 \times 10^{-6}$ K^{-1} [Lan 81]. Depending on the Y_2O_3-content, a lattice constant between $a = 0.512$ nm and 0.516 nm is obtained [Lev 75], resulting in a lattice mismatch of 5.4% between Silicon and 9%-YSZ [Mat 95]. This value could be optimised by a higher concentration of Y_2O_3. However, the minimum concentration is chosen in order to obtain optimal isolation properties, because ZrO_2 is an isolator in which by introduction of two Y^{3+}-ions one free O^{2-}-site is formed, leading to ion conduction. Furthermore, the Y_2O_3 content influences the dielectric properties of YSZ. For 9%-YSZ, a dielectric constant of $\varepsilon \approx 4$ is observed [Ing 98]. In the field of HTSC thin films, YSZ is known to be applied as an interdiffusion barrier for $YBa_2Cu_3O_{7-\delta}$ on silicon, but due to chemical reaction, usually a second buffer layer is introduced.

CeO_2

Similarly to YSZ, CeO_2 shows a cubic fluorite structure with the space-group Fm3m and a lattice constant of a = 0.5411 nm. The thermal expansion coefficient is $\alpha = 10.6 \times 10^{-6}$ K^{-1}, and the dielectric constant is $\varepsilon \approx 22$ at 300 K,

respectively. As YSZ, CeO_2 is chemically not completely inert against $YBa_2Cu_3O_{7-\delta}$, resulting in the formation of a $BaCeO_3$ layer at the interface.

SrTiO₃

The cubic perovskite $SrTiO_3$ (STO) has a lattice constant of $a = 0.3905$ nm. Due to a small lattice mismatch of 2.2 %, it is used as a standard substrate for *c*-axis oriented $YBa_2Cu_3O_{7-\delta}$. The dielectric constant however, amounts ε (300 K) $\approx$ 300, which is particularly inconvenient for HF applications. At a temperature of $T = 105$ K, an antiferro-deformative phase transition occurs, wherein the oxygen octahedrons of adjacent unit cells rotate contrarily, resulting in a tetragonal low temperature phase. By doping with Nb ($SrTi_{1-y}Nb_yO_3$), the crystallographically identical compound is conducting and can be used as an electrode for dielectric measurements (see chapter 4.5.1).

SrZrO₃

At room temperature, $SrZrO_3$ (SZO) crystallises in a slightly distorted orthorhombic perovskite structure. To the authors knowledge, no investigations on $SrZrO_3$ thin films as buffer layer are published. Epitaxial deposition on MgO [Bec 95] and on $SrTiO_3$ [Ern 98] has been reported. Due to a small misfit to the *a*-axis of $SrBi_2Ta_2O_9$ and its orthorhombic structure, *a*-axis oriented $SrZrO_3$ is a potential candidate for a buffer layer material for ferroelectric $SrBi_2Ta_2O_9$ thin films (see chapter 6.6). Moreover, $SrZrO_3$ combines high permittivity with low loss and a positive temperature coefficient of permittivity. Presently, investigations of $SrZrO_3$ are focussed on its well known

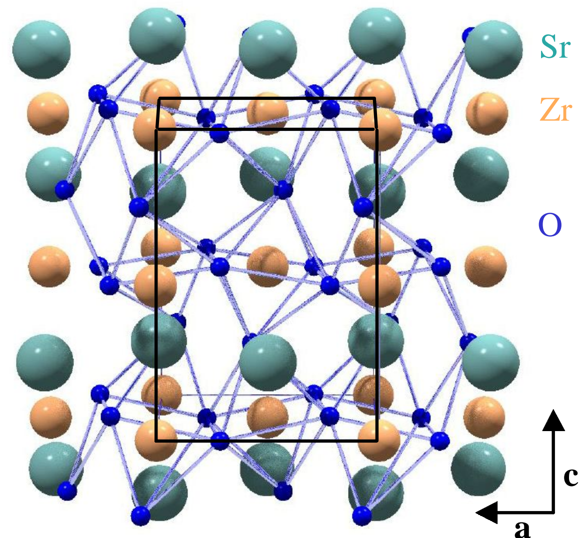

Figure 4.5: The crystal structure of $SrZrO_3$ with lattice constants of $a = 0.5786$ nm, $b = 0.5815$ nm, $c = 0.8196$ nm and the pseudo cubic spacegroup *Pbnm* [Aht 76]. The oxygen atoms are co-ordinated at the corners of the pyramids. The unit cell is indicated by black lines.

properties as a high temperature proton conductor[41] [Yug 97, Sat 97, Sat 98, Esc 95]. Thus, as well as $SrCeO_3$ and $BaCeO_3$ [Iwa 81], this compound receives increasing attention due to its application in fuel cells, gas (hydrogen) sensors, and humidity sensors. Perovskite structures AMO_3 (A = Ca, Sr, Ba and M = Zr, Ce) become high temperature proton conducting by substituting trivalent dopants (e.g. Y^{3+}) for zirconium due to thermally activated proton hopping processes. In conjunction with YSZ, junctions of this oxide ionic conductor and the protonic conductor $SrZrO_3$ have been used to manufacture devices in order to detect hydrogen, oxygen, or water content of atmosphere [Shi 97].

Silicon

Being the standard substrate in semiconductor industry, the semiconducting silicon crystallises in the diamond structure i.e. in a cubic face centred space lattice (space group Fd-3m) with a lattice constant of $a = 0.543$ nm. The silicon atoms are co-ordinated tetrahedrally by four neighbours. The material shows no plastic strain below 500°C, is free of hysteresis and ageing and is available in extremely high purity (only one impurity per 10^{10} atoms). Depending on the doping level, the specific resistance is between 50 Ωcm and 2000 Ωcm. With a value of $\alpha = 2.4 \times 10^{-6}\ K^{-1}$ [Kuk 91], the thermal expansion coefficient is significantly smaller than those of the perovskite like materials used in this work. As a well known problem this results in thermal stress and in the worst case, even in cracks in the subsequent oxide layers, if a critical thickness is exceeded [For 90]. If silicon is exposed to an oxygen atmosphere, a natural SiO_2 layer with a typical thickness of approximately 4 nm is formed. In semiconductor industry, this layer is used as an insulator. In thin film deposition of epitaxial oxides however, this is a major problem, which requires a special strategy, as discussed in chapter 4.4.

---

[41] A large amount of protons (H^+) can be introduced into crystal.

The High Temperature Superconductor $YBa_2Cu_3O_{7-\delta}$

$YBa_2Cu_3O_{7-\delta}$ (YBCO) is the most intensively investigated representative of the known high temperature superconducting barium copper oxides. As illustrated in Figure 4.6, the orthorhombic unit cell is derived from three perovskite unit cells ABO_3 leading to $YBa_2Cu_3O_9$, whereas two oxygen defects are required for the occurrence of superconductivity. The barium and the yttrium ion are placed in the centre of the perovskite cells. The copper ions are co-ordinated at the corners and the oxygen ions at the edges, respectively. Merely six to seven of possible nine oxygen positions are occupied. Depending on the oxygen content, different phases with different properties exist. The tetragonal, antiferromagnetic and insulating phase is observed for $\delta > 0.6$ [Che 87]. An oxygen content of $0.25 \le \delta \le 0.6$ leads to the Ortho-II phase, showing already the desired orthorhombic crystal structure. However, herein every second CuO-chain is absent and the superconducting transition temperature is strongly lowered to $T_c \approx 60$ K. Within an oxygen parameter of $0 \le \delta \le 0.25$, the superconducting Ortho-I phase[42] with a T_c of approximately 93 K is formed. In principle, superconductivity occurs quasi two dimensional in the CuO_2 planes, since the coherence length $\xi_c \approx 0.4$ nm in

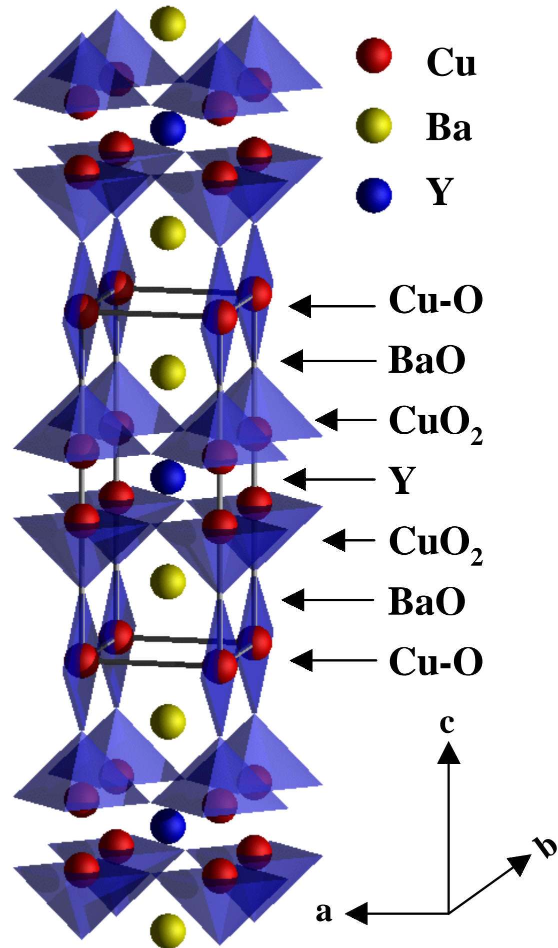

Figure 4.6: The crystal structure of $YBa_2Cu_3O_{7-\delta}$ with lattice constants of $a = 0.382$ nm, $b = 0.388$ nm, $c = 1.168$ nm and the spacegroup P/mmm [Jor 87]. The oxygen atoms are co-ordinated at the corners of the pyramids. The unit cell is indicated by black lines.

[42] Which is meant in this work, if nothing else is specified.

c-direction is smaller than the distance *c* between the planes[43]. The CuO chains progress along the *b*-axis and serve as charge carrier reservoir [Cav 88]. With respect to superconductivity, Yttrium is of secondary relevancy. This atom is replaceable by most of rare earth metals without changing the transition temperature significantly [Tar 87], leading to $REBa_2Cu_3O_{7-\delta}$ as chemical formula. In order to achieve a crystalline growth of the Ortho-I phase, the deposition process is conducted within a certain pressure-temperature range. First, the tetragonal phase is formed during the deposition process. Consecutively, the incorporation of oxygen atoms during cool down leads to the orthorhombic phase [Jor 87], whereas the superconducting properties are optimised by a annealing step at high oxygen pressures (10^5 Pa) and moderate temperatures in the range of 550 °C[44]. Typically, thin films of this material exhibit critical currents of several 10^7 A/cm^2 at 4.5 K (10^6 A/cm^2 at 77 K).

4.3 The Role of Buffer Layers in General

In thin film technology, a substrate as well as layer can serve as a growth base for a functional layer. Consequently, deposited layers, giving a growth base are called “bottom” or “buffer” layers. Within complex multi-layer systems, such a buffer layer has to fulfil several requirements:

(i) It has the function as an effective barrier for the diffusion of substrate elements[45] into the functional layers (e.g. a superconductor or a ferroelectric). In turn, it provides a barrier for layer elements (preferentially metallic elements) into the substrate[46]. To ensure this, a minimum thickness, depending on the material, is necessary.

---

[43] The structural crystal anisotropy of YBCO is described by the parameter $\gamma = \xi_{ab}/\xi_c$ = 5 to 10.

[44] A detailed description of the tempering process can be found in the appendix. A phase diagram of $YBa_2Cu_3O_{7-\delta}$ combined with the appropriate pressure-temperature working range of different deposition methods can be found in [Bor 89, Ham 98].

[45] E.g. Si or Al, if sapphire and alternative Al compounds ($LaAlO_3$) are used as substrates.

[46] For silicon this followed by a change of its semiconducting properties, especially in doped regions of the substrate. Example: Formation of Si/Cu compounds if silicon is used with Cuprate-superconductors.

(ii) The buffer layer material has to be inert against substrate and functional layers, especially at extreme deposition conditions necessary for the sequencing perovskite layers. Otherwise, chemical reactions at the interface lead to the formation of inter-diffusion layers, which impede correct stoichiometry and epitaxial growth of the next layer.

(iii) With respect to crystallinity of the functional layers, the buffer layer material has to grow epitaxially by appropriate lattice parameters comparable to those of the substrate. Additional buffer layers then can match up to the lattice constants of the functional layer. In this context, the previously mentioned lattice mismatch is important.

(iv) Especially in conjunction with silicon substrates the difference in thermal expansion coefficients α of the different materials has to be minimised. The large temperature difference between deposition temperature (up to 1000°C) and device operation temperatures (down to 4K) can cause strain and even cracks on the buffer- and functional layers. Values for α are listed in Table 4.2 and a helpful plot of lattice constant versus thermal expansion coefficient can be found in the work of D.B. Chrisey et al. [Chr 94].

(v) For special applications dielectric properties, microwave losses and electric conductivity of the buffer layer can have a significant influence on the properties of the functional layer. Since all these requirements are mostly not fulfilled by a single material, additional buffer layers are usually introduced.

4.4 Buffers for Functional Oxides on Silicon

Only the incorporation of novel functional layers with the established semiconductor process technology will lead to the fabrication of economically and technically relevant devices. However, the fabrication of epitaxial oxidic thin films on silicon substrates is governed by a fundamental problem: Due to the high reactivity of silicon with oxygen, as soon as the silicon wafer comes into contact with atmospheric oxygen, a ca. 4 nm thick amorphous SiO_2 layer

is formed[47] which impedes epitaxial growth of a consecutively deposited layer. There are two possibilities to solve this problem. First, the SiO_2 layer can be removed by etching with HF acid and the further formation of SiO_2 is avoided by handling of the cleaned substrate in ambient inert gas atmosphere. Herein, the etching time turns out to be critical, since etching leads to increased surface roughness of the substrate. The more elegant way is to remove the SiO_2 layer by chemical reaction while a buffer layer is deposited. In the field of HTSC thin films, where crystalline quality is essential, a large effort was done in order to get an effective solution [Jae 94, Boi 95, Mec 96, Sch 96]. From different studies it became clear, that Yttrium-stabilised ZrO_2 (YSZ) is a suitable buffer layer material for this application [For 90]. A consecutively deposited additional layer of e.g. $BaZrO_3$, CeO_2 or $SrZrO_3$ can be used in order to avoid inter-diffusion between YSZ and the functional layer in order to increase the crystalline quality or to control the epitaxy of the latter.

4.4.1 Deposition of YSZ as the first Buffer Layer on Silicon

Besides the previously mentioned tasks of a buffer layer, YSZ plays a particular role in conjunction with silicon. The natural SiO_2 is removed due to the following chemical reactions [Aji 91, Beh 92, Jae 94, Boi 95, Mec 96]:

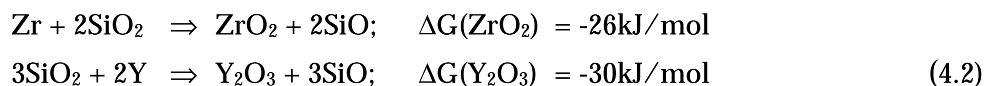

$$\begin{aligned} Zr + 2SiO_2 &\Rightarrow ZrO_2 + 2SiO; \quad \Delta G(ZrO_2) = -26\,kJ/mol \\ 3SiO_2 + 2Y &\Rightarrow Y_2O_3 + 3SiO; \quad \Delta G(Y_2O_3) = -30\,kJ/mol \end{aligned} \tag{4.2}$$

Due to the higher bonding enthalpy of ZrO_2 and Y_2O_3 compared to SiO_2 ($\Delta G = -21\,kJ/mol$), YSZ is stable against silicon and even able to reduce the natural SiO_2 layer. The formed SiO is not stable at temperatures above 800°C [Spa 97] and pressures below 3.5×10^{-4} mbar [NBS 75, For 92]. Thus it is removed by natural sublimation[48] from the interface at typical deposition temperatures of 850°C. PLD is an appropriate technique to provide these reactions due to several reasons. On the one hand, the possibility of thin film deposition at low pressures ($< 5\times10^{-6}$ mbar) enables the above mentioned

---

[47] In semiconductor industries, this strong reaction is used to create isolating SiO_2 layers.

[48] According to the Clausius Clapeyron law.

reactions and avoids formation of silicates ($ZrSiO_4$, Y_2SiO_5) [Mat 95]. On the other hand, a high laser fluence ($J \approx 3J/cm^2$) guarantees the dissociation of ZrO_2 and Y_2O_3 at the target in order to provide the reactions in formula 4.1.

The additional role of YSZ as a reduction layer for SiO_2 requires a special deposition strategy. As for all oxides, the deposition of YSZ needs a sufficient oxygen pressure in contradiction to the low oxygen gas pressure, which is necessary for the above mentioned reaction. Consequently, the deposition is divided into two steps: First, a thin layer with a thickness up to several nanometer of YSZ is deposited at base pressure ($2x10^{-6}$ mbar) in order to ensure the reduction of the complete natural SiO_2 layer. Being the second step, the oxygen pressure is increased to a sufficient value of 5 $x10^{-4}$ mbar and the second layer is deposited in order to obtain an over all thickness of 40 nm. The choice of the YSZ buffer thickness underlies several restrictions:

(i) A sufficient thickness of 40-70 nm to ensure its function as an interdiffusion barrier [Mau 93, Bel 97][49].

(ii) A minimum thickness of 40-100 nm in order to obtain sufficient crystalline quality [Ing 98]. An exponential decay of the FWHM with increasing thickness, saturating at a best values of 0.6° is observed, which coincides with results of [Méc 96] and [Qia 95].

(iii) An upper limit of the thickness of (e.g. 70nm for $YBa_2Cu_3O_{7-\delta}$ [For 90, Pru 92]), since different thermal expansion coefficients (see Table 4.2) of substrate, YSZ and subsequent layers can lead to cracks within the functional layer.

(iv) In the case of ferroelectric devices, the thickness of buffer layers with smaller dielectric constants have to be minimised (see Chapter 6).

Since the deposition rate in PLD depends sensitively on deposition conditions, especially on the ambient oxygen pressure, laser fluence and the target density, thickness measurements by low angle X-ray diffraction (LXRD) are performed at regular intervals. In Figure 4.7, typical measurements of YSZ on silicon are shown. Shorter oscillations correspond to the YSZ layer, whereas

[49] Investigated by Auger-Electron-Spectroscopy (AES) and Sputtered Neutral Mass Spectroscopy (SNMS).

longer oscillations due to a not removed 4.9 nm thick SiO_2 layer are visible in Figure 4.7a.

At optimised deposition conditions of $T_{dep} = 850\,°C$, $d = 40\,mm$, $J \approx 3\,J/cm^2$, $p < 5\,x10^{-6}$ mbar (1st step) and $p = 5\,x10^{-4}$ mbar (2nd step), high quality YSZ films with a FWHM of typically 1° and in best case 0.77° are obtained. The internal stress of the Y-stabilised zirconium is known to avoid better *c*-axis orientation. Particularly, high laser fluences ($J \approx 3\,J/cm^2$) and elevated substrate temperatures ($T_{dep} = 850\,°C$) are crucial deposition parameters of YSZ in order to minimise the polycrystalline YSZ(111) fraction. Moreover, also the ablation rate ($r \approx 0.04$ nm/pulse) is highly sensitive on the laser fluence.

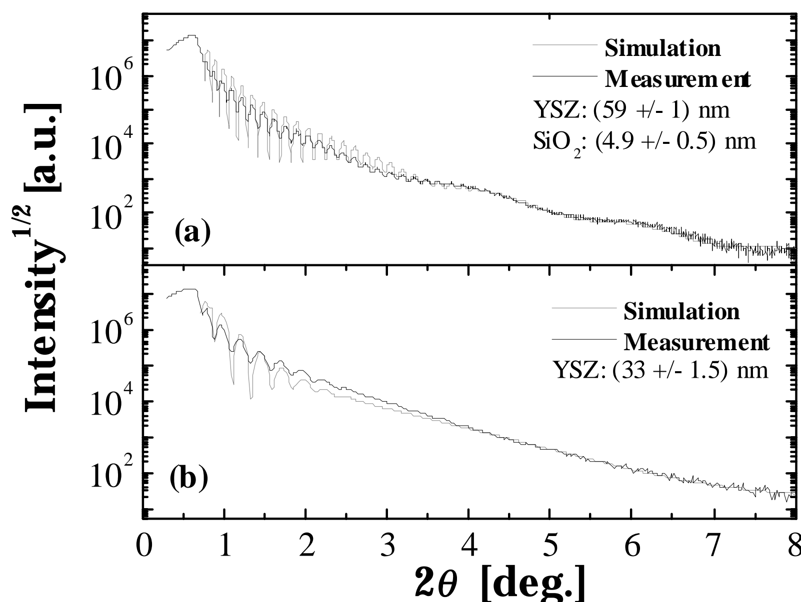

Figure 4.7: Low-angle X-ray diffraction patterns of YSZ on silicon. **(a)** Deposition pressure constant at $5x10^{-4}$ mbar, the natural SiO_2 (5 nm) layer is not removed. FWHM of the (002)-reflection of Si 2.5 °-5 °. **(b)** Due to the application of the 2-step deposition strategy, no SiO_2 layer is visible, and the FWHM of the (002)-reflection of silicon exhibits values below 1 °.

Within the first deposition step, the reduction of the SiO_2 layer, described by formula 4.1, takes place. After complete reaction, an oxygen deficient YSZ is formed, which is assumed to be partially loaded with oxygen at an increased pressure within the second deposition step as a result of the a high oxygen mobility in YSZ. Optimisation series show, that with increasing

thickness of the first layer (up to approximately 20 nm), the crystalline quality is only slightly deteriorated, as illustrated in Figure 4.8a and b. By further increasing the thickness, the formation of polycrystalline YSZ will be favoured, leading to a worse crystallinity with a FWHM of the YSZ(002)-reflection in the range of 2°-3° (Figure 4.8c). Above this limit however, only polycrystalline YSZ is obtained, which is indicated by the exclusive occurrence of the YSZ(111)-reflection in Figure 4.8d.

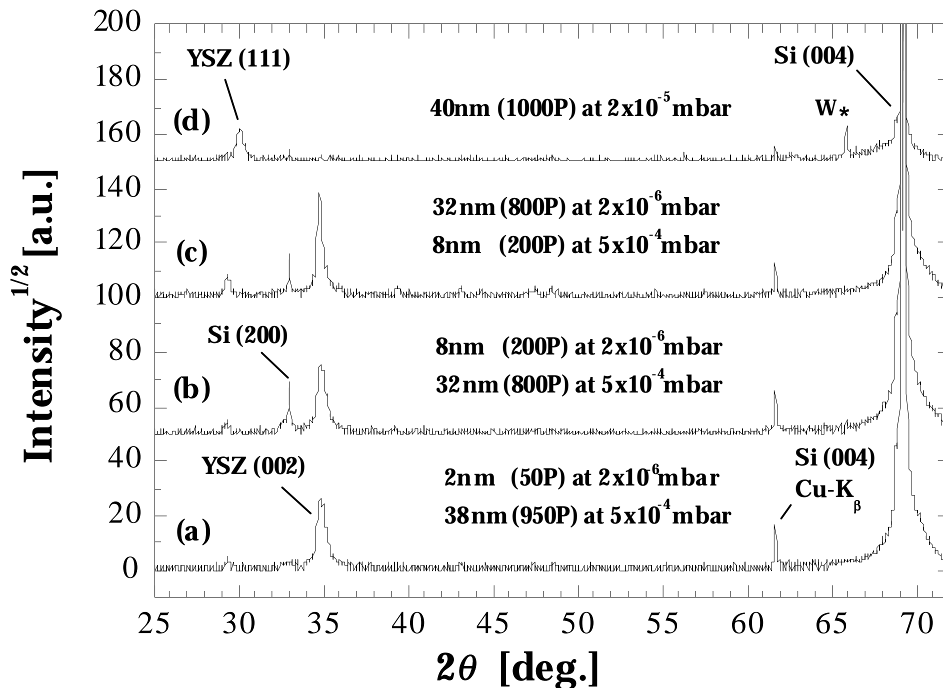

Figure 4.8: XRD patterns in Bragg-Brentano geometry show the crystalline orientation of YSZ on silicon obtained by one- and two-step deposition technique with changing layer thickness. All films were deposited at $T = 850$ °C, $d = 40$ mm and $J = 3$ J/cm². **(a,b)** Optimal properties are observed at a thickness of approximately $d_I \leq 20$ nm, with a FWHM of the YSZ(002)-reflection of 0.7° to 1.3° **(c)** Above a certain limit, polycrystalline YSZ is formed and the FWHM of rocking curves of the YSZ(002)-reflection increases to values in the range of 2°. **(d)** If no first layer at low pressures is deposited, only polycrystalline growth is observed. Parasitic reflections of the X-ray tube due to impurities in the Cu anode are indicated by (*).

4.4.2 Dielectric Properties of YSZ

However, although highly *c*-axis oriented YSZ films on silicon can be obtained by this technique, the resulting dielectric properties are strongly influenced by the growth processes (defects, oxygen deficient interface layers, etc.)

occurring during the deposition. With respect to the fabrication of planar ferroelectric thin film devices, the dielectric properties of the buffer layers should be known in order to ensure that the properties of a ferroelectric functional layer are not superimposed by dielectric properties of the buffer layer.

In general, a deviation from an ideal *C(V)*-characteristic[50] is resulting from dynamic or static processes, respectively. First, a hysteresis in *C(V)*-measurements of dielectric layers can be observed, when charge trapping sites or mobile ions are created within an oxygen deficient interface layer between silicon and YSZ. These charge carriers will slowly migrate with some characteristic time constant according to the applied voltage. Therefore, a resulting internal field will temporarily shift the switching point from higher to lower capacities depending on the direction of the applied DC-voltage, finally leading to a hysteresis. Secondly, a shift of *C(V)*-curves to positive (negative) voltages is observed, when negative (positive) surface charge carriers are confined to the Si/YSZ interface [Ter 62, Gro 65]. These spatially located charge carriers will generate a constant internal field at the interface, which will lead to a fixed shift of the switching point from higher to lower capacities. Moreover, the charge carriers are possibly formed due to a chemical reaction between silicon and YSZ or a thin residual SiO_2 layer. From the magnitude of voltage shift, a trapped charge density, i.e. the amount of charge that contributes to the average shift, can be calculated by $n_s = U_s C_{YSZ}/q_0$. Herein, the difference in workfunctions between silicon and gold-electrode can be neglected at doping values for silicon of $10^{15}\,cm^{-3}$.

In Figure 4.9, *C(V)*-characteristics of different YSZ films deposited on untreated silicon are shown. The PLD deposition temperature $T_{dep} = 850\,°C$, and energy density $J \approx 3\,J/cm^2$ was kept constant for all films. The number of pulses and the pressure was varied. By means of LXRD measurements, the thickness of the films was exactly calculated and the removal of the SiO_2 layer was proven. However, the existence of a very thin SiO_2 layer in the range of 1 nm and below can not be excluded by means of low-angle XRD.

[50] A detailed description of a capacitance-voltage *C(V)* characteristic and the involved processes can be found in chapter 6.4.1.

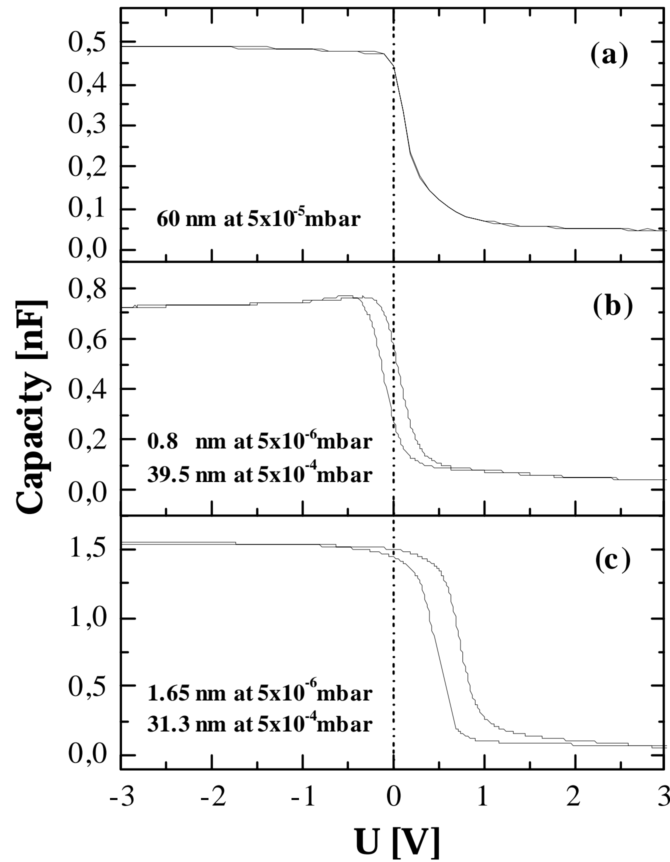

Figure 4.9: *C(V)*-characteristics of YSZ films deposited on untreated silicon by different deposition techniques and overall thickness. The PLD deposition temperature $T_{dep} = 850\,°C$ and laser energy density $J \approx 3\,J/cm^2$ was the same for all films. The number of pulses n and the particular pressure was varied. The thickness has been exactly determined by means of LXRD measurements. **(a)** For a complete 60 nm ($n = 1500$) thick YSZ layer, no hysteresis is observed. A capacitance of $C = 0.49$ nF and a shift of $U_s = 0.22$ V is measured. ($f = 1$ MHz, $U_{AC} = 0.2$ V). **(b)** For a YSZ thickness of $d_1 = 0.8$ nm ($n = 20$) and $d_2 = 39.5$ nm ($n = 980$), a hysteresis of $dU = 0.17$ V a capacitance of $C = 0.75$ nF is observed. ($f = 1$ MHz, $U_{AC} = 0.2$ V). **(c)** For a thickness of $d_1 = 1.65$ nm ($n = 50$) and $d_2 = 31.3$ nm ($n = 950$), an increased hysteresis of $dU = 0.27$ V and an increased capacitance of $C = 1.57$ nF is observed. In Addition, a shift to positive voltages of $U_s = 0.6$ V is visible ($f = 1$ MHz, $U_{AC} = 0.2$ V).

In Figure 4.9a, a *C(V)*-characteristic of a YSZ layer using a single deposition step technique (60 nm at $p = 5 \times 10^{-5}$ mbar) is shown. These layers typically exhibit a strong polycrystalline YSZ fraction, and a FWHM of the YSZ(002) reflection in the range of 2°. In contrast, the *C(V)*-characteristics in Figure 4.9b and c both represent highly crystalline YSZ layers deposited by using the two step technique. In these layers, no polycrystalline fraction is observed and the FWHM typically shows values in the range of 0.7° to 1°. From a detailed

LXRD analysis the overall thickness is determined to 40.3 nm and 33 nm, and a slightly different first layer thickness of 0.8 nm and 1.65 nm was achieved by varying the number of pulses for the layers in Figure 4.9b and c, respectively[51].

From the capacitance in the accumulation range of $C_a = 0.49$ nF, $C_b = 0.75$ nF and $C_c = 1.57$ nF and the area of the gold electrode ($r = 625$ µm), the value of the dielectric constant at room temperature is calculated to $\varepsilon_a = 4.0 \pm 0.3$, $\varepsilon_b = 2.6 \pm 0.3$, $\varepsilon_c = 4.7 \pm 0.3$, respectively. Thus, the YSZ film in Figure 4.9a quantitatively matches the literature value [Ren 96] of $\varepsilon \approx 4$, whereas the YSZ layers in Figure 4.9b and c exhibit an increased and decreased dielectric constant, respectively. This deviation from literature values for highly oriented single crystalline YSZ [Mau 98] is obviously related to the oxygen pressure used for the deposition process. Thus, the effective dielectric constant of the YSZ layers can be associated to the movement of oxygen vacancies [Fei 93]. Due to the complexity of the deposition process however, it is not yet clear, to which extent the oxygen content in the thin interface layer and the second layer influence the resulting dielectric constant.

According to the previously mentioned reasons for hysteresis and shift, some conclusions can be made. First, depending on the thickness of the first layer in Figure 4.9b and c, an increased hysteresis from $dU = 0.17$ V ($d_1 = 0.8$ nm) to $dU = 0.27$ V ($d_1 = 1.65$ nm) is assumed to be originating from an increased amount of mobile charge carriers in the oxygen deficient YSZ layer due to low pressure deposition at $p = 5\ \mathrm{x}10^{-6}$ mbar. Moreover, an additional shift of the $C(V)$-curve to positive voltages by $U_s = 0.6$ V in Figure 4.9c is assumed to be caused by spatially confined negative charges leading to an increased surface states density of $4.79\mathrm{x}10^{11}$ cm^{-2} at the silicon/YSZ interface[52]. However, from this measurement, the occurrence of charges is not yet clear, since the $C(V)$-characteristic of a YSZ layer with a thinner first layer shows a hysteresis, but no shift. Considering the measurement in Figure 4.9a, the deposition of the complete layer at intermediate pressures of $p = 5\mathrm{x}10^{-5}$ mbar

[51] The resulting thickness of the layers is calculated supposing constant deposition rates, which are assumed not to change appreciably within this pressure range.

[52] By applying the formula $n_s = \Delta U\, C_{YSZ} / q_0$.

leads to a complete disappearance of a hysteresis effect, due to the absence of an oxygen deficient layer, which contains mobile charges. Nevertheless a voltage shift of $U_s = 0.22$ V, is observed, which in comparison to Figure 4.9b, results from a smaller density of spatially confined surface states (trapped charges) of $1.35x10^{11}$ cm^{-2}.

In conclusion, the complex processes occurring during the initial growth of YSZ on silicon involving film nucleation and the previously mentioned chemical reactions, avoids a simple picture of the resulting dielectric properties. However, further improvement of YSZ thin films concerning crystalline as well as dielectric properties is expected from the use of the presented two step deposition technique in combination with a further reduction of the first layer thickness.

4.5 $BaZrO_3$ as a Buffer Layer for HTSC Applications

The investigation of $BaZrO_3$ as a buffer layer material is motivated by the fact, that up to now the best high temperature superconducting $YBa_2Cu_3O_{7-\delta}$ single crystals are grown in $BaZrO_3$ crucibles [Erb 96][53]. Extremely low interdiffusion between both materials is the main reason for the high purity of the HTSC (better than 99.995%). Due to this inertness $BaZrO_3$ is a promising material for being used in high quality heterostructures involving $YBa_2Cu_3O_{7-\delta}$ layers. Especially for the development of HTSC devices on appropriate substrates, $BaZrO_3$ can either be used as an interdiffusion barrier or as an intermediate layer to improve or to control the epitaxial growth of $YBa_2Cu_3O_{7-\delta}$.

4.5.1 Dielectric Properties of $BaZrO_3$

Hitherto, there is only little information available on the dielectric properties of $BaZrO_3$ thin films. However, in order to apply $BaZrO_3$ as a buffer layer for $YBa_2Cu_3O_{7-\delta}$, the knowledge of its insulating and dielectric properties, especially as a buffer for low-dissipation substrates in HF applications, is necessary. Consequently, frequency and temperature dependent measurements of

[53] It is as well used for the growth of mercury based HTSC compounds.

the dielectric constant within $Au/BaZrO_3/Nb\text{-}SrTiO_3$ diodes have been performed[54].

As indicated in Figure 4.10, below temperatures of 185 K and above frequencies of 1 kHz, an approximately constant capacity is observed. At lower frequencies and higher temperatures, an increase of the capacity by maximal 25% in conjunction with an increasing dispersion effect occurs. According to the Debye model[55], the maxima of the imaginary part coincide with the reversal point of the real part of the dielectric constant for equal temperatures. Depending on temperature, the contribution of ionic and electronic polarisability to the dielectric constant (compare Figure 6.3) amounts between $\varepsilon_\infty = 63\text{-}65$, whereas the dielectric relaxation lies between $\varepsilon(0) = 4.2$ and 4.5.

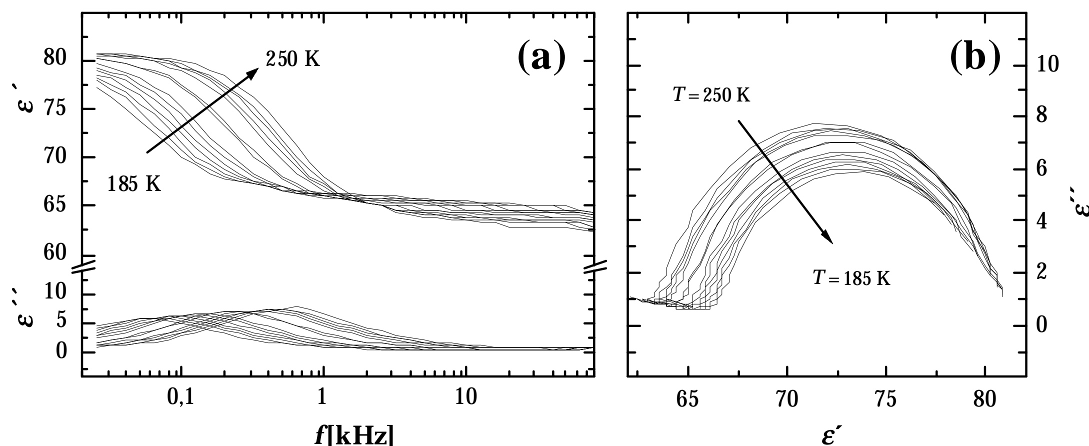

Figure 4.10: (a) Real- $\varepsilon'(f)$ and imaginary- $\varepsilon''(f)$ part of the dielectric constant of a 200 nm thick $BaZrO_3$ film on Nb-doped $SrTiO_3$. **(b)** Cole-Cole plot of the data in (a). For equally scaled ε' and ε'' axes, the semicircle intercepts the ε' axis at an angle of $\gamma = 1/2\pi(\alpha) = 70°$, resulting in a coefficient $\alpha = 0.77$ of the Cole-Cole model.

In contrast to the theoretical Debye-width of the dispersion maximum (1.14 decades), the dispersion maxima are broadened with decreasing temperature up to 1.3 decades. This behaviour can be described by the Havriliak-Negami relation $\varepsilon(\omega) = \varepsilon_\infty + \varepsilon(0)/(1+(i\omega\tau)^{\alpha})^{\beta}$, which corresponds to the Debye relation, modified by a width parameter α and an asymmetry parameter β. Since the dielectric loss tanδ shows a symmetric behaviour and no frequency dependence of its peak position, β is equal to 1. Therefore, cole-cole behaviour

[54] With a HP 4284 LCR Meter, technical details can be found in [Mau 98].

[55] Discussed in detail in chapter 6.2.

is suggested (see also chapter 6.2). From a detailed analysis (Cole-Cole plot) in Figure 4.10, the theoretically expected symmetric semicircle is visible for equally scaled ε' and ε'' axes. From an interception angle of $\gamma = 1/2\pi(1\text{-}\alpha) = 70°$ with the ε'' axis, the width parameter α, i.e. the magnitude of relaxation time distribution is estimated to $\alpha = 0.77$. A fit of the data by the use of the Havriliak-Negami relation results in a dielectric constant of $\varepsilon_\infty \approx 65$ due to ionic and electronic polarisation and a dielectric constant $\varepsilon(0) \approx 4.5$ due to dielectric relaxation. This value for α lies within the range of single crystalline ($\alpha = 0.6$, [Egu 39]) and amorphous $SrTiO_3$ ($\alpha = 0.8$, [Mor 95]).

4.5.2 $BaZrO_3$ as a Buffer Layer for $YBa_2Cu_3O_{7-\delta}$

Resulting from comparable lattice constants, the growth behaviour of $BaZrO_3$ thin films in conjunction with other perovskites (e.g. $YBa_2Cu_3O_{7-\delta}$, $SrTiO_3$, etc.) is similar to that of MgO ([Wu 92], see Table 4.1). TEM, XRD and GID[56] measurements show a cube-to-cube growth of $BaZrO_3$ on $SrTiO_3$ with a highly oriented *c*-axis. The in-plane lattice constant relaxes within 4 nm film thickness by 1:14 dislocations corresponding to the lattice mismatch of 7.17% [Cil 96].

The epitaxial relation of a YBCO/BZO/STO heterostructure has been investigated by Wu et. al. [Wu 92]. Here, additional 45° in-plane rotated $YBa_2Cu_3O_{7-\delta}$ grains have been observed. However, the direct influence on the superconducting properties of $YBa_2Cu_3O_{7-\delta}$ is only known from single crystal growth [Erb 96]. Therefore we show first time, that it is possible, to manufacture high quality $YBa_2Cu_3O_{7-\delta}$ thin films on $BaZrO_3$ buffer layers. As a starting point, $SrTiO_3$ has been used as substrate material in order to study the growth behaviour of $BaZrO_3$. Consecutively, the use of $BaZrO_3$ buffer layers has been extended to heterostructures on silicon substrates, which will be reported in chapter 4.5.3.

In Figure 4.11b, a X-ray diffraction pattern in Bragg-Brentano geometry shows the crystalline properties of a 300 nm thick $YBa_2Cu_3O_{7-\delta}$ deposited on a 200 nm thick $BaZrO_3$ buffer layer. Only (00*l*) reflections of both layers are

[56] Grazing incidence X-ray diffraction, in order to estimate in-plane lattice parameters.

observed without phase impurities or polycrystalline fractions. For single buffer layers from 7 nm to 200 nm thickness, best values of the FWHM of 0.04° approach resolution limit of the X-ray device. Within a bi-layer structure, as shown in Figure 4.11, the crystalline quality of the buffer layer is slightly deteriorated to 0.2° FWHM. In spite of a lattice mismatch of 7.17% and 9.2% for STO/BZO and BZO/YBCO, respectively, the two layer stack exhibits perfect cube-to-cube in plane relation, coinciding with [Cil 96] and [Wu 92], as shown in Figure 4.11a. Beside moderate deposition temperature ($T_{dep} = 750$°C) and laser fluence ($J \approx 2.5$ J/cm²), a change of the deposition pressure from $1x10^{-6}$ mbar to 0.3 mbar results in a shift in 2θ of the $BaZrO_3$ (00*l*)-reflections to smaller values [Mau 98]. This increase of the *c*-axis length originates from a better lattice accommodation in the *ab*-plane[57], which is probably due to oxygen deficiency in the film.

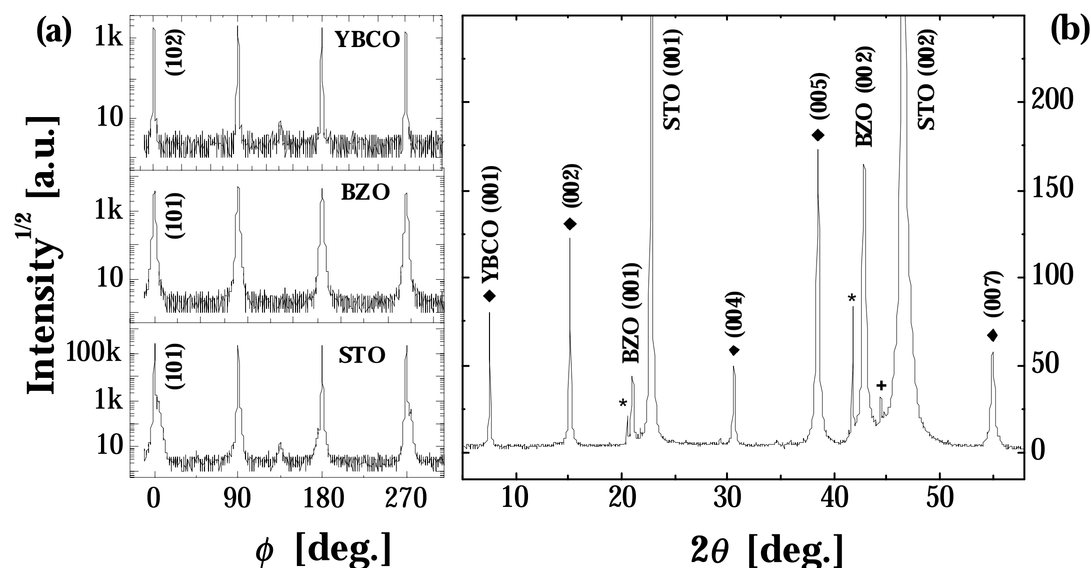

Figure 4.11: A $YBa_2Cu_3O_{7-\delta}$ layer deposited on a 200 nm thick $BaZrO_3$ buffer layer **(a)** A perfect cube-to-cube in-plane relation between substrate (STO), buffer (BZO), and HTSC (YBCO) is indicated by a XRD φ-scan. **(b)** A XRD pattern in Bragg-Brentano geometry shows a highly *c*-axis oriented 2 layer stack with a FWHM of rocking curves of 0.2° for $YBa_2Cu_3O_{7-\delta}$ and $BaZrO_3$, respectively. (+) and (*) indicate parasitic reflections of the X-ray tube.

[57] Lattice constants have been estimated by four circle XRD. Volume conservation of the unit cell and a smaller lattice constant of $SrTiO_3$ leads to increased *c*-axis length.

Investigated by means of REM and AFM measurements, the deposited $BaZrO_3$ films show extraordinary smooth surfaces with a roughness of 0.3 nm (rms) corresponding to one monolayer, leading to a very smooth $YBa_2Cu_3O_{7-\delta}$ surface of 2 nm (rms). Illustrated in Figure 4.12, resistive measurements show a superconducting transition at $T_c \approx 90$ K for both $YBa_2Cu_3O_{7-\delta}$ films deposited on BZO-buffered $SrTiO_3$ and bare $SrTiO_3$ substrates if identical deposition conditions are employed. Since interdiffusion between HTSC and buffer is not expected [Erb 96], an increased defect density due to a necessary lattice accommodation at the interface is assumed to lead to an increase of specific resistance from $\rho = 60\,\mu\Omega$cm (YBCO/STO) to $\rho = 90\,\mu\Omega$cm (bi-layer system). Moreover, at a temperature of $T = 77$ K, critical current densities of 1.3×10^6 A/cm^2 and 1.4×10^6 A/cm^2 are observed for YBCO/STO and the bi-layer system, respectively.

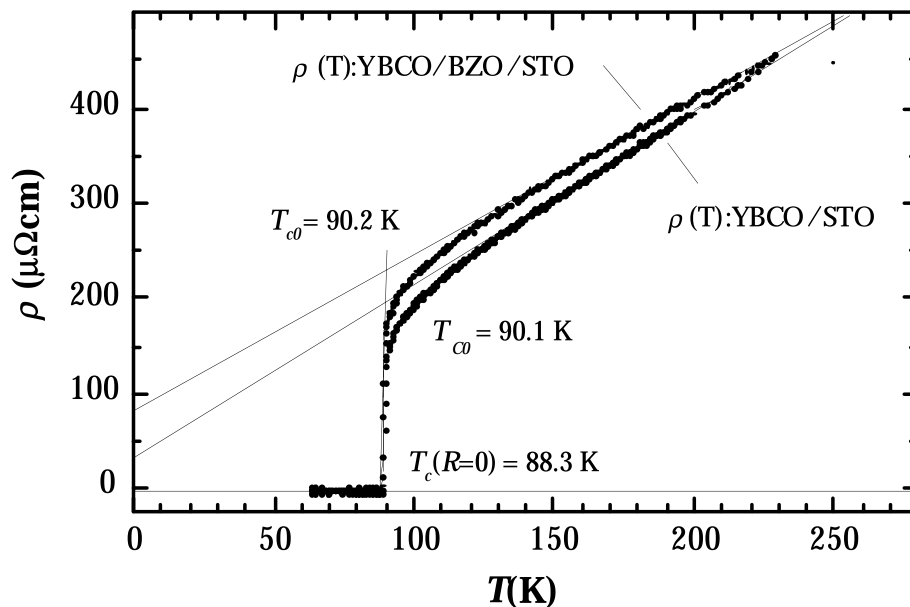

Figure 4.12: Comparison of resistivity measurements of 430 nm thick $YBa_2Cu_3O_{7-\delta}$ films deposited on bare $SrTiO_3$ and BZO-buffered $SrTiO_3$ substrates, respectively.

In conclusion, our investigations show, that crystallographic and electronic properties of $YBa_2Cu_3O_{7-\delta}$ films deposited on a buffer layer are comparable to those on $SrTiO_3$. However, a substantial improvement of the surface morphology was achieved for $YBa_2Cu_3O_{7-\delta}$ films deposited on BZO-buffered $SrTiO_3$ substrates, which exhibit a surface roughness of 2 nm (rms). This

opens various applications of $BaZrO_3$ in HTSC heterostructures, especially when smooth surfaces with a low surface resistance are required (e.g. HF devices).

4.5.3 $BaZrO_3$ as a Buffer Layer for HTSC on Silicon

The use of YSZ as a first buffer layer on silicon (Chapter 4.4) principally forms a growth base for oxide layer such as $YBa_2Cu_3O_{7-\delta}$. However, as a fundamental problem, the direct deposition of $YBa_2Cu_3O_{7-\delta}$ on YSZ leads to strongly deteriorated crystalline and superconducting properties. At high temperatures necessary for $YBa_2Cu_3O_{7-\delta}$ deposition, an interdiffusion layer of $BaZrO_3$ is formed at the initial stage of the $YBa_2Cu_3O_{7-\delta}$ growth due to reaction with YSZ. Thus, the first monolayers of the HTSC are degraded, resulting in a wrong stoichiometry (Ba-deficiency) [Cim 88, Tie 89]. TEM investigations of this interdiffusion layer show a formation of 4-8 nm thick (011) out-of-plane tilted $BaZrO_3$ domains [Wen 93]. Consequently, the properties of $YBa_2Cu_3O_{7-\delta}$ are additionally deteriorated by differently oriented grains, which exhibit an in-plane alignment of 0°, 45° and ±9° relative to the underlying YSZ layer[58] [For 90, For 95]. The origin of the ±9° in-plane rotation has been clarified by Schlom et al. [Sch 96] and Boikov et al. [Boi 94] and is assigned to an extremely small (0.1%) lattice mismatch between the $BaZrO_3$ [111] and YSZ [110] crystal directions. In order to circumvent this problem, CeO_2 has been investigated as an additional buffer layer. Unfortunately, at deposition temperatures above 800°C, the use of CeO_2 leads to the formation of a multitude of $BaCeO_3$ reaction islands with a large lattice mismatch to $YBa_2Cu_3O_{7-\delta}$, leading to pinholes [Boi 97, Sko 93, Cop 93].

The use of a $BaZrO_3$ buffer layer – the reaction product itself – in order to improve the superconducting properties of $YBa_2Cu_3O_{7-\delta}$ on silicon, is one of the important issues of this work. On the one hand, high quality growth of $YBa_2Cu_3O_{7-\delta}$ on $BaZrO_3$ is already verified in the previous chapter. On the other hand, the even higher mismatch between YSZ and $BaZrO_3$ (14.2%) is expected to be counterbalanced by the ability of extremely thin $BaZrO_3$ films

[58] Due to a competition between necessary surface mobility and lattice accommodation, the fraction of the respective orientation depends on the deposition temperature.

to accommodate its lattice constants in the range of 10% [Hwa 91]. Furthermore, the complete heterostructure should not be affected by the thermal expansion coefficient of $BaZrO_3$ [59], if only a few monolayer thick buffer is introduced.

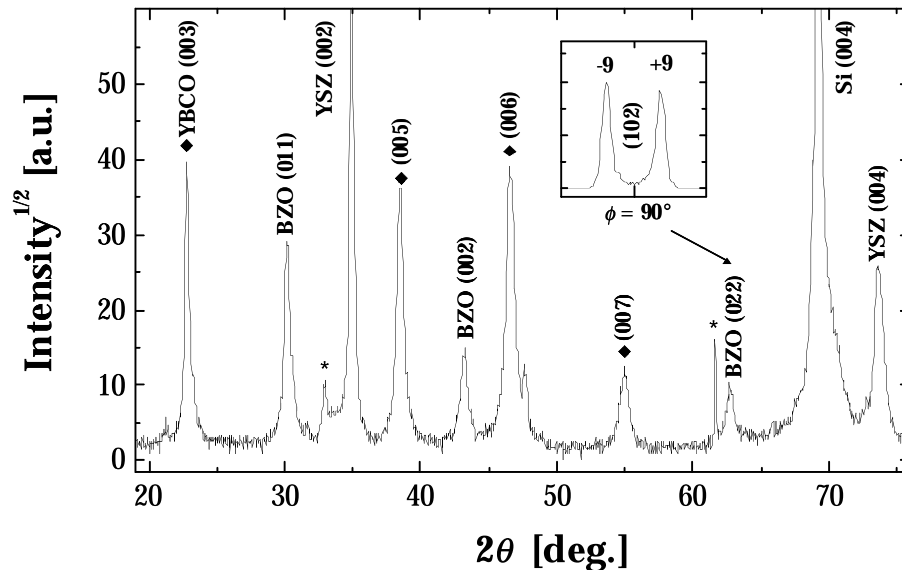

Figure 4.13: A XRD pattern in Bragg-Brentano geometry shows *c*-axis oriented $YBa_2Cu_3O_{7-\delta}$ and YSZ layers without phase impurities. Here, a thicker (50 nm) $BaZrO_3$ buffer layer reveals *c*-axis oriented (002) and 45° out-of-plane tilted ((011), (022)) grains. The resulting in-plane orientation of such a $BaZrO_3$ layer is shown in the insert. This growth orientation is transmitted to the $YBa_2Cu_3O_{7-\delta}$ layer and deteriorates its properties.

In Figure 4.13, a typical $\theta/2\theta$ X-ray diffraction pattern of a heterostructure YBCO(30 nm)/BZO(50 nm)/YSZ(70 nm) on silicon shows a *c*-axis oriented YSZ layer with a nearly optimal FWHM of 1°. In spite of that, the second layer within this heterostructure, $BaZrO_3$, reveals differently oriented grains with *c*-axis orientation and 45° out-of-plane orientation. This is indicated by the appearance of the (0*ll*)-reflections, with a FWHM worse than 1.8°. These results are in good agreement with observations of other groups [Sch 96, Boi 94, Sko 93]. A closer investigation of this tilted $BaZrO_3$ fraction has been performed by four circle XRD χ- and φ-scans (insert in Figure 4.14), showing a ±9° in–plane rotation of these grains analogue to the orientation of a YSZ/YBCO interdiffusion layer, as mentioned by Schlomm et al. [Sch 96]. A

[59] See Table 4.2 “Material Properties”.

$YBa_2Cu_3O_{7-\delta}$ layer, deposited on top of such a mixed orientation nevertheless reveals complete *c*-axis orientation with 2.5° FWHM of rocking curves. This fact and the transmission of the mixed in-plane orientation results in strongly deteriorated superconducting transition temperatures of approximately 85 K.

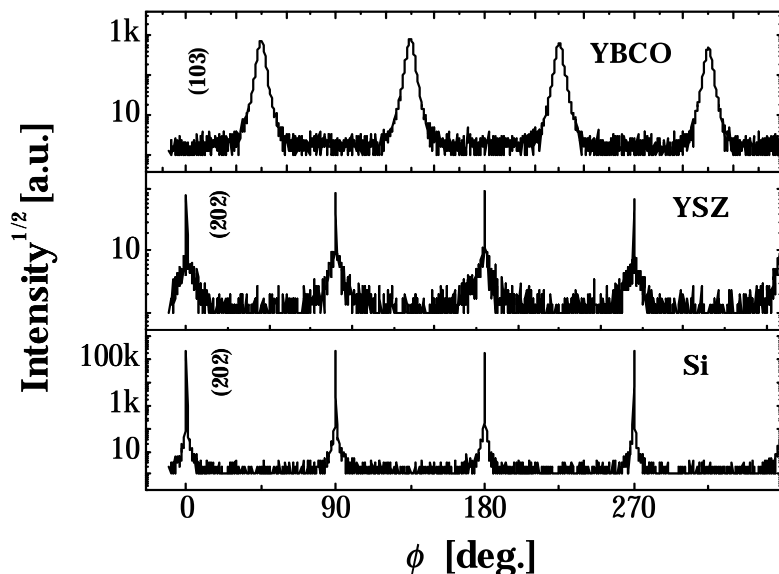

Figure 4.14: Four circle XRD measurement of $YBa_2Cu_3O_{7-\delta}$ deposited on silicon with a BZO(3 nm)/YSZ(40 nm) buffer layer combination. The YSZ layer grows cube-to-cube on silicon, whereas the $YBa_2Cu_3O_{7-\delta}$ layer is 45° in-plane rotated relative to substrate. The 3 nm thick $BaZrO_3$ buffer layer is not visible.

However, if only a few monolayers (3 nm) of $BaZrO_3$ are introduced at low deposition pressures (1x10^{-6} mbar), the lattice in-plane constants (0.4193 nm) are assumed to accommodate to the YSZ lattice constants (0.514 nm). Since such a thin layer is not detectable with standard X-ray diffraction[60], its growth behaviour and influence is interpreted by the resulting growth of the on top deposited $YBa_2Cu_3O_{7-\delta}$ layer. Shown in Figure 4.13a, the $YBa_2Cu_3O_{7-\delta}$ layer now shows a perfect 45° in-plane rotation and no ±9° or 0° in-plane oriented grains are observed on top of the BZO/YSZ buffer layer combination. $\theta/2\theta$-XRD patterns reveal an improved *c*-axis orientation of 1.3° FWHM, which at this point is mainly limited by the crystalline properties of YSZ on silicon (1.7° FWHM).

---

[60] Usually HRTEM measurements are performed in this case.

Generally, $YBa_2Cu_3O_{7-\delta}$ films on top of buffered silicon substrates exhibit smooth surfaces with a terrace-like island growth and a local roughness in the range of one monolayer height (1.15 nm, Figure 4.15b). The superconducting properties of the HTSC films have been characterised by performing inductive and resistive measurements. The transition into the superconducting state occurs at a temperature of 89.6 K, comparable to literature values for $YBa_2Cu_3O_{7-\delta}$ films on silicon [Sei 98] but nevertheless drastically worse than values that are achieved on lattice matched perovskite substrates such as $SrTiO_3$. The broadened transition width of $\Delta T \approx 4.8$ K and the increased specific resistance is assumed to be mainly caused by the crystalline quality of the YSZ layer. On the other hand, partial lowering of the transition temperature can be generated by oxygen deficiencies at the $BaZrO_3/YBa_2Cu_3O_{7-\delta}$ interface, since the $BaZrO_3$ buffer is deposited at an extremely low pressure of $1x10^{-6}$ mbar. Furthermore, stress within the heterostructure due to different thermal expansion coefficients can also lower the transition temperature.

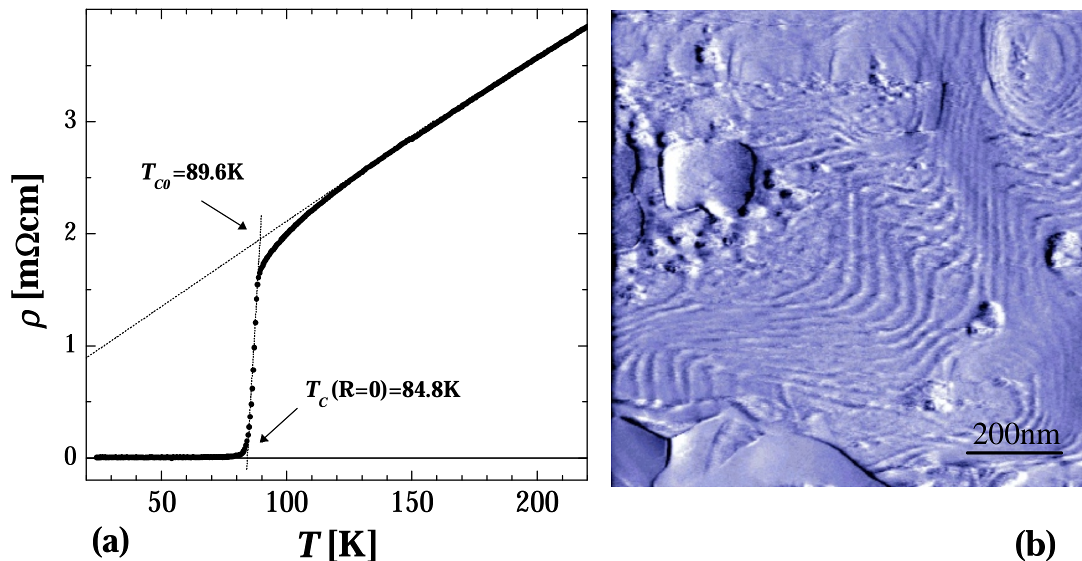

Figure 4.15: (a) A resistivity measurement of a $YBa_2Cu_3O_{7-\delta}$ film on double buffered silicon shows a superconducting transition temperature of 89.6 K (onset) with a broadened transition of $\Delta T \approx 4.8$ K. **(b)** The surface morphology of this film reveals terrace-like island growth with steps corresponding to one monolayer of $YBa_2Cu_3O_{7-\delta}$ (1.15 nm).

This newly investigated buffer layer combination for $YBa_2Cu_3O_{7-\delta}$ thin films on silicon substrates solves principal problems such as the formation of interdiffusion layers and mixed in-plane orientations. Moreover, for comparison, the typically employed YBCO/CeO_2/YSZ/Si heterostructure has been deposited under identical deposition conditions for the $YBa_2Cu_3O_{7-\delta}$ and YSZ layer, resulting in a decreased superconducting transition temperature of $T_c = 87.5$ K and a transition width of $\Delta T_c \approx 6$ K. Thus, a relative improvement of the superconducting properties has been achieved by the use of a $BaZrO_3$ buffer layer. Furthermore, the substitution of CeO_2 by $BaZrO_3$ is particularly avoiding the formation of pin-holes in the superconducting $YBa_2Cu_3O_{7-\delta}$ layer, which is important for applications, where magnetic shielding is an issue. In conclusion, since moderate crystalline properties of the YSZ layer are held to be responsible for the observed transition temperatures and broadened transition widths in both heterostructures, this buffer layer combination has the potential for further improvement of the superconducting properties of the $YBa_2Cu_3O_{7-\delta}$ layer.

5. Lattice Engineering for Artificial Josephson Junctions

During the past years, a number of techniques have been developed for the fabrication of high temperature superconductor Josephson junctions. Two successful and extensively investigated examples are grain boundary junctions on bi-crystalline substrates and ramp-type junctions. However, in spite of their better transport properties, they can only be implemented in a limited lateral geometry. Furthermore, the integration of Josephson junctions into superconducting or even semiconducting devices requires a deposition technique, that allows the application of such a component within a complex multilayer heterostructure. This encouraged us to investigate the growth behaviour of adequate material combinations in order to provide a basis for the fabrication of bi-epitaxial Josephson junctions. Prior to those aspects however, some remarks are made on the theoretical background and the known types of Josephson junctions.

5.1 Preliminary Remarks on the Josephson Effect

The Josephson effect is one of the macroscopic quantum phenomena of superconductivity, predicted by B.D. Josephson in 1962 [Jos 62] and firstly experimentally proofed by Anderson and Rowell [And 63]. Being a central concept of the Ginzburg-Landau theory, a complex order parameter Δ_j is introduced in order to describe the macroscopic wave function of the superconducting electrons [Tin 96]. Two superconductors, which are separated by a thin insulating barrier but are close enough to establish an overlap of the

superconducting wave functions will show Josephson coupling, or in other words, will form a weak link. A current, formed by tunnelling cooper pairs as well as quasi particles flows through the junction and comprises an amount of super-current that is independent of the voltage across the junction, but depends solely on the phase difference $\gamma=\chi_1-\chi_2$. Herein, χ_1 and χ_2 are the phases of the complex order parameters $\Delta_j = |\Delta_j|\, exp(i\chi_j)$ in electrode $j=1$ or 2. The current phase relation is 2π periodic and follows in the simplest (or "classical") case the 1st Josephson equation:

$$I_s = I_c \sin\gamma\,, \tag{5.1}$$

with I_c being the maximum or critical current, which is mainly determined by the properties of the barrier. The time evolution of the phase difference γ is connected to the voltage across the junction via the 2nd Josephson equation:

$$\frac{\partial\gamma}{\partial t} = \frac{2e}{\hbar}V \tag{5.2}$$

Both Josephson equations show a remarkable difference. The first Josephson equation is an approximative description, whereas the second one is solely derived from basic principles of quantum mechanics and comprises only fundamental constants. In general, the whole electrodynamic properties of Josephson junctions are divided into stationary (DC) and non stationary (AC) processes, depending on whether the phase difference is constant in time or not. In the first case, this results in a vanishing voltage across the junction, according to the 1st Josephson equation. The junction supports a constant super-current that is determined by the phase difference and confined by the critical current. In the second case, non-stationary effects appear if a time averaged voltage difference[61] V is maintained across the junction. According to the 2nd Josephson equation, the super-current now will oscillate with a frequency $\omega_V = 2eV/\hbar = V \times 483.6$ MHz/µV.

[61] To prevent breaking of the cooper pairs, this voltage has to be smaller than Δ/e.

I(V)-Characteristics of Josephson Junctions

A real Josephson junction depicts additionally to the channel of Cooper pairs one channel due to quasiparticles. This results in an additional resistive transport channel $I = V/R(V,T)$, which is connected parallel to the Josephson current $I = I_c \sin\gamma$. Furthermore, the intrinsic capacitance C between the electrodes determines decisively the dynamics of the junction. This approach is the basis of the "Resistively and Capacitively Shunted Junction" (*RSCJ*) model [McC 68, Ste 68][62]. Considering the entire net current of such a junction, the substitution of the second Josephson equation for the time dependent voltage yields a second order differential equation:

$$\frac{I}{I_C} = \sin\gamma + \frac{1}{\sqrt{\beta_c}}\frac{d\gamma}{d(\tau)} + \frac{d^2\gamma}{d^2(\tau)^2} \qquad (5.3)$$

with the plasma frequency $\omega_p = (2eI_c/\hbar C)^{1/2}$ within the dimensionless variable $\tau = \omega_p t$ and the McCumber (damping) parameter $\beta_c = (\omega_p R_n C)^2$ [63].

Generally, solutions of equation 5.5 are numerically attainable and every resulting $I(V)$-characteristic should be between two opposite limiting cases: (i) *overdamped* Josephson junctions with $\beta_c \leq 1$ and (ii) *underdamped* junctions with $\beta_c > 1$, as shown in Figure 5.1a and b, respectively. First, in the limit of vanishing capacitance, the McCumber parameter β_c will tend to zero and the differential equation 5.5 is solvable in a closed form. Illustrated in Figure 5.1a, a single valued curve is obtained with zero voltage across the junction for currents below I_c. For currents $I > I_c$, the time averaged voltage follows the relation $V = R_n (I^2 - I_c^2)^{1/2}$ with an ohmic behaviour $V = IR_n$ for currents much larger than the critical current. Secondly, in the case of underdamped Josephson junctions, two stable solutions of equation 5.5 provide a hysteretic behaviour in the $I(V)$-characteristic as can be seen in Figure 5.1b. This hysteresis will increase with increasing β_c, whereby β_c can be determined by the ratio of the critical current to the return current $I_c/I_r = 4/\pi\beta_c^{1/2}$ [Bar 82].

---

[62] In the case of HTSC SNS contacts, the quasiparticle channel is often represented by an Ohmic resistance, whereas in case of a tunneling characteristic it has to be substituted by a quasiparticle characteristic.

[63] An additional dissipative contribution $I_{int} = U(G_{int}\cos\gamma)$ due to interference of cooper pair and quasi particle currents is neglected.

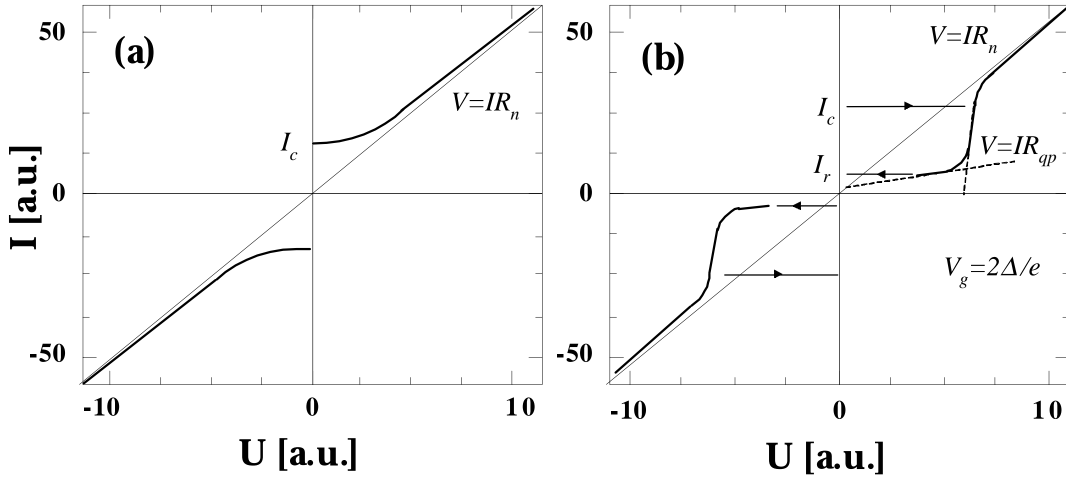

Figure 5.1: **(a)** $I(V)$-characteristic of an overdamped Josephson junction with $R_n = \text{const}$. **(b)** The hysteretic behaviour of an underdamped junction is visible. The asymptotes are formed by the ohmic characteristics of the quasiparticle- and normal conducting resistances. Increasing the current from zero, the voltage across the junction remains at $V = 0$ until a jump to a finite voltage occurs at I_c. Decreasing the current again below I_c, the zero voltage state will be reached for currents which have to be lower than the return current I_r . The asymptotes are formed by the ohmic characteristics of the normal conducting resistance R_n and the quasi particle resistance R_{qp} . V_g corresponds to the gap voltage.

In real Josephson junctions, the components of the RSCJ model are determined by the type of contact. Established Nb/AlO_x/Nb contacts exhibit high capacities and parallel resistances due to single electron tunnelling processes. In contrast, grain boundary contacts and many other HTCS contact types reveal localised states in the barrier as well as short circuits, leading to low capacities and resistances. Moreover, considering thermal activated processes, the characteristics have to be modified by adding a current in equation 5.5, which describes the Josephson noise. Following the theory of Ambegaokar and Halperin [Amb 69], in the case of overdamped contacts a finite resistance is observed also below I_c, resulting from thermal activated phase slip (TAPS).

Despite being out of the scope of this thesis, some important features of Josephson contacts are nevertheless worth mentioning: First, if the width of the junction is smaller than the Josephson penetration depth ($b < \lambda_j$), a magnetic flux that penetrates a Josephson Junction homogeneously induces a spatial dependence of the phase difference, leading to a lateral modulation of the current density. This critical current – magnetic flux relation is described by

the well known Fraunhofer pattern. Josephson junctions with dimensions larger than the Josephson penetration depth ($b > \lambda_j$), will have an inhomogeneous current distribution inside the junction even if a magnetic field is absent due to self field effects produced by the current. This will cause the formation of Josephson vortices inside the barrier, resulting in a voltage across the junction even for currents smaller than I_c and a reduction of the Fraunhofer modulation. These vortices differ from typical Type-II superconductor Abrikosov-vortices since they possess no normal conducting core and thus no upper critical field H_{c2}. Secondly, the critical current is determined by the barrier properties and reveals a temperature dependence on the energy gap Δ, which is described by the Ambegaokar-Baratoff relation [Amb 63] in the case of classical superconductor-insulator-superconductor (SIS) junctions with identical electrodes. Thirdly, under electromagnetic radiation with a frequency in the range of $\omega = 10^7$-10^{12} Hz, the supra-current of a Josephson contact shows equidistant steps at $V_n = n\hbar\omega/2e$, well known as Shapiro steps [Sha 63]. Moreover, non-linear characteristics with additional steps due to a quasiparticle tunnelling current [Tie 63] are the base of the operational mode of HF-detectors and –mixers [Hu 90].

5.2 Types of Josephson Junctions

Generally, Josephson junctions are classified into different types, depending on whether the barrier is metallic (SNS-contact) or insulating (SIS-contact). Typically, the effective thickness of the barrier is in the range of the cooper pair coherence length ξ. Additionally, in microbridge contacts with an extremely small cross section $b < \lambda_L$, a Josephson effect is observed due to coherent vortex motion in the bridge. An intrinsic Josephson effect along the *c*-axis is observed between CuO_2-planes of HTSC with high anisotropy (e.g. $Bi_2Sr_2CaCu_2O_{8+\delta}$) due to strong modulation of the order parameter along the *c*-axis. In HTSC, grain boundary contacts play a major role because of the *d*-wave character of the superconducting wave function. This contact type as well as Josephson junctions, formed by artificial barrier layers represent the most common contact types in the field of HTSC.

5.2.1 Josephson Contacts with Artificial Barriers

SNS Step-Edge Contacts

The application of a typical SIS sandwich structure, known from LTSC[64] devices, is hampered by the small coherence length of HTSC. For example, in the easy growth *c*-direction of $YBa_2Cu_3O_{7-\delta}$, ξ_c is below 0.4 nm. This fact requires a control of interface with monolayer accuracy, which in practice means a high probability of short circuits at the interface. Therefore, instead of using insulating barriers, metallic barrier layers can be employed. Following conventional proximity effect theory, the ratio between thickness and coherence length in the metal should be approximately 1 and thus favours noble metals as barrier material. Since epitaxial growth of HTSC on these metals is not possible, the junction is realised by a *step-edge contact*. Herein, a previously etched step in the substrate generates a complete break of the HTSC film growth, which is consecutively filled by the noble metal. Hitherto, this contact type exhibits high I_cR_n products up to 10 mV at 4.2 K [Ros 93], but a worse reproducibility.

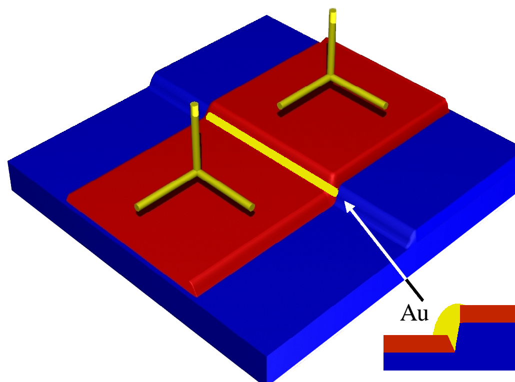

Figure 5.2: Schematic illustration of a step-edge Josephson contact.

Ramp-Junction Contacts

Ramp-junctions make use of the longer coherence length for transport along the *ab*-plane in a HTSC film, which is grown with the *c*-axis along the substrate normal. The deposition of the base electrode and an insulating layer is followed by lithographic patterning and ion milling to expose the edge[65]. After that, the barrier layer and the HTSC top electrode is deposited.

---

[64] **L**ow **T**emperature **S**uper**c**onductors.

[65] Alternatively, wet chemical etching or a shadow mask technique [Sto 95] can be employed in order to manufacture such a ramp. Several attempts in order to improve the ramp junction properties have been made, such as plasma oxidation of the ramp [Shi 88], and PLD patterning [Kor 91].

The main difficulties of this contact type are represented by the deposition of a smooth barrier layer and the fabrication of a well defined ramp. Furthermore, the etching process influences the surface of the base electrode, possibly resulting in a thin damaged layer, which already determines the contact properties. Unfortunately, the etching process restricts the arrangement of Josephson junctions on a chip, which is a drawback concerning the integration into HTSC devices. On the other hand, the possibility of using different barrier materials in conjunction with a variation of the contact area allows a limited adjustment of the contact parameters. Up to now, this contact type shows the lowest spread of contact properties (I_c, R_n) in the order of 10% and relatively high I_cR_n products up to 8 mV at 4.2 K [Sto 95].

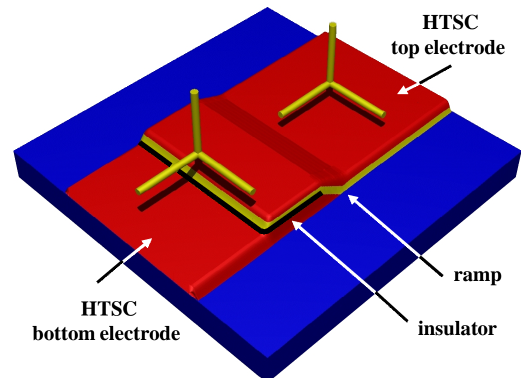

Figure 5.3: Schematic illustration of a ramp-junction Josephson contact.

5.2.2 Grain Boundary Contacts

Depending on the technique by which the grain boundary is generated, actually three types of junctions are currently in the focus of interest.

Bi-Crystal Grainboundary Junctions

In this junction type, the in-plane weak-link behaviour of an epitaxially grown HTSC film is induced via a grain boundary in the substrate. It is created by fusing two substrates together with a relative in-plane rotation larger than 20°. The deposited HTSC adopts the substrate orientation. In this way, a spatially controllable, single layer junction is prepared. Generally, the observed be-

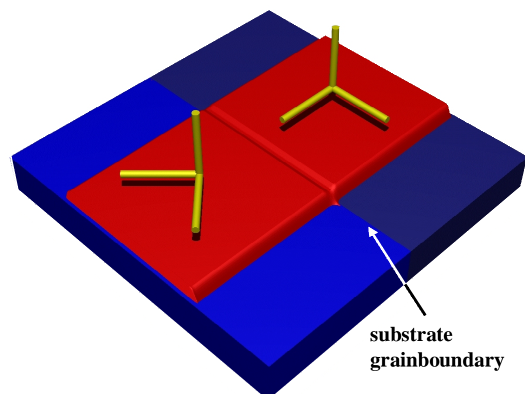

Figure 5.4: Schematic illustration of a bi-crystal Josephson contact.

haviour can be described within the RSJ model (see chapter 5.1). Bi-crystal contacts exhibit comparatively good properties, but the spread of the contact parameter I_c and R_n lies in the range of 25 % [Alf 93]. The main advantage of the method is that the misorientation angle can be chosen freely. Furthermore, this contact type shows a good long-term stability and a high magnetic field resolution. However, the fabrication of devices by this technique has a major disadvantage. It cannot be readily extended for the manufacture of integrated circuits, since the contact arrangement on a chip (substrate) is restricted to a single line. Additionally, bi-crystal substrates are expensive and not available in large quantities.

Step Edge Junctions

Similarly to the previously mentioned SNS step-edge contacts, another possibility to generate a grain boundary is to etch a step into the substrate. In contrast, the angle of inclination and the height of the step is chosen in a way, that the HTSC film coats the whole step. As indicated in Figure 5.5, the *c*-axis of the film in the area of the step is tilted 90°, whereas the *c*-axis of the film grown on the substrate is oriented parallel to the substrate normal. This generates two grain boundaries, whereby the one with the smaller critical current density dominates the contact properties. Due to its flexible design and good contact properties, step-edge contacts represent a technological important contact type, although the inadequate reproducibility is problematic.

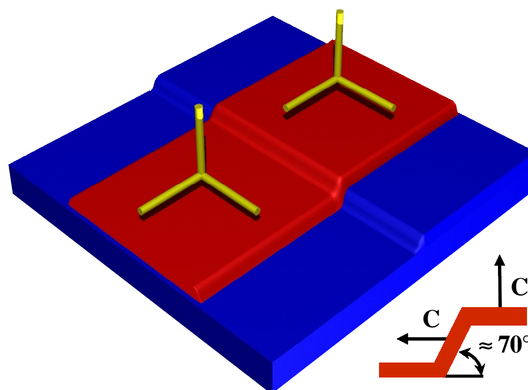

Figure 5.5: Schematic illustration of a step-edge Josephson contact.

Bi-Epitaxial Grainboundary Junctions

One way to overcome the limitations of the previously mentioned contacts is to engineer the bi-crystal substrate by controlling the in-plane epitaxy of deposited dielectric layers on the substrate prior to HTSC deposition. Again, the versatility and ease of multilayer deposition via PLD is advantageous in this field and was firstly demonstrated by Char et al. [Cha 91a]. In this tech-

nique, the grain boundary is freely determined by photolithography prior to the etching process. This allows a variable alignment of grain boundaries and gives the possibility to construct complicated JJ-arrays. Additionally, this type of contact is not restricted to special substrates and allows the integration into multilayer systems in order to combine with other superconducting devices or even the application in semiconductive technology. However, a main disadvantage is the restriction to a 45° misorientation angle, which allows only small critical current densities in the order of typically $10^4\,\mathrm{A/m^2}$ at 4.2 K. Up to now, two main effects impede the technical application of this contact type: First, the grain boundaries usually show a meander like structure with strong disorder and a large number of inhomogeneities. Second, this technology requires a large number of process steps.

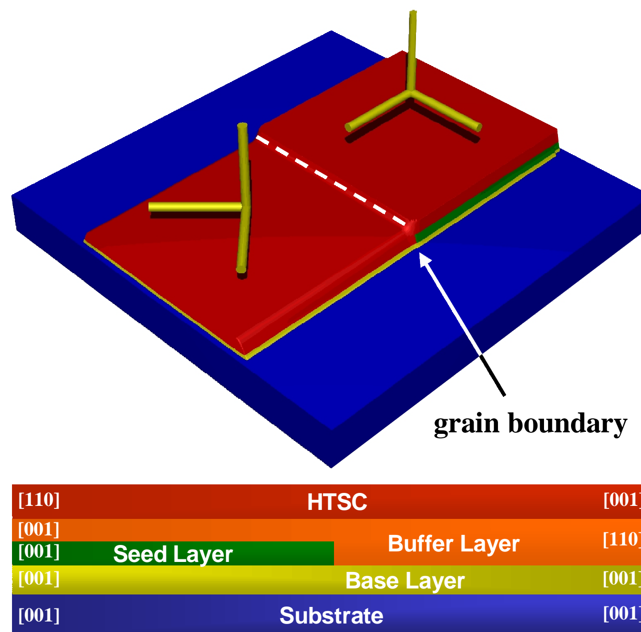

Figure 5.6: Schematic illustration of a bi-epitaxial Josephson contact.

A scheme of a bi-epitaxial junction is shown in Figure 5.6. The manufacturing method of these junctions contains several deposition steps of different layer materials, which serve special purposes. Depending on the chosen substrate, a first set of base layers is deposited in order to match the substrate lattice constant to the subsequent seed- and buffer layers and to avoid possible interdiffusion. For most of the layer sequences in this junction type, two facts

are crucial. First, the combination of the HTSC ($YBa_2Cu_3O_{7-\delta}$, $a = 0.382$ nm) with a rotating buffer layer (CeO_2, $a = 0.541$ nm) results in a clear 45° in-plane rotation between both materials due to a difference in the lattice constants of approximately a factor $\sqrt{2}$. Secondly, a seed layer material with an intermediate lattice constant (e.g. MgO, $a = 0.42$ nm) is deposited on the base layer in order to avoid the in-plane rotation of the consecutively deposited buffer with respect to the base layer. Thirdly, the seed layer is partially removed by a photolithographical process, determining the position of the grain boundaries. This provides a growth base for the buffer layers and eventually the HTSC top electrode, resulting in two areas in-plane rotated against each other.

Substrate	Base layers			Seed layers			Buffer layers		HTSC	Publ.
r-Al_2O_3 [1120]	–	–	–	MgO [100]	–	–	STO [100]/[110]	–	YBCO [100]/[110]	[Cha 91b]
Arb.	Arb.	Arb.	STO [100]	MgO [100]			CeO_2 [100]/[110]		YBCO [100]/[110]	[Cha 91c]
LAO [100]	–	–	–	STO [100]	BZO [100]	YSZ [100]	CeO_2 [100]/[110]	–	YBCO [100]/[110]	[Wu 92]
STO [100]	–	–	–	MgO [100]	CeO_2 [100]	–	CeO_2 [100]/[110]	–	YBCO [100]/[110]	[Nic 95] [a]
r-Al_2O_3 [1120]	CeO_2 [100]	YBCO [100]	STO [100]	MgO [100]	CeO_2 [100]	–	CeO_2 [100]/[110]	–	YBCO [100]/[110]	[Nic 96] [b]
r-Al_2O_3 [1120]	Si [100]	YSZ [100]	CeO_2 [100]	MgO [100]	–	–	YBCO [100]/[110]	CeO_2 [100]/[110]	YBCO [100]/[110]	[Boi 95] [c]
STO [100]	CeO_2 [010]			BZO [110]			STO	YBCO	YBCO [100]/[110]	[Boi 97] [d]
STO [100]	–	–	–	BZO [100]	–	–	YSZ [100]/[110]	CeO_2 [100]/[110]	YBCO [100]/[110]	this work

Table 5.1: Layer sequences for bi-epitaxial Josephson junctions. Depending on the chosen substrate, a first set of layers is deposited in order to match the lattice constant of the substrate to the seed layer. Consecutively, the seed layers are deposited and etched. Prior to HTSC deposition, one ore more buffer layers can be introduced in order to improve the growth of the HTSC.

Notes: (a) Here, a second CeO_2 buffer layer is deposited homoepitaxially onto the etched MgO/CeO_2 seed layer in order to improve the crystallinity of the HTSC; **(b)** A set of base layers is introduced in order to avoid interdiffusion of Aluminium between the Al_2O_3 substrate and $YBa_2Cu_3O_{7-\delta}$. **(c)** Being an important step in hybrid technology, a SOS (silicon on sapphire) substrate is used. Furthermore, an additional double-buffer CeO_2/YBCO improves the crystallinity and stoichiometry of the grain boundary and yields an I_c of 10^7 A/cm^2 and an I_cR_n product of 150 μV at 77 K; **(d)** An additional STO(10 nm)/YBCO(10 nm) was introduced prior to the main $YBa_2Cu_3O_{7-\delta}$ layer in order to reduce deviations from correct stoichiometry in the region of the grain boundary.

This approach, introduced by Char et. al. [Char 91a, Char 91b], was quickly extended in order to investigate a wider range of substrates and dielectric layers. A few of the employed materials and suggested layer sequences are summarised in Table 5.1. A first fundamental investigation of the growth of different materials and occurring relative crystallographic orientations (see Table 4.1) has been done by Wu et al. [Wu 92]. In this work, $BaZrO_3$ has been used first in order to substitute MgO. Due to approximately similar lattice constants, the growth behaviour of both materials is identical. The advantages of $BaZrO_3$ in contrast to MgO are a higher chemical inertness due to an extraordinary high melting point of 2600 °C. However, the main predication of this work is the idea of *continuous lattice match*. Herein, the single seed layer with an intermediate lattice constant is substituted by a set of layers with only slightly different lattice constants in order to avoid an out-of-plane growth of grains, generated by lattice mismatch

5.3 Growth and Control of In-plane Orientation

Within the manufacture of bi-epitaxial Josephson junctions, or in general, of complex multi-layer systems, the sequential deposition of different materials underlies several restrictions, already discussed in chapter 4.3. The chemical inertness between the materials at predominant deposition conditions and similar thermal expansion coefficients are important parameters that have to be considered. However, following the idea of *continuous lattice match*, the in-plane lattice constant is supposed to be the crucial parameter.

On the one hand, the HTSC layer $YBa_2Cu_3O_{7-\delta}$ ($a = 0.384$ nm) and the chosen substrate $SrTiO_3$ ($a = 0.39$ nm) exhibit similar lattice constants with a lattice mismatch of only 2.2 % (see also Table 4.1). On the other hand, CeO_2 plays the role as rotating layer, since the lattice constant of $a = 0.541$ nm fits to the [011]-direction of $SrTiO_3$ and $YBa_2Cu_3O_{7-\delta}$ with a mismatch of only 2.1 % and 0.16 %, respectively[66]. As already mentioned, a set of buffer layers with intermediate lattice constants ($BaZrO_3$, $a = 0.419$ nm and YSZ, $a = 0.514$ nm) is introduced to match the lattice constants continuously (for corresponding mismatches see

[66] In-plane relation: STO[100] || CeO_2[110] || YBCO[100], checked by four circle XRD measurements.

Table 4.1) in order to avoid the rotation on one side of the contact. Now, the question is, if the matching layers are introduced on top or below the CeO_2 layer, as illustrated in Figure 5.7.

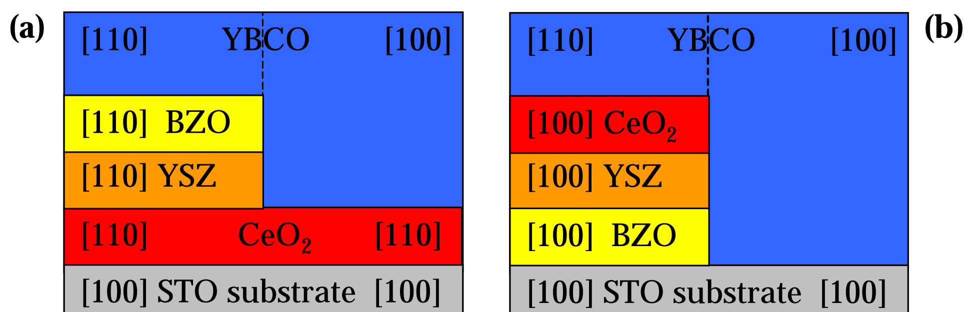

Figure 5.7: Schematic illustration of two possible layer sequences with a continuos lattice match by $BaZrO_3$ and YSZ and expected in-plane relations. **(a)** Lattice match from the CeO_2 layer to the $YBa_2Cu_3O_{7-\delta}$ layer in order to avoid the rotation on the left side. On the right side, the rotation of the CeO_2 layer on the substrate, and a second 45° rotation of the $YBa_2Cu_3O_{7-\delta}$ layer corresponds to an effective 0°/90° rotation. Thus, whether the CeO_2 layer covers the whole substrate or just the left side does not change the resulting in-plane relations between both sides of the heterostructure. **(b)** Lattice match from the substrate to the CeO_2 layer by the introduction of a YSZ and a $BaZrO_3$ layer, subsequent rotation of the $YBa_2Cu_3O_{7-\delta}$ layer (left), and cube-to-cube growth of $YBa_2Cu_3O_{7-\delta}$ on the right side.

Being a first approach according to Figure 5.7a, the growth of a STO/CeO_2/BZO/YBCO heterostructure has been investigated. As can be seen by a $\theta/2\theta$ -scan in Figure 5.8a, $BaZrO_3$ exhibits an out-of-plane growth corresponding to the (011)-direction perpendicular to the substrate normal. This result is in good agreement with Wu et al. [Wu 92] (see Table 4.1). Proven by four-circle X-ray measurements, the $BaZrO_3$ buffer is additionally 45° in-plane rotated on CeO_2. The $YBa_2Cu_3O_{7-\delta}$ layer adopts the in-plane orientation of the $BaZrO_3$ layer, but exhibits a *c*-axis oriented growth, resulting in an effective 45° in-plane rotation of $YBa_2Cu_3O_{7-\delta}$ with respect to the CeO_2 layer. This growth behaviour is also observed in a Si/YSZ/BZO/YBCO heterostructure (Figure 4.13). Hence, in contrast to the shown illustration and to the results of Boikov et al. [Boi 97, Boi 97a], the $BaZrO_3$ layer does not avoid the second rotation of the $YBa_2Cu_3O_{7-\delta}$ layer on the left side in Figure 5.7a. In other words, it does not match the CeO_2 lattice constant to the $YBa_2Cu_3O_{7-\delta}$ lattice constant. Furthermore, a $BaCeO_3$ (011)-peak arises at 28.9° as a result of chemical reaction between CeO_2 and $BaZrO_3$ at predominant deposition temperatures. As said in chapter 4.5.3, this reaction product is known as reason

for the formation of pin-holes due to a large lattice mismatch to $YBa_2Cu_3O_{7-\delta}$ [Boi 97, Sko 93, Cop 93].

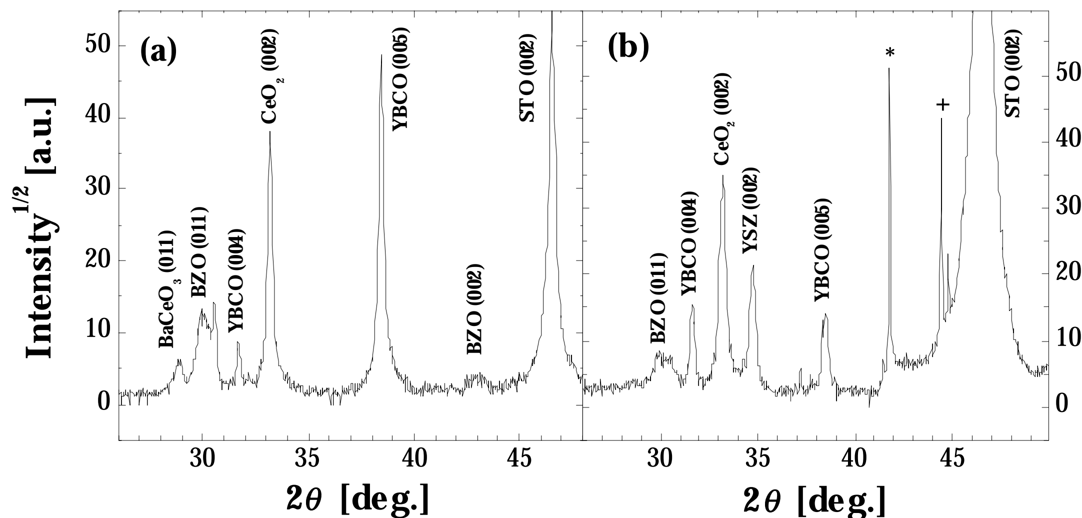

Figure 5.8: **(a)** $\theta/2\theta$ -XRD pattern of a CeO_2/BZO/YBCO heterostructure on $SrTiO_3$. Although the CeO_2- and the $YBa_2Cu_3O_{7-\delta}$ layer are *c*-axis oriented with a FWHM below 0.88°, the $BaZrO_3$ layer shows 45° out-of-plane growth with a (011)-reflection at 30.14°. **(b)** $\theta/2\theta$-scan of a CeO_2/BZO/YSZ/ YBCO heterostructure on $SrTiO_3$. Again, all layers are *c*-axis oriented, except the $BaZrO_3$ layer. Parasitic substrate peaks are indicated by (*/+).

The introduction of YSZ with an intermediate lattice constant between CeO_2 and $BaZrO_3$ into the previously discussed heterostructure now represents a layer sequence following the idea of continuous lattice match (Figure 5.7a). As expected, the YSZ layer grows cube-to-cube on top of CeO_2. Illustrated in Figure 5.8b however, the $BaZrO_3$ layer again shows a (011) growth direction, whereas the residual layers of the heterostructure are *c*-axis oriented. Hence, the $YBa_2Cu_3O_{7-\delta}$ layer shows similar in-plane relations both on the areas with and without YSZ/BZO buffer layers.

In conclusion, the inauspicious growth behaviour of $BaZrO_3$ on top of YSZ and CeO_2 avoids the lattice match from larger (CeO_2) to smaller ($YBa_2Cu_3O_{7-\delta}$) lattice constants. Coinciding with the results of Wu et al. (see Table 4.1) however, the relative in-plane orientation between two materials depends on the deposition sequence. Especially in the case of $BaZrO_3$ and YSZ, the observed orientations BZO(011) || YSZ(001) and BZO[100] || YSZ[100] are different from the inverse deposition sequence, which results in the orientations YSZ(001) || BZO(001) and YSZ[100] || BZO[100]. Considering this fact, a layer

sequence STO/BZO/YSZ/CeO_2 according to Figure 5.7b was deposited. Illustrated in Figure 5.9, a $\theta/2\theta$-scan with exclusively (*00l*)-peaks proves an epitaxial growth of the involved layer materials.

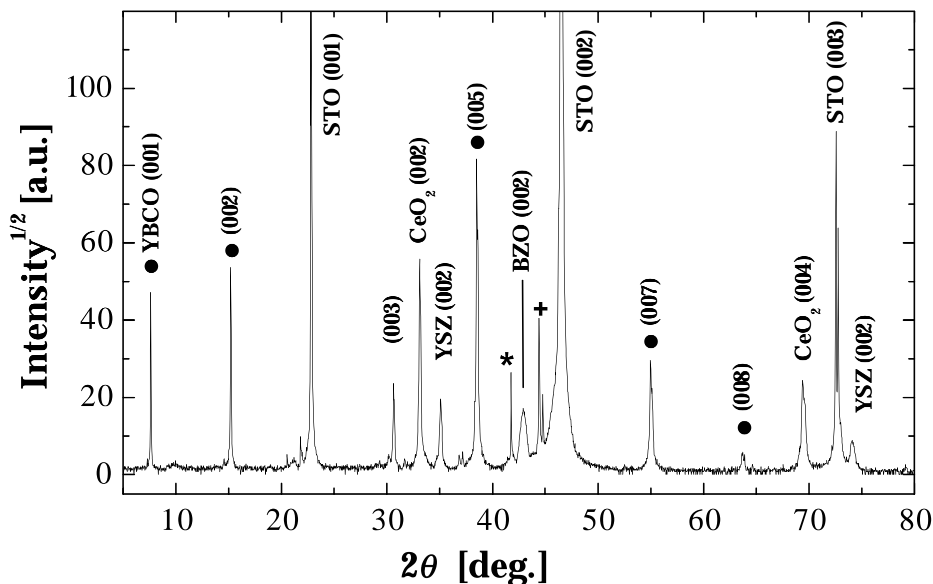

Figure 5.9: A $\theta/2\theta$-scan of a $YBa_2Cu_3O_{7-\delta}$ film (480nm), deposited on a $BaZrO_3$ (20 nm)/ YSZ (100 nm)/CeO_2 (200 nm) buffer layer on $SrTiO_3$. Peaks corresponding to the (*00l*)-direction are observed exclusively. The $YBa_2Cu_3O_{7-\delta}$ reflections are indicated by (•), whereas the (004)- and (006)-peaks are superimposed by the (002)-and (004)-$SrTiO_3$ reflection, respectively. Parasitic substrate peaks are indicated by (*/+).

The (00*l*)-reflections of the $YBa_2Cu_3O_{7-\delta}$ layer are highly oriented with a FWHM of 0.4°. This is surprising, since the underlying buffer layers exhibit a worse alignment with a FWHM of 0.72° (CeO_2), 1.4° (YSZ) and 0.26° ($BaZrO_3$). It is well known, that crystallinity increases with thickness up to a certain value, which is strongly influenced by different thermal expansion coefficients of the employed materials. Therefore, the optimal thickness with reference to crystallinity was chosen in this heterostructure. Although an overall thickness of 800 nm in this case could lead to high stress, no micro cracks have been observed, even after cooling down to liquid helium temperature. The in-plane relations of this layer sequence are shown Figure 5.10.

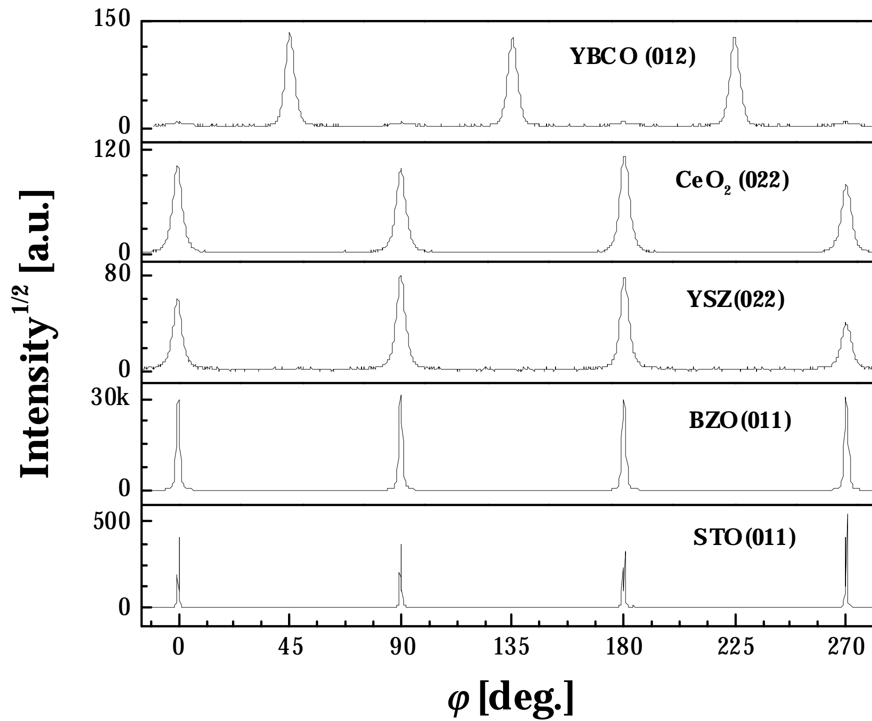

Figure 5.10: φ-scan of the layer sequence STO/BZO/YSZ/CeO_2/YBCO. The set of three buffer layers exhibits a perfect cube-to-cube growth on the $SrTiO_3$ substrate with a FWHM below 3°. The top layer $YBa_2Cu_3O_{7-\delta}$ shows the theoretically expected 45° in-plane rotation with respect to the CeO_2 layer.

In contrast to the previously discussed layer sequences, the orientation of the crystal axes in the substrate plane as well as parallel to the substrate normal of the complete heterostructure correspond to the theoretically expected directions as illustrated in Figure 5.7a. The epitaxial relations between the layers are confirmed by XRD φ-scans:

c-axis: STO (001) $\|$ BZO (001) $\|$ YSZ (001) $\|$ CeO_2 (001) $\|$ YBCO (001)

in-plane: STO [100] $\|$ BZO [100] $\|$ YSZ [100] $\|$ CeO_2 [100] $\|$ YBCO [110]

5.3.1 Superconducting Properties of the $YBa_2Cu_3O_{7-\delta}$ Layer

In order to determine the properties of the $YBa_2Cu_3O_{7-\delta}$ top layer, a complete set of layers including the HTSC layer is deposited in one process sequence. By this, without possible influences of introduced structuring steps, the quality of the HTSC layer on top of three buffer layers verified. Illustrated

in Figure 5.11, high quality superconducting $YBa_2Cu_3O_{7-\delta}$ films are achieved on the set of three buffer layers with a transition onset of $T_c = 91.7$ K and a very small transition width below 0.15 K. These properties of the superconducting film are comparable to best results on $SrTiO_3$. The $R(T)$-measurements have been performed by four-point method taking $U(I)$-curves at different temperatures across 5 µm bridges (30 µm length), which had been structured by standard photolithography and wet chemical (HNO_3) etching.

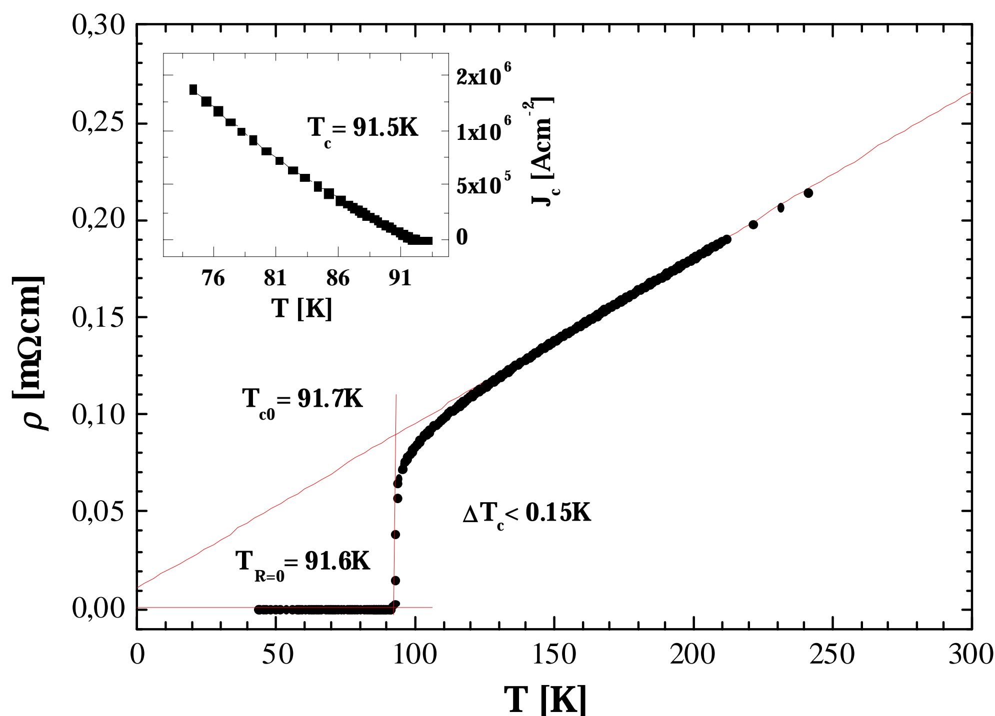

Figure 5.11: $\rho(T)$-curve of a 480 nm thick $YBa_2Cu_3O_{7-\delta}$ layer, deposited in-situ on a BZO (20 nm)/ YSZ (100 nm)/CeO_2 (200 nm) buffer layer set on $SrTiO_3$. A superconducting transition is observed at $T_c = 91.72$ K with a transition width of $\Delta T_c < 0.15$ K. The critical current density j_c versus temperature T is shown in the insert. A critical current density of $j_c = 1.5\text{x}10^{-6}$ A/cm² at 77 K is observed and curve fitting yields a transition temperature of $T_c = 91.5$ K. The measurement was performed using a bridge with 5 µm width and 30 µm length.

In the normal conducting state, a resistivity of $\rho_n(T = 300\text{ K}) \approx 0.27$ mΩcm is observed. Moreover, a linear behaviour of R_n at temperatures above $T = 130$ K leads to an extrapolated resistivity of $\rho(T = 0\text{ K}) \approx 10.6$ µΩcm. Below a temperature of $T \approx 130$ K, an increase of conductivity occurs, resulting from the constitution of superconducting fluctuations [Tin 76]. Plotted in the insert of Figure 5.11, a critical current density of j_c (77 K) = 1.5x10^{-6} A/cm² is observed,

which is a value comparable to what is typically observed in literature for $YBa_2Cu_3O_{7-\delta}$ on a set of buffer layers [e.g. Li 94, Nic 96]. The temperature dependence scales with $I_c(T) \propto (1-T/T_c)^{\alpha}$. Curve fitting yields an exponent $\alpha = 1.4$ and a transition temperature of $T_c \approx 91.5$ K. Moreover, MIB-measurements[67] show an extraordinary homogeneity of the $YBa_2Cu_3O_{7-\delta}$ layer, since the whole sample is transferred into the superconducting state within a temperature range of $\Delta T_c \approx 0.45$ K.

5.3.2 Structuring Steps for Bi-epitaxial Junctions

Although this chapter is mainly focussed on the epitaxial relations of a new layer sequence for bi-epitaxial grain boundary junctions, some preliminary investigations have been performed concerning the realisation of such a grain boundary. In this work, only single junctions are structured, being a first approach to the extension to arbitrary structures, which is assumed to be easily realised if the variety of processing steps are under control. The first assumption, that this structuring (i.e. the partial removal of one ore more layers) just means the insertion of additional process steps into the deposition sequence of a rather complex heterostructure, turns out to be to simple. The experimental difficulties and effects of etching processes on the growth of a compound such as $YBa_2Cu_3O_{7-\delta}$ motivate a closer look on the different steps. Thus, in Figure 5.12, four possible process sequences are illustrated in order to emphasise the technical challenge and the complexity of processing that is involved in the preparation of this junction type. In particular, the following steps are executed:

Buffer layer deposition steps: **(1)** Substrate cleaning, mounting onto the heater by an adequate glue, and subsequent heat treatment in vacuum. Being an important and often underestimated requirement, a substrate surface with residual organic contamination or a rough surface can impede the growth of epitaxial high quality thin films at this initial stage. **(2)** Deposition of a seed layer combination, as discussed in chapter 4.1 and 5.3. **(3)** Check of layer crystallinity and thickness by XRD and LXRD, respectively.

[67] Mutual Inductance Bridge: the superconducting screening current of the sample changes the induced voltage of a copper coil (a reference coil and lock-in technique is used).

Structuring steps: **(4)** Photolithography: Coating and pre-baking of the photoresist, subsequent exposure through a mask by the use of a mask-aligner and development of the photoresist. A post-baking process is employed in order to harden the photoresist for the etching step[68]. **(5)** Ion beam etching at $U = 400$ V and $I = 40$ mA with typical etching rates of 1.2 nm/min. A wet chemical etching technique is not applicable, since YSZ withstands to most acids (even HF). **(6)** Removal of partially polymerised photoresist by an oxygen plasma (30 min, 150-200 W, 1 mbar). In addition, a subsequent IBE cleaning step can be introduced in order to obtain completely clean surfaces. **(7)** Check of the resulting structure (step height and surface roughness) by means of optical microscopy and AFM and therefore a cross check of the previously assumed etching rate.

HTSC deposition steps: **(8)** Treatment prior HTSC deposition by repetition of step (1). Additionally, by annealing the sample at elevated temperatures (740°C) and pressures (10 mbar O_2), a re-crystallisation process can be performed [Ver 97]. **(9)** Deposition of the second buffer layer and the HTSC, with deposition parameters discussed in chapter 4.1 and 5.3. **(10)** Non-destructive check of layer crystallinity and superconducting properties by means of XRD and susceptibility measurements, respectively. **(11)** Structuring of the HTSC film by repetition of steps (4) to (6) in order to prepare a four point measurement. Cooling with LN_2 during the IB-etching process avoids oxygen loss in the HTSC. Due to a different roughness of the $YBa_2Cu_3O_{7-\delta}$ layer on the etched substrate and the buffer layer side, a resulting different etching rate hinders the application of a wet chemical etching technique. **(12)** Measurement of the transport properties at variable temperatures.

Illustrated in Figure 5.12, different possible process sequences within the previously investigated layer sequence have been carried out in this work. The advantages and disadvantages of the particular sequences are shortly discussed in order to determine the optimal process technology: The sequence illustrated in Figure 5.12a corresponds to the complete deposition of a buffer layer ("trilayer") set in order to realise continuous lattice match. However, a

[68] Coating: Photoresist MAP 275; Optimised parameters: spinning speed 6000 s^{-1}, spinning time 30 s; Pre-baking: 25 min at 100 °C; Exposure: 60 s; Development: MAP 331 ca. 30 s; Post-baking: 30 min at 110 °C.

good crystallinity is achieved only for an over-all thickness of approximately 70-100 nm. First of all, this means a high step and therefore a mixture of step edge and bi-epitaxial contact properties. Moreover, an exact estimation of real thickness by LXRD will only work up to approximately 100 nm. Even if oscillations are observed, the signal superimposition of three layers complicates the analysis of the particular layer thickness. Therefore, only an indirect way of thickness estimation is possible by performing LXRD measurements of single layers and calculation of the particular ablations rates. The resulting thickness of the trilayer then can be calculated assuming constant ablation rates of the PLD process and similar deposition rates on different materials, an assumption however, which is not necessarily correct. Furthermore, an extended ion beam etching process due to an overall thickness of approximately 100 nm will result in a high surface damage of the substrate and a high degree of polymerisation of the photoresist.

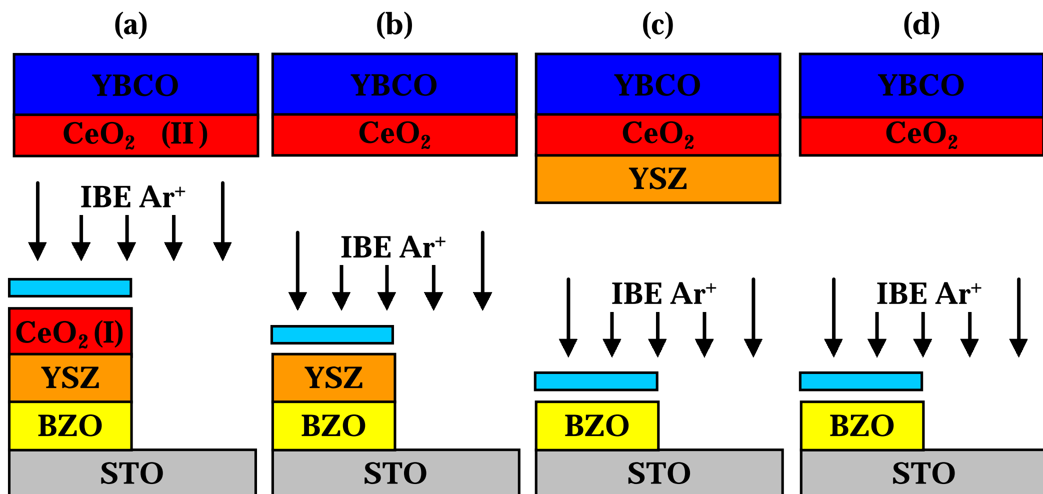

Figure 5.12: Possible deposition and structuring sequences for the manufacture of a bi-epitaxial junction applying the layer sequence STO/BZO/(YSZ)/CeO_2/YBCO. The light blue layer indicates the photoresist.

The crystalline quality of the HTSC can be improved by the introduction of an additional CeO_2 layer, which does not change the epitaxial relations of the structure, since a double rotation in the layer sequence STO[100] || CeO_2[110] || YBCO[100] on the right side in Figure 5.12a results in a 0°/90° rotation, whereas the CeO_2 layer grows homoepitaxially on the left side.

Shown in Figure 5.12b, a seed layer combination BZO/YSZ ("bi-layer") and a subsequent deposition of a CeO_2/YBCO layer combination contains the complete sequence except the fact, that again at the right side of the schematic a double rotation occurs. Moreover, the deposition of only two seed layers with an overall thickness of approximately 40 nm allows an exact thickness analysis by means of LXRD, as shown in Figure 5.13. Further arguments for this process sequence are the reduced step height and a minimised etching time in order to reduce surface damage by ion beam etching.

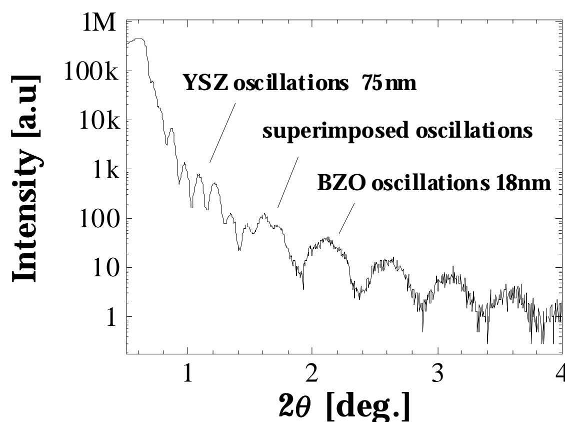

Figure 5.13: Low-angle X-Ray diffraction pattern of a BZO(18 nm)/YSZ(75 nm) bi-layer on $SrTiO_3$. Intensity oscillations for YSZ and $BaZrO_3$ as well as superimposed oscillations are visible. The thickness is calculated using the Bragg relation.

Motivated by the intention to reduce the step height even further, a single $BaZrO_3$ layer has been employed as seed layer. The theoretically expected epitaxial relations (see Table 4.1) again should lead to a double rotation STO[100]] || YSZ[110] || CeO_2[110] || YBCO[100] on the right side in Figure 5.12c. However, it turns out, that the particular deposition conditions of YSZ on $SrTiO_3$ and $BaZrO_3$, are strongly different. Either epitaxial growth of YSZ is observed on $SrTiO_3$ or $BaZrO_3$ but never simultaneously on both sides. Finally, the layer sequence in Figure 5.12d corresponds to an approach without a lattice matching YSZ layer. Herein, increased lattice mismatch results in present fractions of 45° rotated CeO_2 grains on $BaZrO_3$ (see Table 4.1). This growth behaviour has been checked by four circle X-ray measurements and is in good agreement with investigations performed by Wu et. al. [Wu 92]. In conclusion, only the process and layer sequences of Figure 5.12a and b seem to meet the requirements of an epitaxial grain boundary junction. However, due to the disadvantages previously mentioned for version (a), the bi-layer concept of version (b) is the most promising one.

Surface Damage by an incident Ion Beam

Due to the absence of a direct etch stop indication and a lack of certainty with respect to the absolute layer thickness and material dependent ion beam etching rates[69], the process has to be executed slightly longer as calculated in order to ensure a complete removal of the seed layers. Although the process time is optimised, an interaction of ion beam and substrate surface will always occur. Even tough no obvious strong damage of the surface was observed by optical microscopy and AFM, a consecutively deposited $YBa_2Cu_3O_{7-\delta}$ layer can be used to reveal surface defects since film growth and nucleation is strongly influenced by the substrate morphology. Illustrated in Figure 5.14, investigations by optical microscopy (dark field mode) exhibit an increased particulate density at the substrate side, especially along polishing scratches and the grain boundary. Intentionally, the $YBa_2Cu_3O_{7-\delta}$ layer shown in Figure 5.14, was deposited at a relatively high oxygen pressure (0.7 mbar), known to be a condition under which the formation of CuO_2 outgrowths is favoured. The size[70] of the particulates ranges from 0.3 to 0.6 μm on both sides, being slightly smaller at the substrate

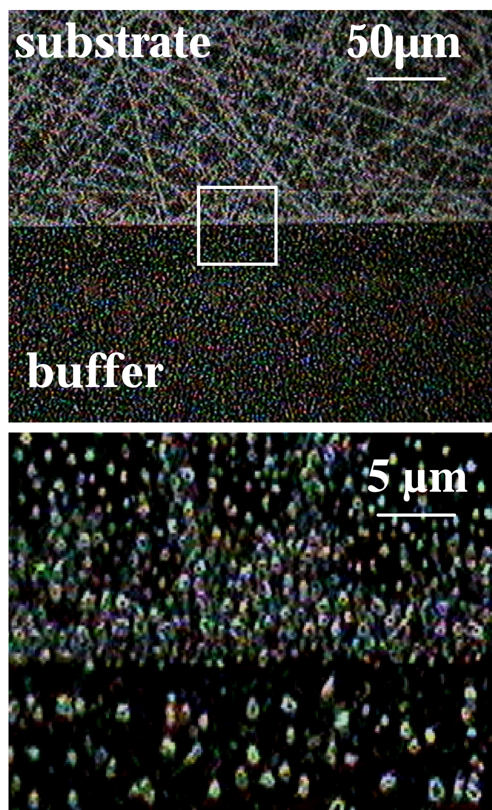

Figure 5.14: Surface of a $YBa_2Cu_3O_{7-\delta}$ film deposited on a structured seedlayer. Investigation by optical microscopy (dark field mode) exhibits an increased particulate density at the bare substrate side, especially along scratches and grain boundary.

[69] The etching rate strongly depends on material properties and a variety of IBE processing parameters. Ideally, an etch stop is defined by mass spectrometry indicating when Barium, the last element corresponding definitely to the lowest layer, is completely removed. AFM (step height, roughness), XPS (elements), optical microscopy (progression of the boundary), and XRD (crystallinity) measurements are performed in order to calculate etching rates and to prove the result of the etching process.

[70] The observed particulates are no droplets, which are known to exhibit a round shape and typical size of roughly 1 μm.

side. The defect density however, differs strongly with a value of $n \approx 0.3/\mu m^2$ on the buffer layer side and $n \approx 1.1/\mu m^2$ on the substrate side, respectively.

With respect to the superconducting properties, samples with such morphologies have been investigated by means of MIB-measurements, as shown in Figure 5.15. The curve indicates two superconducting areas: One, assumed to be the area on the buffer layer side, typically exhibits a sharp transition at temperatures in the range of 85 K, followed by a break in the curve at strongly reduced temperatures, which indicates the onset of a broadened transition of a second area, assumed to be the substrate side. In transport measurements, however a superconducting transition was never observed on the substrate side, resulting from the absence of a percolation path on the seed layer area.

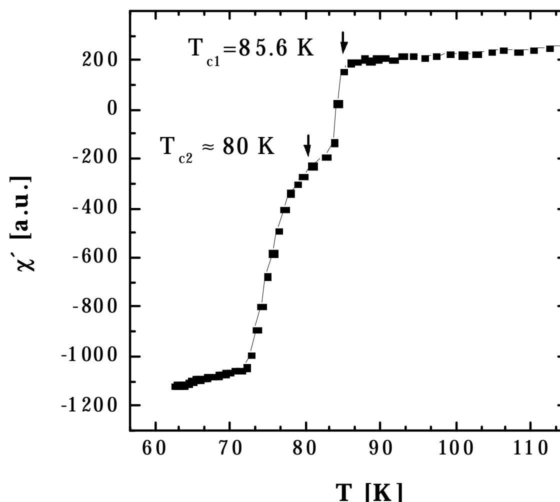

Figure 5.15: Susceptibility (MIB) measurement of a $YBa_2Cu_3O_{7-\delta}$ film deposited on an etched heterostructure with a strongly damaged surface.

It is known from various investigations, especially in the field of semiconductor process technology, that damage by incident ions is enhanced at already present defects of the surface, such as polishing scratches in the substrate, as illustrated in Figure 5.14. On the other hand, an ion beam with a lowered intensity can smooth a damaged surface. In Figure 5.16, scanning electron microscopy results of a $YBa_2Cu_3O_{7-\delta}$ thin film are shown. Prior to the HTSC deposition, different areas of a $SrTiO_3$ substrate with a typical surface roughness of 1 nm (rms) were exposed to an intense Ar^+ ion beam (400 V, 40 mA) for a certain time. Consecutively, selected areas were exposed to an Ar^+ ion beam with low intensity (200 V, 20 mA). Although after this treatment no apparent damage or increased defect density of the substrate surface was observed by optical microscopy[71], the consecutively deposited $YBa_2Cu_3O_{7-\delta}$

[71] SEM measurement are not possible at insulating surfaces.

layer reveals the effect of such a strategy. Even the areas, which have not been exposed to an intense ion beam show an improvement of the $YBa_2Cu_3O_{7-\delta}$ surface morphology with increasing time of "ion beam polishing". Furthermore, the area, which is exposed to intense radiation for 20 min, exhibits an extraordinary high roughness, which is strongly reduced after 20 min of smoothing by the low intensity ion beam.

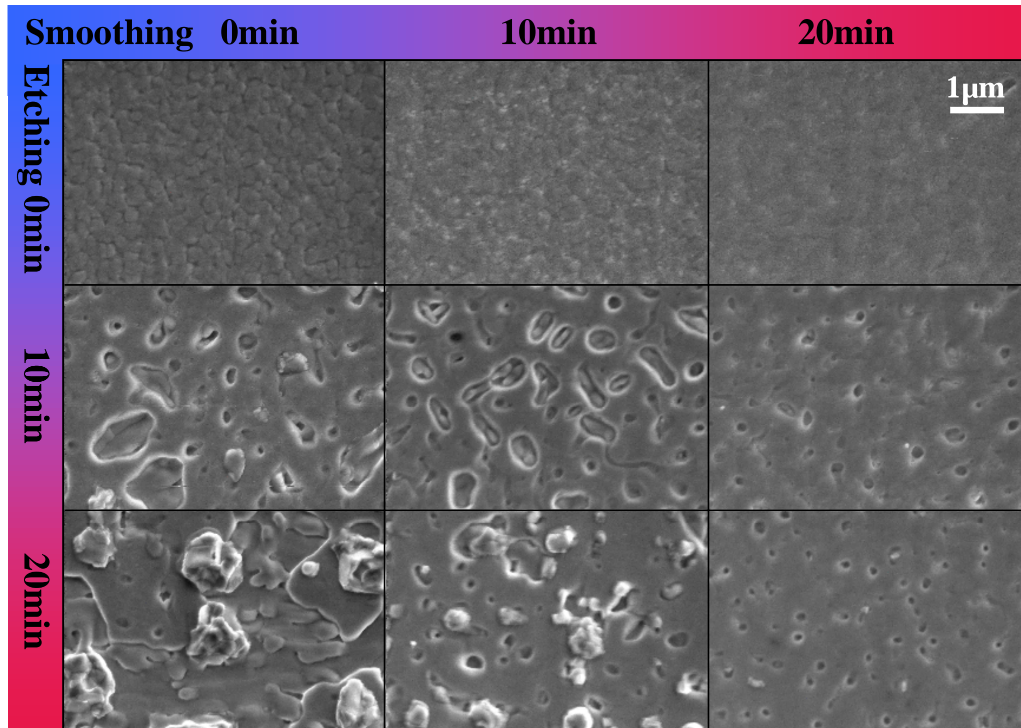

Figure 5.16: Scanning electron microscopy (SEM) measurement of a $YBa_2Cu_3O_{7-\delta}$ film deposited on a $SrTiO_3$ substrate, whose surface was damaged by IBE (Ar^+, 400 V, 40 mA, time scale on vertical axis) and subsequently smoothed by an ion beam with lower intensity (Ar^+, 200 V, 20 mA, time scale on horizontal axis).

Theoretically, this effect can be understood within the frame of microscopic dynamics of surface roughness induced by IBE [Fas 99]. Incident Ar^+ ions will induce a surface instability leading to a self-organisation process on the surface. A competition between sputtering (roughening) and diffusion (smoothening) of the surface will occur, depending on ion fluence and energy, as well as substrate temperature. The sputter rate depends on the ratio of removed surface atoms to incident ions, which, in turn, depends on the surface curvature. Under certain conditions, the etching rate in holes or deepenings such as polishing scratches is larger than on elevations. Furthermore, other

effects such as formation of periodic structures or nano-dots due to interaction of an incident ion beam with a surface have been observed.

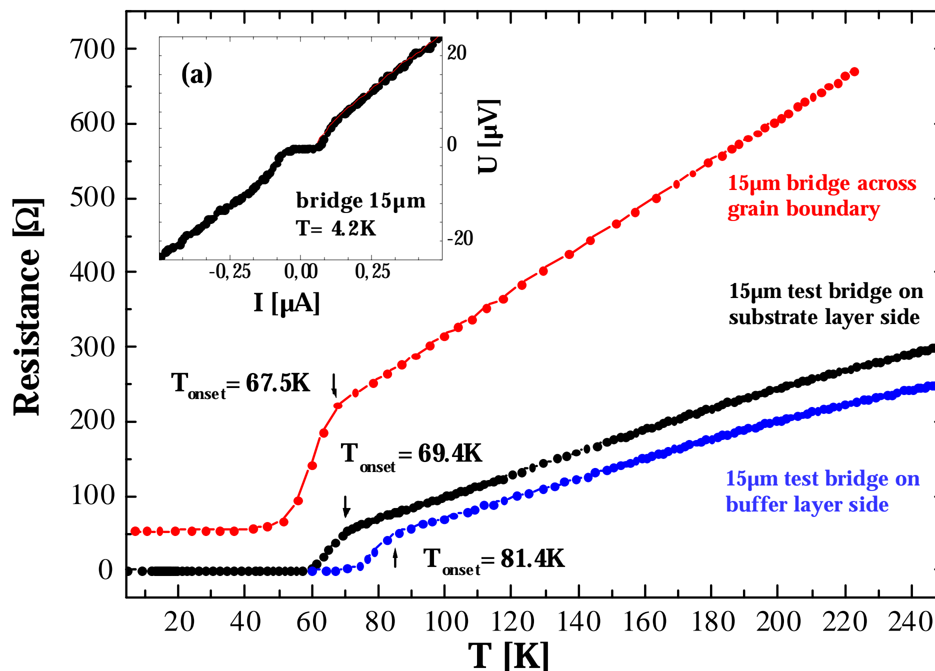

Figure 5.17: $R(T)$-curves of a 480 nm thick $YBa_2Cu_3O_{7-\delta}$ layer, deposited on a structured $BaZrO_3$ (10 nm)/YSZ (65 nm) bi-layer using an additional CeO_2 (200 nm) buffer layer prior to the HTSC deposition, according to Figure 5.12b. A superconducting transition is observed at $T_c = 81.4$ K (buffer layer) and $T_c = 69.4$ K (substrate), respectively. Across the grain boundary, the transition temperature is lowered to $T_c = 67.5$ K. **(a)** $U(I)$-characteristic of the grain boundary junction. Weak RSJ-behaviour is observed with an I_cR_n-product of 3.4 μV and a low critical current density of 1.0 A/cm².

Using this technique, superconducting $YBa_2Cu_3O_{7-\delta}$ layers could be achieved on both sides of the heterostructure. Figure 5.17 shows $R(T)$-measurements performed both on substrate and buffer layer side as well as across the grain boundary. As expected, the superconducting properties on top of the buffer layer, which was not exposed to the ion beam are significantly better than those on substrate side and grain boundary, respectively. Superconducting transitions are observed at $T_c = 81.4$ K on the buffer layer and $T_c = 69.4$ K on the substrate side, respectively. Across the grain boundary, the transition temperature is lowered to $T_c = 67.5$ K, obviously dominated by the properties of the substrate side. The transition width for both buffer and substrate side amounts a rather high value of $\Delta T_c \approx 10$ K, whereas the grain boundary shows an additionally increased transition width of $\Delta T_c \approx 15$ K.

For the $YBa_2Cu_3O_{7-\delta}$ layer on the buffer layer and substrate side, a similar normal conducting resistivity of $\rho_{n,buffer} = 2.7$ mΩcm and $\rho_{n,substr.} = 3.0$ mΩcm is observed at $T = 300$ K, respectively. In contrast, the grain boundary bridge exhibits a strongly increased value of $\rho_{n,GB} = 7.2$ mΩcm, which is assumed to be originating from oxygen loss in the grain boundary. At $T = 4.2$ K, the observed residual resistivity $\rho_{GB} = 390$ μΩcm of the grain boundary corresponds to the asymptotic resistivity of the normal conducting state. It is resulting from an extremely low critical current, which is exceeded by the measurement current. In Figure 5.17a, the insert shows an $U(I)$-characteristic of the grain boundary at a temperature of $T = 4.2$ K. Due to a low noise measurement set-up, it is possible to observe a voltage drop below 10 μV. The $U(I)$-characteristic indicates *RSJ*-behaviour (see chapter 5.1) and data fitting yields an asymptotic resistance of $R_n = 48\ \Omega$ ($\rho_{GB} = 387$ μΩcm) and a critical current of $I_c = 78$ nA. Thus, an I_cR_n-product of 3.4 μV and a critical current density of $J_c = 1.1\ A/cm^2$ is obtained at $T = 4.2$ K. In comparison, bi-epitaxial Josephson junctions typically show a critical current density in the range of $J_c\,(T = 4.2\ K) \approx 10^4\ A/cm^2$ to $J_c\ (T = 77\ K) < 10\ A/cm^2$. I_cR_n–products are ranging from 10^2-10^3 μV at $T = 4.2$ K down to 10 μV at $T = 77$ K [Yan 95, Nic 96, Boi 97].

Several facts may contribute to the degradation of the superconducting properties of the junction and the film. First, the lowered transition temperature of $T_c = 81.4$ K on the buffer layer side compared to the measurements presented in chapter 5.3.1 ($T_c = 91.5$ K), indicates a decrease of the superconducting properties of the whole sample. This fact is assumed to be originating from local heating of the sample by IBE and thereby induced oxygen loss, which particularly occurs at the grain boundary. This is believed, since the crystalline properties have been measured by means of XRD measurements prior IBE etching, in which a FHWM of 0.37° for the YBCO(005)-reflection was observed. Moreover, the lowered T_c on the substrate side indicates a not perfectly smoothened surface by the IBE technique previously mentioned. In Figure 5.18a, AFM measurements of the grain boundary morphology show, that the HTSC layer is not closed across the grain boundary and the spread of growth island leads to a meandering structure of the grain boundary. A continuous trench with a depth of approximately 250 nm and width of 900 nm is observed in contrast to bi-crystal grain boundary contacts,

which typically show a depth of 25 nm and a width of 200 nm. Moreover, AFM-measurements in the phase-contrast mode indicate soft material inside this trench, possibly resulting from polymerised photoresist. The roughness of the $YBa_2Cu_3O_{7-\delta}$ film amounts 13 nm (rms).

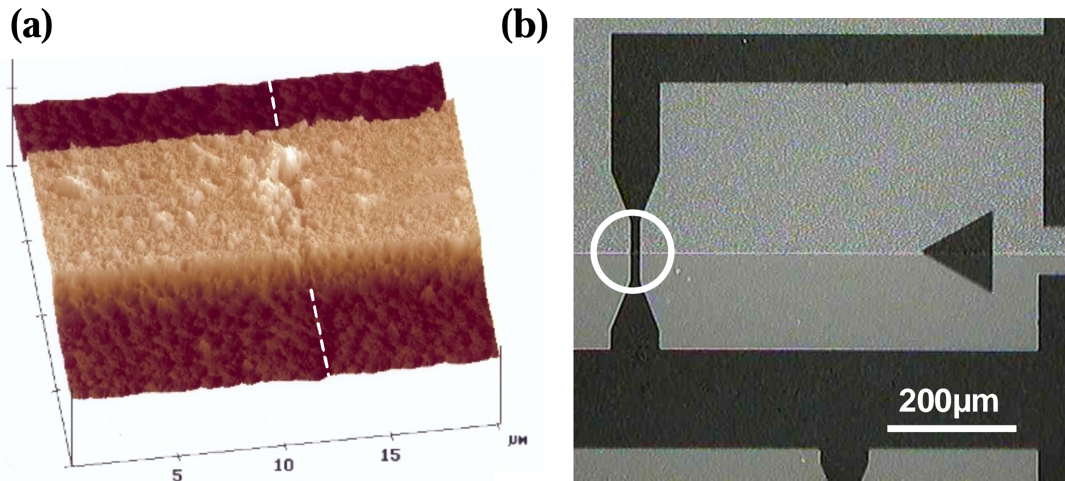

Figure 5.18: (a) AFM image of a grain boundary junction measured with a Digital Instruments Nanoscope®. **(b)** Optical microscopy image of the structure, the triangle aims along the grain boundary.

In conclusion, a new layer sequence for bi-epitaxial grain boundary Josephson junction has been found and its epitaxial relations have been intensively studied. To the authors knowledge, with respect to crystallinity and superconductivity, the properties of an in-situ deposited layer sequence belong to best results obtained hitherto in this field and are even comparable to properties observed on lattice matched substrates without buffer layers. Preliminary investigations have been performed in order to realise a bi-epitaxial grain boundary junction by the use of this layer sequence. However, the properties observed on the prepared junctions are not sufficient for technological applications. By detailed analysis of film surface morphologies at different stages of the inserted structuring steps, it is clearly shown that the degradation of superconducting properties is a result of the variety of process steps. Several approaches in order to improve this process have been investigated. Especially the aspects of an incident ion beam on surfaces are discussed in detail. Thus, a basis for further investigations in the field of bi-epitaxial grain boundary Josephson junctions is given.

6. Buffer Layers for Ferroelectric $SrBi_2Ta_2O_9$ on Silicon

Among the various physical phenomena observed on perovskite-like compounds, intensively studied examples are superconductivity (e.g. $YBa_2Cu_3O_{7-\delta}$), ferromagnetism (e.g. $La_xCa_{1-x}MnO_3$), and ferroelectricity[72] (e.g. $PbZr_{1-x}Ti_xO_3$). The latter is one of the most promising phenomena for near-future industrial applications. Within a certain temperature range, these materials exhibit a spontaneous polarisation, arising from spontaneous mutual alignment of dipoles. Therefore, the possibility to inverse the remanent polarisation by an electric field is a crucial feature of ferroelectrics in to order store information. On the other hand, piezo-, pyroelectric-, and electro-optical effects can be explored. A further step is to use this variety of properties in highly integrated devices.

This chapter will start with an overview of some important devices, and a motivation for the choice of the investigated materials will be given. Some basics on ferroelectricity, a microscopic model, and a classification of ferroelectric materials will be discussed. Consecutively, the emphasis is on the growth of $SrBi_2Ta_2O_9$ and the necessity of buffer layers to allow epitaxial growth on silicon substrates. Moreover, measurements of the electrical properties of this material within diode structures and ferroelectric domains, investigated by AFM, will be discussed. Eventually, the possibility to use $SrZrO_3$ as a new buffer layer material for ferroelectric $SrBi_2Ta_2O_9$ will be reported.

---

[72] First discovered in 1920 by Valasek in Rochelle salt [Val 20].

Application of Ferroelectric Materials

There is nowadays a growing interest on the development of non-volatile memory cells. As illustrated in Figure 6.1, within an array of 1T/1C- memory cells in a FRAM, the ferroelectric is used in the capacitor in order to store information in form of remanent polarisation, whereas the transistor serves as access control[73] [Dor 94]. Beside the non-volatility, the high dielectric constant of ferroelectric materials (e.g. $Ba_{1-x}Sr_xTiO_3$, $\varepsilon = 320$ at 50 nm [Sch 99a]) is a crucial factor in order to maximise the packing density by minimising structures (capacitor area) at unchanging capacities of at least 30 fF. Additionally, FRAMs exhibit a high switching speed, allow a larger number of read/write accesses and show radiation resistance.

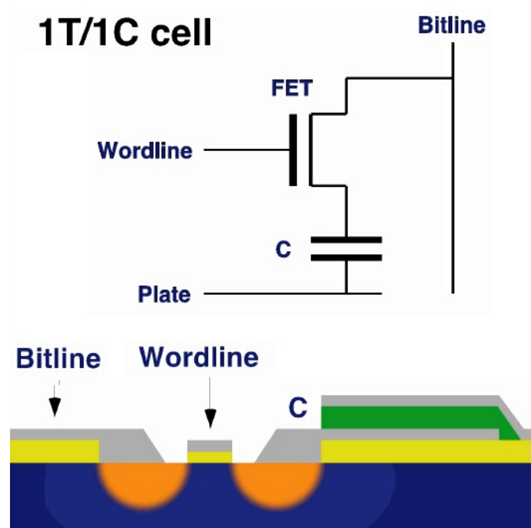

Figure 6.1: Circuit and cross section of **F**erroelectric-**R**andom-**A**ccess-**M**emory (FRAM).

In contrast, in a MFS-FET the ferroelectric is used as the gate insulator material due to its remanent polarisation, as illustrated in Figure 6.2. At high voltages the polarisation is fixed, leading to band bending in the semiconductor, which causes a modulation of the channel conductivity depending on the polarisation direction. This allows a non-destructive readout but requires a high modulation of the channel conductivity, a fact that is particularly problematic because additional buffer layers between silicon and the ferroelectric are necessary. Furthermore, as all ferroelectric

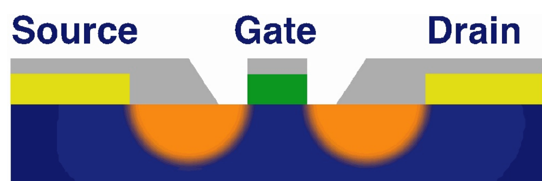

Figure 6.2: Cross section of a **M**etal-**F**erroelectric-**S**emiconductor-**F**ield-**E**ffect-**T**ransistor (MFS-FET), as a special variant of a **M**etal-**I**nsulator-**S**emiconductor- (MIS-) FET.

[73] In contrast to a **D**ynamic **R**andom **A**ccess **M**emory (DRAM), wherein the information is stored as electrical charge with a destructive read/write process (e.g. rewriting information).

materials show pyroelectric, piezoelectric and electro-optical activity, a wide field of applications are investigated nowadays, such as IR- and UV-sensors [Bjö 95, Jin 98], actuators [Wat 95], force detectors [Ito 96], optical devices (opt. memory, displays, waveguide) [Gop 96, Gil 97, Arm 96, Tay 96], and tuneable microwave devices in conjunction with HTSCs [Tay 98].

Application of Ferroelectric $SrBi_2Ta_2O_9$ in Memory Technology

One of the most promising compounds for memory technology is $SrBi_2Ta_2O_9$ (SBT). This material shows very small polarisation fatigue, low imprint tendency, and low leakage current [Sco 88, Koi 96]. A crucial condition in the choice of the material in ferroelectric devices is its fatigue behaviour. This means the decrease of polarisation with increasing number of switching cycles. The structure and composition of $SrBi_2Ta_2O_9$ seems to be responsible for the exceedingly good fatigue behaviour. No measurable decrease of polarisation could be observed in $SrBi_2Ta_2O_9$ within up to 10^{12} alternations of the polarisation [Dat 95]. In contrast, $Pb(Zr_xTi_{1-x})$ exhibits strong losses after 10^6 switching cycles [Du 98]. Being a possible reason for fatigue, electrons are accumulated in trapping sites at domain boundaries, leading to a stabilisation of the corresponding domains. This effect is amplified by defects in the proximity of the perovskite blocks, in which the polarisation is generated. However, since bismuth is the most volatile component in $SrBi_2Ta_2O_9$, these defects occur mostly in the (Bi_2O_2)-layers (see Figure 6.4), in contradiction to $Pb(Zr_xTi_{1-x})O_3$ films, where the loss of the volatile component Pb leads to defect formation directly inside the perovskite blocks.

6.1 Fundamentals of Ferroelectricity

Electric Polarisation of Crystals

A crystal in an electric field $\vec{E}$ exhibits a polarisation $\vec{P}=\chi\varepsilon_0\vec{E}=(\varepsilon-1)\varepsilon_0\vec{E}$. Herein, the dielectric susceptibility χ is a measure for the macroscopic response of a material to an applied electrical field[74]. In an atom, the

[74] Generally, χ is a tensor. For isotropic materials (e.g. a cubic crystal), a scalar is sufficient.

polarisability α describes the induced dipole moment $\vec{p} = \alpha \vec{E}_{loc}$ by a local electric field[75]. Therefore, the polarisation $\vec{P}$ can be calculated as an average dipole moment per volume. Three different mechanisms contribute to the polarisability of a dielectric material:

(i) *Orientation polarisation*: Permanent, but disordered dipoles in molecules or in subgroups of the unit cell are aligned by an outer electrical field. For high thermal energies the degree of alignment is given approximately by the ratio of orienting electrostatic energy ($\vec{p}\vec{E}$) and disorienting thermal energy ($3k_BT$), which leads to a polarisation of $\vec{P} \approx N\vec{p} \cdot (\vec{p}\vec{E}/3k_BT)$ with the density of dipoles N. Since dipoles generally are not free in rotation, they can only take an equilibrium position along the lattice directions and have to overcome potential barriers due to lattice forces between different orientation states. The system needs a relaxation time τ to attain thermal equilibrium, which increases, when the energy for reorientation exceeds the thermal energy.

(ii) *Ionic displacement polarisation*: Applying an electrical field leads to displacement of ions or whole lattice segments against each other. The temperature dependence is weak compared to that of the orientation polarisation.

(iii) *Electronic displacement polarisation*: Deformation and displacement of the electron shell gives an additional contribution to α.

Since polarisation in alternating electric fields is always associated with a relaxation process, the frequency behaviour of the complex dielectric constant depends on the characteristic time constants of the previously mentioned mechanisms. The "fast" processes (ionic, electronic) determine the optical material properties and contribute as constant terms ε_∞ and P_∞ in the dielectric constant and in the polarisation, respectively[76]. However, the orientation

---

[75] The local field E_{loc} results from the external macroscopic field E, the depolarisation field of the sample surface, the dipole field of the remaining atoms and the Lorentz-field. For a cubic system applies the Lorentz relation: $E_{local} = E + P/3\varepsilon_\infty$ [Kit 46].

[76] With time constants of 10^{-17}-10^{-16} s (electronic) and 10^{-14}-10^{-13} s (ionic), they do not play a role within the accessible instrument range. Theoretically, the frequency dependency of these mechanisms can be calculated within the Lorentz-Model, where the particles with a dipole moment are treated as damped harmonic oscillators.

polarisation plays a role in quasi-static time scales and is known as *dielectric relaxation* with $P(0) = P_{(t\rightarrow\infty)} - P_\infty$ and dielectric constant ε (0).

In the Debye-model, the dielectric relaxation describes a dipole as a particle moving in a double-well potential where orientation processes are related to thermal activated hopping between the local minima. If an electric *AC*-field is applied to this system, the Debye-relations describe the frequency dependence of the complex dielectric constant by $\varepsilon(\omega) = \varepsilon_\infty + \varepsilon(0)/(1+i\omega\tau)$ [Bur 85] as illustrated in Figure 6.3. In this simple model, the temperature dependence of the characteristic relaxation times τ can be described by the Arrhenius law $\tau^{-1} = \nu_0 \, exp\,(-E_B / k_B T)$, if similar characteristic frequencies ν_0 and energy barriers E_B for all dipoles are assumed. The relaxation will lead to a positive phase shift δ between electrical field and polarisation, where the losses are defined by the dielectric loss angle $\tan(\delta) = \mathrm{Im}(\varepsilon) / \mathrm{Re}(\varepsilon)$, the ratio of dissipative and oscillating energies.

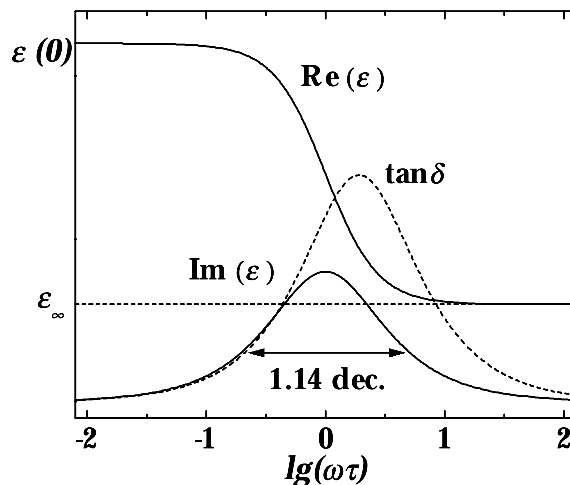

Figure 6.3: Frequency dependence of the dielectric constant ε and the dielectric loss $\tan(\delta)$ according to the Debye-model plus the constant contribution of ionic and electronic polarisation. Generally, the relation of Re(ε) and Im(ε) is connected via the Kramers-Kronig relations.

The assumption of constant relaxation times leads to deviations from real systems, i.e. broadened or asymmetric dispersion curves[77]. The implementation of a normalised probability distribution for relaxation times improves the model, whereas in turn a Dirac delta distribution leads back to the Debye-model. The three most popular concepts in order to describe dispersion curves empirically, are combined in the Havriliak-Negami relation $\varepsilon(\omega) = \varepsilon_\infty + \varepsilon(0)/(1+(i\omega\tau)^\alpha)^\beta$. Different combinations of the width parameter α and the asymmetry parameter β lead to (i) Cole-Cole ($0 \le \alpha \le 1$, $\beta = 1$) [Col 41], (ii) Cole-Davidson ($\alpha = 1$, $0 \le \beta \le 1$) [Dav 51], and (iii) Havriliak-Negami-

[77] Some experimental results, in particular for gases and fluids, coincide with the Debye-model.

behaviour ($0 \leq \alpha \leq 1$, $0 \leq \beta \leq 1$) [Hav 66], whereas $\alpha = \beta = 1$ represents the Debye-model.

Classification of Real Systems and Microscopic Models

For the most materials, the polarisation decreases with temperature and vanishes above the Curie-temperature T_c due to thermal motion. Depending on the transition from the para- into the ferroelectric phase, ferroelectric crystals are classified into two groups: (i) order-disorder transitions and (ii) displacement transitions. The first class includes materials, which contain hydrogen bridge bonds (e.g. KH_2PO_4). Herein, the ferroelectric properties are related to the redistribution of single ions i.e. motion of H-protons in the hydrogen bridges. In a quantum-mechanical approach this process can be explained by a thermal activated movement of hydrogen atoms in double-well potential in conjunction with mutual coupling of the dipoles [Str 97]. These materials show a low Curie-temperature and low spontaneous polarisation compared to the second class, mainly represented by perovskites. Generally, within the same approach, a displacement transition can be explained, if the mutual coupling is strong and atoms are moving effectively in a parabolic potential [Str 97]. Obviously, a perovskite-like structure favours this type of transition. Within the ABO_3 structure (see Figure 4.4), the B^{4+}-cations are coordinated in an oxygen octahedron that is surrounded by a cube of A^{2+}-cations. At the transition into the ferroelectric phase, a dipole moment emerges due to the displacement[78] of the sub-lattice of the B-cations relative to the O^{2-}-octahedral.

Being an important fact for the development of ferroelectricity in perovskites, the O^{2-} -ions are not placed on a lattice site with cubic structure. Therefore – in contrast to a cubic system - the Lorentz-relation does not apply [Kop86]. Under certain conditions [Sla 50], this is followed by a polarisation catastrophe: The local electric field, induced by ion polarisation increases faster than the linear part of the lattice restoring force, leading to an asymmetric displacement of the ions. The ion displacement is limited to finite values

[78] The displacement for SBT is 0.02 nm [Sch 99].

by higher-order terms of the restoring force[79]. Using the Lyddane-Sachs-Teller relation $\omega_L^2/\omega_T^2 = \varepsilon(0)/\varepsilon_\infty$, which gives the correlation between lattice vibration frequencies and real part of the static dielectric constant, the Curie-Weiss law follows: $\varepsilon_{stat} \propto 1/(T - T_C)$.

The Landau theory of phase transitions describes the transition from the paraelectric phase (low symmetry) into the ferroelectric phase (high symmetry) using a power series expansion of the free energy in powers of the order parameter [Str 97, Lin 96, Xu 74]. Within this theory, a discontinuous change in the polarisation P and a discontinuity of the static dielectric constant ε at T_c corresponds to a 1st order phase transition, shown by most of the ferroelectric materials. Depending on the temperature, systems with 1st and 2nd order transitions [Wei 95] and a tricritical point[80] in KH_2PO_4 [Str 97] have been observed.

6.2 Growth of $SrBi_2Ta_2O_9$ Thin Films on Silicon

The implementation of oxidic functional thin films into semiconductor technologies requires the deposition on silicon as a substrate material [Des 98, Fuj 98]. A large number of buffer layer materials such as Y_2O_3 [Lee 99], $SrTiO_3$, MgO [Kan 99], Si_3N_4 [Lee 99a] and Al_2O_3 [Jin 98, For 92] have been investigated in order to grow $SrBi_2Ta_2O_9$ on silicon substrates. However, the spontaneous formation of an amorphous SiO_2 inter-diffusion layer in oxidic environment can hardly be controlled by the use of these buffers. As discussed in chapter 4.3, YSZ as a first buffer layer solves this problem and allows epitaxial growth of subsequent layers. YSZ is deposited with a typical thickness of approximately 40nm, which is a value that is large enough to ensure its function as inter-diffusion[81] barrier and to obtain a high quality epitaxial bottom layer.

---

[79] Within the "soft-mode" model the polarisation catastrophe is explained by a decrease of the lowest transverse optical lattice mode with approach to the transition temperature, corresponding to a decrease of restoring forces.

[80] A continuous change of polarisation, but not a 2nd order transition, indicated by different temperature behaviour of the heat capacity c_p.

[81] Which, in this case, would decrease the dielectric and ferroelectric properties of SBT.

In order to improve the epitaxial growth of $SrBi_2Ta_2O_9$, additional buffer layers can be introduced. Here, CeO_2 ($a = 0.541$ nm) is a commonly used material that matches the lattice constants from YSZ ($a = 0.514$ nm) to $SrBi_2Ta_2O_9$ ($a = 0.5531$ nm, $b = 0.5534$ nm), which leads to *c*-axis growth of SBT. Since the polarisation plane of $SrBi_2Ta_2O_9$ lies in the crystallographic *a*-*b*-plane, it is desirable to force the crystal to grow with this plane along the substrate normal in order to obtain optimal ferroelectric properties in planar multilayer devices (such as capacitors, MFS diodes). Here, $SrZrO_3$ (SZO) is a new candidate that is investigated for the first time in this work.

6.2.1 Properties of $SrBi_2Ta_2O_9$

Below the Curie-temperature, $SrBi_2Ta_2O_9$ exists in an orthorhombic Aurivillius-structure. Thus, it belongs to a subgroup of perovskites with the general structure $(X_2O_2)^{2+}(A_{x-1}B_xO_{3x+1})^{2-}$, with X=Bi, A=Sr, B=Ta, and x=2. The structure forms an alternating stacking sequence along the *c*-axis of $(Bi_2O_2)^{2+}$-layers and $(SrTa_2O_7)^{2-}$-perovskite blocks, as shown in Figure 6.4. Consecutive $(Bi_2O_2)^{2+}$–layers are displaced along the *a*-axis by $a/4$. The TaO_6-octahedrons are tilted against the *c*-axis by an angle of 6.5° [Shi 99]. The layered structure of $SrBi_2Ta_2O_9$ leads to the orientation of the spontaneous polarisation mainly in *ab*-plane. In spite of the difference in the ionic radii between Sr (0.22 nm) and Bi (0.15 nm), a substitution of Sr^{2+} by Bi^{3+} is possible, where Sr^{2+} vacancies ensure charge neutrality. As a result, the obliquity of the TaO_6-octahedral increases with the remanent

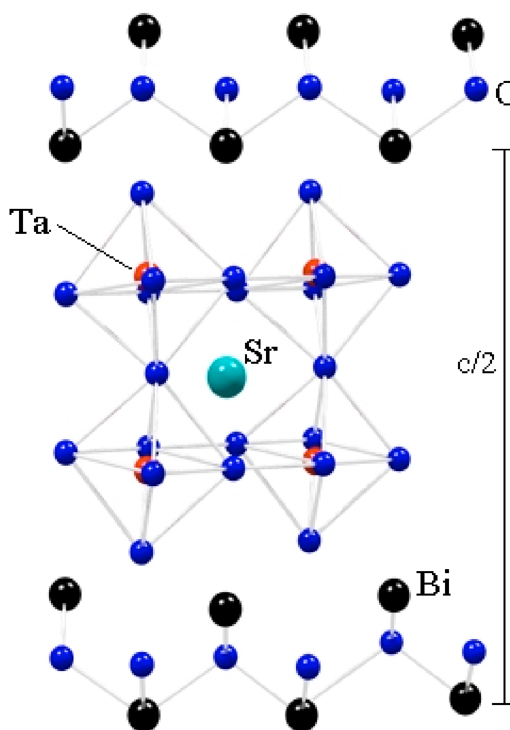

Figure 6.4: The structure of $SrBi_2Ta_2O_9$: Alternating (Bi_2O_2)–layers and perovskite blocks of Ta-ions, which are co-ordinated by tilted oxygen octahedrons.

polarisation[82] [Bha 98]. Besides the ferroelectric phase, a non-ferroelectric fluorite-like cubic phase exists, which is transformed into the perovskite phase above temperatures of 700°C [Hyu 98]. Bismuth deficiency due to the high vapour pressure of Bi and resulting re-evaporation from the substrate is a well know problem in thin film deposition techniques. As a result, a common defect in $SrBi_2Ta_2O_9$ films is the lack of (Bi_2O_3) layers, which was investigated by TEM measurements [Tay 98]. At temperatures above 800°C, where the Bi-loss is extremely high, a more critical problem arises. Here, the Bi-deficiency leads to the formation of a stable pyrochlore-phase (pc-SBT) with the spacegroup Fd3m and a lattice constant of $a = 1.05$ nm [Rod 96]. Bi-enriched targets have been used in order to compensate for the Bi loss during film deposition [Bäu 99]. Some important quantities of $SrBi_2Ta_2O_9$ single crystals are listed in Table 6.1.

quantity	unit	value
spacegroup		Fmm2 $\alpha=\beta=\gamma=90°$
lattice parameters a, b, c	[nm]	0.55306(5), 0.55344(5), 2.49839(24)
density	[g/cm^3]	7.5
Curie-temperature	[°C]	310
dielectric constant (25°C)		180
spont. polarisation (25°C)	[C/m^2]	5.8 10^2
piezoelectric constant	[m/V]	2.3 10^{-11}

Table 6.1: Properties of $SrBi_2Ta_2O_9$ single crystals [Rae 92].

6.2.2 Structural Characterisation

To emphasise the importance of a YSZ buffer, a $\theta/2\theta$-scan of a 300nm thick $SrBi_2Ta_2O_9$ film, deposited directly on a silicon substrate is shown in Figure 6.5. The (115)- and (200)/(020)-peaks[83] of $SrBi_2Ta_2O_9$ correspond to the most intense peaks in a powder simulation. Rocking curves of the (115)-reflection show a constant intensity within a range of 20°, which proves that only polycrystalline $SrBi_2Ta_2O_9$ is achieved on silicon. Additionally, the strongest polycrystalline (111)-reflection of the pyrochlore-phase is visible at $2\theta = 14.5°$. The

---

[82] Resulting from compressive stress in the perovskite blocks due to the higher ionic radius of Sr^{2+} and higher distances between perovskite blocks and (Bi_2O_3)-layers.

[83] Extinction conditions for a face centred lattice type allow either even or odd values for all Miller indices.

formation of this phase is favoured at deposition temperatures above 800°C and deposition pressures below 0.8 mbar. From low-angle X-ray diffraction, a remaining 4 nm thick SiO_2 layer is detected. Hence, without an appropriate buffer epitaxial growth of $SrBi_2Ta_2O_9$ on silicon is impossible.

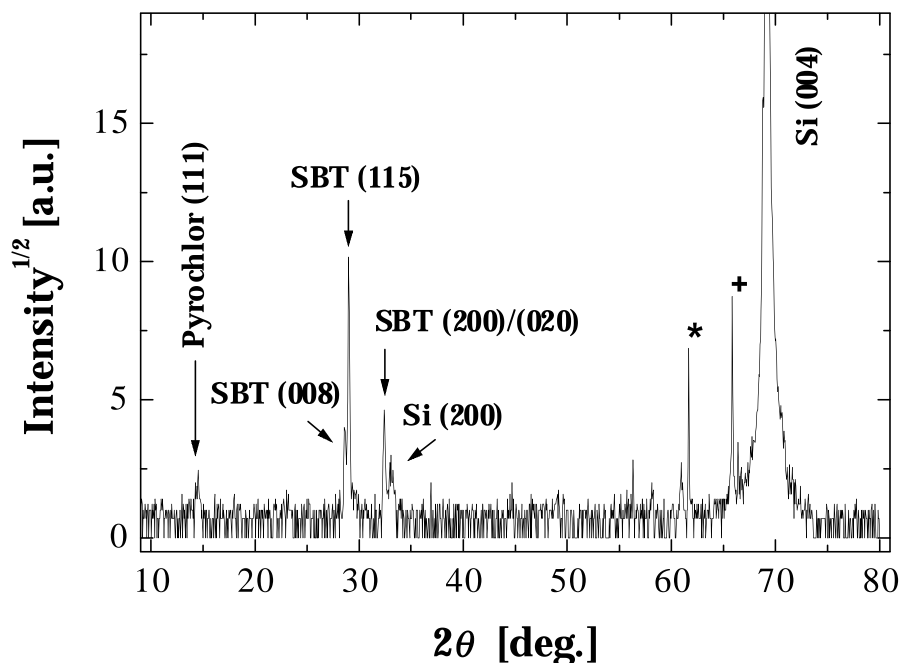

Figure 6.5: X-ray diffraction pattern ($\theta/2\theta$-scan) of $SrBi_2Ta_2O_9$ film (300nm), deposited directly on silicon. The $SrBi_2Ta_2O_9$- and the pyrochlore (111)-reflection is visible. Beside the main Si(004) substrate reflection, the forbidden Si(002)-reflection is visible, due symmetry breaking at substrate surface. Parasitic substrate peaks are indicated by (*/+).

Introduction of YSZ and YSZ/CeO2 Buffer Layers

Figure 6.6 shows a comparison between $SrBi_2Ta_2O_9$ films deposited on silicon with a single YSZ buffer layer (a) and a YSZ/CeO_2 buffer layer combination (b), respectively. Although the YSZ layer is highly *c*-axis oriented with 1.2° FWHM of rocking curves, no SiO_2 was detected by LXRD, and identical deposition parameters as for $SrBi_2Ta_2O_9$ on silicon have been used, the introduction of a single YSZ layer leads only to a pure *a*-axis oriented pyrochlore film.

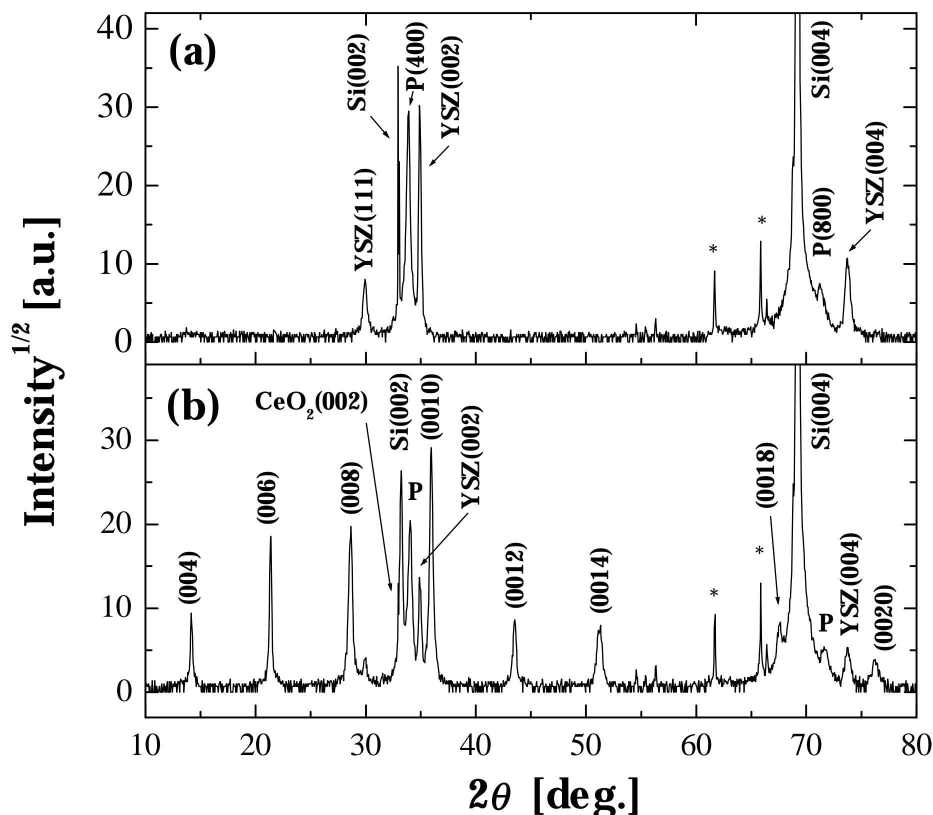

Figure 6.6: **(a)** X-ray diffraction pattern ($\theta/2\theta$ -scan) of a pc-SBT film (50nm), deposited on a 40nm YSZ buffer layer on silicon. The pyrochlore (400)-reflection exhibits a FWHM of 1.5°, whereas the YSZ (002)-peak shows a FWHM of 1.4°. The presence of the YSZ (111)-reflection shows, that a small amount of randomly oriented YSZ crystallites is still present. **(b)** A $SrBi_2Ta_2O_9$ film grown on a buffer layer combination YSZ(40nm)/CeO_2(20nm) exhibits a *c*-axis oriented $SrBi_2Ta_2O_9$ with FWHM of 1.2°. The (400)- and (800)-reflections of the pyrochlore-phase (P) are visible. The (002)-reflection of the CeO_2 layer, theoretically situated at $2\theta = 33.08$, is superimposed by the Si(002)-peak and leads to a broadening of this peak.

The visible peaks in Figure 6.6a at $2\theta = 34°$ and $2\theta = 71.5°$ with a FWHM of 1.4° are related to the (400)- and (800) reflections of the pyrochlore-phase[84]. This is shown by four-circle X-ray measurements, which additionally show a cube-to-cube in-plane relation of both layers (Figure 6.7). Within the accessible pressure and temperature range the growth of a *c*-axis oriented $SrBi_2Ta_2O_9$ is not possible, which is consistent with work of Ishikawa [Ish 99], done on YSZ substrates. Impurity phases of Bi_2O_3 or $Bi_{7.80}Ta_{0.20}O_{2.20}$, as reported in literature [Let 98], are not observed.

[84] This 2θ-values could wrongly be identified as the (117)- and (2 2 $\underline{14}$)-reflections of $SrBi_2Ta_2O_9$.

In contrast, if an additional CeO_2 layer (20 nm) is implemented, the $SrBi_2Ta_2O_9$ film exhibits a clear *c*-axis orientation with FWHM of 1.2° for the (006)-reflection (Figure 6.6b). Within this $\theta/2\theta$-diffraction pattern, again a small *a*-axis oriented (1.2° FWHM) pyrochlore amount is visible. The whole stack of layers shows a good cube-to-cube in-plane orientation with respect to the silicon substrate, which is proofed by four-circle X-ray measurements (φ-scans) as shown in Figure 6.7b. In contrast, the use of a single YSZ as buffer on silicon leads to a clear cube-to-cube growth of the pyrochlore phase in Figure 6.7a.

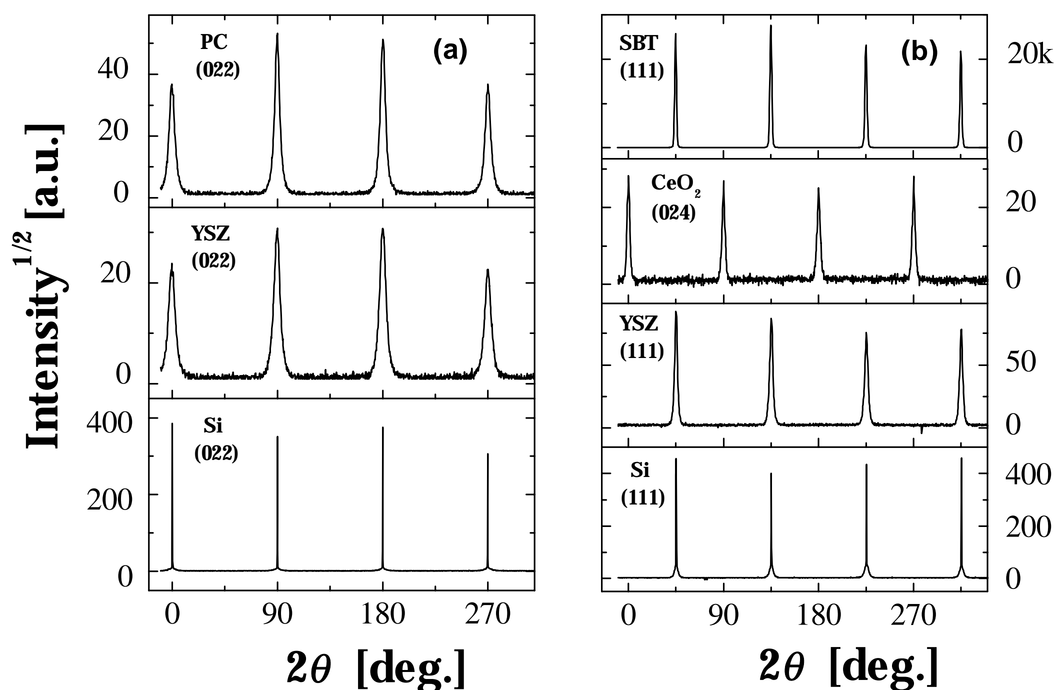

Figure 6.7: **(a)** In-plane orientation of $SrBi_2Ta_2O_9$ deposited on silicon under utilisation of a single YSZ buffer layer. φ-scans at the pyrochlore(022), YSZ(022) and the Si(022)-reflection show a cube–to-cube growth of all layers and the formation of the pyrochlore-phase exclusively. **(b)** φ-scans at the SBT(111), YSZ(111), CeO_2(024) and the Si(111)-reflection. As a result of the similar lattice constants of silicon and CeO_2, the (111)-reflections of both materials are not dissolvable, and thus the (024) peak of CeO_2 was used. Therefore, the 45°-shift of this peak means again a cube-to-cube growth of the complete stack.

These X-ray results are supported by AFM studies with a commercial Atomic Force Microscope (AFM[85]) [Mar 98, Auc 98]. Illustrated in Figure 6.8a,

[85] Multimode, Digital Instruments, Santa Barbara, CA (USA).

$SrBi_2Ta_2O_9$ films deposited without buffer show a typical surface morphology of polycrystalline films with an average surface roughness of 5.6 nm (rms). In contrast, $SrBi_2Ta_2O_9$ films deposited using a YSZ/CeO_2 buffer layer combination, exhibit terraces which correspond to ½ unit-cell steps along the *c*-axis and a roughness of 4.4 nm (rms) as shown in Figure 6.8b. Small grains visible on the top right in Figure 6.8b correspond to the pc-SBT phase.

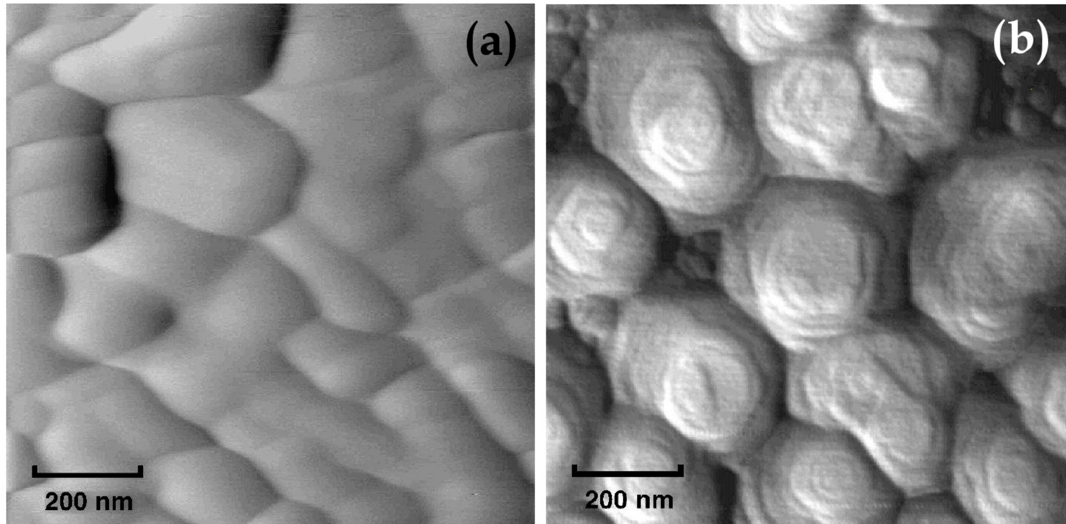

Figure 6.8: AFM contact mode measurements. Topography of **(a)** a $SrBi_2Ta_2O_9$ (300nm) film deposited directly on Si and **(b)** a buffered YSZ(40nm)/CeO2(20nm)/SBT(300nm) film on silicon, which shows terraces corresponding to unit-cell steps along the *c*-axis. The vertical scale for both images is 20nm.

Relation of Oxygen Pressure, Phase Formation and Surface Morphology

Bismuth is the most volatile component in the $SrBi_2Ta_2O_9$ compound with an extremely low vapor pressure, which additionally decreases in the oxidised state. Therefore, the ambient deposition pressure and the target composition influences strongly the formation of the $SrBi_2Ta_2O_9$- and the pyrochlore-phase, respectively. If targets with integral stoichiometry (1:2:2) are used, the Bi-deficient Pyrochlore-phase disappears at a deposition temperature of 800 °C and a pressure of 0.8 mbar, whereas for targets with Bi-excess (1:2.3:2) a pressure of 0.5 mbar is sufficient to avoid the formation of this phase. X-ray measurements show a decreasing pyrochlore content with increasing oxygen pressure and vice versa an increasing $SrBi_2Ta_2O_9$ fraction.

This observation is supported by SEM measurements, shown in Figure 6.9, which exhibit an increasing $SrBi_2Ta_2O_9$ grain density with pressure. For

targets with integral stoichiometry (1:2:2), the film surface is built by a closed $SrBi_2Ta_2O_9$ grain morphology if a deposition pressure of 0.8 mbar is exceeded. This interpretation is supported by EDX measurements, where the Ta:Bi ratio in the small grains amounts 1:0.45 corresponding to a theoretical value of 1:0.35 for pyrochlore, whereas in the big grains a ratio 1:1.01 nearly perfectly meets the integral stoichiometry for $SrBi_2Ta_2O_9$.

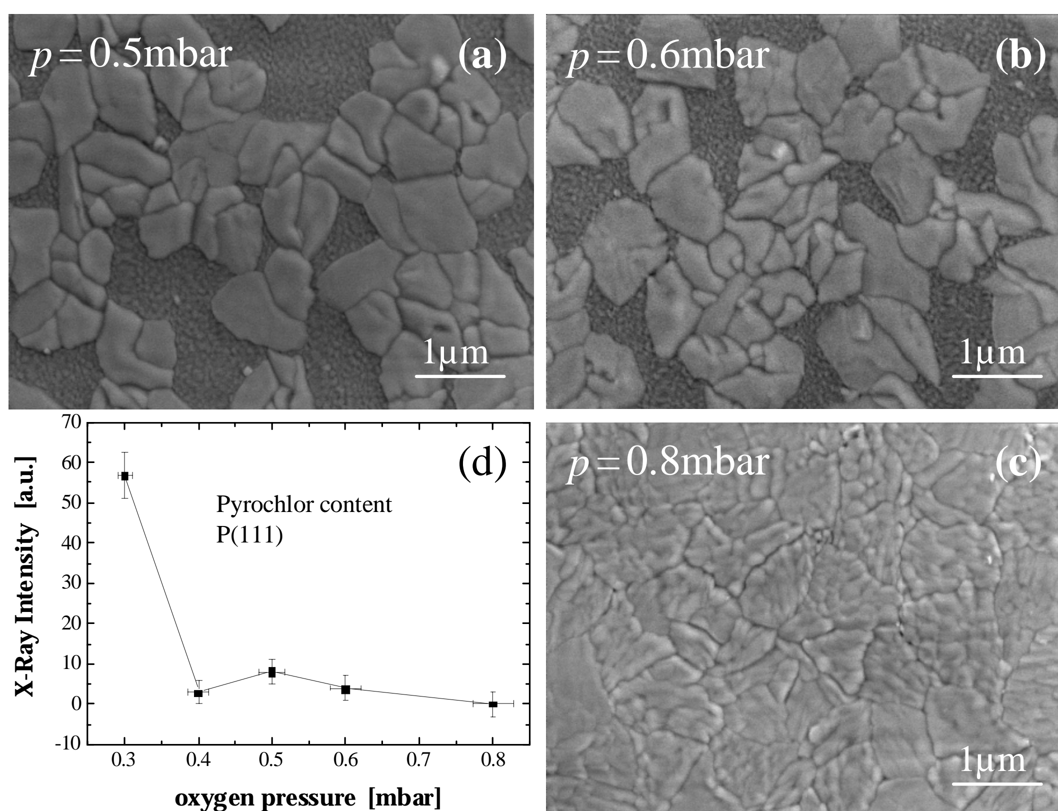

Figure 6.9: SEM micrographs (6x6 µm) of $SrBi_2Ta_2O_9$ films deposited on silicon with oxygen pressures of (a) 0.5 mbar, (b) 0.6 mbar and (c) 0.8 mbar, respectively. In figure (a) and (b), two separated growth areas are visible: Big bright grains (400-800 nm size) correspond to the $SrBi_2Ta_2O_9$ phase, while the pyrochlore-phase is represented by small dark grains with approximately 50 nm in size. In (c) the pyrochlore-phase vanishes at pressures above 0.8 mbar, which is in agreement with X-ray measurements (d).

6.3 Dielectric and Ferroelectric Properties of $SrBi_2Ta_2O_9$

As previously mentioned, FRAMs and MIS-FETs represent two important applications of ferroelectric thin films. Therefore, gate structures (e.g. MFS-diodes) and capacitor structures, being the basic modules of these devices, have been manufactured in order to investigate the applicability of $SrBi_2Ta_2O_9$ as an alternative ferroelectric material.

6.3.1 Preliminary Remarks on Diode Structures

Ideal MIS-Diodes

Within the treatment of an ideal[86] MIS-diode as a voltage dependent capacitor [Pfa 59], a potential difference between metal and semiconductor[87] leads to four different scenarios and a typical *C(V)*-characteristic shown in Figure 6.10. (i) $U < 0$ V: The valence-band of the semiconductor is bent up and approaches the fermi-level E_F, which does not change its position, since the isolator avoids current flow. The exponential dependence of the charge carrier density on the energy difference between band edge and E_F leads to an *accumulation* of majority charge carriers (holes). (ii) $U = 0$ V: Planar band condition; the band of the semiconductor is not bent and the total voltage drops at the insulator. (iii) $U > 0$ V: The distance between valence-band and fermi-level increases, while the conduction band approaches the latter. The holes move into the interior, leaving uncompensated ionised acceptors,

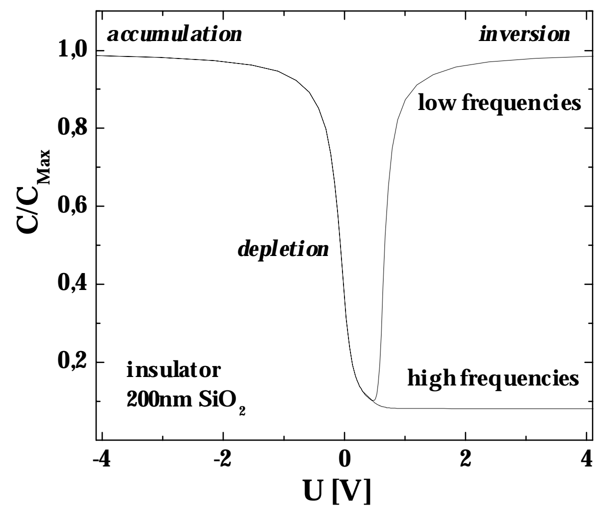

Figure 6.10: Simulation of a *C(V)*-characteristic for an ideal MIS diode with 200 nm SiO_2 as insulator at high and low frequencies (10^{15} cm^{-3} p-doped Si).

[86] Equal electrochemical potentials between metal- and semiconductor electrons.

[87] To simplify, a p-doped semiconductor is considered; semiconductor grounded.

which leads to ***depletion***. (iv) $U >> 0\,V$: further increase of the voltage leads to the formation of an *inversion* layer, i.e. accumulation of minority carriers (electrons) at the interface.

The total capacity consists of an in-series connection of insulator and semiconductor, where the latter is determined by the differentiation of the surface charge density (charge concentration due to band bending) with respect to the applied potential. This considerations only apply, if minority, as well as majority charge carriers can follow the spatial distribution that is imposed by the applied AC-voltage (1 kHz-1 MHz). At high frequencies[88], surface charge carriers of the inversion layer do not contribute to the capacity (see Figure 6.10), leading to a constant low capacity that depends on insulator capacity and semiconductor doping.

Real MIS-Diodes

The accumulation of minority charge carriers can be impeded by the finite conductivity of a real insulator [Sze 81] due to mechanisms, such as Schottky-emission (at the interface), Pole-Frenkel-conductivity (in the bulk), ionic and ohmic (thermal excited ions and electrons) conductivity, and tunnelling-processes [Ash 76, Die 95]. In real MIS-diodes, some corrections have to be considered: (i) A difference in the electronic work functions of metal and semiconductor leads to a formation of an electric dipole, due to charges at the metal/insulator interface and a space-charge region of the semiconductor, followed by a shift of the *C(V)*-curve along the voltage axis. (ii) On the other hand, different kinds of charge trapping sites influence the position as well as the shape of the *C(V)*-curve. Especially with silicon, a not completely removed SiO_2 layer will generate fixed oxygen charges. (iii) The interruption of the semiconductor periodicity at its surface is governed by a high density of charge trapping sites within the band gap [Gro 65], followed by an elongation of the *C(V)*-curve, depending on the frequency.

MFS-Diodes

However, in the case of a MFS-diode a voltage dependent polarisation changes the situation drastically. The applied voltage is now composed by the

---

[88] For SiO_2 as insulator, this effect is observed above a frequency of 100Hz [Gro 65].

band bending of the semiconductor, the voltage drop at the insulator, and the part of the polarisation. Simulations [Mil 91, Mil 92] show, that the size of the hysteresis depends only weakly on the remanent polarisation but increases with the coercitive field. This fact is understandable, when the *C(V)*-curve is changed from zero voltage to negative voltages and back again. A difference in capacity results, because the semiconductor remains in the inversion state, as long as the remanent polarisation is larger than a typical value of 0.1 μC/cm², which is sufficient to change the semiconductor state from planar band condition to inversion [Han 98]. The voltage, at which the transition from inversion to depletion takes place, consequently depends linearly on the coercitive field. Furthermore, a decreasing thickness of the film is governed by a decreasing hysteresis, whereas deviations from this behaviour appear, when the thickness is smaller than the domain size in the material [Ren 96].

6.3.2 Results on Diode Structures

In order to measure[89] *C(V)*-characteristics of the samples, gold electrodes with a typical area of 0.5x0.5 mm² have been deposited onto the $SrBi_2Ta_2O_9$ top-layer by standard vapor deposition [Sch 99].

Influence of the Buffer Layer

Since a hysteresis in *C(V)*-curves can be created by mobile ions or trapping sites [Han 98], measurements of the single YSZ layers have been performed (see chapter 4.3.2, Figure 4.9a). Here the complete removal of the SiO_2 due to the reaction with YSZ layer simplifies the interpretation of the measurements. Within Voltages of -4 V and +4 V no hysteresis is observable. From the capacity in the accumulation region a dielectric constant of YSZ could be estimated to $\varepsilon \approx 4$, which quantitatively matches literature values [Mau 98]. A shift of the *C(V)*-curve of +0.22 V to positive voltages is related to negative surface charges at the interface Si/YSZ [Ter 62, Gro 65]. From this shift, a trapped charges density of $n \approx 1.35 \times 10^{11}$ 1/cm² can be estimated. This value is equal or smaller than for common MOS-diodes (2×10^{11} 1/cm²) or CeO_2-layers (3×10^{11} 1/cm²) [Nag 96].

---

[89] Hewlett-Packard HP 4284A-LCR meter, details in [Sch 99].

The size of the memory window mainly depends on the film thickness and the coercitive field. Consequently, it is independent on the insulating buffer between ferroelectric and substrate. On the other hand, a high dielectric constant of the insulator is followed by a higher voltage drop at the ferroelectric film. This leads to saturation of the polarisation at lower voltages, which affects read/write voltages of devices. Furthermore, the capacity of the insulator decreases with increasing thickness, resulting in a decrease of the electric field in the ferroelectric. In order to attain sufficient hysteresis for a 300 nm thick $SrBi_2Ta_2O_9$ film ($E_C = 30$ kV/cm, $V_{DC} = \pm 6$ V), the buffer layer thickness is limited to about 40 nm.

Measurements without Buffer Layer – Au/SBT/Si MFS Structures

Figure 6.11 shows the capacitance versus bias voltage of an Au/SBT/Si heterostructure with a 300 nm thick $SrBi_2Ta_2O_9$ layer. The behaviour is very similar to what is expected for a metal-ferroelectric-semiconductor (MFS) diode measured at high frequencies.

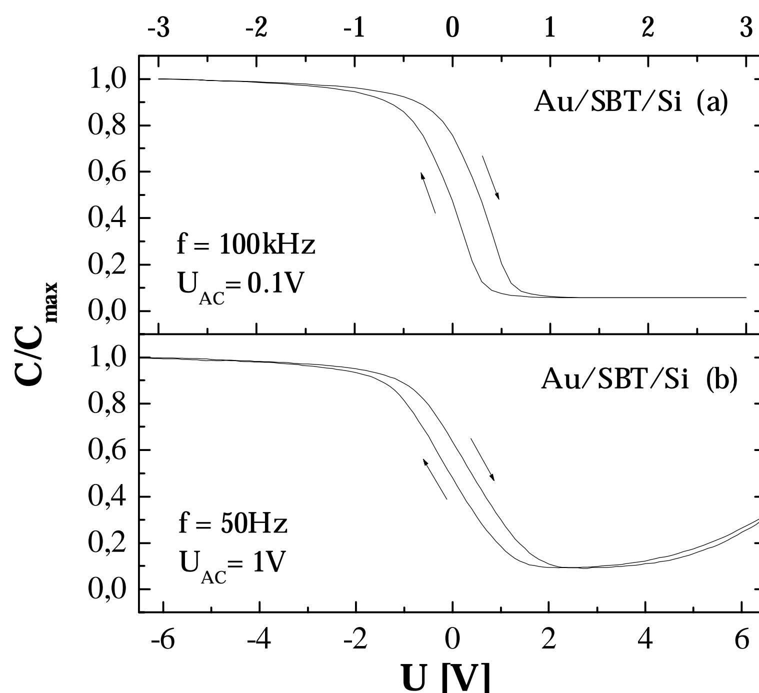

Figure 6.11: (a) A *C(V)*-curve of a 300nm $SrBi_2Ta_2O_9$ film on silicon measured at 100 kHz and an *AC*-voltage of 0.1 V shows a memory window of 0.3 V, the maximal attainable value is 0.45 V. **(b)** Measurements at low frequencies (50Hz) show a stretched curve with a memory window of 0.44 V and an increase of capacitance at high voltages due to inversion charges.

Induced by the coercive field of $SrBi_2Ta_2O_9$ [Han 98], the ferroelectricity of these polycrystalline $SrBi_2Ta_2O_9$ films generates a typical memory window of 0.45 V, which lies in the range of literature values from 0.3 V and 1.4 V ($V_{DC} = \pm 8$ V, $d_{SBT} = 300$-350 nm) [Kan 99, Xio 99]. The capacity in the inversion range amounts 6% of the accumulation value. The losses (tanδ, not shown) as well as phase shift are maximal at planar band conditions, at which per definition the voltage drops completely at the insulator. The maximum of phase shift results from charges, which can not follow the *AC*- signal since they are confined to trapping sites at the interface. Measurements at lower frequencies (50 Hz) in Figure 6.11b show an increase of the total capacity in the inversion range. In contrast to the measurement in Figure 6.11a, the minority charge carriers can now follow the applied *AC*-field. The same applies to interface states at the silicon surface, which provoke a frequency dependence in the capacity and cause an elongation of the hysteresis. With variation of the *AC*-voltage, the energy levels in the Si band gap move up and down followed by a change of their charge state when the Fermi level is exceeded [Sze 81].

As illustrated in Figure 6.12, at low frequencies ($f < 100$kHz) the dielectric constant is slightly decreasing from $\varepsilon = 160$ to 143, whereas the losses are slightly increasing from $\tan\delta = 0.012$ to 0.17. Above a frequency of 100 kHz, the losses and the dielectric constant show an increase to $\tan\delta = 0.83$ and a decrease to $\varepsilon = 53.9$, respectively. Since measurements with capacitor structures (see chapter 6.3.3) show only a weak decrease in logarithmic scale, it is obvious that the high losses are not related to the $SrBi_2Ta_2O_9$ film.

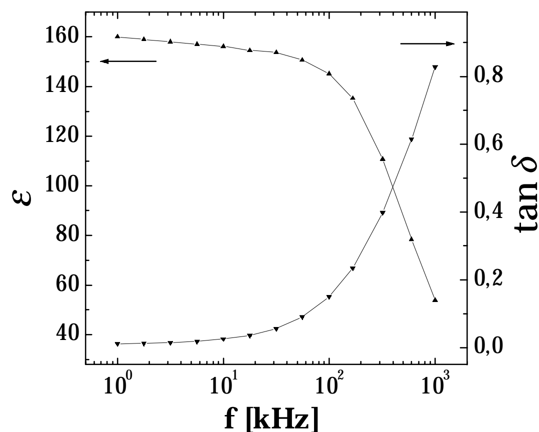

Figure 6.12: Frequency dependence of the dielectric constant and the loss of a 300 nm thick $SrBi_2Ta_2O_9$ film on silicon. The dielectric constant was estimated from the accumulation capacitance and an assumed 4 nm thick SiO_2 layer with $\varepsilon = 4$.

The comparison of *C(V)*-characteristics for samples deposited with different deposition pressures (followed by a change in the surface morphology, see chapter 6.2.2), shows an increasing memory window with oxygen

pressure. On the one hand, a smaller pyrochlore content possibly causes a larger hysteresis. On the other hand, the coercitive field should decrease with grain size (see chapter 6.4), since below a critical size the grains correspond to a single domain particle. This requires an essentially higher electrical field to flip the polarisation [Ren 96]. The previously predicted influence of the film thickness is clearly shown by measurements, done in films with thickness of 200, 250, and 300 nm which show memory windows of 0.14, 0.24, and 0.28 V, respectively.

MFIS Structures with YSZ and CeO_2/YSZ Buffer Layers

As previously mentioned, a YSZ buffer layer forces the formation of the pyrochlore phase. Figure 6.13a shows a *C(V)*-characteristic of a 50 nm thick pc-SBT film, obtained on YSZ(40 nm)-buffered silicon. A memory window of 0.43 V is observed. Charge trapping sites and mobile ions can be excluded as origin of the hysteresis, since in this case the course of the hysteresis would show a reversed direction and the size of the memory window should depend on the turn speed [Han 98]. The dependence of the memory window size on the film thickness (50 nm/0.43 V, 300 nm/0.52 V) is weak compared to $SrBi_2Ta_2O_9$ films deposited directly on silicon (200 nm/0.14 V, 300 nm/0.28 V). However, compared to the latter, the characteristic is strongly elongated and shifted to positive voltages. This behaviour is resulting from negative charges in trapping sites at the interface, which lead to a decrease of the accumulation capacity with *AC*-frequency. Moreover, the *C(V)*-curve is shifted to negative voltages at high frequencies. This can be explained by trapped negative charges or interface states at the silicon surface, which are no longer able to follow the *AC*-signal.

In Figure 6.13b, a *C(V)*-characteristic of an Au/SBT(50 nm)/CeO_2/YSZ/Si heterostructure is shown. Here, the use of CeO_2 as an additional buffer generates *c*-axis oriented $SrBi_2Ta_2O_9$ and increases the memory window to 0.87 V. The remanent capacitance can be switched between ±3 V. This represents an improvement compared to SBT(50 nm)/YSZ/Si (0.43 V) and even to 300 nm thick $SrBi_2Ta_2O_9$ films deposited directly on silicon (0.6 V). As it was observed by Han et al [Han 98] and predicted by Miller and McWorther [Mil 92], the memory window is mainly related to the coercitive field and very little

influenced by the amplitude of the remanent polarisation (for $P_r > 0.1$ C/cm²). Since the polarisation of $SrBi_2Ta_2O_9$ along the *c*-axis is very small and nevertheless a quite big memory window is observed, the coercitive field of *c*-axis oriented film is assumed to be essentially larger than that of polycrystalline $SrBi_2Ta_2O_9$ on silicon.

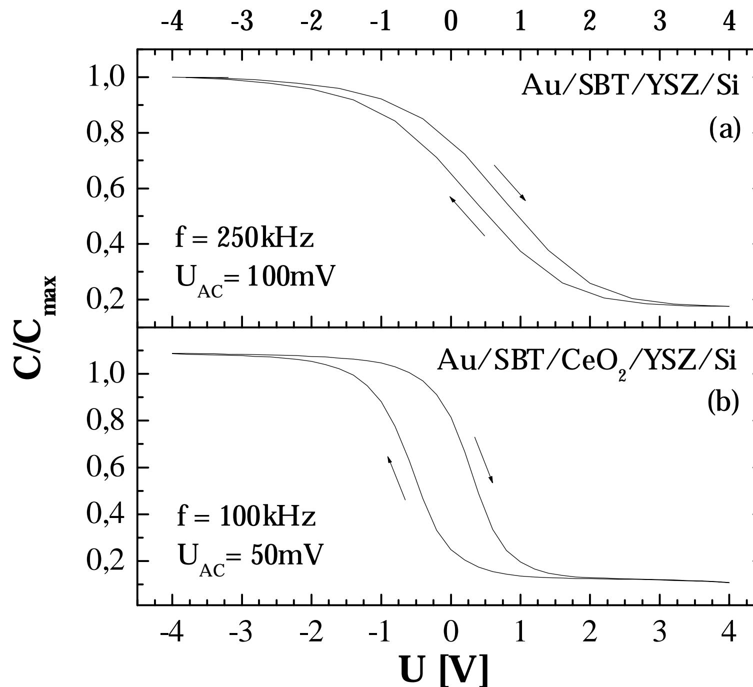

Figure 6.13: (a) The *C(V)*-characteristic of pc-SBT(50nm) on YSZ(40nm)-buffered silicon shows a memory window of 0.43 V (f = 250 kHz, $V_{AC} = 0.1$ V, $V_{DC} = \pm 4$ V). **(b)** The measurement of a *c*-axis oriented 50 nm thick $SrBi_2Ta_2O_9$ film on Si/YSZ(40 nm)/CeO_2(20 nm) exhibits a memory window of 0.87 V (f = 100 kHz, $V_{AC} = 50$ mV, $V_{DC} = \pm 5$ V).

6.3.3 Results on Capacitor Structures

In order to manufacture capacitor structures, polycrystalline $SrBi_2Ta_2O_9$ has been deposited on Pt-buffered silicon substrates and gold pads have been evaporated onto the heterostructure [Sch 99]. In Figure 6.14a, a measurement of such a capacitor structure is shown. Within a butterfly-like shape of *C(V)*-characteristic[90], maximums correspond to the inflexion points in the hysteresis curve e.g. the coercitive field. Since the maximums of the capacity are equal

[90] The characteristic can be understood by the differentiation of a hysteresis with respect to the electric field: $\partial P/\partial E = \varepsilon_0 \chi = \varepsilon_0 (\varepsilon\text{-}1) \approx \varepsilon_0 \varepsilon \propto \varepsilon_0 C$.

for positive and negative voltages, a non-ohmic contact due to interdiffusion at the SBT/Pt and Au/SBT interface can be excluded [Lee 98]. The shift of the curve centre to negative voltages mainly results from different work functions of gold ($W_A = 5.1$ eV) and platinum ($W_A = 5.65$ eV). From the voltages of the capacity maximums in Figure 6.14a, the coercitive field is estimated to 27 kV/cm and 60 kV/cm, respectively.

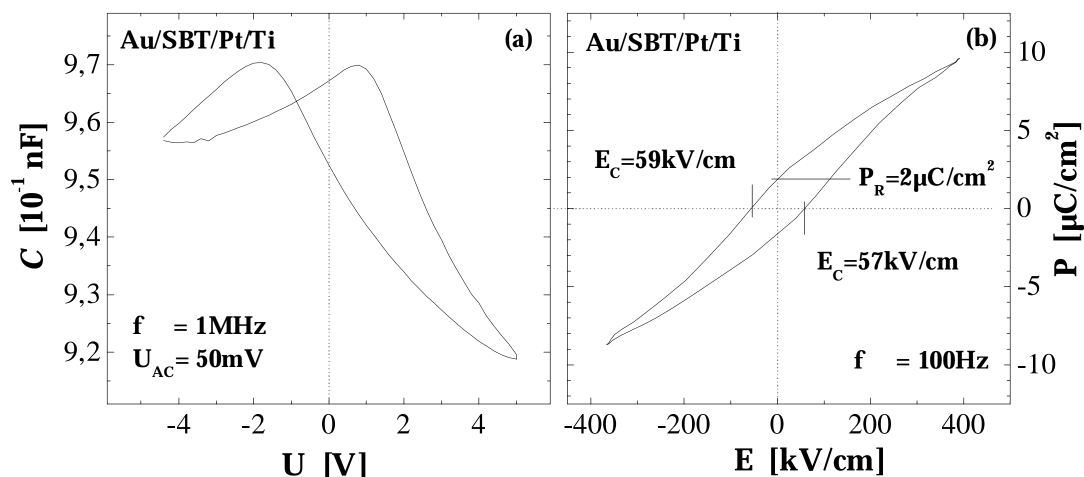

Figure 6.14: (a) *C(V)*-characteristic of a Pt/SBT(300 nm)/Au ferroelectric capacitor measured at $f = 1$ MHz and $U_{AC} = 50$ mV. **(b)** *P(E)*-hysteresis curve of the same capacitor. The coercitive field is 57 kV/cm (59 kV/cm), and the remanent polarisation amounts 2 µC/cm².

In order to determine the polarisation from the hysteresis curve *P(E)*, a Sawyer-Tower circuit[91] was used [Sch 99, Sch 99a, Saw 29]. The measurement in Figure 6.14b shows a coercitive field of about 58 kV/cm and a remanent polarisation of 2 µC/cm², comparable to values in the range of 1.7 µC/cm² observed by other groups [Bha 98, Yan 97, Ras 99]. The small shift of the coercitive field to negative values is presumed to result from internal fields due to the different work functions of the electrodes. Furthermore, slow moving trapped charges can be situated at the electrode surfaces. This explains the larger shift in the *C(V)*-measurement in Figure 6.14a, since here the DC voltage was altered with a rate of 0.2 V/s, compared to the Sawyer-Tower measurement in Figure 6.14b, which was measured at 100 Hz. Thus, a slow variation of the voltage leads to the formation of space charge regions, which

[91] In-series connection of the sample with a reference capacitor.

contribute to the capacity, whereas at sufficient fast variation of the electric field this contribution is decreased and the residual shift corresponds to trapped charges, which are confined to the interface. Since the films show polycrystalline growth and the polarisation is aligned mainly in the *ab*-plane, only a small fraction of the polarisation is aligned perpendicular to the film surface. This fact is assumed to cause the observed smaller remanent polarisation, compared to values for $SrBi_2Ta_2O_9$ single crystals (5.8 μC/cm). A size effect [Str 97] due to stray fields in the capacitor can be excluded, since the ratio of film thickness and electrode diameter in the samples is 1:10^3.

Frequency dependent measurements of *C(V)*-characteristics show an increase of capacity and a constant shift to negative voltages. As shown in Figure 6.15a and in contrast to MFS diode structures (see Figure 6.12), the resulting dielectric constant ε decreases linearly with logarithmic scaled frequency from 133 to 95 at 1 kHz and 1 MHz, respectively. This behaviour can be described by the Rayleigh-theory[92]. For materials with randomly distributed pinning centres, the application of this theory to ferroelectrics describes the dielectric constant as a sum $\varepsilon = \varepsilon_{init} + \alpha E_0$. Here, ε_{init} is resulting from lattice displacement and reversible domain wall movement, whereas the contribu-

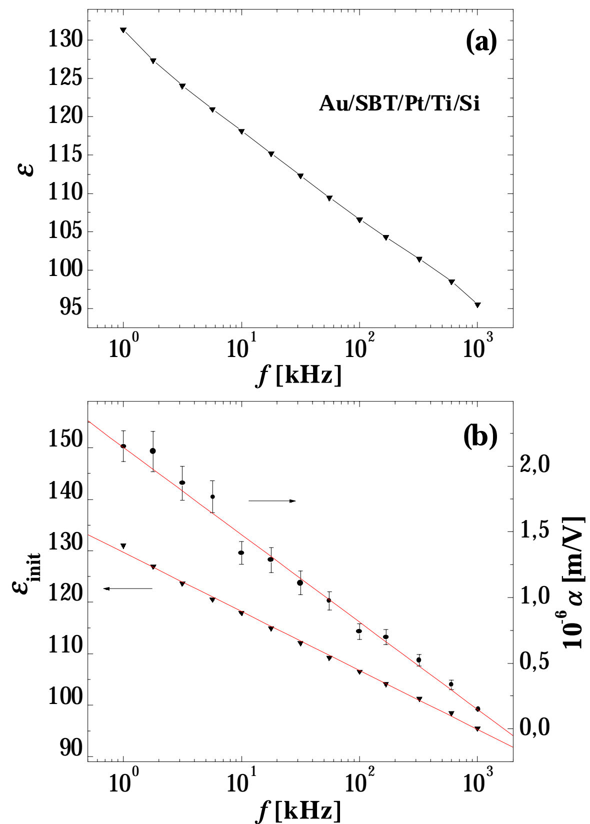

Figure 6.15: (a) Frequency dependence of the dielectric constant (V_{DC} = 0.8 V, V_{AC} = 50 mV). **(b)** The logarithmic dependence of the Rayleigh parameters α and ε_{init} on frequency.

92 Originally established for magnetic materials in weak fields (< H_c res. E_c).

tion αE_0 originates from irreversible domain wall movement between metastable states, which is generated by the outer electric field $E_0 = U_{AC}/d$ [93] [Tay 97]. In order to prove, if the observed logarithmic decrease of the dielectric constant in Figure 6.15a is originating from reversible or irreversible domain wall movement, the electric field E_0 is (i.e. *AC*-amplitude[94]) can be varied at constant frequencies. From an observed linear increase of ε with *AC*-voltage, the slope and the dielectric constant at zero voltage yields the Rayleigh-parameters α and ε_{init} , respectively. As illustrated in Figure 6.15b, both parameters exhibit a logarithmic dependence on frequency.

The fraction of the irreversible domain wall movement $\alpha E_0/\varepsilon_{init}$ amounts 2% at 1 kHz and $E_c = 14$ kV/cm, which is comparable to a value of 3% for $BaTiO_3$ (300 nm) on $YBa_2Cu_3O_{7-\delta}$ with a remanent polarisation of 1.25 μC/cm² [Sch 99a]. In contrast, $Pb(Zr_xTi_{1-x})O_3$ films show an irreversible domain wall fraction of 21% resulting from a larger remanent polarisation of 20 μC/cm² [Tay 97]. The low remanent polarisation of SBT compared to PZT films is one possible reason for the exceedingly good fatigue behaviour of $SrBi_2Ta_2O_9$ [Ara 96]. Within this approach, an accumulation of charges at the domain walls compensates the discontinuity of the polarisation. For a lower polarisation in $SrBi_2Ta_2O_9$, the charge density and consequently the pinning is weaker. A second reason for the good fatigue behaviour is thought to be the high mobility of Bi in $SrBi_2Ta_2O_9$. Bi losses are compensated by oxygen vacancies exclusively in the BiO_2-layers and thus defects are not situated in the perovskite blocks. As a third reason, charges in trapping sites can be released easier in $SrBi_2Ta_2O_9$, since the strength of the pinning depends on the one hand on the defect type, but on the other it is strongly influenced by the potential progression in the domain walls, which in turn depends on the remanent polarisation [Ash 76].

[93] With the film thickness *d*.

[94] The applied *AC*-voltage of 500 mV (14 kV/cm) is smaller than the estimated coercitive field.

6.4 Ferroelectric Domains in $SrBi_2Ta_2O_9$

The domain structure of a ferroelectric determines the macroscopic properties, such as dielectric constant and memory window. Therefore, a microscopic understanding of the physical phenomena on the scale of ferroelectric domains is necessary to investigate the interrelation between morphology and dielectric as well as ferroelectric properties, respectively. This is motivated especially by the progressing miniaturisation of electronic devices, where the film morphology is of increasing importance.

Preliminary Remarks about Ferroelectric Domains

In contrast to an ideal ferroelectric crystal, where a homogeneous polarisation is the state of minimal energy, a real crystal exhibits domains of different polarisation due to existing crystal surfaces and defects. Consequently, the spatial variation of the polarisation is a source of a depolarisation field which is compensated by the formation of a multi-domain state. The domain structure that is formed after the transition from the para- into the ferroelectric phase without outer field, depends on crystal symmetry, sample geometry and spontaneous polarisation. Since the transition region between different domains deviates from the ideal crystal symmetry, domain walls deliver an additional contribution to the energy, which is consisting of three contributions: (i) existing polarisation, (ii) dipole-dipole interaction, which accounts for the change of the dipole momentum along the wall, and (iii) elastic energy, which describes the interaction between polarisation and deformation.

Within the frame of the Landau-theory, the minimisation of the free energy gives a tangent hyperbolic-like dependence of the polarisation $\vec{P} = \vec{P}_S \tanh(x/d)$ of a wall of $2d$ thickness. Typical values for the domain wall thickness are in the range of a few nanometer (e.g. 0.5-2 nm in $BaTiO_3$), depending on elastic constants, the dielectric constant,

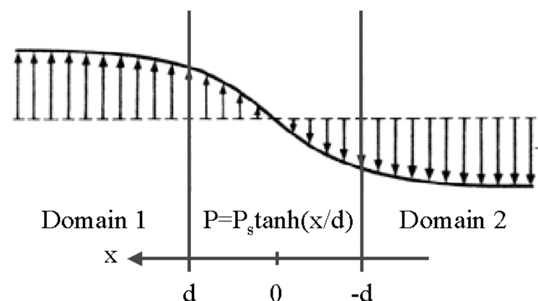

Figure 6.16: At the transition between two ferroelectric domains, the polarisation changes its size in contradiction to magnetic polarisation, where the vector is rotated [Zhi 59].

temperature, polarisation in the domains, and corresponds to the correlation radius in the Landau-theory [Wan 94, Kre 79]. Considering the depolarisation field, the domain size D follows $D \propto \sqrt{d}$, with d as film thickness [Zhi 59].

The existence of domains plays a major role in the formation of a hysteresis in ferroelectrics. As illustrated in Figure 6.17, starting from an initial random multi-domain state, the increase of an electric field results in reversible domain wall displacement and a linear increase of polarisation. On the one hand, pinning of domain walls by crystal defects avoids saturation already at low fields. On the other hand, at sufficient high fields, domains are inverted or can overcome defect potential barriers, resulting in a fast increase of polarisation up to saturation and a slower further increase due to ionic and electronic polarisability. Already before field reversal, the polarisation decreases, due to premature flop-over processes of domains. The interrelation of film morphology (grain size, roughness) and dynamic domain properties (domain wall movement, domain growth, initiation of flop-over processes, pinning) is a fundamental question affecting the hysteresis of ferroelectric thin films.

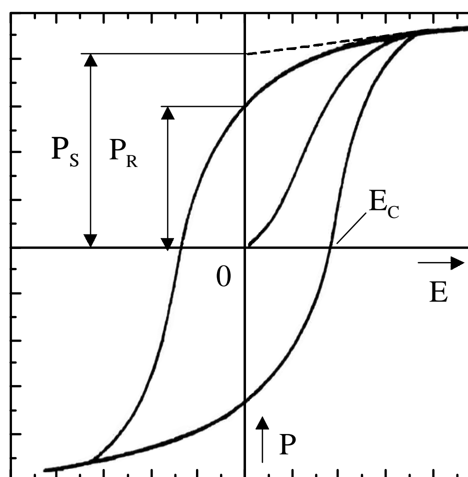

Figure 6.17: Typical $P(E)$-hysteresis of a ferroelectric with saturation polarisation P_S, remanent polarisation P_R and coercitive field E_C.

AFM Measurements in the Piezo-Response Modus

Beside other techniques [Sch 99, Ren 96, Lin 96, Jaf 71, Sta 63], the use of an AFM[95] in the piezo-response modus allows non-destructive imaging of ferroelectric domains in sub-μ scale. Since the imaging by an AFM takes several minutes, processes with time constants below this value can not be observed. In order to uncover ferroelectric domains, an AC-voltage at 10 kHz[96] was applied between the conductive AFM tip and the backside of the sample

[95] A Digital Nanoscope III™ at the Institut für Physikalische Chemie, Prof. Butt and Dr. Raiteri. Detailed information about AFM can be found in [Sch 99, page 79] and elsewhere.

[96] Far below the resonance frequency of the cantilever (ca. 100 kHz).

substrate during imaging in contact modus [Mar 98, Mar 99]. A voltage parallel to polarisation of the ferroelectric is governed by increased film thickness due to the inverse piezoelectric effect and vice versa. This response to the applied field is probed by sub-nm oscillations of the tip, superimposed to the static deflection kept by the AFM feedback loop. Depending on the polarisation direction, the vibrations of the sample are 0° or 180° phase shifted relative to the excitation amplitude. Phase shift and amplitude of the cantilever can be detected by a lock-in amplifier and recorded simultaneously with the sample topography [Sch 99]. The amplitude of the oscillations $\Delta d_z \approx 2 q_{333} \varepsilon_0 \varepsilon P V$ depends on the longitudinal electrostriction coefficient q_{333}, the dielectric constant, the polarisation P, and the applied AC-voltage [Jaf 71, Wei 95]. The amplitude of the AC-voltage was chosen $15\,V_{rms}$, a value that is relatively high, compared to other groups [Gru 99, Hu 99]. However, this is a reasonable value, since for $SrBi_2Ta_2O_9$ films on silicon without underlying metallic electrode, only a fraction of the voltage drops at the film. For a samples with Pt as bottom electrode, a voltage of 1.5 V is sufficient to attain contrast between opposite polarised domains. In all cases the resulting field is well below the coercitive field of 57 kV/cm.

$SrBi_2Ta_2O_9$ Domains on Silicon

In Figure 6.18, the topography (a), amplitude (b) and phase shift (c) of a 300 nm thick $SrBi_2Ta_2O_9$ film, measured in contact mode is shown. This film was deposited at lower O_2 pressure (0.3 mbar) in order to investigate as well the response of the pc-SBT phase, which already was observed in X-ray measurements. In Figure 6.18a, small (50 nm) pc-SBT grains appearing between two $SrBi_2Ta_2O_9$ grains, show no evident piezoelectric response and no fixed phase relation between applied voltage and surface oscillation. In the amplitude image (Figure 6.18b), domain walls (dark regions) can be seen between ferroelectric domains (bright regions). From the phase signal, it is possible to identify ferroelectric domains with opposite dipole orientation of 0° and 180° inside the $SrBi_2Ta_2O_9$ grains. In most cases, domain boundaries coincide with grain boundaries. Cylindrical shaped domains, observed in $BaTiO_3$ [Tsu 97] do not appear. A dependence of the images on the scan direction due to a permanent polarisation of the tip, followed by a cantilever torsion [Lüt 93], is excluded.

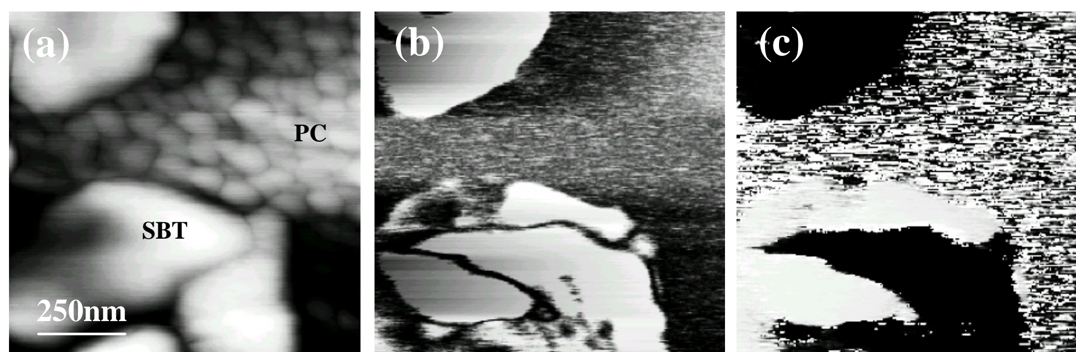

Figure 6.18: **(a)** Topography of SBT(300 nm) grown on silicon. $SrBi_2Ta_2O_9$- and pyrochlore-phase are marked (height range is 50 nm). **(b)** Amplitude signal of the piezoelectric response, to an *AC*-voltage (15 V_{pp}, 10 kHz). White areas correspond to maximal surface oscillation, full scale is 0.05 nm. **(c)** Phase signal of the piezoelectric response. Bright areas correspond to a maximal phase shift of 180°, whereas dark region correspond to 0° phase shift. Within high-noise areas in (b) and (c) no surface oscillation and phase relation is observed, respectively.

Measurements of pc-SBT films deposited on YSZ-buffered silicon, show only a weak (< 4% of the imaged surface) coupling of phase signal and excitation frequency. Since in literature no data about the piezoelectric properties of this phase is available, it can be assumed, that the effect is small or possibly resulting from a small amount of $SrBi_2Ta_2O_9$. Grain boundaries and domain boundaries do not always coincide. Also within single grains several domains can be observed, which has been as well observed by other groups [Lüt 93, Gru 99]. Figure 6.19 shows a grain (a), where the amplitude signal of the surface oscillations (b) in the middle of the grain tends to zero, corresponding to an decrease of the polarisation within the domain wall.

The magnitude of the surface oscillations corresponds to a piezo electric coefficient of $1x10^{-3}$ nm/V, whereas the literature value for single crystals amounts $2.3x10^{-3}$ nm/V [Sho 39]. The different polarisation orientation of the two domains is visible in Figure 6.19c. A line scan of the amplitude signal across the domain wall (Figure 6.19d) is directly proportional to spontaneous polarisation and follows a tanh-function, as previously mentioned. The fitting of this function gives a wall width[97] of $2d = 14.72 \pm 0.27$ nm, comparable to literature values of 10 nm [Hu 99]. Although the transition in the phase signal between 0° and 180° theoretically takes place discontinuously, a transition width of 7 nm is observed, giving an lower limit for resolution of domains

[97] Which is defined as width between positive and negative maximal value of the polarisation.

with this method. From the analysis of different samples, a minimum grain size of 150 nm for the formation of multi-domain states in a single grain can be given. Consequently, the grain size is assumed to exert essential influence on properties, such as coercitive field and dielectric constant and losses [Set 93].

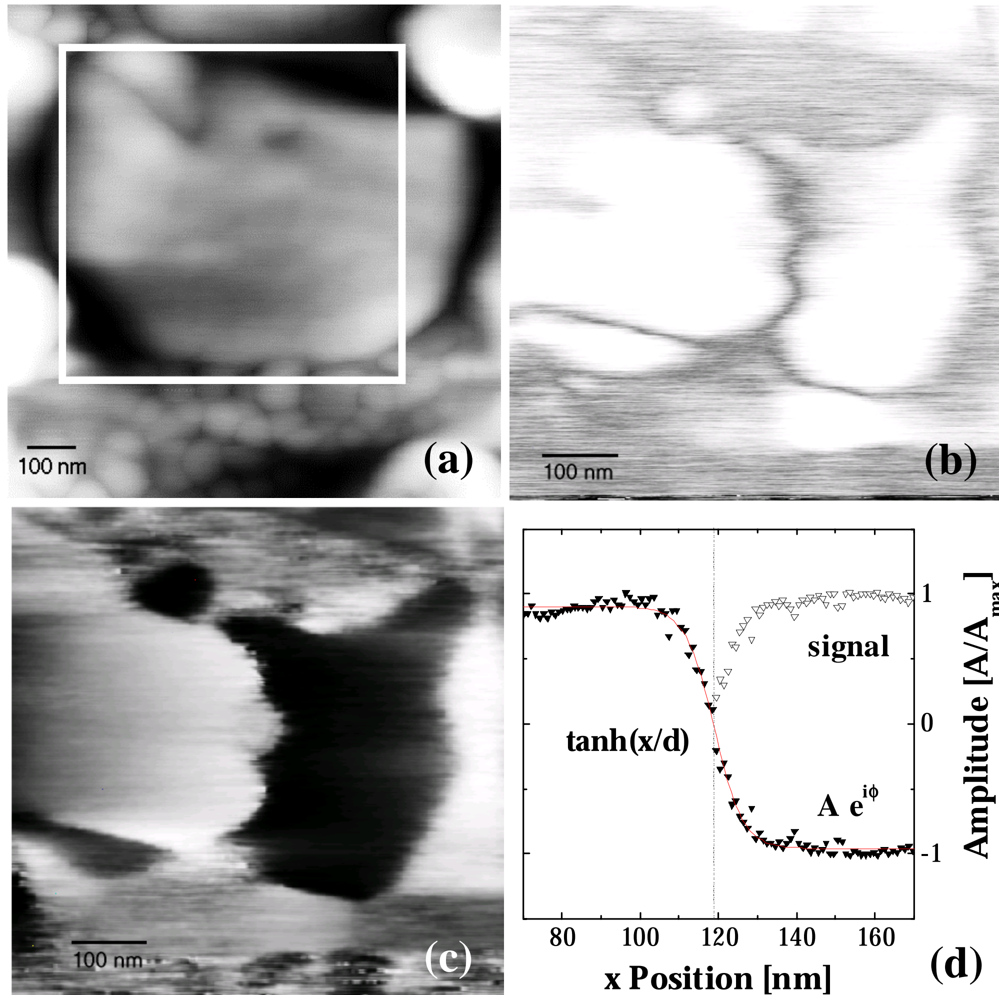

Figure 6.19: (a) 300 nm thick $SrBi_2Ta_2O_9$ film on silicon. Topography of a grain with a diameter of 500 nm (20 nm height range). **(b)** In the amplitude signal, the domain wall is visible due to decreasing polarisation in the domain wall. **(c)** Two regions with different polarisation are observed. **(d)** Fitting a line scan across the domain wall by a tanh-function delivers a transition width of 14.72 ±0.27 nm.

Switching of Domains in $SrBi_2Ta_2O_9$

Ferroelectric domains in $SrBi_2Ta_2O_9$ are switched by moving the conducting cantilever tip to the middle of the scan area and applying a *DC*-voltage of

30 V for about 10 s. Figure 6.20a shows the topography of a $SrBi_2Ta_2O_9$ film deposited on silicon. In the phase signal, shown in Figure 6.20b to d, the initial polarisation (b) is inverted by applying +30 V (c) and restored by applying −30 V (d). Again, grain boundaries and domain boundaries are correlated. Within a period of 3 h, the polarisation of the domains is stable, proofed by repeated AFM scans at the same surface area. Measurements of heterostructures with Pt used as bottom electrode show, that a voltage of ±10 V is sufficient to flip the polarisation, since in the case of Si/buffer/SBT heterostructures only a fraction of the voltage drops at the ferroelectric.

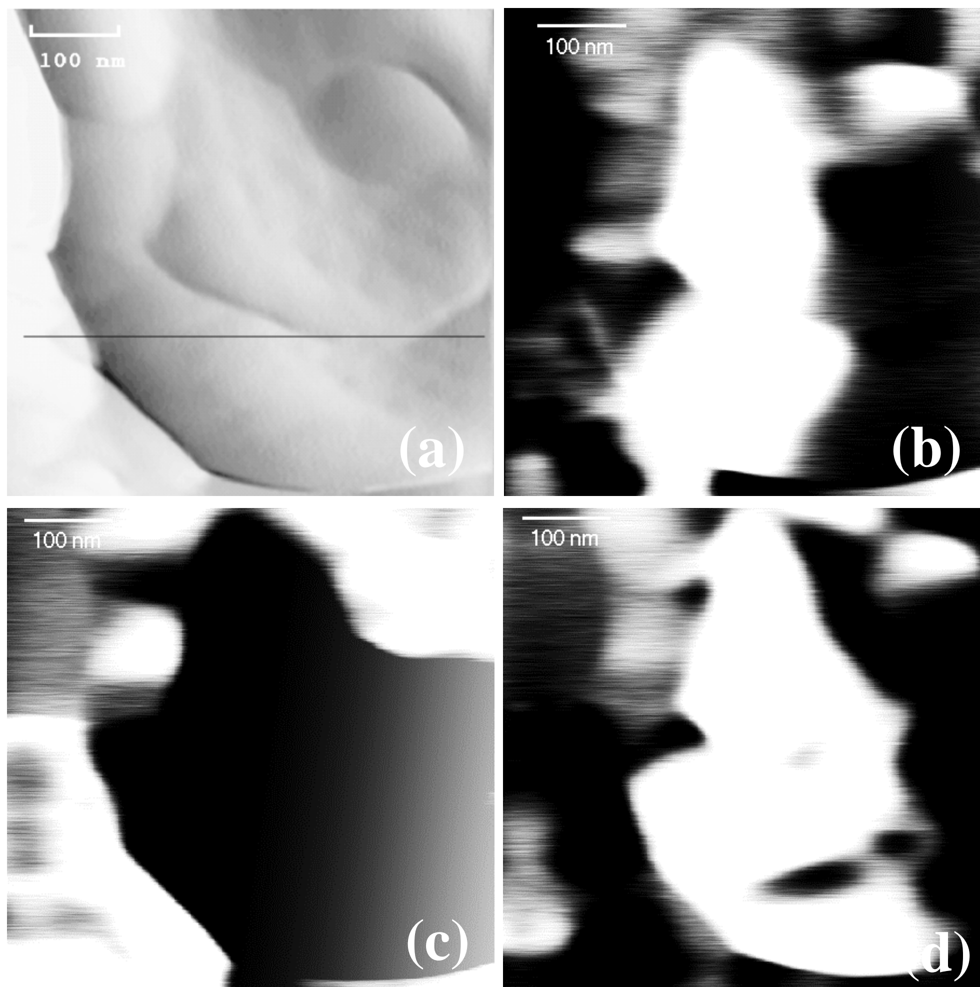

Figure 6.20: Switching of domains in $SrBi_2Ta_2O_9$. **(a)** Topography **(b)** Initial phase signal **(c)** Phase signal after inversion of the polarisation by applying +30 V. **(d)** Restored polarisation by applying -30 V.

Another picture arises, if *c*-axis oriented $SrBi_2Ta_2O_9$ films deposited on a YSZ/CeO_2 buffer layer combination are investigated. Measurements of the surface oscillation (phase signal) exhibit practically no contrast, if only the vertical amplitude of the cantilever is measured. A common AFM mode in order to investigate surfaces more sensitively, is to record the torsion of the cantilever. Here, only at the grain boundaries of *c*-axis oriented $SrBi_2Ta_2O_9$ grains a relevant torsion signal could be detected, whereas the centre of those grains shows an extremely small signal. Being a possible reason, the electrical field between tip and sample is changed in the proximity of a grain boundary, resulting in increased field component parallel to the film surface. Thus the higher piezoelectric constant in the crystallographic *ab*-plane of $SrBi_2Ta_2O_9$ causes an increased amplitude of surface oscillations parallel to the sample surface.

Measurements in the AFM Non-Contact Mode

AFM measurements in the non-contact mode ($r_{tip} \approx 10\text{-}200\,\text{nm}$) are governed by the problem of capillary forces due to a water adsorption layer on the film surface, screening charges and a worse lateral resolution as a matter of principle (50-80 nm, 10 nm at best, [Lüt 93, Auc 98]). In spite of these disadvantages, it is a reasonable method in order to estimate the local polarisation quantitatively. A polarised surface generates surface charges and therefore an electrical field at the sample surface. This leads to induced charges Q_T in the tip and an attractive force between tip and sample. The cantilever is excited by an external *AC*-voltage with a frequency near its resonance. Thereby induced charges $Q_E = -CU_0 \sin(\omega t)$ interact with the static electrical field and generate an additional oscillating electrostatic force $F(\omega) = -E_z Q_E$ between tip and sample[98].

[98] Since the force $F(\omega)$ depends on the magnitude of the polarisation, only domain walls are visible. Due to electrostriction ($\propto E^2$), an additional observed force $F(2\omega) \propto ½\, U_0^2\, dC/dz$, is modulated by 2ω and can be expressed by a distance dependent capacity between tip and sample [Mar 88, Sau 90, Kuc 91]. The dependencies of the oscillation amplitude on the forces are confirmed by our measurements [Schu 99].

Approaching the sample surface, this force will change the oscillation amplitude of the cantilever[99]. In order to receive quantitative information about the remanent polarisation a model of G. Zavala et al. is used, assuming an electrical field E_z of a circular polarised region, in which the polarisation $P = P_0(r\text{-}r_0)/r_0$ decreases linearly from the centre [Zav 97]. The measurement of the oscillation amplitude versus distance and the corresponding data fit is shown in Figure 6.21.

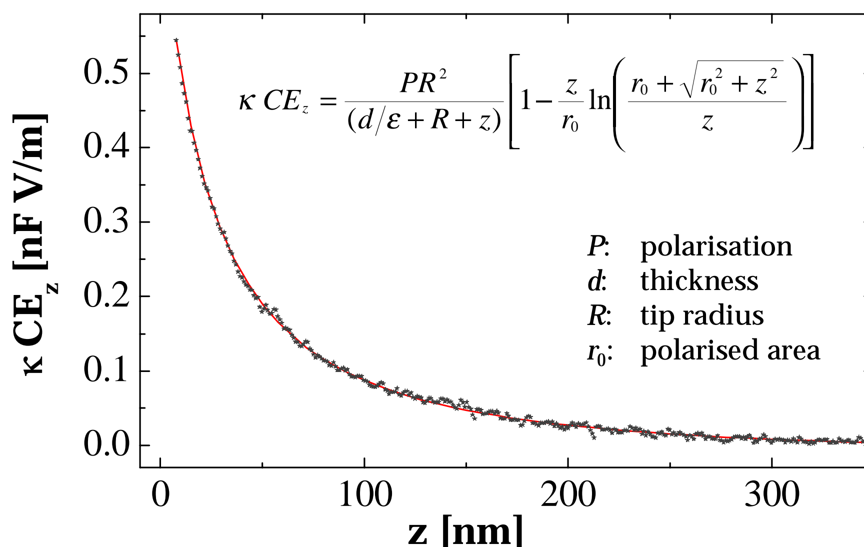

Figure 6.21: The surface oscillation amplitude of a $SrBi_2Ta_2O_9$ film versus distance. The dotted line represents a fit according to the inserted formula. The quantity κCE_z corresponds to ratio of the measured surface oscillation amplitude and the *AC*-amplitude. The force curve was measured 200 seconds after the sample was polarised. The best fit of the data is obtained for $r_0 = (159 \pm 12)$ nm and $P = (3.4 \pm 0.3)\ \mu C/cm^2$.

The tip Radius $R_0 = (40 \pm 3.5)$ nm is estimated from the measurement of $F(2w)$ under assumption of a capacity $C(z) = 2\pi\varepsilon_0 R^2/(R+z+d/\varepsilon)$ between tip (a hemisphere with radius R_0) and surface (a semi-infinite plane) [Lor 70, Schu 99]. The dielectric constant $\varepsilon = 135$ and the film thickness $d = 350$ nm are measured by the previously discussed techniques. The best curve fit is obtained for $r_0 = (159 \pm 12)$ nm and $P = (3.4 \pm 0.3)\ \mu C/cm^2$. This value coincides with literature values of polycrystalline $SrBi_2Ta_2O_9$ films with a typical polarisation of $(8 \pm 2)\ \mu C/cm^2$ [Shi 98, Shi 99], if the time dependent decrease of the

[99] Therefore, the gauge of the spring force constant κ of the cantilever is performed by the use of a reference cantilever, giving a value of 3 ± 0.45 N/m [Cle 93, Sad 95, Schu 99].

oscillation amplitude (i.e. the polarisation) is considered. After applying a voltage in order to polarise the sample, a strong decrease of the polarisation in the first 100 seconds and a saturation to approximately 60% of the initial value is observed in our measurements, leading to an initial value of $P = (5.6 \pm 0.3)\ \mu C/cm^2$. Being a possible reason for this time dependent decrease, the polarisation is compensated by accumulation of charge carriers at the sample surface. A second conceivable reason, an adsorption layer of water, can be excluded, since the force characteristic of the cantilever is not changed in the adhesion (non-contact) range. The comparison between contact- and non-contact mode measurements shows, that regions with high piezoelectric surface oscillations correspond to regions with a 20 times higher polarisation than those with no surface oscillation.

6.5 $SrZrO_3$ as an Alternative Buffer Layer for $SrBi_2Ta_2O_9$

As discussed in detail in the previous chapters, the use of an YSZ/CeO_2 buffer layer combination allows the growth of highly *c*-axis oriented $SrBi_2Ta_2O_9$ thin films on silicon substrates. Although a big memory window of 0.87 V is already achieved by this approach, the *c*-axis orientation has a fundamental drawback. However, as the spontaneous polarisation resides along the *ab*-plane (see Figure 6.4), growth of $SrBi_2Ta_2O_9$ films in this crystal direction is essential for practical devices. Furthermore, increased information density of such devices by minimising structure sizes (thickness and area) has a significant impact on the ferroelectric properties. The minimisation of thickness incorporates a decrease of permittivity ε_r and an increase of leakage current, a fact, which is believed to be improved if *a*-axis orientation of the $SrBi_2Ta_2O_9$ layer is achieved. Moreover, attaining high remanent polarisation P_r and low coercitive fields E_c is important, if the device area is decreased and low switching voltages are required. Thus, by the enforcement to grow $SrBi_2Ta_2O_9$ with its easy polarisation axis parallel to the substrate (device) normal, it is possible to take full advantage of the material properties.

In chemical techniques, off stoichiometric Sr-deficient $SrBi_2Ta_2O_9$ films [Nog 96], texture control by buffer layers [Che 95], postgrowth crystallisation at low oxygen partial pressures [Ito 96], and rapid thermal annealing [Hay 97] are the important process variables employed in order to achieve *a*-axis oriented $SrBi_2Ta_2O_9$ films. In vapor phase techniques, pulsed laser deposition, being the most successful technique for $SrBi_2Ta_2O_9$ film growth, variations in the Sr/Bi ratio [Tho 96], oxygen pressure [Ois 97], substrate temperature [Nag 96], and plasma assisted PLD [Ras 99] have been attempted without success.

Up to now, no successful attempt to growth $SrBi_2Ta_2O_9$ ferroelectric thin films with its *ab*-plane perpendicular to the substrate surface of silicon has been reported. Thus, we investigate the possibility to use $SrZrO_3$ as a new buffer layer in the layer sequence Si/YSZ/SZO/SBT. To the authors knowledge, up to now no report on the deposition of $SrZrO_3$ thin films on silicon is published. The use of $SrZrO_3$ is motivated by the fact, that both $SrBi_2Ta_2O_9$ and $SrZrO_3$ present an orthorhombic structure (see chapter 4.1 for $SrZrO_3$ and chapter 6.2.1 for $SrBi_2Ta_2O_9$) and that $SrZrO_3$ contains common chemical elements as both YSZ and $SrBi_2Ta_2O_9$. Moreover, a small lattice mismatch of -5.5% for SBT[010] along SZO[110] and 1.76% for SBT[001] along SZO[003] should preferentially favour *a*-axis growth of the $SrBi_2Ta_2O_9$ layer if this growth direction is also achieved for the $SrZrO_3$ layer.

6.5.1 Structural Characterisation

Growth of $SrZrO_3$ on $SrTiO_3$

Being a first step in order to prove the parameters for deposition with correct stoichiometry, $SrZrO_3$ has been deposited on single crystalline $SrTiO_3$ substrates, which show no chemical reaction with $SrZrO_3$ up to temperatures of 1000 °C [Lan 98]. Furthermore, by this approach it has been clarified, that up to deposition temperatures of 850 °C no structural phase transition occurs, which is observed in $SrZrO_3$ single crystals. Highly *c*-axis oriented $SrZrO_3$ films have been obtained presenting rocking curves with FWHM below 0.1° at deposition temperatures between 500 °C and 850 °C and low oxygen pressures between $1x10^{-6}$ and $2x10^{-5}$ mbar. The small lattice mismatch of 3.5%

(Table 4.1) between the STO[100] and SZO[010] in-plane lattice constants is held to be responsible for this high crystalline quality. Thus, an in-plane rotation of the $SrZrO_3$ layer by 45° on the substrate is expected, but not yet proved by means of four-circle X-ray diffraction measurements, since this was not within the scope of this thesis.

Growth of $SrZrO_3$ on Silicon

The direct deposition of $SrZrO_3$ on silicon leads to a complete polycrystalline growth, although the lattice mismatch between both materials is only 5.2% for cube-to-cube growth (Table 4.1). This behaviour is assumed to be originating from the amorphous SiO_2 layer, which is not reduced by $SrZrO_3$. Thus, the already successful proven two step deposition technique of a YSZ layer (see chapter 4.3.1) is applied again in order to give an epitaxial growth base for the $SrZrO_3$ layer. At sufficient laser energy densities ($J \approx 3\,Jcm^{-2}$) and a thickness of 40 nm[100], the FWHM of the rocking curve of the YSZ(002)-reflection in Figure 6.22 lies between 0.95° and 1.1°.

Without a significant change of the film quality, the $SrZrO_3$ layer can be deposited at laser energy densities between 1.5 J/cm^2 and 2.5 J/cm^2, temperatures between 750°C and 800°C and an oxygen pressure of $5x10^{-4}$ mbar. The $SrZrO_3$ films were deposited with a typical thickness of 105 nm. These parameters led to highly *a*-axis oriented $SrZrO_3$ films, proven by XRD patterns in Bragg-Brentano geometry, as illustrated in Figure 6.22. Beside the (00*l*)-reflections of silicon and YSZ, strong SZO(200)- and SZO(400)-reflections are observed. Rocking curves show typically a FWHM between 1.3° and 1.6°. Moreover, a surface roughness of approximately 0.21 nm (rms) was determined by means of AFM measurements. The epitaxial growth of *a*-axis $SrZrO_3$ on *c*-axis oriented YSZ is a striking result, since this growth behaviour requires two strongly different in-plane lattice constants of $SrZrO_3$ matching the cubic template YSZ. Therefore, it is clearly shown, that $SrZrO_3$ can be employed as a buffer layer on YSZ-buffered silicon for the subsequent deposition of further layers. Moreover, in contrast to mostly cubic materials used in this

[100] Two step deposition: 1.6 nm (50 pulses) at $2x10^{-6}$ mbar, and 30.9 nm (950 pulses) at $5x10^{-4}$ mbar. Thinner films (1.6+15 nm) yield an increased FWHM of typically 1.4°.

field, $SrZrO_3$ makes an rectangular (orthorhombic) template available on top of silicon.

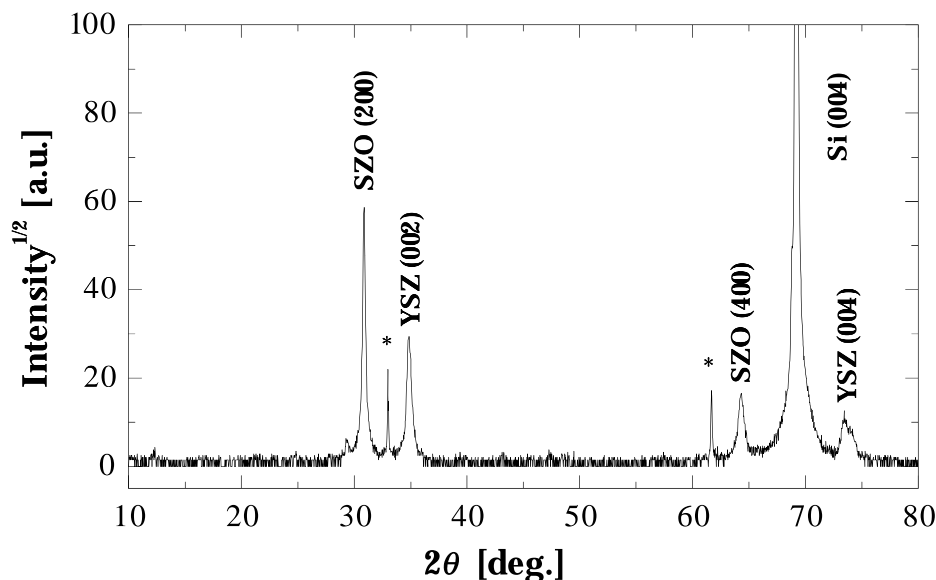

Figure 6.22: Typical $\theta/2\theta$-scan of a $SrZrO_3$ film deposited on YSZ-buffered silicon. The presence of the SZO(200)- and SZO(400)-reflection clearly shows the *a*-axis orientation of the film. The SZO (200)-reflection exhibits a FWHM of 1.55°, whereas the YSZ (002)-peak shows a typical FWHM of 1.1°. The thickness of 32.5 nm (1.6+30.9 nm) for the YSZ layer and 105 nm for the $SrZrO_3$ layer was exactly estimated by means of LXRD measurements. PLD deposition parameters for $SrZrO_3$: $T = 750$ °C, $p = 5 \times 10^{-4}$ mbar, $J \approx 2.2$ J/cm^2, $f = 3$ Hz, $d = 40$ mm, spot size ≈ 2x2 mm. Parasitic X-ray peaks are indicated by (*).

Growth of $SrBi_2Ta_2O_9$ on YSZ/$SrZrO_3$ Buffered Silicon

For the top $SrBi_2Ta_2O_9$ layer, various deposition parameters have been investigated. These parameters proved to be decisive for the crystalline growth as observed in X-ray diffraction and microscopy (SEM, AFM). The typical laser energy densities for $SrBi_2Ta_2O_9$ deposition were about 1.5 to 2.5 Jcm^{-2} without significant influence on the film properties. The typical thickness of the $SrBi_2Ta_2O_9$ layers were around 150 nm. After deposition at temperatures between 750 °C and 850 °C, the trilayers were cooled down to approximately 250 °C within 30 minutes at the $SrBi_2Ta_2O_9$ deposition pressure, in order to ensure that no oxygen loss from the layers occurs. After this procedure, the chamber was vented to atmospheric pressure and cooled down to room temperature.

In Figure 6.23a, three X-ray diffraction patterns in Bragg-Brentano geometry are shown. The oxygen pressure has been varied between 0.2 mbar and 0.8 mbar. Below a pressure of $p \approx 0.5$ mbar, the SBT(200)-reflection starts to appear at $2\theta \approx 32°$. At a pressure of $p = 0.2$ mbar, best values for the rocking curve of the SBT(200)-reflection are obtained between 1.8 and 2.1° FWHM. No evidence for other phases was detected, especially the possible confusion with reflections of concurrence phases was checked, such as pc-SBT(400) at $2\theta \approx 34.1°$ [Rod 96], SZO(200) at $2\theta \approx 30.9°$, or the β-Bi_2O_3 phase at $2\theta \approx 32.3°$ [Cho 98, Let 98].

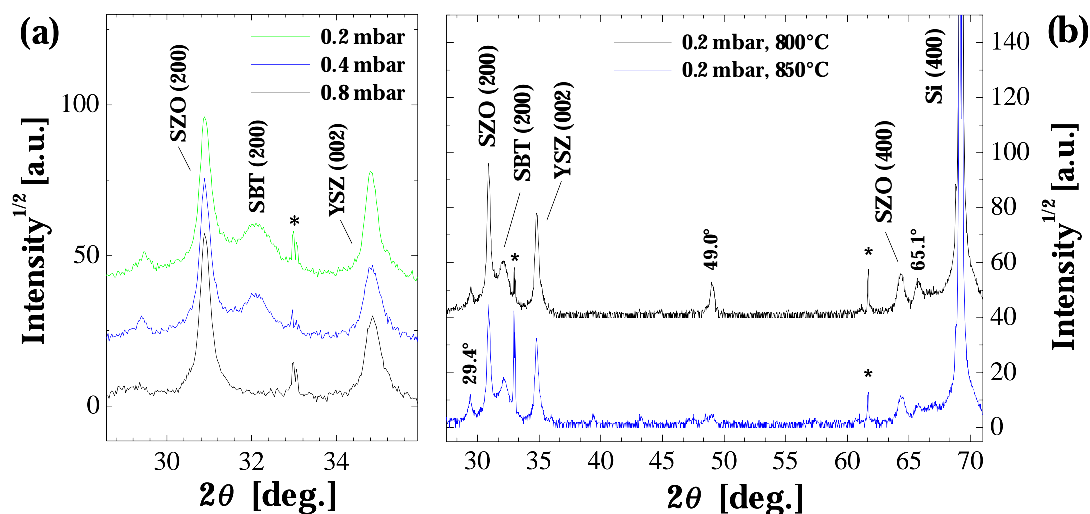

Figure 6.23: (a) X-Ray diffraction patterns ($\theta/2\theta$-scans) of a 150 nm thick[101] $SrBi_2Ta_2O_9$ film deposited on YSZ(40 nm)/SZO(105 nm)/Si at different pressures. At pressures below $p \approx 0.5$ mbar, the SBT(200)-reflection emerges with a typical FWHM of 1.8-2.1°. **(b)** $\theta/2\theta$-scans of YSZ/SZO/SBT heterostructures on silicon at an optimum oxygen pressure of $p = 0.2$ mbar, but at different deposition temperatures. At $T = 850$°C, the (044)-peak of an out-of plane oriented pyrochlore phase at $2\theta = 49°$ and the SBT(116)-peak at $2\theta = 65.1°$ are suppressed. The peak at $2\theta = 29.4°$ is related to a Y_2O_3 impurity phase of the YSZ target. Parasitic peaks due to X-ray tube impurities are indicated by (*).

In Figure 6.23b, the influence of the deposition temperature is shown in two $\theta/2\theta$-scans, which contain all relevant reflections. Beside the SBT(200)-reflection and strong YSZ(002)- and SZO(200)-peaks, two additional peaks at

[101] Because of the large surface roughness and an over-all thickness of the heterostructure in the range of 300 nm, LXRD is not applicable. For that reason, the thickness was estimated from average ablation rates of polycrystalline SBT films on silicon.

$2\theta = 65.1°$ and $2\theta = 49°$ are visible. At elevated temperatures of 850°C, these peaks are suppressed. First, the reflection at $2\theta = 65.1°$ is frequently observed with a FWHM of rocking curves ranging from 1.8 to 2.3° when $SrBi_2Ta_2O_9$ is deposited. Substantiated by powder diffraction simulations, this peak corresponds to the (2 2 12)-reflection, which indicates a SBT(116)-growth orientation[102]. It is correlated to the formation of the SBT(200)-orientation in the sense, that its intensity decreases with increasing intensity of the SBT(200)-reflection. Thus, this fact is considered to be a competition between both growth orientations. Secondly, the peak at $2\theta = 49°$ is exclusively observed with increasing intensity of the SBT(200)-orientation and arises only at low pressure conditions ($p < 0.5$ mbar) with a typical FWHM between 1.8 and 1.95°. From powder diffraction simulations [Mar 01a], this peak is proven to be related to the (044)-reflection of 45° out-of-plane oriented cubic pyrochlore (pc-) phase ($a = 1.051$ nm, Fd3m), which can be represented by the chemical composition formula $Sr_{0.2}(Sr_{0.5}, Bi_{0.7})Ta_2O_{6.75}$ [Rod 96]. The occurrence of this phase is related to increased Bismuth loss at decreased oxygen deposition pressure. This behaviour coincides with observations made in chapter 6.2.2 for $SrBi_2Ta_2O_9$ deposited directly on silicon. Moreover, a small peak arising at $2\theta = 29.4°$ might be related to the strongest polycrystalline (222)-reflection of a randomly oriented pyrochlore phase. Since it is also observed at depositions of single YSZ layers, it is assumed to be exclusively originating from impurity phases of this compound. Powder diffraction simulations show, that at $2\theta = 29.4°$ the strongest polycrystalline reflection of the Y_2O_3 phase is found, possibly resulting from incorrect stoichiometry of the YSZ target.

By means of AFM measurements, the surface morphology of $SrBi_2Ta_2O_9$ films has been investigated. In Figure 6.24, the influence of oxygen pressure on the surface morphology is shown. Films deposited at low deposition pressures ($p = 0.4$ mbar) show a more pronounced in plane orientation and rectangular shape of the grains than those deposited at higher oxygen pressures ($p = 0.8$ mbar). Moreover, the surface roughness increases with decreasing oxygen pressure from 3.7 nm to 7.0 nm (rms), a value that is much higher than

[102] The (116)-reflection is forbidden by symmetry because of A-face centring: (*hkl*) only with k+1 even.

for polycrystalline or *c*-axis oriented $SrBi_2Ta_2O_9$ films [Sch 99]. The lateral grain dimensions for both films are estimated to (50 ± 20) nm x (150 ± 30) nm. Thus, three dimensional island growth is assumed to take place, since the lateral island size is in the range of the film thickness.

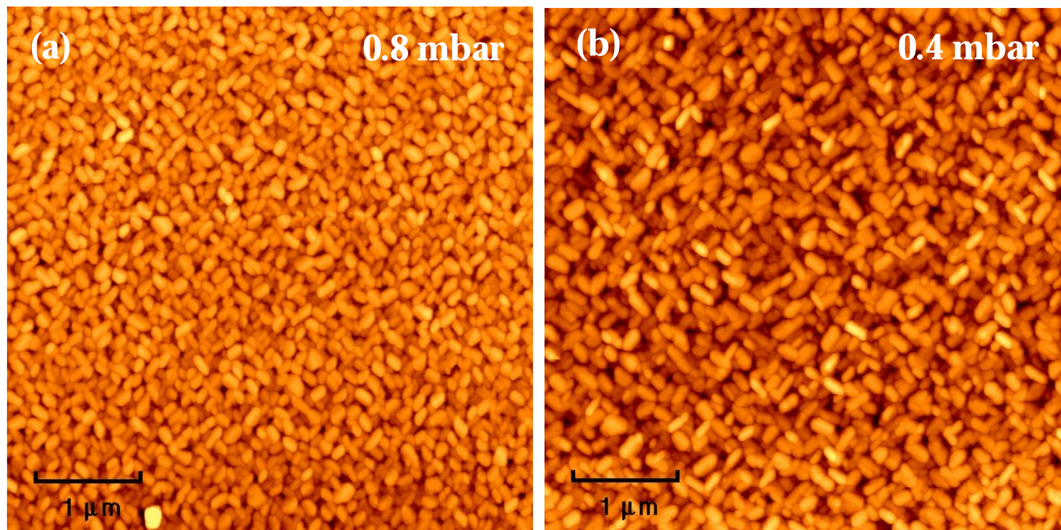

Figure 6.24: AFM measurements of $SrBi_2Ta_2O_9$ films deposited on YSZ/SZO-buffered silicon. **(a)** At high deposition pressures ($p = 0.8$ mbar), smooth surfaces exhibit a weakly pronounced in-plane alignment and rectangular shape. The colour scale corresponds to 30 nm. The roughness amounts 3.7 nm rms. **(b)** At lower deposition pressures ($p = 0.4$ mbar) a rougher surface with pronounced rectangular grains and in-plane alignment indicates *a*-axis growth of the $SrBi_2Ta_2O_9$ layer. The colour scale corresponds to a height of 57 nm. The roughness amounts 7.0 nm rms.

As illustrated in Figure 6.25, a magnified AFM image of a $SrBi_2Ta_2O_9$ film deposited at low oxygen pressures ($p = 0.4$ mbar) indicates *a*-axis growth of the $SrBi_2Ta_2O_9$ layer already by an obvious rectangular shape of grains. This grain morphology is in agreement with observations reported in literature [Pig 99, Lee 00]. Although appropriate graphical analysis tools are missing in order to quantify the grain size, orientation angle and degree of in-plane orientation, the presented AFM measurement allows some qualitative considerations. A significant proportion of grains is preferentially aligned along four axes, whereas pairs of perpendicular axes are rotated by an angle of approximately 19.5° against each other. Thus, the observed surface morphology indicates a well defined epitaxy relation to the $SrZrO_3$ template by twinned

growth of crystallites and motivates a detailed XRD analysis in order to find an appropriate growth model.

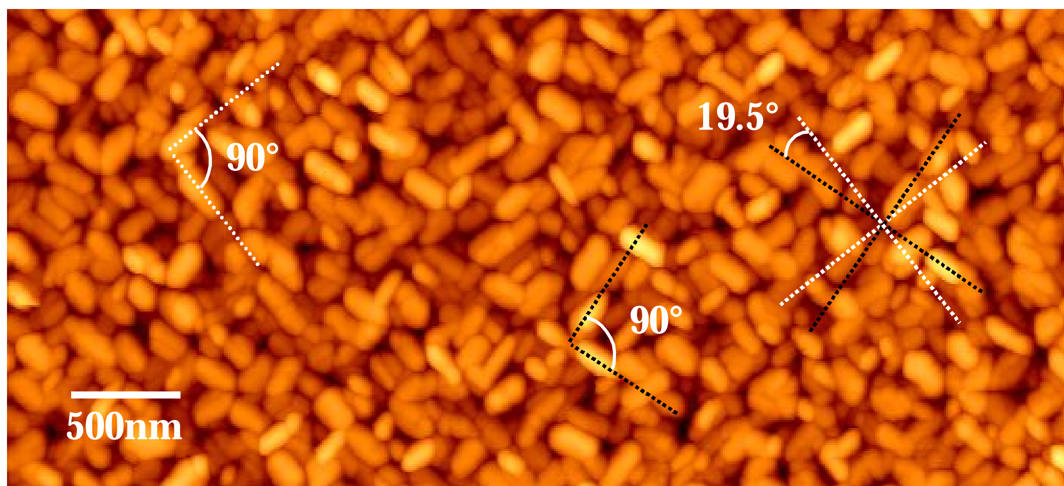

Figure 6.25: AFM measurement of a $SrBi_2Ta_2O_9$ film deposited on YSZ/SZO-buffered silicon at a deposition pressure of $p = 0.4$ mbar. Grains with a pronounced rectangular shape are aligned along four axes, which enclose an angle of 19.5° and 90°. The colour scale corresponds to 57 nm.

Epitaxial Relations within the Si/YSZ/SZO/SBT Heterostructure

In order to obtain more detailed information on the epitaxial relation between $SrBi_2Ta_2O_9$, $SrZrO_3$ and YSZ, four-circle XRD measurements have been performed. In Figure 6.26b and c, the expected cube-to-cube orientation of YSZ on (001)-oriented silicon is proven by ϕ-scans of the Si{111}- and the YSZ{111}-reflections. However, the ϕ-scan of the SZO{112} set of equivalent reflections in the upper graph shows no trivial epitaxial relation. A central peak at the same position as the YSZ(111)-reflection is observed in conjunction with two neighbouring reflections with a distance of $\Delta\phi \approx 18.5°$. This triple of peaks is observed with a ϕ-periodicity of 90°. From simple symmetry considerations, groups of two or four reflections corresponding to the (112), $(1\underline{1}2)$, $(11\underline{2})$, $(1\underline{12})$-reflections of $SrZrO_3$ would have been expected. The existence of three peaks indicates additional domain orientations caused by twinning. Moreover, from the ϕ-scan of the YSZ(111)-reflection in Figure 6.26b, it is obvious that the central SZO(112)-peak corresponds exactly to the ϕ-angle of the (111)-reflection of YSZ. Thus, the (112)-reflection of the $SrZrO_3$ layer is aligned along this twin-plane.

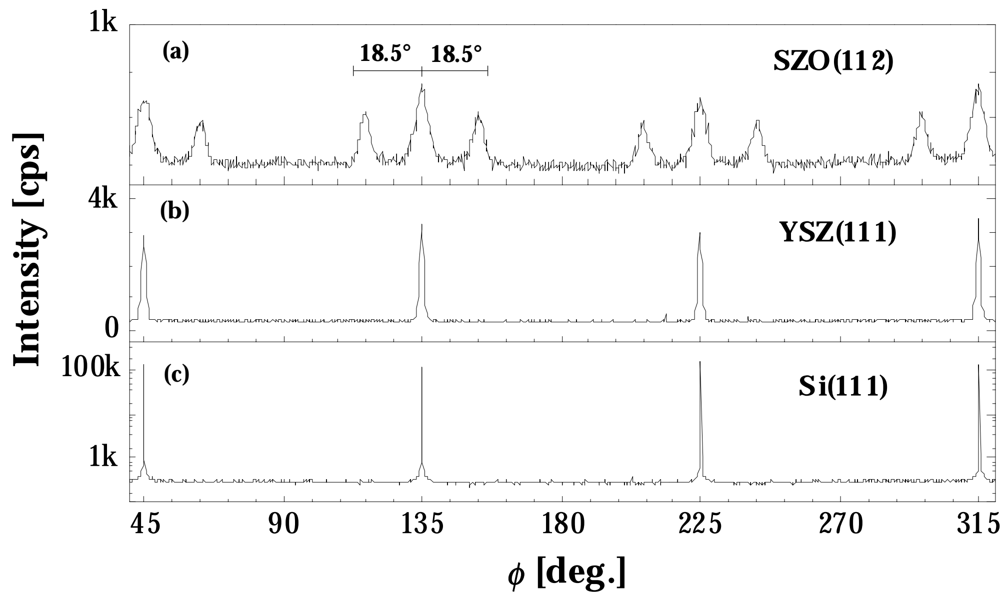

Figure 6.26: Four-circle XRD measurement (ϕ-scan) of a Si/YSZ(40 nm)/SZO(105 nm) heterostructure. As expected, the YSZ layer exhibits a clear cube-to-cube orientation on silicon. The upper graph shows a ϕ-scan of the {112}-reflections of $SrZrO_3$. The central peak is suited at the same ϕ angle as the {111}-reflections of the YSZ layer. Additionally, two neighbouring peaks with lower intensity are observed with an angle distance in ϕ of 18.5°.

In Figure 6.27, a possible growth model for *a*-axis oriented $SrZrO_3$ is shown, explaining the observed reflections in the ϕ-scan of Figure 6.26a. For clarity, the $SrZrO_3$ layer is represented by its unit cell and Zr atoms (red). The YSZ template is illustrated by a cubic lattice with a lattice constant of 5.14 nm. According to this model, the $SrZrO_3$ film will present four domains, wherein the (012) and $(01\underline{2})$ crystallographic twin-planes are aligned along the (011) and $(01\underline{1})$ planes of YSZ. Thus, the elevated intensity of the central $SrZrO_3$ peak is due to the superimposition of corresponding reflections of two different domains. Within the limit of error, the distance of $\Delta\phi \approx 18.5°$ between neighbouring peaks in Figure 6.26 can also be explained by those geometrical considerations, here leading to an angle of $\Delta\phi \approx 19.5°$. Moreover, these results are similar to what has been recently obtained for $SrRuO_3$ layers deposited on YSZ [Lee 00].

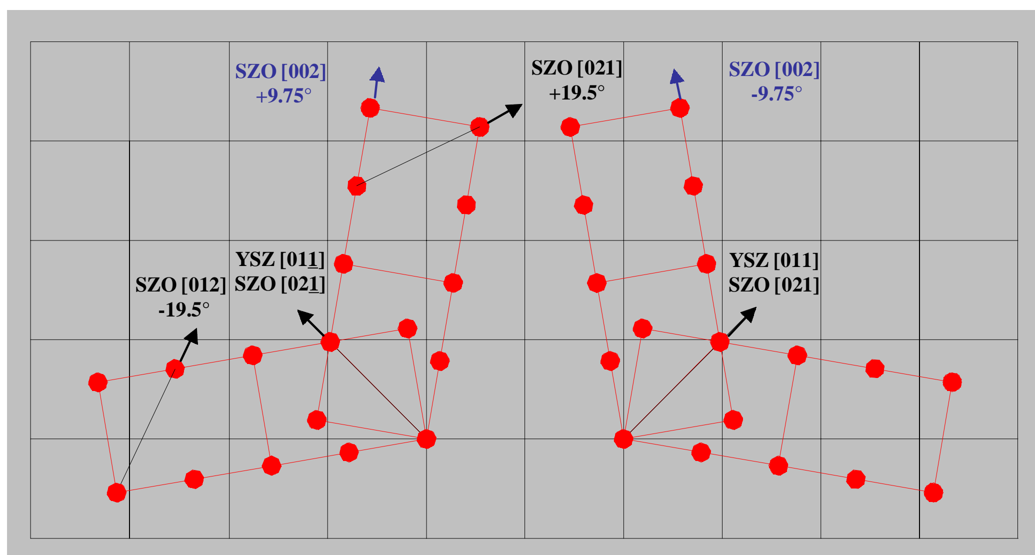

Figure 6.27: Illustration of the growth model for *a*-axis oriented $SrZrO_3$ on top of a cubic YSZ lattice with a lattice constant of $a = 5.14$ nm. To simplify, the $SrZrO_3$ layer is represented by the unit cell and Zr atoms (red). The projection of the SZO(112)-reflection into the *bc*-plane corresponds to the [021] lattice direction within the unit cell. This twinning plane is aligned parallel to the [011] and [01$\bar{1}$] directions of YSZ [Wie 01].

For further clarification, plane scans[103] through the SZO(112)- and SBT(135)-reflections have been performed. Coinciding with the results of the ϕ-scan presented in Figure 6.26a, a 90° periodic triple of SZO{112}-peaks is observed at a radius[104] of $R_{SZO(112)} = 1.68$ in Figure 6.28a. The enclosed angle of $\Delta\phi = 19 \pm 1°$ matches the predicted value of the model. At $R_{SZO(110)} = 0.95$, the SZO{110} set of equivalent reflections emerges. From the growth model it is clear, that a lattice plane aligned parallel to one of the main unit cell axis will result in a pair of peaks oriented along the YSZ{011} directions. The observed angle of 9.3 ± 0.5 matches the theoretically expected value of 9.75°. The occurrence of a pair of peaks at a radius of $R = 0.73$ with an alignment corresponding to that of the SZO{110} reflections could not be clarified.

[103] Plane scans are four circle X-ray measurements of intensities in a certain plane in reciprocal space. Moreover, both measurements have been optimised for the particular reflections. Thus, the estimated angle approximately matches the real value. However, angles between additionally observed reflections can be alternated.

[104] Which can be calculated in *hk*-units of the YSZ template, by $R = [(kb^*)^2+(lc^*)^2]^{1/2}$.

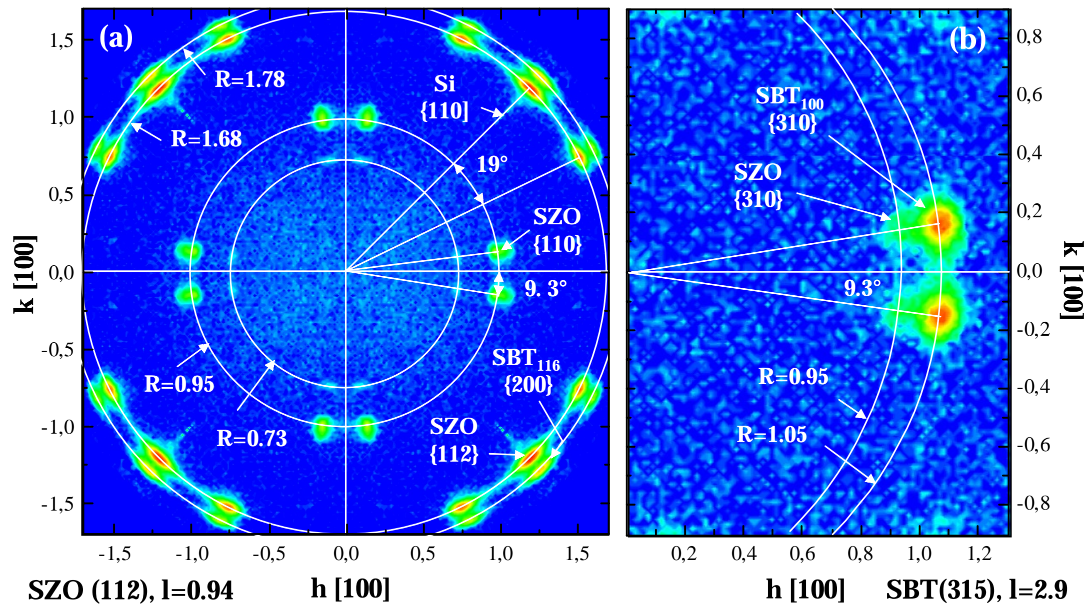

Figure 6.28: Plane scans through the SZO(112)-and SBT(315)-reflections of a 150 nm thick $SrBi_2Ta_2O_9$ film deposited on YSZ(40 nm)/SZO(105 nm)-buffered silicon. The units of the *h*- and *k*-axes correspond to the matrix of the silicon substrate. **(a)** A triple of peaks at the SZO{112} set of equivalent reflections indicates the multi-domain epitaxial growth of the $SrZrO_3$ layer. At a radius of $R = 1.78$, a triple of peaks corresponding to the $SBT_{116}\{200\}$ reflections is observed from (116)-oriented SBT. At *hk*-values slightly smaller than 1, the SZO{110} reflections emerge. **(b)** At a radius of $R = 1.05$, a pair of peaks with an enclosed angle of 9.3° is observed, which could be related to the (310)-reflection of (100)-oriented $SrBi_2Ta_2O_9$. At a slightly smaller radius, weakly intense SZO{310}-reflections appear.

Moreover, concerning the growth of the possible $SrBi_2Ta_2O_9$ orientations, in Figure 6.28a, a further triple of peaks is observed at radius of $R_{SBT(100)} = 1.78$, which is originating by the {200}-reflections of (116)-oriented $SrBi_2Ta_2O_9$ [Wie 01]. In Figure 6.28b, a plane scan through the calculated position $SBT_{100}(315)$-reflection is illustrated. Interestingly, the SBT(315)-reflections are not observed, but a pair of intense peaks emerges with the same enclosed angle as the SZO{110} reflection in Figure 6.28a. From the growth model, such a pair of peaks can only be related to a main axis of the $SrZrO_3$ or $SrBi_2Ta_2O_9$ layer. Since a residual intensity $R = 0.95$ corresponds to the (310)-reflection of the $SrZrO_3$ layer (compare Figure 6.28a), the intense peaks at $R = 1.05$ are assumed to originate from the $SrBi_2Ta_2O_9$ layer, although the corresponding $SBT_{100}(310)$-reflection theoretically should be situated at $R = 0.98$. Thus, from these measurements the multi-domain growth of (116)-oriented $SrBi_2Ta_2O_9$

and $SrZrO_3$ is clearly seen, whereas such a growth behaviour could not be completely verified for the SBT(100)-orientation.

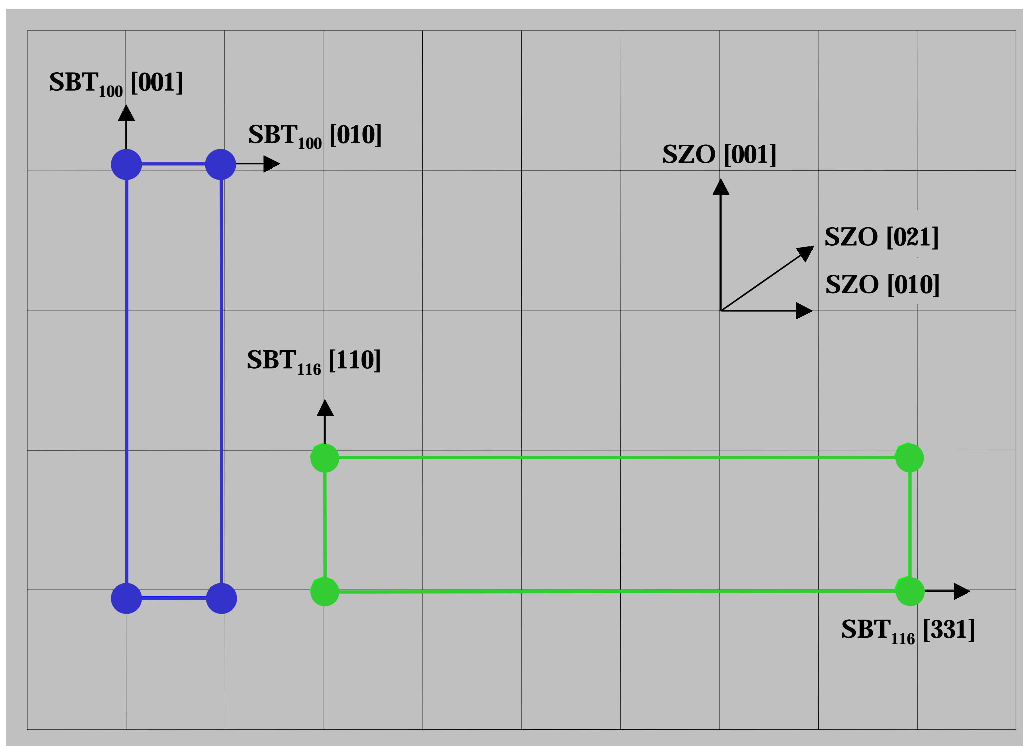

Figure 6.29: Illustration of a growth model of (100)- and (116)-oriented $SrBi_2Ta_2O_9$ on top of a single $SrZrO_3$ domain with lattice constants of $b = 5.813$ nm and $c = 8.196$ nm and the (100)-orientation aligned parallel to the substrate normal. To simplify, the $SrBi_2Ta_2O_9$ layer is represented by the projection of the unit cell and Sr atoms with blue colour for (100)-orientation and green colour for (116)-orientation.

Considering the observed results, the epitaxial relation between *a*-axis oriented $SrBi_2Ta_2O_9$ and $SrZrO_3$ layer is expected to be $SBT_{100}[010] \parallel SZO[010]$ and $SBT_{100}[001] \parallel SZO[003]$, as illustrated in Figure 6.29. Assuming this in-plane orientation, small lattice mismatches of -5.1% and 1.76% are obtained, respectively (see Table 4.1). Moreover, the SBT[061] lattice row shows a lattice mismatch of -2.6% along the SZO[021]- and the YSZ[220]-lattice vector, the direction of best matching between $SrZrO_3$ and YSZ. On the other hand, considering the observed SBT(116) growth orientation, the epitaxial relations are not obvious. As shown in Figure 6.29, the projection of this growth orientation into the (*bc*)-plane of $SrZrO_3$ results in an orthorhombic lattice with lattice constants 0.7824 nm for SBT[110] and 3.428 nm for SBT[331], respectively. Thus, as found by Wiehl et. al [Wie 01], the expected epitaxial relation is

assumed to be $SBT_{116}[110] \parallel SZO[001]$ and $SBT_{116}[331] \parallel SZO[060]$ with corresponding lattice mismatches of -1.75% and -4.6%, respectively.

In conclusion, from the presented growth model, the existence of four $SrZrO_3$ domains is substantiated. Simple geometric considerations can explain the occurrence of a triple of SZO{112} reflections situated at the same ϕ-angle as the YSZ{111}-reflection. The calculated distance between neighbouring peaks of $\Delta\phi = 19.5°$ was proven by means of plane scans through the SZO(112)-reflection, in which an angle of $\Delta\phi = (19 \pm 1)°$ was obtained, whereas the measured angle in ϕ-scans turned out to be reduced to $\Delta\phi = (18.5 \pm 1)°$. These deviations may have several reasons. Generally, the broadening of reflections in the range of 3°-5° corresponds to a large distribution of domain orientations. The maximum of this distribution however, should be situated at the theoretical value. On the other hand, the model assumes an orientation of the domains due to an in-plane match of the SZO(012) and the YSZ(011) orientation. From a closer look to Figure 6.27, it is clear that only a small fraction of Zr atoms virtually fit to the underlying YSZ template. Therefore, the $SrZrO_3$ unit cell might position at a different angle or it will grow slightly distorted in order to minimise the average lattice mismatch.

Because of the existence of four domains, a refinement of the $SrZrO_3$ orientation matrix on top of YSZ is extremely difficult to be done. However, the observed lattice constants coincide with theoretical values within the limits of error. Being an object of further investigations, the $SrZrO_3$ lattice constants have to be exactly determined in order to refine the presented growth model and to exclude a misalignment of $SrZrO_3$ domains due to a distorted $SrZrO_3$ unit cell. Furthermore, by refinement of four-circle XRD measurements, the YSZ lattice has been found to be slightly distorted to lattice constants $a = b = 0.513$ nm and $c = 0.5147$ nm, a fact that is not considered in our growth model. However, since such deviations are also observed in the refinement of the silicon matrix, this effect is believed to be resulting from a measurement error due to the planar geometry of the sample.

With respect to the growth of the SBT(100)- and SBT(116)-orientation, no clear picture is obtained from XRD measurement solely. However, the combination of the presented growth model in Figure 6.29, AFM measurements in Figure 6.25, and the observed reflections in XRD measurement strongly

indicate a four domain growth of both $SrBi_2Ta_2O_9$ orientations on top of $SrZrO_3$. Further investigations are necessary in order to identify the particular X-ray reflections and to determine the exact ratio between the SBT(100)- and SBT(116)-orientation.

6.5.2 Dielectric Properties

Dielectric Properties of the YSZ/SZO Bi-layer

In Figure 6.30, *C(V)*-characteristics of a single YSZ layer and a $SrZrO_3$/YSZ bi-layer are shown in order to extract the dielectric constant of $SrZrO_3$ within a bi-layered heterostructure (i.e. an in-series connection of capacitors). By means of LXRD measurements, the thickness of the YSZ layer was exactly determined to 32.95 nm in both samples. Since the deposition was performed at identical parameters, a similar first layer thickness of 1.65 nm is assumed to result in equal dielectric constants of $\varepsilon_{YSZ} = (4.7 \pm 0.3)$ for the YSZ layer.

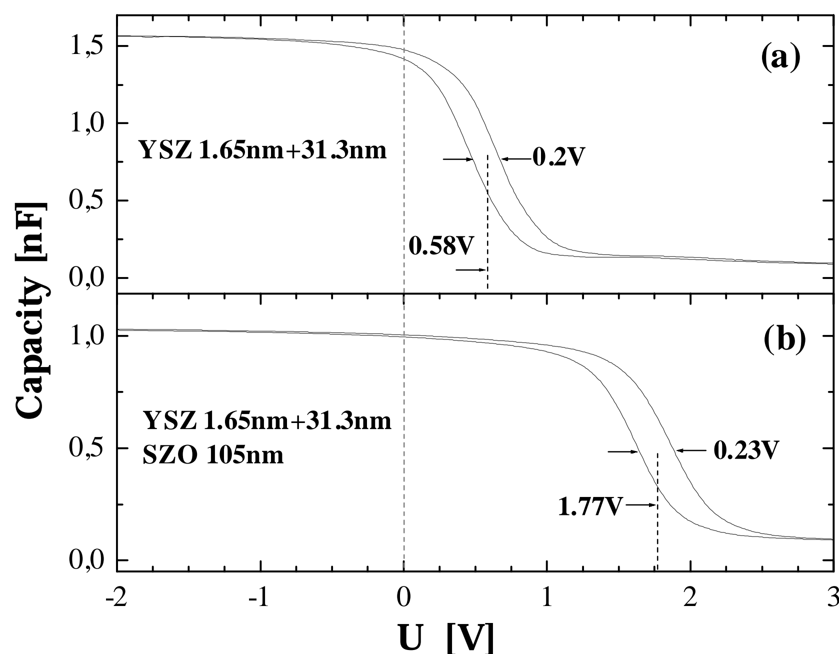

Figure 6.30: (a) *C(V)*-characteristic of a YSZ layer on silicon. Due to charge trapping sites (see chapter 4.3.2), a hysteresis of 0.2 V and a shift of 0.58 V is observed ($f = 1$ MHz, $V_{AC} = 0.2$ V, $V_{DC} = \pm 3$ V). **(b)** A measurement of an *a*-axis oriented 105 nm thick $SrZrO_3$ film on YSZ-buffered silicon exhibits a slightly increased hysteresis of 0.23 V, but a strongly increased shift of 1.77 V (f = 1 MHz, $V_{AC} = 0.2$ V, $V_{DC} = \pm 4$ V). For both samples, the thickness was exactly determined by means of LXRD measurements.

Thus, from the saturated value of capacitance $C = 1.05$ nF in Figure 6.30b, the radius of the gold electrode $r = 625$ µm, and the thickness of the $SrZrO_3$ layer $d = 105$ nm, a dielectric constant of ε_{SZO} (1 MHz) = (29±0.4) is obtained. This value lies within the range of available literature values for $SrZrO_3$ at room temperature of 26.5 to 38 [Per 65, Kel 73, Ros 00]. As shown in Figure 6.31b, the dielectric constant decreases linearly with frequency from ε_{SZO} (100 kHz) = 41.5 to ε_{SZO} (1 MHz) = 29. The calculation is based on the decrease of absolute capacitance in Figure 6.31b and the assumption of a constant contribution of the YSZ layer.

By the mechanisms discussed in chapter 4.3.2 and 6.3.1, the shift of $U_s = 0.58$ V and the hysteresis of $\Delta U = 0.2$ V in the *C(V)*-characteristic of the YSZ layer in Figure 6.30a is related to trapped charges confined at the YSZ/Si interface and mobile charge carriers within an oxygen deficient YSZ layer, respectively. Thus, the slightly increased hysteresis $\Delta U = 0.22$ V of the YSZ/ $SrZrO_3$ bi-layer in Figure 6.30b is assumed to be originating from an increased oxygen deficiency of the YSZ layer. The strongly increased shift $U_s = 1.77$ V however, cannot be related to some changes in the YSZ layer, but is obviously resulting from the second interface between YSZ and $SrZrO_3$. From the additional shift of the *C(V)*-curve $U_s = 1.77\text{-}0.58$ V = 1.19 V and the effective capacitance $C_{SZO} = 3.08$ nF of the $SrZrO_3$ layer, a surface states density of $n_{SZO} = 1.86 \times 10^{12}$ cm^{-2} is obtained. Frequency dependent measurements show an increase of the shift up to $U_s = 2.3$ V at lower frequencies (100 kHz), indicating that surface states can increasingly follow the applied *AC*-voltage. On the other hand, only a weak influence of frequency on absolute capacitance (see Figure 6.31a) and hysteresis is observed.

Dielectric Properties of $SrBi_2Ta_2O_9$ on YSZ/$SrZrO_3$-buffered Silicon

In order to calculate the dielectric constant of $SrBi_2Ta_2O_9$ on YSZ/SZO-buffered silicon, *C(V)*-measurements have been performed in a frequency range from 100 kHz to 1 MHz. The frequency dependence of the absolute capacity C_{max} of the YSZ/SZO buffer layer combination with and without $SrBi_2Ta_2O_9$ as well as the resulting dielectric constants ε_{SZO} and ε_{SBT} are shown in Figure 6.31a and b, respectively.

The dielectric constant was calculated using the particular absolute capacity and the individual layer thickness of 150 nm, 105 nm, and 33 nm for the $SrBi_2Ta_2O_9$, $SrZrO_3$, and YSZ layer, respectively. As illustrated in Figure 6.31a, from a similar linearly decrease of capacitance C in both measurements, a significant decrease of the dielectric constant from ε_{SBT} (100 kHz) = (29.5±0.5) to ε_{SBT} (1 MHz) = (18±0.5) is obtained. A *C(V)*-characteristic in Figure 6.32 exhibits a hysteresis of 0.53 V (black curve). As indicated by the red curve, the size of the hysteresis strongly depends on the turn speed of the measurement. The decrease of the *DC*-voltage step size from ΔV_{DC} = 100 mV to ΔV_{DC} = 10 mV at constant delay times of 0.5s leads to a nearly complete disappearance of the hysteresis to 80 mV. This behaviour strongly differs from what has been observed for the YSZ/SZO bi-layer, wherein the hysteresis was independent on the turn speed. Hence, this behaviour can only be attributed to the $SrBi_2Ta_2O_9$ layer. On the other hand, a nearly constant hysteresis of U_H = (0.53±0.4) V is observed over the whole frequency range and at changing *AC*-voltages from 50 mV to 100 mV. However, from this measurement a clear picture can not be obtained, but the dependence on turn speed strongly suggests that the observed memory window is not related to ferroelectricity. Furthermore, the influence of domain wall movement and surface morphology on the *C(V)*-characteristic is a subject for further investigations.

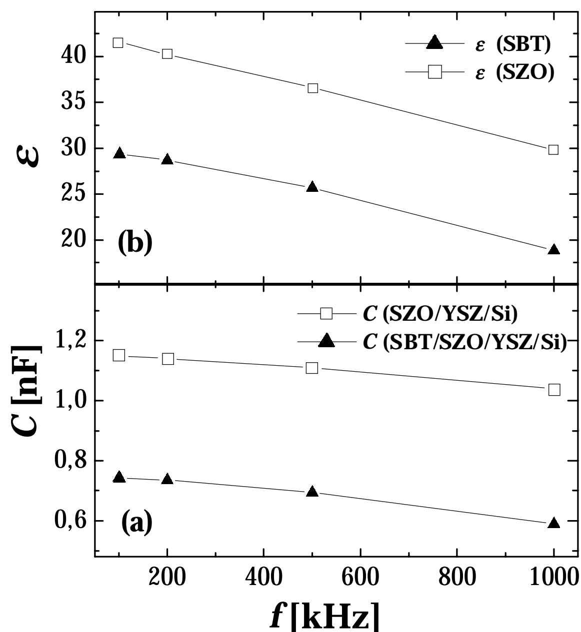

Figure 6.31: Frequency dependence of the absolute capacitance C and the dielectric constant ε of the YSZ/SZO- and the YSZ/SZO/SBT-heterostructure on silicon, respectively (V_{DC} = ±6 V, ΔV_{DC} = 100 mV, V_{AC} = 0.2 mV).

In comparison to the bi-layer in Figure 6.30b, a smaller absolute shift to U_s = 0.38 V is observed, which is assumed to originate from a smaller voltage drop at the YSZ/SZO interface due to the additional $SrBi_2Ta_2O_9$ layer and a

SZO/SBT interface with a lower density of surface states. Additionally, at lower turn speeds of $\Delta V_{DC} = 10$ mV and frequencies of $f = 100$ kHz the shift is increased to $U_s = 0.46$ V and up to $U_s = 1.1$ V, respectively. However, due to the complexity of the heterostructure, the particular contribution of surface states at three interfaces can not be exactly determined, since the nature of surface states is strongly influenced by the deposition process.

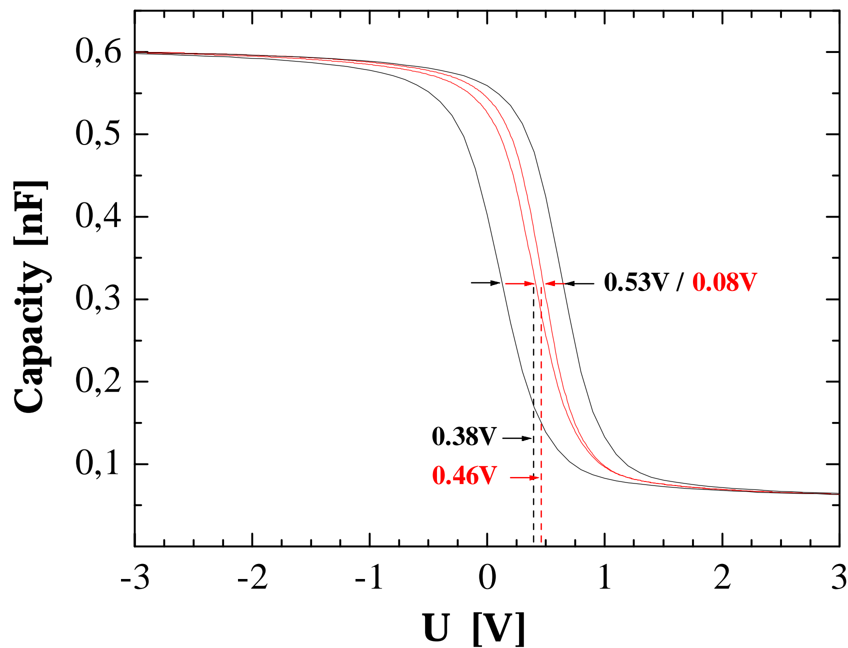

Figure 6.32: *C(V)*-characteristics of a 150 nm thick $SrBi_2Ta_2O_9$ layer with mixed (100)/(116)-orientation on a SZO(105 nm)/YSZ(1.65+31.3 nm)-buffered silicon substrate. A hysteresis of 0.53V (f = 1 MHz, $V_{AC} = 0.2$ V, $V_{DC} = \pm 3$ V, $\Delta V_{DC} = 100$ mV) is decreased to 0.08 V by decreasing the turn speed ($\Delta V_{DC} = 10$ mV), whereas the shift is increased from 0.38 V to 0.46 V.

Although from *a*-axis oriented $SrBi_2Ta_2O_9$ improved ferroelectric properties by increased polarisation along the film normal have been expected, the observed hysteresis is assumed to be not originating from ferroelectricity. In contrast to the results obtained for *c*-axis oriented $SrBi_2Ta_2O_9$ on CeO_2/YSZ buffered silicon, the improvement of the crystalline quality by the introduction of a 2-step deposition technology for YSZ leads to the formation of oxygen vacancies in the YSZ layer. The hereby occurring non-ferroelectric hysteresis in the buffer layers aggravates the interpretation of the observed *C(V)*-characteristics for the heterostructure, which includes the $SrBi_2Ta_2O_9$ layer. However, the dielectric constant of the as-deposited $SrBi_2Ta_2O_9$ could

be clearly determined to $\varepsilon_{SBT} \approx 29.5$ at 100 kHz, which is comparable to what has been observed for *c*-axis $SrBi_2Ta_2O_9$ ($\varepsilon_{SBT} \approx 20$) in chapter 6.3, but strongly differs from the dielectric constant up to $\varepsilon_{SBT} \approx 160$ observed in polycrystalline $SrBi_2Ta_2O_9$ films (Figure 6.12).

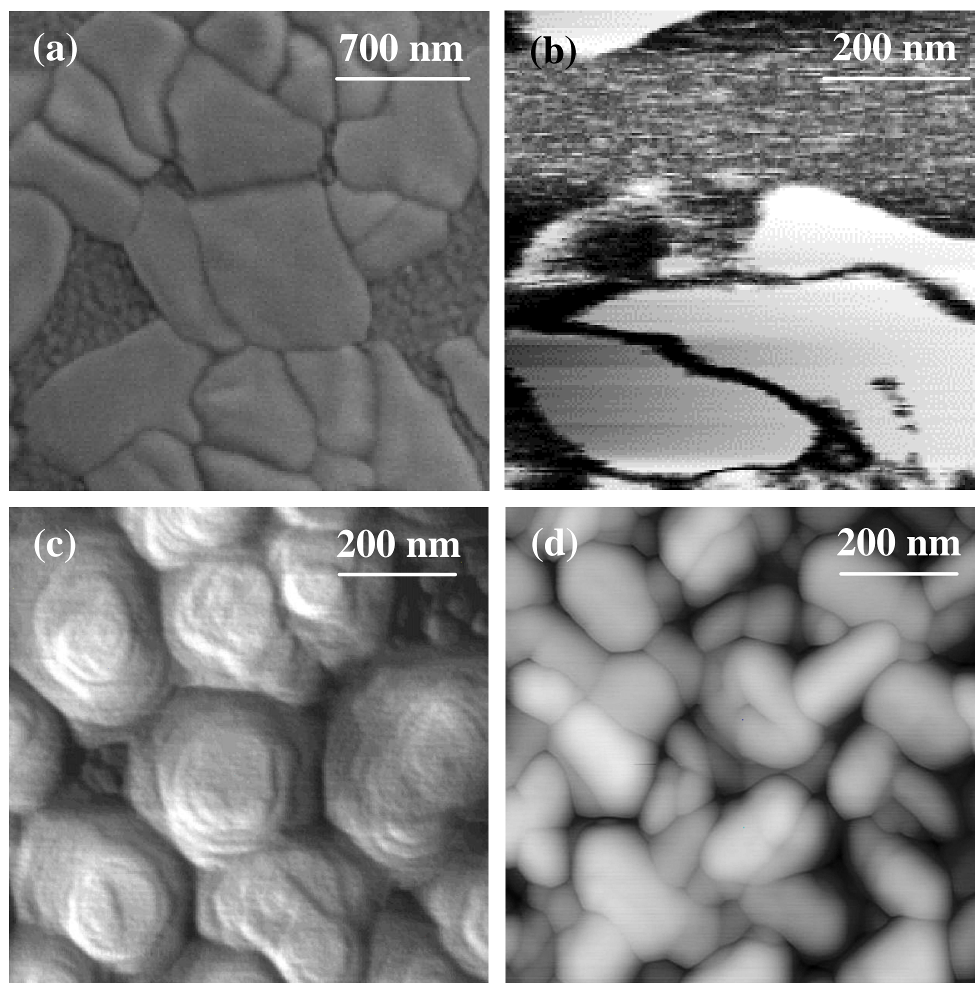

Figure 6.33: Grain morphology and ferroelectric domains in differently oriented $SrBi_2Ta_2O_9$ films. **(a)** SEM measurement of polycrystalline oriented SBT directly deposited on silicon with a typical grain size of 400-800 nm. Small grains in dark areas correspond to the pyrochlore phase. **(b)** Piezo-response AFM measurement (surface oscillation amplitude) of a domain on polycrystalline SBT with a domain size of roughly 150-200 nm. **(c)** NC-AFM measurement of a *c*-axis oriented SBT film on CeO_2/YSZ-buffered silicon. Grains with a size of typical 200 nm and terraces corresponding to an unit cell height are visible. **(d)** C-AFM measurement of mixed (100)/(116) oriented $SrBi_2Ta_2O_9$ on YSZ/SZO-buffered silicon. Grains exhibit a typical size below 200 nm.

The strong lowering of the dielectric constant in comparison to polycrystalline $SrBi_2Ta_2O_9$ can be understood by considering the grain morphology of

the $SrBi_2Ta_2O_9$ films. The mixed growth of randomly oriented $SrBi_2Ta_2O_9$ and the pyrochlore phase on silicon yields $SrBi_2Ta_2O_9$ grains with a typical size 400-800 nm, visible in Figure 6.33a. As discussed in chapter 6.4, such $SrBi_2Ta_2O_9$ films show ferroelectric domains (Figure 6.33b) with a typical size of 150-200 nm and a memory window of 0.45 V, although the polarisation is randomly oriented. By the use of a CeO_2/YSZ buffer layer combination, *c*-axis oriented $SrBi_2Ta_2O_9$ was obtained with a typical grain size slightly larger than 200 nm (Figure 6.33c) and a memory window of 0.87 V, which is believed to occur because of the in-plane hysteresis of grains (roughness). In contrast, $SrBi_2Ta_2O_9$ films with mixed (100)/(116) orientation on YSZ/SZO-buffered silicon exhibit a significantly reduced grain size smaller than 200 nm and practically no memory window, as illustrated in Figure 6.33d.

Generally it is well known, that electrical properties of ferroelectric thin films are strongly influenced by the film thickness and resulting grain size [Sak 93, Uda 95]. First, the coercitive field is drastically increased and the resulting memory window is decreased below a critical thickness (i.e. grain size) in the range of a few hundred nanometers. It has been found in polycrystalline $PbTiO_3$ films that this thickness is of about 200-300 nm with a corresponding grain size of 150 nm [deK 91][105]. These results coincide with the observations in polycrystalline $SrBi_2Ta_2O_9$ films in this work, as reported in chapter 6.3.2. This effect is resulting from a transition from a multi-domain state in large grains to a predominant single-domain state in smaller grains, indicating that single domained grains are energetically more stable than being split into domains. Such a single domain state requires an essentially higher electrical field to flip the polarisation, since its strength is related to the ease of domain nucleation and domain wall motion [Ren 96]. Secondly, permittivity is related to the density of domain walls and their mobility at low field. Thus, due to a lack of domain walls in fine grained films, the polarisation change due to domain wall movement at low fields is insignificant and consequently the associated permittivity is low.

[105] It should be pointed out, that for polycrystalline films, grain size is a function of thickness [Sak 93, deK 91]. It was found by Ren et al. [Ren 96] that grain size, rather than film thickness, is the controlling factor determining domain structure and consequently electrical properties.

In conclusion, there are several possibilities to improve the ferroelectric properties of $SrBi_2Ta_2O_9$ films on YSZ/SZO-buffered silicon: The shown measurements have been performed with a series of thin films, whose emphasis was on the clarification of the epitaxial relation in the Si/YSZ/SZO/SBT heterostructure. Thus, the particular layer thickness is not ideal for the application in MFS-diodes. First, as already mentioned in chapter 6.3.2 and discussed in the previous paragraph, the size of the memory window strongly depends on the film thickness (grain size) and an increase from 150 nm to at least 300 nm (as used for the *c*-axis oriented SBT films) is expected to improve the memory window. Second, the capacity of the insulator decreases with increasing thickness, resulting in a decrease of the electric field in the ferroelectric. In order to achieve sufficient hysteresis, the buffer layer thickness should be lowered to about 40 nm for a reasonable $SrBi_2Ta_2O_9$ film thickness and coercitive field. Moreover, as shown in Figure 6.23, the increase of deposition temperature and pressure should lead to a further suppression of the (116)-orientation and thus an improved alignment of the polarisation along the device normal, if purely *a*-axis oriented $SrBi_2Ta_2O_9$ is achieved. On the other hand, the reduction of deposition rate (laser energy density and pulse repetition rate) in conjunction with an increased substrate temperature will lead to an increased species mobility on the substrate and thus the formation of larger grains wherein multi domain states should be favoured. Furthermore, the use of $SrZrO_3$ as a buffer layer is an advantage in the general sense, that a high dielectric constant of the insulator is followed by a higher voltage drop at the ferroelectric film. This leads to saturation of the polarisation at lower voltages, which affects read/write voltages of devices.

7. Conclusion

As a main goal of this work, a new pulsed laser deposition (PLD) system has been designed and established in order to investigate complex heterostructures of oxidic thin films. The system features a high flexibility with a sixfold target holder and fast target exchange, a heater design that enables easy substrate mounting and an accessible temperature range up to 1000°C. The vacuum system allows thin film deposition at different ambient gases and stable pressures ranging from $1x10^{-7}$ mbar up to several mbar. Optimal thin film quality is achieved by high temperature homogeneity and reliable temperature measurement of the substrate as well as a sophisticated laser beam optics that guarantees homogeneous laser energy density and provides laser beam scanning facility for large area thin film deposition.

Understanding the physical phenomena involved in pulsed laser deposition is a major requirement to accomplish high quality thin films by optimising a variety of deposition parameters. Hence, the basic theoretical models of laser-target interaction, plasma formation, expansion and finally material condensation on a heated substrate have been reported. Hereby, the emphasis was on the interrelation of processing parameters and film nucleation in order to give some practical advises for thin film deposition by PLD.

After a general introduction into epitaxy and material properties, chapter 3 was devoted to the use of buffer layers in order to allow and to improve epitaxial growth of functional oxide layers on technical substrates. By the introduction of a new two step deposition technique for Y-stabilised ZrO_2, a high crystalline growth template for subsequent oxide layers on silicon was achieved. However, it was found, that the dielectric properties of the YSZ layer are sensitive to the oxygen content and interface morphology, mainly

influenced by the thickness of the first layer, which was deposited at low pressures. Thus, charge trapping sites and mobile ions due to oxygen vacancies in the YSZ layer lead to a significant hysteresis and shift in *C(V)*-characteristics. Based on the YSZ growth template, $BaZrO_3$ has been investigated as an additional buffer layer material for the high-T_c superconductor $YBa_2Cu_3O_{7-\delta}$ on technological relevant silicon substrates. Within a first approach on $SrTiO_3$ substrates, the effective dielectric constant of $BaZrO_3$ was determined to $\varepsilon \approx 65$. Possibly caused by the movement of oxygen vacancies due to PLD deposition at low pressures, an observed dispersion behaviour could be described by modified Debye relations (Cole-Cole). The extraordinary high crystalline quality of $BaZrO_3$ buffer layers with a FWHM of rocking curves below 0.05° and a surface roughness of 0.4 nm rms enables perfect cube-to-cube growth of $YBa_2Cu_3O_{7-\delta}$ on $BaZrO_3$. The HTSC exhibits crystalline and electronic properties comparable to what is typically obtained on single crystalline $SrTiO_3$. Comparative measurements show, that besides a slightly elevated transition temperature of $T_c = 90.2$ K, a substantial improvement of the $YBa_2Cu_3O_{7-\delta}$ surface roughness to 2 nm rms was achieved. Consequently, the application of $BaZrO_3$ was extended as an additional buffer in $YBa_2Cu_3O_{7-\delta}/BaZrO_3/YSZ$ heterostructures on silicon. By means of detailed four circle X-ray analysis it was shown, that the introduction of a few monolayers $BaZrO_3$ completely avoids ±9° in-plane rotated grains of the $YBa_2Cu_3O_{7-\delta}$ layer, which are usually observed for direct deposition on YSZ. Resistive measurements show a transition temperature above 89 K, which is a value comparable to best results for the usually applied CeO_2/YSZ buffer layer combination.

In chapter 5, the possibility to utilise the previously investigated materials for controlling the growth orientation of a $YBa_2Cu_3O_{7-\delta}$ layer is reported. Based on the idea of continuous lattice match [Wu 92], a new layer sequence $YBa_2Cu_3O_{7-\delta}/CeO_2/YSZ/BaZrO_3$ on $SrTiO_3$ for bi-epitaxial grain boundary Josephson junction has been found and its epitaxial relations have been clarified. To the authors knowledge, with respect to crystallinity and superconductivity ($T_c = 91.7$ K and $\Delta T_c = 0.15$ K), the properties of an in-situ deposited layer sequence belong to best results obtained hitherto in this field and are even comparable to properties observed on lattice matched substrates without

buffer layers. Preliminary investigations have been performed in order to realise a bi-epitaxial grain boundary junction by the use of this layer sequence. However, the properties observed on the prepared junctions are not sufficient for technological applications. By detailed analysis of film surface morphologies at different stages of the inserted structuring steps, it is clearly shown that the reduction of superconducting properties is a result of the variety of process steps. Several approaches in order to improve this process have been investigated. Especially the aspects of an incident ion beam on surfaces are discussed in detail. Thus, a basis for further investigations in the field of bi-epitaxial grain boundary Josephson junctions is given.

Chapter 6 is dedicated to the ferroelectricity of $SrBi_2Ta_2O_9$ thin films on silicon substrates and the ability to enforce a crystalline orientation of this functional layer by the introduction of buffer layers. By using a YSZ/CeO_2 buffer layer combination, highly *c*-axis oriented $SrBi_2Ta_2O_9$ films with rocking curves of 1.2° FWHM have been obtained. A clear cube-to-cube in-plane relation of the whole heterostructure was proven by four circle X-ray analysis. In contrast, the deposition on bare and on YSZ-buffered silicon results in the occurrence of the polycrystalline $SrBi_2Ta_2O_9$ and the pyrochlore phase, respectively. For the *c*-axis oriented $SrBi_2Ta_2O_9$ layer, from AFM measurements we have been able to identify terraces with a dimension of roughly 200 nm and a height corresponding to the *c*-axis unit cell.

In spite of the fact, that the easy direction for the polarisation of $SrBi_2Ta_2O_9$ is known to lie along the *ab*-plane, a memory window of MFIS structures of 0.87 V was observed for 50 nm thick *c*-axis $SrBi_2Ta_2O_9$ oriented films. Hence, an improvement of the memory window by nearly a factor three was achieved in comparison to polycrystalline $SrBi_2Ta_2O_9$ films on bare silicon with a memory window of 0.3 V for 300 nm thick films. If solely YSZ is introduced as buffer layer on silicon, the non-ferroelectric pyrochlore phase dominates the growth and leads to charge trapping sites at the interface and shifted *C(V)*-characteristics. The capacitance of the MFS-device with *c*-axis oriented $SrBi_2Ta_2O_9$ could be switched by a factor 4 (from 200 to 800 pF) by applying 3 V. These improvements are mainly due to the better crystalline quality of the those films and the absence of amorphous SiO_2 at the Si/YSZ interface. Measurements of ferroelectric Si/Ti/Pt/SBT/Au capacitor

structures show hysteresis loops with a maximum remanent polarisation of $P_r = 6.5\ \mu C/cm^2$, and a coercitive field of $E_c = 35 kV/cm$. Furthermore, by means of AFM measurements in the piezo-response mode, ferroelectric domains have been imaged and from the observed domain wall width the resolution limit of the this AFM method was determined to approximately 7 nm. By applying a *DC*-voltage of 30 V, reversible switching of the domain polarisation was observed in AFM images. From AFM measurements in the non-contact mode, the local polarisation of $SrBi_2Ta_2O_9$ was determined to $3.4\ \mu C/cm^2$.

An alternative buffer layer combination $SrZrO_3$/YSZ on silicon has been investigated in order to enforce the growth of $SrBi_2Ta_2O_9$ with its polarisation axis along the substrate (device) normal. $SrZrO_3$ layers are highly *a*-axis oriented and show a four domain in-plane relation with the YSZ layer. Substantiated by four circle X-ray measurements, a growth model has been presented, which explains the observed X-ray diffraction patterns by geometric considerations. The $SrBi_2Ta_2O_9$ layer on top of this buffer layer combination indicates *a*-axis as well (116)-oriented grains. With respect to the SBT(100) and SBT(116) in-plane orientation, no clear picture is obtained from XRD measurement solely. However, the combination of a growth model and AFM measurements with a matching predominant grain orientation strongly indicate a four domain growth of both $SrBi_2Ta_2O_9$ orientations on top of $SrZrO_3$. Further investigations are necessary in order to identify the particular X-ray reflections and to determine the exact ratio between the SBT(100)- and SBT(116)-orientation. Preliminary investigations of the ferroelectric properties have been performed. A strong influence of mobile ions and charge trapping sites aggravates the interpretation of *C(V)*-characteristics. However, the dielectric constant of $SrZrO_3$ and $SrBi_2Ta_2O_9$ could be determined to $\varepsilon \approx 29$ and $\varepsilon \approx 20$, respectively. The strong lowering of the dielectric constant for $SrBi_2Ta_2O_9$ was explained by the surface morphology with smaller grain sizes than observed for *c*-axis and polycrystalline $SrBi_2Ta_2O_9$.

8. Appendix

Historical Overview

1960	Development of the first ruby laser
1963	First experimental and theoretical work about the interaction between intensive laser radiation and solid-state surfaces
1965	Deposition of thin films (CdTe, Sb_2S_3, MoO_3, $PbCl_2$, etc.) by a ruby laser [Smi 65]. However, a only small bandwidth of materials as a result of limited laser energies and available wavelengths
1968	CO_2 laser and Nd^{3+}:YAG laser
1969	first ferroelectric perovskite-oxide films ($BaTiO_3$)
1975	Development of Q-Switch ⇒ short laser pulses with high energy density, more materials
1986	Discovery of high-T_c superconductivity
1987	Perovskite-type-superconductors deposited by PLD in oxygen

Table 8.1: History of pulsed laser deposition.

PLD Deposition Parameters for $YBa_2Cu_3O_{7-\delta}$

For deposition of $YBa_2Cu_3O_{7-\delta}$, the optimum oxygen pressure is in the range of 0.1 mbar to 0.6 mbar. Best superconducting properties ($T_c > 91$ K, $\Delta T_c < 0.2$ K) are achieved for higher oxygen pressures. In this case, the surface morphology shows a high density of CuO_2 outgrowths and an increased overall roughness. Targets with high density, intensive pre-ablation, moderate laser energy densities and laser beam scanning avoid droplet formation. In order to optimise the surface properties (less outgrowths, low roughness), lower oxygen pressures are appropriate (0.15-0.3 mbar), governed by slightly decreased superconducting transition temperatures and widths ($T_c \approx 90$ K, $\Delta T_c < 1$ K). Optimised deposition parameters and important processing steps for achieving optimal superconducting properties are:

Pre-ablation:

- target polishing
- number of pulses: 2000, repetition rate: 10 Hz
- $E = 103$ mJ, spot size: 2x2 mm^2, $J = 2600$ mJ/cm^2

Ablation:

- number of pulses: 3000, repetition rate: 3 Hz
- laser beam scanned across rotating target
- ablation rate: 0.8 nm/pulse $\Rightarrow$ thickness: 240 nm
- $E = 103$ mJ, spot size: 2x2 mm^2, $J = 2600$ mJ/cm^2
- deposition temperature: $T = 830$ °C
- oxygen pressure: $p = 0.6$ mbar
- target-substrate distance: $d = 38$ mm

Oxygen loading and cool down:

- cool down from 830 °C to 780 °C with 15 K/min at 0.6 mbar
- increase of oxygen pressure from 0.6 mbar to 1000 mbar within a temperature ramp from 780 °C to 730 °C (15 K/min)
- further cool down from 730 °C to 580 °C at 1000 mbar
- oxygen loading 60 min at 1000 mbar and 580 °C
- cool down to room temperature with 15 K/min at 1000 mbar

Deposition Parameters of Materials used in this Work

Material	BZO	YSZ	YSZ 1st	YSZ 2nd	SZO	CeO_2	SBT	YBCO
Bottom layer/substrate	STO YSZ	STO	Si	Si	YSZ	STO BZO	CeO_2 SZO	STO BZO CeO_2
Temperature T [°C]	650-750	850-870	850-870	850-870	750-800	750-830	750-850	830
Pressure p [mbar]	10^{-6}	0.3	5×10^{-6}	5×10^{-4}	5×10^{-4}	0.1-0.25	0.2-0.4	0.3-0.6
Energy Density J [Jcm^{-2}]	2.0-2.3	>3.0	>3.0	>3.0	1.5-2.5	2.0-2.3	1.5-2.5	2.6
Repetition Rate f [Hz]	3	3	3	3	3	3	3	3
Distance d [mm]	22	<20	<20	<20	35-40	35-40	35-40	30-35
Dep. Rate n [nm/p]	0.11	0.04	0.04	0.04	0.035	0.12	0.13-0.16	0.16
ω-scan FWHM [°]	0.04-0.2	0.3-1.0	-	0.6-1.4	1.3-1.6	0.3-0.6	1.8-3	0.15-0.4

Table 8.2: Deposition parameters of the materials with temperature *T*, oxygen pressure *p*, laser energy density *J*, pulse repetition rate *f*, and target to substrate distance *d*. Moreover, the typically obtained FWHM of rocking curves is listed.

Target Preparation

There are a few intrinsic restrictions placed on the targets used in a PLD system. Successful depositions can be made from pressed powders, sintered pellets, cast material, single crystals and metal foils. The main differences between these different target morphologies is in the nature of the target erosion and the generation of particulates (droplets). A good rule of thumb is that high-density and highly homogenous target yield the best films. However, even the best targets must be resurfaced (sanded flat) at regular intervals in order to perform optimally. The whole set of materials, that has been investigated in this work is based on self-manufactured sintered ceramic targets. Due to the target holder dimensions, pellets with a diameter of 25 mm a thickness of 3-5 mm have been manufactured. In general, the stoichiometric pulverulent initial material has to be grinned intensively (ball mill and by hand) in order to yield high dense and homogenous targets. The powder is pressed into pellets by a hydraulic press with maximal pressure of 20 kN. For $YBa_2Cu_3O_{7-\delta}$ and $SrBi_2Ta_2O_9$ the initial powder consists of carbonates with a stoichiometric amount of the required elements. The powder has to be calcinated and once more grinned before the pellets are pressed. This step has to

be carried out extremely accurate. The sintering process is performed on top of a Al_2O_3 plate at temperatures just below the melting point of the material. To avoid crack formation the sintered pellets are heated up and cooled down with a rate below 1K/min. The optimal preparation parameters for the investigated materials are listed in the table below:

Material	Pressure [kN]	Calcination Temp. [°C]	Calcination Duration [h]	Sintering Temp. [°C]	Sintering Duration [h]
$BaZrO_3$	8-10	-	-	1450-1500	24
CeO_2	10	-	-	1100	12
YSZ [(a)]	20	-	-	1100-1200	24
$YBa_2Cu_3O_{7-\delta}$ [(b)]	20	850-860	24	955	24
$SrBi_2Ta_2O_9$ (Sr:Bi:Ta)=(1:2:2) [(c)]	15	800	24	94	24
$SrBi_2Ta_2O_9$ (Sr:Bi:Ta)=(1:2.3:2)	15	840	8	940	24

Table 8.3: Target preparation parameters. **(a)** 9 mol% ZrO_2, 91 mol% Y_2O_3. **(b)** The calcination step has been performed twice at a temperature of 850°C (1st) and 860°C (2nd). **(c)** Different target compositions have been investigated. Consistence with X-Ray powder simulations was observed for all compositions. Best results have been achieved for a target composition 1:2.3:2 [Sch 99].

Bibliography

[Aji 94] E.M. Ajimine, F.E. Pagaduan, M.M. Rahman, C.Y. Yang, *Appl. Phys. Lett.* **59**, 2889 (1994)

[Akh 82] A.D. Akhsakhalyan, Yu.A. Bityurin, S.V. Gapanov, A.A. Gudkov, V.I. Luchin, *Sov. Phys. Tech. Phys.* **27**, 969 and 973 (1982)

[Alf 93] L. Alff, R. Gerdemann, K.-D. Husemann, A. Beck, T. Träuble, B. Mayer, R. Gross, *Proceedings of the first conference on Applied Superconductivity,* 1199, Göttingen (1993)

[Amb 63] V. Ambegoakar, A. Baratoff, *Phys. Rev. Lett.* **10**, 486 (1963)

[Amb 69] V. Ambegaokar, B.I. Halperin, *Phys. Rev. Lett.* **39**, 3113 (1969)

[And 59] P.W. Anderson, *Phys. Rev. Lett.* **109**, 1492 (1959)

[And 63] P.W. Anderson, J.M. Rowell, *Phys. Rev. Lett.* **10**, 230 (1963)

[And 94] O.G. Andrianov, S.O. Klimonsky, V.A. Kusikov, E.N. Lubin, *Physica C* **235-240,** 575 (1994)

[Ara 96] C.P. Araujo, J.F. Scott, G.W. Taylor, *Ferroelectric Thin Films: Synthesis and Basic Properties,* Vol. **10**, Part I, Gordon and Breach Publisher (1996)

[Arn 99] N. Arnold, D. Bäuerle, *Appl. Phys. A* **68**, 363 (1999)

[Ash 90] N.W. Ashcroft and N.D. Mermin, *Solid State Physics,* Saunders College, Philadelphia, USA (1990)

[Ath 76] A. Athee. M. Athee, A.M. Glazer, A.W. Hewat: Structure of orthorhombic $SrZrO_3$ by neutron powder diffraction, *Acta Cryst.* **B32**, 3243 (1976)

[Auc 98] O. Aucielio, A. Gruverman, R. Ramesh, *MRS Bulletin* **1**, 33 (1998)

[Bal 95] R.W. Balluffi, A.P. Sutton, *Interfaces in Crystalline Materials,* Oxford University Press Inc., New York (1995)

[Bar 82] A. Barone, G. Paterno, *Physics and Applications of the Josephson effect,* p.131, John Wiley and Sons, New York (1982)

[Bat 73] V.A. Batanov, V.B. Fedorov, *JETP Lett.* **17**, 247 (1973)

[Bäu 96] D. Bäuerle, *Laser processing and Chemistry*, Springer, Berlin, Heidelberg (1996)

[Bec 95] L. Beckers, F. Sanchez, J. Schubert, W. Zander, Ch. Buchal, *J. Appl. Physics* **79** (6), 3337 (1995)

[Bed 86] J.G. Bednorz, K.A. Müller, *Z. Phys. B* **64**, 189 (1986)

[Beh 92] H. Behner, J. Wecker, Th. Mathée, K. Samwer, *Surface and Interface Analysis* **18**, 685 (1992)

[Bel 97] I. Belousov, E. Rudenko, S. Linzen, P. Seidel, *J. of Low Temp. Phys.* **106**, 433 (1997)

[Bha 98] S. Bhattacharyya, A.R. James, S.B. Krupanidhi, *Solid State Communications* **108** (10), 759 (1998)

[Bjö 95] C. Björmander, K. Sreenivas, A.M. Grishin, K.V. Rao, *Appl. Phys. Lett.* **67**, 58 (1995)

[Bla 92] D.H.A. Blank, R.P.J. Ijsselstein, P.G. Out, H.J.H. Kuiper, J. Floksura, H. Rogalla, *Mater. Sci. Eng.* **B13**, 67 (1992)

[Bla 98] D.H.A. Blank, G.J.H.M. Rijnders, G. Koster, H. Rogalla, *Appl. Surf. Sci.* **138-139**, 17 (1999)

[Bla 99] D.H.A. Blank, G.J.H.M. Rijnders, G. Koster, H. Rogalla, *Appl. Surf. Sci.* **127-129**, 633 (1999)

[Boi 94] Y.A. Boikov, Z.G. Ivanov, G. Brorsson, T. Claeson, *Superconductor Science and Technology* **7**, 281 (1994)

[Boi 95] Y.A. Boikov, Z.G. Ivanov, A.N. Kiselev, E. Olsson, T. Claeson, *J. Appl. Phys.* **78**, 4591 (1995)

[Boi 97] Y.A. Boikov, Z.G. Ivanov, T. Claeson, *Phys. Solid State* **39** (10), 1542 (1997)

[Boi 97] Y.A. Boikov, T. Claeson, D. Erts, F. Bridges, Z. Kvitky, *Phys. Rev. B* **56**, 11314 (1997)

[Boi 97a] Y.A. Boikov, Z.G. Ivanov, T. Claeson, *Superconductor Science and Technology* **10**, 801 (1997)

[Bor 89] R. Bormann, J. Nölting, *Appl. Phys. Lett.* **54**, 2148 (1989)

[Bur 85] G. Burns, *Solid State Physics*, Academic Press Inc., New York (1985)

[Byk 74] Yu.A. Bykovskii, N.N. Degtyarenko, V.F. Elesin, V.E. Kondrashov, E.E. Lovetskii, *Sov. Phys. Tech. Phys.* **18**, 1597 (1974)

[Cav 88] R.J. Cava, B. Batlogg, K.M. Rabe, E.A. Rietmann, P.K. Gallagher, L.W. Rupp Jr., *Physica C* **156**, 523 (1988)

[Cer 81] C. Cercignani, in *Rarefied Gas Dynamics*, Vol. **I**, edited by S.S. Fisher, AIAA, New York, 305 (1981)

[Cer 96] L. Ceresara, A. Iembo, F. Fuso, M. Labardi, M. Allegrini, E. Arimondo, A. Diodati, B.E. Watts, F. Leccabue, G. Bocelli, *Supercond. Sci. Technol.* **9**, 671 (1997)

[Cha 91a] K. Char, M.S. Colclough, S.M. Garrison, *Appl. Phys. Lett.* **59**, 2725 (1991)

[Cha 91b] K. Char, M.S. Colclough, S.N. Garrison, N. Newman, G. Zaharchuk, *Appl. Phys. Lett.* **59** (6), 733 (1991)

[Char 91c] K. Char, M.S. Colclough, L.P. Lee, G. Zaharchuk, *Appl. Phys. Lett.* **59** (17), 2177 (1991)

[Che 74] F.F. Chen, *Introduction to Plasma Physics*, Plenum, New York, chap. 1, (1974)

[Che 87] I.W. Chen, S. Keating, X. Wu, J. Xu, P.E. Reyes-Morel, T.Y. Tien, *Adv. Ceram. Mater.,* special issue **2**, 457 (1987)

[Che 92] L.C. Chen, E.L. Hall, K.A. Lou, *Mat. Res. Soc. Symp. Proc.* **273**, 377 (1992)

[Che 95] S.Y. Chen, X.-F. Du, I.-W. Chen, *Mater. Res. Soc. Symp. Proc.* **361**, 15 (1995)

[Cho 98] J.H. Cho, S.H. Bang, J.Y. Son, Q.X. Jia, *Appl. Phys. Lett.* **72**, 665 (1998)

[Chr 90] D.B. Chrisey, J.S. Horwitz, K.S. Grabowski, M.E. Reeves, M.S. Osofski, C.R. Gosset, *Mat. Res. Soc. Symp. Proc.* **191**, 229 (1990)

[Chr 94] D.B. Chrisey, G.K. Hubler, *Pulsed Laser Deposition*, Wiley-Interscience, New York (1994)

[Cil 96] J.F.M.Cillessen, R.M. Wolf, J.B. Giesbers, P.W.M. Blom, K.O. Grosseholz, E. Pastoor, *Appl. Surf. Sci.* **96** (8), 744 (1996)

[Cim 88] M.J. Cima, J.S. Schneider, S.C. Peterson, W. Coblenz, *Appl. Phys. Lett.* **53**, 1137 (1988)

[Cle 93] J.P. Cleveland, S. Manne, D. Bocek, *Rev. Sci. Instrum.* **64**, 403 (1993)

[Col 41] K.S. Cole and R.H. Cole in *Dispersion and absorption in dielectrics*, *J. Chem. Phys.* **9**, 341 (1941)

[Cop 93] C.A. Copetti, H. Soltner, J. Schubert, W. Zander, O. Hollricher, CH. Buchal, H. Schulz, N. Tellmann, N. Klein, *Appl. Phys. Lett.* **63**, 1429 (1993)

[Cul 78] B.D. Cullity, *Elements of X-ray diffraction*, Addison-Wesley Inc. (1978)

[Dat 95] R. Dat, J.K. Lee, O. Auciello, *Appl. Phys. Lett.* **67** (4), 572 (1195)

[Dav 51] D.W. Davidson, R.H. Cole, *J.Chem Phys.* **19**, 1417 (1951)

[deK 91] M. de Keijser, G.J.M. Dormens, P.J. VanVeldhoven, D.M. De Leeuw, *Appl. Phys. Lett.* **59**, 3556 (1991)

[deL 95] L. de Ligny, P. Richet, *Phys. Rev. B* **53** (6), 3013 (1995)

[Des 95] S.B. Desu, D.P. Vijay, *Materials Science and Engineering B* **32**, 74 (1995)

[Des 98] S.B. Desu, H.S. Cho, M. Nagata, *Phys. Stat. Solid A* **165**, 213 (1998)

[Die 95] G.W. Dietz, W. Antpöhler, M. Klee, R. Waser, *J. Appl. Phys.* 78, 572 (1995)

[Dij 87] D. Dijkamp et al., *Appl. Phys. Lett.* **51**, 619 (1987)

[Dor 94] G.J.M. Dormans, P.K. Larsen, *Appl. Phys. Lett.* **65**, 3326 (1994)

[Dou 95] C. Doughty, A.T. Findikoglu, T. Venkatesan, *Appl. Phys. Lett.* **66**, 1276 (1995)

[Dre 87] R.W. Dreyfus, R. Kelly, R.E. Walkup, *Nucl. Instrum. Meth. B* **23**, 557 (1987)

[Du 98] X. Du, I.W. Chen, *Mat. Res. Soc. Symp. Proc. V* **493**, 311 (1998)

[Dye 88] P.E. Dyer, J. Sidhu, *J. Appl. Phys.* **64**, 4657 (1988)

[Dye 90] P.E. Dyer, A. Issa, P.H. Key, *Appl. Phys. Lett.* **57**, 186 (1990)

[Dye 92] P.E. Dyer, P.H. Key, P. Monk, *Appl. Surf. Sci.* **54**, 160 (1992)

[Egu 39] E. Eguchi, J.K. Lee, *J. Mater. Sci.* **28**, 5809 (1939)

[Erb 96] A. Erb, E. Walker, R. Flükiger, *Physica C* **245**, 245 (1996)

[Ern 98] F. Ernst, A. Recnik, P.A. Langjahr, P.D. Nellist, M. Rühle, *Acta Mater.* **47** (1), 183 (1998)

[Esc 95] J. Eschenbaum, J. Rosenberger, R. Hempelmann, D. Nagengast, A. Weidinger, *Sol. State Ionics* **77**, 222 (1995)

[Fas 99] S. Fasko, T. Dekorsy, C. Koerdt, C. Trappe, H. Kurz, A. Vogt, H.L. Hartnagel, *Science* **258**, 1551 (1999)

[Fei 93] W.A. Feil, B.W. Wessels, J, *Appl. Phys.* **74** (6), 3927 (1993)

[Fle 65] R.L. Fleischer, P.B. Price, R.M. Walker, *J. Appl. Phys.* **36**, 3654 (1965)

[Fog 89] E.C. Fogerassy, C. Fuchs, J.P. Stuert, P. Siffert, J. Perriere, F. Rochet, *J. Less Common Metals* **151**, 249 (1989)

[Fon 96] J. Fontcuberta, B. Martinez, A. Seffar, S. Pinol, J.L. Garcia-Munoz, X. Obradors, *Phys. Rev. Lett.* **76**, 1122 (1996)

[For 90] D.K. Fork, D.B. Fenner, R.W. Barton, J.M. Phillips, G.A.N. Connel, J.B. Boyce, T.H. Geballe, *Appl. Phys. Lett.* **57**, 1161 (1990)

[For 90] D.K. Fork, D.B. Fenner, G.A.N. Conell, J.M. Phillips, T.H. Geballe, *Appl. Phys. Lett.* **57**, 1137 (1990)

[For 91] D.K. Fork, T.H. Geballe, *Appl. Phys. Lett.* **50**, 2294 (1991)

[For 92] D.K. Fork, S.M. Garrison, M. Hawley, T.H. Geballe, *J. Mat. Res.* **7** (7), 255 (1992)

[For 92] D.K. Fork, A. Barrera, T.H. Geballe, A.N. Viano, D.B. Fenner, *Appl. Phys. Lett.* **57**, 2504 (1992)

[Fuj 98] N. Fujimura, D.T. Thomas, S.K. Streiffer, A.J. Kingon, *Jap. Journ. of Appl. Phys.* **37**, 5185 (1998)

[Gap 77] S.V. Gapanov, B.M. Luskin, B.A. Nesterov, N.N. Salashchenko, *Sov. Phys. Solid State* **19**, 1736 (1977)

[Geo 91] D.B. Geohegan, *Mat. Res. Soc. Symp. Proc.* **201**, 557 (1991)

[Geo 92] D.B. Geohegan, *Appl. Phys. Lett.* **60**, 2732 (1992)

[Geo 92a] D.B. Geohegan, in *Laser Ablation of Electronic Materials: Basic Mechanisms and Applications*, edited by E. Fogarassy and S. Lazare, Springer-Verlag, Heidelberg, p. 73 (1992)

[Geo 93] D.B. Geohegan, Appl. Phys. Lett. 62, 1463 (1993)

[Ger 97] S. Gerhold, *Diploma Thesis*, Frankfurt (1997)

[Gie 97] J.B. Giesbers, M.W.J. Priens, J.F.M. Cillessen, H.A. Vanesch, *Microelectronic Engineering* **35**, 71 (1997)

[Gil 97] D.M. Gill, C.W. Conrad, G. Ford, B.W. Wessels, S.T. Ho, *Appl. Phys. Lett.* **71**, 2968 (1997)

[Gir 89] C.D. Girault, D. Damiani, J. Aubreton, A. Catherinot, *Appl. Phys. Lett.* **58**, 1597 (1989)

[Gol 58] V. Goldschmidt, *Geochemistry*, Oxford University Press, New York (1958)

[Gop 96] V. Gopalan, R. Raj, *Appl. Phys. Lett.* **68**, 1323 (1996)

[Gri 97] A.M. Grishin, M. Yamazato, Y. Yamagata, K. Ebihara, *Appl. Phys. Lett.* **72**, 620 (1996)

[Gro 65] A.S. Grove, B.E. Deal, E.H. Snow, *Solid States Electronics* **8**, 2011 (1965)

[Gru 99] A. Gruvermann, *Appl. Phys. Lett.* **75** (10), 1452 (1999)

[Ham 98] R.H. Hammond, R. Bormann, *Physica C* **162-164**, 703 (1998)

[Han 98] J.P. Han, T.P. Ma, *Appl. Phys. Lett.* **72** (10), 1185 (1998)

[Hav 66] D.W. Havriliak, S. Negami, *J. Polymer Sci.* **C14**, 99 (1966)

[Hay 97] T. Hayashi, T. Hara, H. Takahasi, *Jap. J. Appl. Phys.,* Part 1 **36**, 5900 (1997)

[Hel 89] H. Helvajian, R. Welle, *J. Chem. Phys.* **91**, 2616 (1989)

[Hem 94] J. Hemberger, *Diploma Thesis*, Technische Hochschule Darmstadt (1994)

[Hoh 91] W. Hoheisel, M. Vollmer, F. Träger, in *Laser Ablation: Mechanisms and Applications*, Springer-Verlag, Heidelberg, p. 77 (1991)

[Hor 94] J.S. Horwitz, J.A. Sprague, in *Pulsed Laser Deposition of Thin Films,* edited by D.B. Chrisey and G.K. Graham, John Wiley & Sons, New York, 229 (1994)

[Hu 90] Q. Hu, P.L. Richards, in *Superconducting devices,* ed. S.T. Ruggiero, D.A. Rudman, Academic Press, San Diego (1990)

[Hu 99] G.D. Hu, J.B. Xu, I.H. Wilson, *Appl. Phys. Lett.* **75** (11), 1610 (1999)

[Hub 63] J. Hubbard, *Proc. R. Soc.,* Ser. A **276**, 238, London (1963)

J. Hubbard, *Proc. R. Soc.* Ser. A **277**, 237, London (1964)

J. Hubbard, *Proc. R. Soc.* Ser. A **281**, 401, London (1964)

[Hug 75] T.P. Hughes, *Plasmas and Laserlight,* Wiley, New York (1975)

[Hwa 91] D.M. Hwang, Q.Y. Ying, H.S. Kwok, *Appl. Phys. Lett.* **58**, 2429 (1991)

[Hwa 95] H.Y. Hwang, S.W. Cheong, P.G. Radaelli, M. Marezio, B. Battlog, *Phys. Rev. Lett.* **75**, 914 (1995)

[Hyu 98] S.J. Hyun, B.H. Park, S.D. Bu, J.H. Jung, *Appl. Phys. Lett.* **73** (17), 1904 (1998)

[Ing 98] S. Ingebrandt, *Diploma Thesis,* Universität Mainz (1998)

[Ish 99] K. Ishikawa, N. Nukaga, K. Funakubo, *Jap. J. Appl. Phys. Lett.* **38,** L258 (1999)

[Ito 82] N. Itoh, T. Nakayama, *Appl. Phys. Lett.* **92A**, 471 (1982)

[Ito 96] Y. Ito, M. Ushikubo, S. Yohoyama, H. Matsunaga, T. Atsuki, T. Yonezawa, K. Ogi, *Jap. J. Appl. Phys.,* Part 1 **35**, 4925 (1996)

[Iwa 81] H. Iwahara, T. Esaka, H. Uchida, N. Maeda, *Sol. States Ionics* **3/4**, 359 (1981)

[Jae 94] C. Jaeckel, C. Waschke, H.G. Roskos, H. Kurz, *Appl. Phys. Lett.* **64**, 3326 (1994)

[Jaf 71] B. Jafee, W.R. Cook, H. Jaffe, *Piezoelectric Ceramics,* Academic Press, London (1971)

[JCP 96] *JCPDS-ICDD Crystallographic Database* (1996)

[Jin 98] F. Jin, G.W. Auner, R. Naik, N.W. Schubring, J.V. Mantese, A.B. Catalan, A.L. Micheli, *Appl. Phys. Lett.* **73**, 2838 (1998)

[Jin 98a] Jing-Pin Han, T.P. Ma, *Appl. Phys. Lett.* **72**, 1185 (1998)

[Jod 93] S. Jodeh, J. Villanueva, S. Deshmuk, G.P. Reck, *J. Phys. Chem.* **41**, 567 (1993)

[Joh 70] D.W. Johnson, L.E. Cross, F.A. Hummel, *J. Appl. Phys.* **41** (7), 2828 (1970)

[Jor 87] J.D. Jorgensen, M. Beno, D. Hinks, L. Soderholm, K. Volin, R. Hitterman, J. Grace, J. Schuller, C. Segre, K. Zhang, M. Kleefisch, *Phys. Rev. B* **36**, 3920 (1987)

[Jös 82] B. Jöst, B. Schueler, F.R. Krueger, *Z. Nat. Forsch.* **37a**, 18 (1982)

[Jos 62] B.D. Josephson, *Phys. Lett.* **1**, 251 (1962

[Kan 99] T. Kanashima, M. Okuyama, *Jap. J. Appl. Phys.* **38**, 2044 (1999)

[Kau 90] W. Kautek, B. Roas, L. Schultz, *Thin Solid Films* **191**, 317 (1990)

[Kel 85] R. Kelly, J.E. Rothenberg, *Nucl. Instrum. Meth. B* **7/8**, 755 (1985)

[Kel 88a] R. Kelly, R.W. Dryfus, *Surf. Sci.* **198**, 263 (1988)

[Kel 88b] R. Kelly, R.W. Dryfus, *Nucl. Instrum. Meth. B* **32**, 341 (1988)

[Kel 90] R. Kelly, *Nucl. Instrum. Meth. B* **46**, 441 (1990)

[Kel 92] R. Kelly, *Phys. Rev. A* **46**, 860 (1992)

[Kel 94] R. Kelly, in *Pulsed Laser Deposition of Thin Films,* edited by D.B. Chrisey and G.K. Graham, John Wiley & Sons, New York, 229 (1994)

[Kel 75] P.C. Kell, A.C. Greenham, G.C.E. Olds, *J. of the American Ceramic Soc.* **56** (7), 352 (1975)

[Kel 94] R. Kelly in *Pulsed Laser Deposition*, ed. D.B. Chrisey, G.K. Hubler, Wiley-Interscience, New York (1994)

[Kim 92] H.S. Kim, H.S. Kwok, *Appl. Phys. Lett.* **61**, 2234 (1992)

[Kis 87] J. Kissel, F.R. Krueger, *Appl. Phys. A* **42**, 69 (1987)

[Kit 46] C. Kittel, *Phys. Rev.* **70**, 965-970 (1946)

[Koi 96] H. Koike, *Proc. ISSCC*, NEC (1996)

[Kop 86] K. Kopitzki, *Einführung in die Festkörper-Physik,* Teubner Studienbücher, Stuttgart (1986)

[Kor 89] G. Koren, J. Baseman, A. Gupta, M.I. Lutwyche, R.B. Laibowitz, *Appl. Phys. Lett.* **55**, 2450 (1989)

[Kor 90] G. Koren, J. Baseman, A. Gupta, M.I. Lutwyche, R.B. Laibowitz, *Appl. Phys. Lett.* **56**, 2144 (1990)

[Kor 91] G. Koren, E. Aharoni, E. Polturak, *Appl. Phys. Lett.* **58**, 634 (1991)

[Kre 79] R. Kretschmar, K. Binder, *Phys. Rev. B* **20**, 1065 (1979)

[Kuc 91] H. Kuchling, *Taschenbuch der Physik,* Verlag Harri Deutsch (1991)

[Kum 93] W.K.A. Kumuduni, Y. Nakayama, Y. Nakata,T. Okada, M. Maeda, *J. Appl. Phys.* **74**, 7510 (1993)

[Lam 00] Lambda Physik GmbH, *Site Preparation Compex 100/200/300,* Göttingen, (2000)

[Lan 81] Landolt-Börnstein, *Numerical Data and Functional Analysis in Science Technology,* New Series III/16a, Springer Verlag, Berlin, New York, Heidelberg (1981)

[Lan 98] P.A. Langjahr, F.F. Lange, T. Wagner, M. Rühle, *Acta Mater.* **46** (3), 773 (1998)

[Lee 00] H.N. Lee, S. Senz, N.D. Zakharov, C. Harnega, A. Pignolet, D. Hesse, U. Gösele, *Appl. Phys. Lett.,* **77**(20), 3260 (2000)

[Lee 98] J.S. Lee, H.H. Kim, H.J. Kwon, Y.W. Jeong, *Appl. Phys. Lett.* **98** (2), 166 (1998)

[Lee 99] H.N. Lee, Y.T. Kim, S.H. Choh, *J. of the Korean Phys. Soc.* **34**, 454 (1999)

[Lee 99a] W.J. Lee, C.H. Shin, C.R. Cho, J.S. Lyu, J.H. Lee, B.W. Kim, C.H. Shin, H.C. Lee, *J. of the Korean Phys. Soc.* **35**, S509 (1999)

[Let 98] J. Letterie, C.I. Weber, D.G. Schlomm, *Appl. Phys. Lett.* **73** (14), 2057 (1998)

[Let 98] J. Lettieri, C.I. Weber, D.G. Schlom, *Appl. Phys. Lett.* **73**, 2057 (1998)

[Lev 75] E.M. Levin, H.F. McMurdie, M.K. Reser, *Phase diagramms for ceramists, American Ceramic Society* **163** (1975)

[Lev 76] V.A. Levitskii, D.Sh. Tsagareishvili, G.G. Gvelesiani, *Powder Metallurgy Int.* **19** (5), 34 (1976)

[Li 94] M.Y. Li, H.L. Hao, W.J. Chang, C.L. Lin, C.H. Li, Y. Xu, C.C. Chi, W. Guan, M.K. Wu, *Physica C* **235-240**, 589 (1994)

[Lin 96] M.E. Lines, A.M. Glass, *Principles and Applications of Ferroelectric Materials,* Oxford Science Publications (1996)

[Lor 70] P. Lorrain, D. Corson, *Electromagnetic Fields and Waves,* Freeman and Company, New York (1970)

[Lüt 93] R. Lüthi, H. Haefke, K.P. Meyer, *J. Appl. Phys.* **52** (13), 1103 (1993)

[Lyn 89] L. Lynds, B.R. Weinberger, D.M. Potrepka, G.G. Peterson, M.P. Lindsay, *Physica C* **159**, 61 (1989)

[Mar 01] J.C. Martinez, to be published

[Mar 88] Y. Martin, D.W. Abraham, H.K. Wickramasinghe, *Appl. Phys. Lett.* **52**, 1103 (1988)

[Mar 01a] J.C. Martinez, private communication

[Mat 95] Th. Matthée, J. Wecker, A. Bardal, K. Samwer, *Thin Solid Films* **258**, 264 (1995)

[Mat 75] J.W. Matthews, in: *Epitaxial Growth*, Part B, edited by J.W. Matthews, Academic Press, New York (1975)

[Mau 93] M. Maul, *Thesis*, Technische Hochschule Darmstadt (1993)

[Mau 98] M. Mauer, *Diploma Thesis*, Universität Mainz (1998)

[McC 79] G.M. McCelland, K.L. Saenger, J.J. Valentini, D.R. Herschbach, *J. Phys. Chem.* **83**, 947 (1979)

[McC 68] D.E. McCumber, *J. Appl. Phys.* **39**, 2503 (1968)

[Mes 82] A. Messiah, *Quantenmechanik,* de Gruyter, New York (1982)

[Met 89] S. Metev, K. Metava, *Appl. Surf. Sci.* **43**, 121 (1989)

[Mil 91] S.L. Miller, J.R. Schwank, R.D. Nasby, M.S. Rodgers, *J. Appl. Phys. Lett.* **70**, 2849 (1991)

[Mil 92] S.L. Miller, P.J. McWorther, *J. Appl. Phys. Lett.* **72** (12), 5999 (1992)

[Mis 94] D.S. Misra, B.D. Padalia, S.P. Pai, R. Pinto, S.B. Palmer, *Thin Solid Films* **245**, 186 (1994)

[Mis 91] D.S. Misra, S.B. Palmer, *Physica C* **176**, 43 (1991)

[Mit 69] T. Mitsui, *Ferroelectric Compounds,* Landolt-Bernstein Bd. **3**, Springer Verlag (1969)

[Mor 95] K. Mori, H. Kawano, T. Matsui, Y. Nakayam, *J. Appl. Phys.* **78** (3), 1914 (1995)

[Mue 90] R.E. Muenchhausen, K.M. Hubbard, S. Foltyn, R.C. Estler, N.S. Nogar, C. Jenkins, *Appl. Phys. Lett.* **56**, 578 (1990)

[Mue 91] R.E. Muenchhausen, S. Foltyn, N.S. Nogar, R.C. Estler, E.J. Peterson, X.D. Wu, *Nucl. Instrum. Meth. A* **303**, 204 (1991)

[Nag 96] K. Ngashima, T. Hirai, H. Koike, Y. Fujisaki, Y. Tauri, *Jpn. J. Appl. Phys.* **35**, L1680 (1996)

[Nag 96] M. Nagata, D.P. Vijay, X. Zhang, S.B. Desu, *Phys. Stat. Sol. B* **157**, 75 (1996)

[Nak 91] T. Nakata, M. Kakehata, F. Kannari, *J. Phys. D,* (1991)

[Nak 94] Y. Nakata, W.K.A. Kumuduni, T. Okada, M. Maeda, *Appl. Phys. Lett.* **64** (19), 2599 (1994)

[Nak 97] T. Nakamura, R. Muhammet, T. Shiosaki, *Proc. 6th Int. Symp. On Integrated Ferrolelectrics,* Gordon and Breach (1997)

[NBS 75] *Wavelength and Transition Probabilities for Atoms and atomic Ions*, National Bureau of Standards, Washington DC 20234 (1975)

[Nic 95] S. Nicoletti, H. Moriceau, J.C. Villegier, D. Chateigner, *Physica C* **242**, 99 (1995)

[Nic 96] S. Nicoletti, H. Moriceau, J.C. Villegier, D. Chateigner, B. Bourgeaux, C. Cabanel, J.Y. Laval, *Physica C* **269**, 255 (1996)

[Nix 89] W.D. Nix, *Metall. Trans. A* **20A**, 2217 (1989)

[Nog 96] T. Noguchi, T. Hase, Y. Miyaska, *Jpn. J. Appl. Phys.,* Part 1 **35**, 4900 (1996)

[Noo 87] I. Noorbatcha, R.R. Lucchese, Y. Zeiri, *J. Chem. Phys.* **86**, 5816 (1987)

[Noo 88] I. Noorbatcha, R.R. Lucchese, Y. Zeiri, *J. Chem. Phys.* **89**, 5251 (1988)

[Nov 88] Y. Novis, J.J. Pireaux, A. Brezini, E. Petit, R. Caudano, P. Lutgen, G. Feyder, S. Lazare, *J. Appl. Phys.* **64**, 365 (1988)

[Ois 97] Y. Oishi, Y. Matsumuro, M. Okuyama, *Jpn. J. Appl. Phys.,* Part 1 **36**, 5896 (1997)

[Oki 95] Y. Okimoto, T. Katsufuji, T. Ishikawa, A. Urushibara, T. Arima, Y. Tokura, *Phys. Rev. Lett.* **75**, 109 (1995)

[Opo 66] H. Opower, W. Press, *Z. Nat. Forsch.* **21a**, 344, (1966)

[Pas 91] D.W. Pashsley in *Processing of Metals and Alloys,* ed. R.W. Cahn, *Materials Science and Technology,* Vol. **15**, VCH Verlag, Weinheim, Germany (1991)

[Pei 37] R. Peierls, *Proc. R. Soc.* Ser. A **49**, 72 (1937)

[Per 65] C.H. Perry, D.J. McCarthy, *Phys. Rev.* **138** (5a), 1537 (1965)

[Pfa 59] W.G. Pfann, C.G.B. Garret, *Proc. IRE* **47**, 2011 (1959)

[Pig 99] A. Pignolet, C. Harnega, A.R. James, S. Senz, N.D. Zakharov, D. Hesse, sub. to Proc. Mater. Res. Soc. Symp. Y: *Ferroelectric Thin Films VIII,* Boston, USA (1999)

[Pru 92] W. Prusseit, S. Corsépius, M. Zwerger, P. Berberich, H. Kinder, O. Eibl, C. Jaekel, U. Breuer, H. Kurz, *Physica C* **201**, 249 (1992)

[Qia 95] J. Qiao, C.Y. Yang, *Mat. Sci. and Eng.* **R14**, 157 (1995)

[Rae 92] A.D. Rae, J.G. Thompson, R.L. Withers, *Acta Cryst.* **B48**, 418 (1992)

[Ras 99] A.C. Rastogi, S. Tirumala, S.B. Desu, *Appl. Phys. Lett.* **74** (23), 3492 (1999)

[Rea 71] J.F. Ready, *Effects of High Power Laser Irradiation,* Academic, New York (1971)

[Ren 96] S.B. Ren, C.J. Lu, J.S. Liu, H.M. Shen, Y.N. Wang, *Phys. Rev. B* **54** (20), 14337 (1996)

[Rie 94] E. Riedel, *Anorganische Chemie*, 3. Auflage, de Gruyter, Berlin (1994)

[Rij 97] G.J.H.M. Rijnders, G. Koster, D.H.A. Blank, H. Rogalla, *Appl. Phys. Lett.* **70** (14), 1888 (1997)

[Rod 96] M.A. Rodriguez, T.J. Boyle, B.A. Hernandez, C.D. Buchheit, M.O. Eatough, *J. Mat. Res.* **11** (9), 2282 (1996)

[Ros 00] Ch. Rossel, IBM Research Division-Zürich Research Laboratory, private comm.

[Sad 95] J.E. Sader, I. Larson, P. Mulvaney, *Rev. Sci. Instrum.* **66**, 3789 (1995)

[Sae 81] K.L. Saenger, *J. Chem. Phys.* **75**, 2467 (1981)

[Sae 91] K.L. Saenger, *J. Appl. Phys.* **70**, 5629 (1991)

[Sak 93] Y. Sakashita, H. Segawa, *J. Appl. Physics* **73**, 7857 (1993)

[San 92] F. Sanchez, M. Varela, X. Queralt, R. Aguiar, J.L. Morenza, *Appl. Phys. Lett.* **61** (18), 2228 (1992)

[Sat 97] N. Sata, H. Matsuta, Y. Akiyama, Y. Chiba, S. Shin, M. Ishigame, *Sol. State Ionics* **97**, 437 (1997)

[Sat 98] N. Sata, H. Yugami, Y. Akiyama, T. Hattori, S. Yamaguchi, M. Ishigame, *Sol. State Ionics* **121**, 321 (1998)

[Sau 90] F. Saurenbach, B.D. Terris, *Appl. Phys. Lett.* **56** (13), 1703 (1990)

[Saw 29] C.B. Sawyer, C.H. Tower, *Phys. Rev. B* **35**, 269 (1929)

[Sch 99] J. Schumacher, *Diploma Thesis*, Universität Mainz (1999)

[Sch 01] J. Schumacher, J.C. Martinez, R.Raiteri, M.Maier, H.J. Butt, H. Adrian, to appear in *Ferroelectrics* (2001)

[Sch 96] D.G. Schlomm, E.S. Hellmann, E.H. Hartford, C.B. Eom, J.C. Clark, J. Mannhart, *Journal of Mat. Res.* **11**, 1336 (1996)

[Sch 98] Ch. Schwan, F. Martin, G. Jakob, J.C. Martinez, H. Adrian, *Mat. Res. Soc. Symp. Proc.* **493**, 93 (1998)

[Sch 99a] Ch. Schwan, *Thesis,* Universität Mainz (1999)

[Sco 88] J.F. Scott, B. Pouligny, *J. Appl. Phys. Lett.* **64**, 1547 (1988)

[Sei 98] P. Seidel, S. Linzen, G. Kaiser, F. Schmidl, Y. Tian, A. Matthes, A. Wunderlich, H. Schneidewind, in *Superconducting and related Oxides: Physics and Nanoengineering III*, Proceedings of SPIE Vol. 3481 (1998)

[Set 93] N. Setter, E. Colla, *Ferroelectric Ceramics*, Birkhäuser Verlag (1993)

[Sha 63] S. Shapiro, *Phys. Rev. Lett.* **11**, 80 (1963)

[Shi 99] Y. Shimakawa, Y. Kubo, F. Izumi, *Appl. Phys. Lett.* **74** (13), 1904-1906 (1999)

[Shi 88] T. Shiota, K. Takechi, Y. Takai, *Proc. 1st Int. Symp. On Supercon.,* (ed. K. Kitizawa, T. Ishiguru), 755, Springer, Tokyo (1988)

[Shi 97] T. Shimara, G. Egusa, H. Iwahara, K. Katahira, K. Yamamoto, *Sol. States Ionics* **97**, 477 (1997)

[Shi 98] Y. Shimakawa, Y. Nakagawa, Y. Kubo, *Ferroelec. Thin Films* **7**, MRS Pittsburgh (1998)

[Shi 99] Y. Shimakawa, Y. Kubo, F. Izumi, *Appl. Phys. Lett.* **74** (13), 1904 (1999)

[Sho 39] W. Shockley, *Phys. Rev.* **56**, 317 (1939)

[Sin 90] R. K. Singh, J. Narayan, *Phys. Rev. B* **41**(13), 8843 (1990)

[Sin 90a] R.K. Singh, O.W. Holland, J. Narajan, *J. Appl. Phys.* **68**, 233 (1990)

[Sin 91] S. Sinharoy, D.R. Lampe, H. Buhay, *Proc. 3rd Int. Symp. on Integrated Ferrolelectrics,* Gordon and Breach (1991)

[Sko 93] G.I. Skofrounick, A.H. Carim, S.R. Foltyn und R.E. Muenchhausen, *Journal of Materials Research* **8**, 2785 (1993)

[Sla 50] J.C. Slater, *Phys. Rev.* **78**, 748 (1950)

[Smi 65] H.M. Smith, A.F. Turner, *Appl. Opt.* **4**, 147 (1965)

[Spa 97] M. Spankova, S. Gazi, S. Chromik, A. Rosova, I. Vavra, S. Benacka, *J. of Low Temp. Phys.* **106**, 439 (1997)

[Spr 72] J.A. Sprague, J.E. Westmoreland, F.A. Smidt Jr., P.R. Malmberg, *Trans. ANS* **16**, 163 (1972)

[Sta 63] H.L. Stadler, P.J. Zachmanidis, *J. Appl. Phys.* **34** (11), 3255 (1963)

[Ste 68] W.C. Stewart, *Appl. Phys. Lett.* **12**, 277 (1968)

[Sto 95] C. Stölzel, *Thesis,* Technische Hochschule Darmstadt (1995)

[Str 97] B.A. Stryer, A.P. Levanuk, *Ferroelectric Phenomena in Crystals,* Springer Verlag (1997)

[Str 98] M. Strikovski, J.H. Miller, *Appl. Phys. Lett.* **73** (12), 1733 (1998)

[Sze 81] S.M. Sze, *Physics of Semiconductor Devices,* John Wiley & Sons (1981)

[Tar 87] J.M. Tarascon, L.H. Greene, B.G. Bagley, W.R. McKinnon, P. Barboux, G.W. Hull, in *Novel Superconductivity* (ed. S.A. Wolf, V.Z. Kresin), Plenum, New York (1987)

[Taw 87] A. Tawfink, M.K. El-Nimr, D. El-Cony, *Powder Metallurgy Int.* **19** (5), 34 (1987)

[Tay 96] P. Tayebati, D. Trivedi, M. Tabat, *Appl. Phys. Lett.* **69**, 1023 (1996)

[Tay 97] D.V. Taylor, D. Damjanovic, *J. Appl. Phys.* **82** (4), 1973 (1997)

[Tay 98] G.W. Taylor, A.S. Bhalla, J.F. Scott, *Ferrolect. Rev.* **1**, 33-41 (1998)

[Ter 62] L.M. Terman, *Solid States Electronics* **5**, 285 (1962)

[Tho 96] D.T. Thomas, N. Fujimura, S.K. Streiffer, O. Auciello, A.J. Kingon, *Proc. of the 10th Int. Symp. on Appl. of Ferroelectrics,* Vol. **1**, 495 (1996)

[Tie 63] P.K. Tien, J.P. Gordon, *Phys. Rev. Lett.* **129**, 647 (1963)

[Tie 89] L.A. Tiety, C.B. Carter, D.K. Lathrop, S.E. Russek, R.A. Buhrmann, J.R. Michael, *J. Mat. Res.* **4**, 1072 (1989)

[Tin 76] M. Tinkham, Introduction to Superconductivity, 1nd ed., ch. 7.6, McGraw-Hill (1976)

[Tin 96] M. Tinkham, Introduction to Superconductivity, original edition, McGraw-Hill (1996)

[Tsh 90] H. Tshiwaba, N. Tsuji, H. Mori, S. Suzuki, Y. Ueda*, Appl. Phys. Lett.* **56**, 1332 (1990)

[Tsu 97] S. Tsunekawa, T. Fukada, T. Osaki, Y. Yoneda, H. Terauchi, *Appl. Phys. Lett. 71*, 1486 (1997)

[Uda 95] K.R. Udayakumav, P.J. Schuele, J. Chen, S.B. Krupanidhi, L.E. Cross, *J. Appl. Physics* **77**, 3981 (1995)

[Urb 93] H.M. Urbassek, D. Sibold, *Phys. Rev. Lett.* **70**, 1886 (1993)

[Val 20] J. Valasek, *Phys. Rev.* **15**, 537-542 (1920)

[Ven 88] T. Venkatesan, X.D. Wu et al., *Appl. Phys. Lett.* **53**, 1431 (1988)

[Ver 97] K. Verbist, O.I. Lebedev, G. Van Tendeloo, M.A.J. Verhoeven, A.J.H.M. Rijnders, D.H.A. Blank, H. Rogalla, *Appl. Phys. Lett.* **70** (3), 1167 (1997)

[Wan 94] Y.G. Wang, W.L. Zhong, P.L. Zhang, *Phys. Rev. B* **51** (8), 5311 (1994)

[War 69] B.E. Warren, *X-ray Diffraction,* Addison-Wesley, Readling, Massachusetts, USA (1969)

[War 30] H. v. Wartenberg, H. Werth, *Z. Anorg. Allgem. Chem.* **190**, 178 (1930)

[Wat 95] S. Watanabe, T. Fujiu, *Appl. Phys. Lett.* **66**, 6762 (1995)

[Wec 92] Wecker et al., *Mat. Res. Soc. Symp. Proc.* **275** (1992)

[Wei 95] C. Weissmantel, C. Hamann, *Grundlagen der Festkörper-physik,* Springer Verlag (1995)

[Wen 93] J.G. Wen, C. Traeholt, H.W. Zandbergen, K. Joosse, E.M.C.M. Reuvekamp, H. Rogalla, *Physica C* **218**, 29 (1993)

[Wie 92] K. Wien, *Nucl. Instrum. Meth. B* **65**, 149 (1992)

[Wie 01] Leonore Wiehl, to be published

[Wu 90] X.D. Wu, R.E. Muenchausen, S. Foltyn, R.C. Estler, R.C. Dye, C. Flamme, N. Nogar, A.R. Garcia, J. Martin, J. Tesmer, *Appl. Phys. Lett.* **56**, 1481 (1990)

[Wu 92] X.D. Wu, L. Luo, R.E. Muenchhausen, K.N. Springer, S. Foltyn, *Appl. Phys. Lett.* **60** (11), 1381 (1992)

[Xio 99] S.B. Xiong, S. Sakai, *Appl. Phys. Lett.* **75** (11), 1613 (1999)

[Xu 74] Y. Xu, *Ferroelectric materials and their Applications,* North-Holland, Amsterdam (1974)

[Yan 95] H.C. Yang, J.H. Lu, S.D. Lin, L.C. Ku. M. Cho, W.B. Lian, M.Y. Chem, *J. Appl. Phys.* **78** (3), 1871 (1995)

[Yan 98] P. Yang, N. Zhou, L. Zheng, I. Lu, C. Lin, *Phys. D: Appl. Phys.* **30**, 527 (1998)

[Ytr 77] T. Ytrehus, in *Rarefield Gas Dynamics*, **Vol. II**, edited by J.L. Potter, AIAA, New York, p. 1197 (1977)

[Yug 97] H. Yugami, H. Naito, H. Arashi, *Appl. Surf. Sci.* **113/114**, 222 (1997)

[Zav 97] G. Zavala, J.H. Fendler, S. Trolier-McKinstry, *J. Appl. Phys.* **81** (11), 7480 (1997)

[Zel 66] Ya.B. Zel`dovich, Yu.P. Raizer, in *Physics of Shock Wave and High Temperature Hydrodynamic Phenomena,* Vol. **I**, Academic Press, New York, p. 94 (1966)

[Zhi 59] P.N. Zhirnov, *Soviet Physics JETP* **35** (8), No. 5, 822 (1959)

Publications

Rastertunnelmikroskopie an den Vanadiumoxiden V_2O_5 und V_6O_{13} und Aufbau eines Tieftemperatur-Rastertunnelmikroskops

M. Maier, *Diplomarbeit,* Technische Hochschule Darmstadt (1996)

Tip induced changes of atomic scale images of the vanadiumpentoxide surface

R.A. Goschke, K. Vey, M. Maier, U. Walter, E. Goering, M. Klemm and S. Horn, *Surface Science* **348** (3), 305-310 (1996)

Current dependence of grain boundary magnetoresistance in $La_{0.67}Ca_{0.33}MnO_3$ films

W. Westerburg, F. Martin, S. Friedrich, M. Maier and G. Jakob, *Journal of Applied Physics* **86**, 2173-2177 (1999)

Transport and magnetic properties of $La_{1-x}Ca_xMnO_3$ films ($0.1 < x < 0.9$)

G. Jakob, F. Martin, S. Friedrich, W. Westerburg and M. Maier, *Physica B,* **284-288**, 1440 (2000)

Alternative Buffer-Layers for the of $SrBi_2Ta_2O_9$ on silicon substrates

J. Schumacher, J.C. Martinez, F. Martin, M. Maier and H. Adrian, *Ferroelectrics,* accepted (2000)

$BaZrO_3$ as a buffer layer for high Tc superconducting thin film applications

M Maier, M. Mauer, F. Martin, J.C. Martinez and H. Adrian, IOP Publishing, accepted (2000), Proceedings of the 4th European Conference on Applied Superconductivity 1999, Sitges, Spain

$Bi_2Sr_2CaCu_2O_{8+x}$ epitaxial thin films on silicon substrates

S. Ingebrandt, J.C. Martinez, M. Basset, M. Mauer, M. Maier and H. Adrian, IOP Publishing, accepted (2000), Proceedings of the 4th European Conference on Applied Superconductivity 1999, Sitges, Spain

Acknowledgements

The last few years and the work that has filled up a good part of it (the results of which you may have just read) have been at the same time challenging and interesting, stressful and enjoyable. Many people have contributed - except maybe for the stressful part, which was mostly machine- and self-made. It has been more than a valuable experience.

First of all, I would like to thank my supervisor for giving me the opportunity to complete this PhD thesis in his work group, for always being interested in the experiments and analyses, and for providing all the support a PhD student can ask for.

I am deeply grateful to my person in charge, the head of our device group, for many useful and enlightening discussions. My work has probably benefited more than I can estimate from his knowledge and understanding of physics. Also, I wish to thank all the other post-doctors of my workgroup, who also have always been very helpful and supportive in every way. I owe thanks to many physicists for good collaborations and fruitful discussions about pulsed laser deposition and physics of thin films.

I am indebted to all the engaged young physicists, that have been working on the Laserablation system and which I call “my” Diploma-students. Without their initiative, I would probably never have pursued many of the topics which make up this work. For their good company, the interesting discussions, the never-ending entertainment, and their good sense of humour, I am thankful to my colleagues, and all other members of my workgroup.

Yet most of all, I wish to thank my parents, who have helped me to arrive at this point. Neither last not least I wish to thank my girlfriend, who had to abide a frequently confused physicist.

Eidesstattliche Erklärung

Hiermit erkläre ich an Eides statt, daß ich die vorliegende Arbeit selbständig und nur unter Verwendung der angegebenen Hilfsmittel angefertigt habe.

Bisher habe ich noch keinen Promotionsversuch unternommen.

Mainz, 2001